MICROFLUIDICS AND IMAGING TECHNIQUES FOR HIGH-THROUGHPUT STUDIES OF EARLY EMBRYONIC DEVELOPMENT

A Dissertation

Presented to

The Academic Faculty

by

Thomas J. Levario

In Partial Fulfillment

of the Requirements for the Degree

Doctor of Philosophy in the

School of Chemical and Biomolecular Engineering

Georgia Institute of Technology

August 2016

MICROFLUIDIC AND IMAGING TECHNIQUES FOR HIGH-THROUGHPUT STUDIES OF EARLY EMBRYONIC DEVELOPMENT

Approved by:

Dr. Hang Lu, Advisor
School of Chemical and Biomolecular Engineering
Georgia Institute of Technology

Dr. Todd Streelman
School of Biology
Georgia Institute of Technology

Dr. Victor Breedveld
School of Chemical and Biomolecular Engineering
Georgia Institute of Technology

Dr. Stanislav Y. Shvartsman
School of Engineering and Applied Science
Princeton University

Dr. Julie Champion
School of Chemical and Biomolecular Engineering
Georgia Institute of Technology

Date Approved: May 11, 2016

To my family for being there and exercising great patience.

ACKNOWLEDGEMENTS

I wish to thank my labmates for being awesome. I wish to thank my advisor Dr. Hang Lu for providing me the freedom to explore my own ideas, while giving plenty of guidance so that I did not lose my way. I wish to thank my thesis committee for providing a fresh perspective on our work and helping to structure our ideas.

I wish to thank my family for being patient with this process. I especially want to thank my wife Kaileen for being understanding, and really giving me the strength to push through this process. I wish to thank my mother, father, brother Mark, and sister Jennie for also understanding how difficult this was for me to be away from them. And I really have to thank my brother's boy, Charlie, for being so adorable, and providing me motivation to get this done.

TABLE OF CONTENTS

Page

ACKNOWLEDGEMENTS iv

LIST OF TABLES ix

LIST OF FIGURES x

SUMMARY xxiv

CHAPTER

1 INTRODUCTION 1

1.1 Background 1

1.2 *Drosophila melanogaster* as a Model for Development 2

1.3 Fluorescence Microscopy for Imaging Development 4

1.4 Microfluidics and Automation for Manipulating *Drosophila* Embryos 6

1.4.1 Microfluidic Sorting of Embryos 7

1.4.2 Microfluidics-Assisted Microinjection of Embryos 8

1.4.3 Microfluidics-Enabled Spatial Perturbation of Embryos 9

1.4.4 Microfluidic Arraying of Embryos for Imaging 10

1.5 Image Analysis Software for Developmental Biology 11

1.5.1 Automated Cell Lineaging 12

1.5.2 Virtual Embryos 13

1.5.3 Computer Vision for Automated Phenotyping 14

1.6 Thesis Contributions and Significance 16

2 AN OPTIMIZED MICROFLUIDIC ARRAY FOR DORSAL-VENTRAL IMAGING AND PROVIDING PRECISE ENVIRONMENTAL PERTURBATION TO LIVE DROSOPHILA EMBRYOS 18

2.1 Introduction 18

2.2 Materials and Methods 20

2.2.1 Fabrication of the Dorsal-Ventral (DV) Array 21

2.2.2 Fly Strains and Embryo Loading 22

2.2.3 Finite Element Modeling of Fluid Dynamics and Oxygen Transport within the DV Array 23

2.2.4 Time-Lapse Confocal Microscopy 24

2.2.5 On-Chip Oxygen Manipulation 25

2.2.6 Cell Cycle Kinetics Quantification 27

2.3 Results 27

2.3.1 DV Array Optimization for End-On Imaging of Live Embryos 27

2.3.2 Embryos Show Normal Developmental Progression after Trapping in the DV Array 38

2.3.3 Nuclear Cycle Kinetics Analysis Indicates Embryos Develop at a Normal Rate in the DV Array 41

2.3.4 Effects of Anoxia Exposure are Short-Lived and Delay Overall Development 46

2.4 Discussion and Conclusions 59

3 HIGH-THROUGHPUT ARRAYING AND IMAGING OF LATERALLY ORIENTED LIVE DROSOPHILA EMBRYOS 62

3.1 Introduction 62

3.2 Materials and Methods 63

3.2.1 Single-Layer Anterior-Posterior (AP1) Array Fabrication and Preparation 63

3.2.2 *Drosophila* Strains and Embryo Preparation 64

3.2.3 AP1 Array Loading 65

3.2.4 Time-Lapse Confocal Microscopy 65

3.2.5 Finite Element Modeling of AP1 Array Fluid Dynamics 66

3.3 Results and Discussion 66

3.3.1 AP1 Design for Arraying Laterally Oriented Embryos 66

3.3.2 AP1 Facilitates Simple and Efficient Arraying of Laterally Oriented Embryos 70

3.3.3 AP1 Arraying Allows All Dorsal-Ventral Orientations to be Viewed On-Chip Simultaneously 74

3.3.4 AP1 Arraying Does Not Affect Nuclear Cycling Dynamics 77

3.3.5 Two Simultaneous Mitotic Wave-fronts is More Commonly Observed than a Single Mitotic Wave-front 80

3.3.6 Effect of Nuclear Cycle Number on Mitotic Wave-front Properties 87

3.4 Conclusion 94

4 STATISTICAL COMPARISON OF INTERCELLULAR DYNAMICS VIA MICROFLUIDICS AND COMPUTER VISION 96

4.1 Introduction 96

4.2 Materials and Methods 97

4.2.1 Fabrication of the Two-Layer Anterior-Posterior (AP2) Array 97

4.2.2 Three-Dimensional Finite Element Modeling of AP2 Array Fluid Dynamics 98

4.2.*3 Drosophila melanogaster* Strains and Embryo Preparation 99

4.2.4 AP2 Arraying of Embryos for Time-Lapse Microscopy 99

4.2.5 Algorithm for Quantifying Single-Cell Dynamics 100

4.3 Results 100

4.3.1 Development of the AP2 Array 100

4.3.2 Construction of Spatiotemporal Capicua Patterning Heat-maps 104

4.3.3 Quantifying Developmental Dynamics 109

4.3.4 Effects of Developmental Dynamics by Culture Temperature 125

4.3.5 Effects of RTK Gain-of-Function on Capicua Signaling Dynamics 133

4.4 Discussion and Conclusions 149
5 OVERALL CONCLUSIONS AND FUTURE DIRECTIONS 153
5.1 Thesis Contributions 153
5.2 Future Directions 157
APPENDIX A: Publications and Other Scientific Activity 160
A.1 Published/Accepted Manuscripts 160
A.2 Manuscripts in Review or in Preparation 161
A.3 Conference Presentations 161
APPENDIX B: Photomask Designs 164
B.1 Photomask for Chapter 2 Single-Layer Dorsal-Ventral (DV) Array 164
B.2 Photomask for Chapter 3 Single-Layer Anterior-Posterior (AP1) Array 165
B.3 Photomasks for Chapter 4 Two-Layer Anterior-Posterior (AP2) Array 166
APPENDIX C: Matlab Code for Quantifying Nuclear Cycling Dynamics 167
APPENDIX D: Matlab Code for Single-Cell Measurements of Capicua Dynamics 170
REFERENCES 178

LIST OF TABLES

Page

Table 2.1: Summary of the observed relationship between anoxia-induced developmental arrest, cell cycle phase arrest checkpoint, and embryo survival after recovery from anoxia-induced developmental arrest 59

LIST OF FIGURES

Page

Figure 2.1: Method protocol: Load device with live embryos. *In vivo* live imaging of end-on oriented embryos. Delivery of gas-phase stimuli (in this case humidified nitrogen gas), and continue *in vivo* live imaging developmental responses. Confocal microscopy images of live embryo development are then automatically segmented and used for morphometric analysis and data extraction to analyze developmental responses to stimuli. 20

Figure 2.2: Optimized dorsal-ventral live imaging array. a) Fully constructed dorsal-ventral microfluidic array with channels filled with green dye. b) Scanning electron micrograph of embryo traps and focusing channel. 22

Figure 2.3: Delivery of anoxic gas via serpentine channel. a) Frames from video showing delivery of humidified nitrogen gas to live embryos on-chip. b) Zoom-in of boxed region in (a) indicating embryos remain oriented for end-on imaging with a reservoir of PBST found in resistance channels that keep embryos from drying out during anoxia exposure. 26

Figure 2.4: COMSOL simulations of combined fluid and mass transport in the original microfluidic array. a) Line plots depicting oxygen concentration along the serpentine channel as a function of time in a microfluidic array with dimensions equivalent to that described by our previous large array. Even after 10 minutes of circulating anoxic gas there is still a significant oxygen concentration gradient along the serpentine channel. b) Surface plots depicting oxygen concentration in the serpentine channel and PDMS at the entrance and exit of the large microfluidic array. Significant oxygen concentration gradient in the serpentine channel from entrance to exit of the large microfluidic array. 29

Figure 2.5: Overall layout for the optimized dorsal-ventral live imaging array with main serpentine channel (■), focusing channels (■), and embryo traps and resistance channels (■).b) Zoom-in of boxed region of (a) with dimensions of the embryo trap and resistance channel. 31

Figure 2.6: COMSOL simulations of combined fluid and mass transport for the optimized dorsal-ventral live imaging array. a) Line plots depicting oxygen concentration along the serpentine channel as a function of time in a microfluidic array with dimensions equivalent to that described in this paper. After 1 minute of circulating anoxic gas there is <2% oxygen present within the serpentine channel, and <0.1% oxygen after 2 minutes. b) Surface plots depicting oxygen concentration in the serpentine channel and PDMS at the entrance and exit of the small microfluidic array. Constant oxygen concentration in the serpentine channel from entrance to exit of the small microfluidic array. 32

Figure 2.7: Device loading and COMSOL simulation for the original dorsal-ventral microfluidic array. a) Typical device loading for microfluidic array employing previously developed embryo trap, ▼ indicate empty traps, ▼ indicate traps with embryos successfully loaded. b) Frames from live embryo loading in (a) showing embryos do not successfully trap in device. ○ is tracking a single embryo through successful trapping. c) COMSOL simulation of the non-optimized microfluidic array exhibiting Dean flow and high flow velocity in the serpentine channel relative to embryo traps and resistance channels. 34

Figure 2.8: Device loading and COMSOL simulation for the optimized dorsal-ventral microfluidic array. a) Typical device loading for optimized microfluidic array. ▼ indicate empty traps, ▼ indicate traps with embryos successfully loaded. b) Frames from live embryo loading in (a) showing embryos successfully trap in device. ○ is tracking a single embryo through successful trapping. c) COMSOL simulation of the optimized microfluidic array exhibiting Dean flow and lower flow velocity in the serpentine channel relative to the non-optimized microfluidic array in Figure 2.7. 36

Figure 2.9: Each pair of images are single time points from a time-lapse imaging video of a live developing embryo expressing a Histone-GFP transgene within the microfluidic array. The video was 3 hours in total length, and each time-point is stamped with the time that each event occurred. The time is relative to the start time when the confocal microscope began scanning. Top image is a merge of bright-field and Histone-GFP channels, while the bottom image is only the Histone-GFP channel. From left to right: tope row: nuclear cycle 10, nuclear cycle 11, nuclear cycle 12, nuclear cycle 13; bottom row: stage 5, stage 6, stage 7, and stage 8. 40

Figure 2.10: The average area of a nucleus trajectory for a single embryo; the same embryo found in Figure 2.9. i-viii indicate the time point at which each image in Figure 2.9 was taken. i) Stage 4, nuclear cycle 10. ii) Stage 4, nuclear cycle 11. iii) Stage 4, nuclear cycle 12. iv) Stage 4, nuclear cycle 13. v) Stage 5. vi) Stage 6. vii) Stage 7. viii) Stage 8. 42

Figure 2.11: High magnification imaging of cell cycle. a) 63X confocal imaging of Histone-GFP expressing embryo and nuclear cycle phases. ▼ indicates the same nuclei proceeding from nuclear cycle 12 interphase to prophase to metaphase to anaphase to telophase. After telophase, the nuclei was lost due to significant z-drift caused by yolk contractions during nuclear cycle 13 interphase. b) Nuclear area trajectory for embryo found in (a). ix-xiv indicate the time point at which each image in (a) was taken. ix) Interphase, nuclear cycle 12. x) Prophase, nuclear cycle 12. xi) Metaphase, nuclear cycle 12. xii) Anaphase, nuclear cycle 12. xiii) Telophase, nuclear cycle 12. xiv) Interphase, nuclear cycle 13. 44

Figure 2.12: Quantifying on-chip developmental dynamics. a) Average nuclear area trajectory ± S.E.M. for embryos developing on-chip exhibits stereotyped oscillations that corresponds with stage 4-5 of development (n = 35 embryos). b) Measured nuclear cycle duration for Histone-GFP expressing embryos developing on-chip as extracted by examining the peak widths found in Figure 2.12. Average ± S.E.M. duration of nuclear cycle 10, 11, 12, 13, and stage 5 are 7.8 ± 0.2 minutes (n = 27 embryos), 9.9 ± 0.2 minutes (n = 32 embryos), 11.4 ± 0.1 minutes (n = 35 embryos), 16.9 ± 0.2 minutes (n = 35 embryos), and 59.3 ± 1.4 minutes (n = 25 embryos), respectively. 45

Figure 2.13: Immediate effects of anoxia exposure on embryo development. a) Frames from *in vivo* live imaging a Histone-GFP expressing embryo progressing through nuclear cycle 13 (control). b) Frames from *in vivo* live imaging a Histone-GFP expressing embryo progressing through nuclear cycle 13 that exhibits anoxia-induced metaphase arrest. c) Average ± S.E.M. nuclear area trajectory for embryos grown in (i) normoxia (n = 35 embryos), and (ii) experiencing 10 minutes of anoxia during nuclear cycle 13 (n = 14 embryos). Shaded region in (ii) indicates when anoxia was delivered. Black triangle indicates telophase to interphase 14 transition. d) Average ± S.D. durations for nuclear cycles 10, 11, 12, 13, and stage 5 for embryos grown in normoxia (control, n = 35 embryos), and experiencing 10 minutes of anoxia during nuclear cycle 13 (NC 13 arrest, n = 14 embryos). Nuclear cycles 10-12 and stage 5 durations are not significant (NS) while nuclear cycle 13 is statistically different from control (****p<0.0001. T-test). 49

Figure 2.14: Recovery from anoxia-induced developmental arrest. a) Frames from *in vivo* live imaging a Histone-GFP expressing embryo that successfully recovers from anoxia-induced developmental arrest. i) nuclear cycle 12, ii) nuclear cycle 13, iii) nuclear cycle 13 arrest in metaphase, iv) nuclear cycle 13 anaphase-telophase transition, v) stage 5, and vi) ventral furrow formation. b) Frames from *in vivo* live imaging a Histone-GFP expressing embryo that does not recover from anoxia-induced developmental arrest. i) nuclear cycle 12, ii) nuclear cycle 13, iii) nuclear cycle 13 arrest in metaphase, iv) nuclear cycle 13 anaphase-telophase transition (white triangles indicate fused daughter nuclei), and v-vi) nuclear delamination. 51

Figure 2.15: Plots showing the timing of milestone events for individual embryos on-chip with population averages for the timing of each event (|). Milestones include nuclear division (ND) 10, 11, 12, and 13, and ventral furrow formation (VFF). Embryos 1-14 are grown entirely in normoxia, and embryos 15-27 are exposed to brief anoxia in nuclear cycle 13 (anoxia indicated by -). The timing of nuclear division 13, and ventral furrow formation are statically different from control (****p<0.0001. T-test). 53

Figure 2.16: Effects of brief anoxia on nuclear cycle kinetics for cycles 12, 13, and 14. a) Average ± S.D. durations for nuclear cycles 10, 11, 12, 13, and stage 5 for embryos grown in normoxia (control, n = 35 embryos), and experiencing 10 minutes of anoxia during nuclear cycle 12 (NC 12 arrest, n = 3 embryos), 13 (NC 13 arrest, n = 14 embryos), and 14 (Stage 5 arrest, n = 17 embryos). Nuclear cycles not experiencing anoxia exhibit durations that are not significant (NS) while nuclear cycles that experience anoxia are statistically different from control (*p<0.05 and ****p<0.0001. T-test). b) Plots showing the timing of milestone events for individual embryos on-chip with population averages for the timing of each event (|). Milestones include nuclear division (ND) 10, 11, 12, and 13, and ventral furrow formation (VFF). Embryos 1-14 are grown entirely in normoxia, embryos 15-24 are exposed to brief anoxia in nuclear cycle 14 (anoxia indicated by -), embryos 25-35 are exposed to brief anoxia in nuclear cycle 13, and embryos 35-38 are exposed to brief anoxia in nuclear cycle 12. The timing of subsequent milestones are statically different from control (*p<0.05, **p<0.01, and ****p<0.0001. T-test). 55

Figure 2.17: Morphological comparison between interphase and metaphase arrest. a) Frames from *in vivo* live imaging a Histone-GFP expressing embryo progressing through nuclear cycle 13 (control). b) Frames from *in vivo* live imaging a Histone-GFP expressing embryo progressing through nuclear cycle 13 that exhibits anoxia-induced metaphase arrest. c) Frames from *in vivo* live imaging a Histone-GFP expressing embryo progressing through nuclear cycle 13 that exhibits anoxia-induced interphase arrest. 57

Figure 2.18: Average ± S.E.M. nuclear area trajectory for embryos grown in (i) normoxia (n = 35 embryos), and (ii) experiencing 10 minutes of anoxia during nuclear cycle 14 (n = 17 embryos), nuclear cycle 13 metaphase arrest (n = 8 embryos), and nuclear cycle 13 interphase arrest (n = 6 embryos). Shaded region in (ii-iv) indicates when anoxia was delivered. Closed triangle indicates telophase to interphase 14 transition. Open triangle indicates onset of gastrulation. 58

Figure 3.1: 3D representation of a *Drosophila* embryo loading into a single embryo trap in the AP1 array for time-lapse imaging. Trap geometry dictates that embryos enter the trap laterally with the anterior-posterior axis running along the length of the trap. 67

Figure 3.2: The optimized AP1 array. a) Overall device layout with dimensions consisting of 4 individual units: serpentine channel, focusing channels (x16), embryo traps (x20), and resistance channels (x20). Embryos enter the device through the inlet to the serpentine channel at the top of the device. Embryos travel along the serpentine until they encounter an embryo trap, at which cross-flow through focusing channels, embryo traps, and resistance channels drive embryos into embryo traps. Once all traps are occupied by a single embryo, remaining embryos are carried by the serpentine to the device outlet at the bottom of the device. b) Scanning electron micrograph of PDMS mold showing two embryo traps in two different rows connected by the serpentine channel. c) Optical micrograph of entire microfluidic array device with channels filled green dye. 69

Figure 3.3: Efficient trapping and arraying of lateral oriented *Drosophila* embryos via the optimized AP1 array. Typical loading results are depicted in this figure wherein filled triangles indicate traps with embryos successfully loaded while open triangles indicate empty traps with no embryo loaded. 71

Figure 3.4: Comparison of the optimized design and an initial design of the AP1 array. a) The optimized AP1 array with narrow focusing channels (see top row). b) An initial design of the AP1 array that closely mimicked the optimized dorsal-ventral array from Chapter 2. As such, this initial design employed wide tapering focusing channels (see top row). 72

Figure 3.5: The importance of microfluidic design architecture and trapping efficiency. Device loading experiments and COMSOL simulations for a) an initial device design and b) the optimized device design. i) Typical loading results. Filled triangles- traps with embryos successfully loaded, open triangles- empty traps with no embryo loaded. The optimized device exhibits an average loading efficiency of 87 ± 6 %, while the initial device clogged within the serpentine channel every time. ii) Time-lapse optical micrographs of embryo loading. Open circle in a.ii indicates the nascent clog that resulted in a.i, while the open circle in b.ii tracks a single embryo from device entry to successful loading. iii) COMSOL simulations of flow rate through the microchannels. The initial design exhibits a decreased flow rate within the serpentine in transitioning from the first row to the second row, which is consistent with clog location in loading experiments, while the optimized device exhibits uniform flow rate throughout the serpentine channel. 73

Figure 3.6: Imaging morphogenesis and embryo orientation. Maximum intensity projection time-lapse confocal microscopy images of his-GFP expressing embryos from a) dorsal, b) lateral, and c) ventral sides. Anatomical axes are indicated in i) by: A- anterior, P- posterior, D- dorsal, V- ventral, L- left, and R- right. Filled triangle- cephalic furrow, open triangle- pole cell migration, filled circle- transverse furrow invagination, open circle- stomodeal invagination. Ventral furrow formation is visible in c.ii as a wide groove along a majority of the anterior-posterior axis. Time is relative to the start time on the confocal microscope. 75

Figure 3.7: Embryo orientation preference for the AP1 array. a) The dorsal-ventral orientation of laterally oriented embryos within the AP1 array. Error bars are standard deviation. b) The anterior-posterior orientation of laterally oriented embryos within the AP1 array. The anterior-posterior orientation refers to which pole enters the trap first. 77

Figure 3.8: Maximum intensity projection time-lapse confocal microscopy images of a stage 4 his-GFP expressing embryo with the green channel on top and the transmitted light channel on bottom. Nuclear cycles a) 10, b) 11, c) 12, and d) 13 are depicted. Anatomical axes are indicated in a) by: A- anterior, P- posterior, L- left, and R- right. Time is relative to the start time on the confocal microscope. 78

Figure 3.9: Nuclear cycle durations for his-GFP expressing embryos in control conditions (off-chip), within the optimized lateral array device (on-chip: AP1 array), and within the dorsal-ventral array that previously described in Chapter 2 of this thesis (on-chip: DV array). The durations are averages with standard deviation error bars. n = 7, 24, and 30 embryos for off-chip, AP1 array, and DV array conditions, respectively. All nuclear cycle durations are not statistically different between experimental conditions based on a student's T-test ($p > 0.05$). 80

Figure 3.10: Mitotic wave-front phenotypes. Single z-slice time-lapse confocal microscopy images of two his-GFP expressing embryos exhibiting either a) two mitotic wave-fronts, or b) one mitotic wave-front during nuclear division 13. White arrows indicating cells that have transitioned from metaphase to anaphase. Anatomical axes are indicated in by: A- anterior, P- posterior, L- left, and R- right while imaging through the ventral side of the embryo. Time is relative to the first frame in which all cells are in metaphase just prior to mitotic wave-front initiation. 81

Figure 3.11: Wave-front count for all imaged embryos with the indicated pole at which the mitotic wave-front initiated. For embryos exhibiting two wave-fronts, the wave-front initiation site refers to the pole at which the first wave-front appeared if a temporal delay in wave-front initiation was observed. If no delay between two wave-fronts was observed then those embryos are labeled "simultaneous". 83

Figure 3.12: Quantitative analysis of wave-front propagation properties. a) Measured duration for all cells to transition from metaphase to anaphase for embryos exhibiting two wave-fronts and one wave-front. Average ± standard error of the mean indicated by whiskers. b) Measured speed of mitotic wave-fronts for embryos exhibiting two wave-fronts and one wave-front. Average ± standard error of the mean indicated by whiskers. Mitotic wave-front speeds for embryos exhibiting one of two wave-fronts are not statistically different from each other based on a student's T-test ($p > 0.05$). 85

Figure 3.13: Measured temporal delay in mitotic wave-front initiation for embryos exhibiting two wave-fronts. Delay is calculated as posterior minus anterior initiation times. Positive values indicate anterior wave-front appeared first, and negative values indicate posterior wave-front appeared first. 87

Figure 3.14: Wave-front propagation properties as a function of nuclear cycles 10-13. a) Measured duration for all cells to transition from metaphase to anaphase for all embryos. Average ± standard error of the mean indicated by whiskers. Nuclear division durations were measured at 1.11 ± 0.08 (n = 34 embryos), 1.50 ± 0.09 (n = 38 embryos), 2.28 ± 0.12 (n = 42 embryos), and 2.68 ± 0.15 min (n = 47 embryos) for nuclear cycles 10, 11, 12, and 13, respectively. b) Measured speed of mitotic wave-fronts for all embryos. Average ± standard error of the mean indicated by whiskers. Wave-front speeds were measured at 243.5 ± 17.4 (n = 34 embryos), 169.6 ± 7.3 (n = 38 embryos), 110.1 ± 4.8 (n = 42 embryos), and 98.0 ± 5.5 μm/min (n = 47 embryos) for nuclear cycles 10, 11, 12, and 13, respectively. 90

Figure 3.15: Wave-front propagation properties as a function of nuclear cycles 10-13 for embryos exhibiting one or two mitotic wave-fronts during nuclear cycle 13. a) Measured duration for all cells to transition from metaphase to anaphase for all embryos. Average ± standard error of the mean indicated by whiskers. For two wave-fronts, nuclear division durations were measured at 0.98 ± 0.06 (n = 29 embryos), 1.31 ± 0.06 (n = 33 embryos), 2.09 ± 0.08 (n = 37 embryos), and 2.45 ± 0.13 min (n = 42 embryos) for nuclear cycles 10, 11, 12, and 13, respectively. For one wave-front, nuclear division durations were measured at 1.90 ± 0.18 (n = 5 embryos), 2.70 ± 0.30 (n = 5 embryos), 3.70 ± 0.51 (n = 5 embryos), and 4.60 ± 0.43 min (n = 5 embryos) for nuclear cycles 10, 11, 12, and 13, respectively. b) Measured speed of mitotic wave-fronts for all embryos. Average ± standard error of the mean indicated by whiskers. For two wave-fronts, wave-front speeds were measured at 246 ± 20 (n = 29 embryos), 170 ± 8 (n = 33 embryos), 108 ± 5 (n = 37 embryos), and 98 ± 6 μm/min (n = 42 embryos) for nuclear cycles 10, 11, 12, and 13, respectively. For one wave-front, 227 ± 24 (n = 5 embryos), 162 ± 20 (n = 5 embryos), 122 ± 18 (n = 5 embryos), and 92 ± 8 min (n = 5 embryos) for nuclear cycles 10, 11, 12, and 13, respectively. 92

Figure 3.16: Comparison of mitotic wave-front speed as collected in this thesis and by the work of Idema et al. Thesis Data refers to individual embryo data collected in this thesis using our microfluidics-enabled high-throughput imaging technique. Idema et al. Data refers to data set averages for 3 and 2 embryos collected on separate days. 94

Figure 4.1: Single-layer AP1 array introduces optical aberrations when imaging at embryo mid-section. a) Optical confocal micrographs at the mid-section of a Cic-Venus expressing embryo within the single layer AP1 array described in chapter 3. i) Cic-Venus channel (top) and transmitted light channel (bottom). * indicates visible Cic-Venus reflection in PDMS sidewalls. ii) Merge of Cic-Venus and transmitted light channels. * indicates visible Cic-Venus reflection in PDMS sidewalls. b) Intensity plot along the ventral epithelium in which PDMS sidewalls induce optical aberration (top side of embryo in (a)). Gray box indicates the area of the epithelium that is artificially dimmed due to PDMS sidewall interference. 101

Figure 4.2: Two-layer AP2 microfluidic array schematic. a) Left: Overall device layout from a top-down view depicting the main serpentine channel, focusing channels, embryo traps and resistance channels. Right: Close up of embryo trap design in both the top layer that guides embryos to the center of the trap, and the base layer wherein the imaging plane is located for time-lapse confocal microscopy. b) Left: Dorsal-ventral cross-section of an embryo (red) in the trap with imaging plane (blue) indicated. PDMS (gray) and glass cover slips (pink) are also depicted. Center: Anterior-posterior cross-section of an embryo in the trap with imaging plane indicated. Right: Three-dimensional perspective of an embryo in the trap. 102

Figure 4.3: Array loading and COMSOL simulation results. a) Initial design that simply incorporates a wide base in the trapping unit to the optimized single-layer AP1 array from chapter 3. i) Typical loading results for the initial design with an average trapping efficiency of 58% (n = 6 experiments). White asterisks indicate traps with embryos successfully loaded while black asterisks indicate empty traps. ii) Surface plots of superficial velocity at channel mid-plane from COMSOL three-dimensional finite element modeling. Most fluid follows the serpentine channel in this design. b) Optimized two-layer AP2 array design. i) Typical loading results for the optimized design with an average trapping efficiency of 98% (n = 3 experiments). White asterisks indicate traps with embryos successfully loaded while black asterisks indicate empty traps. ii) Surface plots of superficial velocity at channel mid-plane from COMSOL three-dimensional finite element modeling. Most fluid is diverted to the embryo trap in this design. 104

Figure 4.4: Cic-Venus spatial distribution. a-f) Time-lapse confocal microscopy optical micrographs depicting an embryo that is homozygous for *cic-venus* transgene. Left images are merges of the Cic-Venus and transmitted light channels while right images are from the Cic-Venus channel only. Time is relative to imaging start time. a) imaging start point, b-e) stage 4 of embryogenesis with nuclear cycles b) 10, c) 11, d) 12, and e) 13, and f) stage 5 of embryogenesis with nuclear cycle 14. g) Cic-Venus anterior-posterior (0-1) spatial gradient during nuclear cycle i) 12, ii) 13, and iii) 14. Individual embryo spatial gradients are blue line plots with the population average in red. n = 22 embryos. 106

Figure 4.5: Re-mapping of the four-dimensional imaging data to three-dimensional representations. a) Raw four-dimensional imaging data of a single Cic-Venus expressing embryo including 360 images per embryo. b) Imaging data from (a) are imported to ImageJ, cropped, and straightened with the built-in ImageJ function Straighten to produce 360 gradient images for a total of 720 images. The vertical dimension represents the anterior-posterior direction, and the horizontal direction represents the apical-basal direction. c) Imaging data from (b) are imported to Matlab and reduced to a single Cic-Venus line-plot by taking the maximum along the vertical anterior-posterior direction of each image and stacked in a heat-map representation of Cic-Venus spatiotemporal dynamics. 109

Figure 4.6: A detailed illustration highlighting the timing of *Drosophila* embryogenesis upon the Capicua spatiotemporal patterning heat-maps described earlier. Prior to stage 4, no nuclei are visible as they are located deep within the egg yolk. During stage 4, nuclei become visible and proceed through 4 synchronous nuclear cycles, specifically, nuclear cycles 10-13. Onset of nuclear cycle 14 marks the onset of stage 5. Exit of stage 5 is marked by major morphogenic movements including cephalic furrow formation at the onset of gastrulation. Asterisk indicates cephalic furrow. 112

Figure 4.7: a) Single embryo average Cic-Venus fluorescence. Dotted red lines represent transitions between nuclear cycles (division phase). Nuclear localization of Cic-Venus increases from cycle to cycle as indicated by increasing Cic-Venus intensity. b) Confocal micrographs of embryo surface with Cic-Venus channel (top), transmitted light (middle), and merge (bottom). i-iii) Optical micrographs that correlate with (i-iii) in (a): i) 5 minutes before observed minimum in Cic-Venus intensity. ii) Exact time of observed minimum in Cic-Venus intensity. iii) 5 minutes after observed minimum in Cic-Venus intensity. Dotted red lines are tracking furrow canal migration. 114

Figure 4.8: a) Average Cic-Venus fluorescence normalized to average. Individual embryo traces (blue lines) are normalized by subtracting the population average minimum (red line) and dividing by the difference of the population average maximum and population average minimum. (n = 20 embryos). b) Average Cic-Venus fluorescence normalized to individual. Individual embryo traces (blue lines) are normalized by subtracting the individual trace minimum (red line) and dividing by the difference of the individual trace maximum and individual trace minimum. (n = 20 embryos). 117

Figure 4.9: Timing of developmental milestones. a) Relative timing of developmental milestones. Top: Average ± SEM average Cic-Venus fluorescence curve from nuclear cycle 11 division to FCM (n = 30 embryos). Bottom: Measured relative timing of developmental milestones for individual embryos with population average ± SEM indicated for nuclear cycle 12 Cic-Venus peak intensity (NC12 peak), nuclear cycle 12 nuclear division (NC12 division, nuclear cycle 13 Cic-Venus peak intensity (NC13 peak), nuclear cycle 13 nuclear division (NC13 division), nuclear cycle 14 Cic-Venus peak intensity (NC14 peak), and furrow canal migration (FCM). Time zero represents nuclear cycle 11 division. Horizontal axes in top and bottom graphs are aligned to illustrate connection between Cic-Venus fluorescence traces and features. b) Quantified durations of nuclear cycles 12 (NC12) and 13 (NC13), and nuclear cycle 14 to onset of furrow canal migration (NC14 to FCM). Red lines represent population averages ± SEM. 119

Figure 4.10: Image processing flow chart for measuring single-cell Cic-Venus fluorescence. a) The Cic-Venus spatiotemporal patterning heat-map was cropped to isolate the developmental phase of interest. Time frame to crop was determined based on the average Cic-Venus fluorescence curves. Nuclear cycle 14 is depicted here. b) Cropped image from (a) is segmented using the relative difference filter developed by Charles Zhao. c) Objects in the segmented image from (b) were filtered based on morphological parameters from the built-in Matlab function Regionprops. d) Filtered objects from (c) were skelentonized using Matlab built-in function Bwmorph, and subsequently smoothed. e) Skeletonized objects from (d) are extended forward and backward in time (left and right) to construct full length cell path throughout nuclear cycle 14. f) Sample single-cell Cic-Venus fluorescence trace through nuclear cycle 14.121

Figure 4.11: Capicua nucleocytoplasmic shuttling kinetics. a) Single-cell Cic-Venus traces for early nuclear cycle 14 (n = 256 single-cells). Blue lines represent single-cell traces and red line represents the population average trace. b) Fitting single-cell Cic-Venus traces to one phase association equation. Blue circles represent experimental trace for a single-cell and red line represents best fit model prediction. c) One phase association rate constant fits for single-cell Cic-Venus traces in nuclear cycles 13 and 14. Blue circles represent single-cell fits and red line represents population average ± SEM. Measured average ± SEM rate constants of 0.207 ± 0.006 and 0.210 ± 0.004 min^{-1} for nuclear cycles 13 and 14, respectively (Mann Whitney test, $p>0.05$, n = 244 and n = 256 single-cells for cycles 13 and 14, respectively). d) One phase association time constant fits for single-cell Cic-Venus traces in nuclear cycles 13 and 14. Blue circles represent single-cell fits and red line represents population average ± SEM. Measured average ± SEM time constants of be 6.0 ± 0.2 and 5.2 ± 0.1 min for nuclear cycles 13 and 14, respectively (Mann Whitney test, $p>0.05$, n = 244 and n = 256 single-cells for cycles 13 and 14, respectively). 125

Figure 4.12: Temperature effects on average Capicua dynamics. a) Average Cic-Venus fluorescence through nuclear cycles 12-14 as a function of temperature. n = 30, 32, and 18 embryos for 25, 27.5, and 30 ^{o}C, respectively. Blue lines represent individual embryo traces and redlines represent population average traces. b) Population average average Cic-Venus fluorescence traces from (a). Error bars are standard error of the mean (SEM). c) Relative cumulative timing of Cic-Venus developmental milestones as a function of temperature. Time is relative to the onset of nuclear cycle 12. Milestones include: Cic-Venus peak intensity for nuclear cycle 12 (pink, NC12 peak), nuclear cycle 12 nuclear division (purple, NC12 division), Cic-Venus peak intensity for nuclear cycle 13 (blue, NC13 peak), nuclear cycle 14 nuclear division (green, NC13 division), Cic-Venus peak intensity for nuclear cycle 14 (yellow, NC14 peak), and furrow canal migration (red, FCM). Dots are individual embryos while line and error bars represent average ± SEM. 128

Figure 4.13: Temperature effects on nuclear cycle duration for nuclear cycles 12, 13, and early nuclear cycle 14 encompassing onset of nuclear cycle 14 to furrow canal migration (FCM). a) Measured cycle durations for embryos grown at 25, 27.5 and 30 ^{o}C. b) Measured scaled cycle durations for embryos grown at 25, 27.5, and 30 ^{o}C. Cycle durations are scaled for each embryo by the total duration measured for nuclear cycle 12 onset to FCM. n = 30, 32, and 18 embryos for 25, 27.5, and 30 ^{o}C, respectively. Statistical significance was tested using the Kruskal-Wallis test with Dunn's multiple comparisons test. ****: $p<0.0001$, ***: $p<0.001$, **: $p<0.01$, and ns (not significant): $p>0.05$. 130

Figure 4.14: Temperature effects on single-cell Capicua dynamics. Single-cell Cic-Venus fluorescence traces through nuclear cycle a) 13 and b) 14 as a function of temperature. n = 256 cells for 25, 27.5, and 30 ^{o}C, respectively. Blue lines represent single-cell traces and red lines represent population average traces. Population average single-cell Cic-Venus fluorescence traces for nuclear cycle c) 13 and d) 14. Dots represent experimental data of population average single-cell Cic-Venus fluorescence while lines represent one phase association model best fits. 131

Figure 4.15: Temperature effects on single-cell Cic-Venus one phase association model best fit parameters for nuclear cycles 13 (a and c), and 14 (b and d). n = 256 single-cells for 25, 27.5, and 30 ^{o}C, respectively. Average ± SEM rate constants for nuclear cycle 13: 0.207 ± 0.006, 0.2423 ± 0.007, and 0.261 ± 0.008 min^{-1} at 25, 27.5 and 30 ^{o}C. Average ± SEM rate constants for nuclear cycle 14: 0.210 ± 0.003, 0.272 ± 0.006, and 0.272 ± 0.005 min^{-1} at 25, 27.5 and 30 ^{o}C. Average ± SEM time constants for nuclear cycle 13: 6.1 ± 0.2, 5.3 ± 0.2, and 5.0 ± 0.2 min at 25, 27.5 and 30 ^{o}C. Average ± SEM time constants for nuclear cycle 14: 5.2 ± 0.1, 4.1 ± 0.1, and 4.0 ± 0.1min at 25, 27.5 and 30 ^{o}C. Statistical significance was tested using the Kruskal-Wallis test with Dunn's multiple comparisons test. ****: $p<0.0001$, **:$p<0.01$, and ns (not significant): $p>0.05$. 133

Figure 4.16: Spatiotemporal patterning of Cic-Venus for a) *cicv*/+ (wild-type control), and *cicv*/+,tor^{D4021}/+ embryos. Heat-maps are centered at nuclear division 13 (hour 1). Heat-maps are individually normalized to the maximum intensity within the heat-map. Each heat-map is the average of 3 individual embryos. Color represents the normalized Cic-Venus intensity. c) The ratio of the heat-maps found in (a) and (b). Color represents the ratio value, wherein values greater than one indicate higher levels of Capicua in the mutant relative to wild-type, and values less than one indicate lower levels of Capicua in the mutant relative to wild-type. 137

Figure 4.17: Principal Component Analysis of Capicua Spatiotemporal Dynamics. a) Measure of variance captured by the first 40 principal components for *cicv*/+ embryos. b) Dominant spatial modes describing Capicua anterior-posterior nuclear in *cicv*/+ embryos. c) Time-dependent amplitudes of the first principal components for *cicv*/+ embryos. d) Comparing raw Capicua spatiotemporal patterning heatmap for a single WT embryo with the reconstructed Capicua spatiotemporal patterning heatmap using principal component 1 and the associated time-dependent amplitudes. 139

Figure 4.18: Reconstruction and Analysis of Capicua Spatial Patterning. a) Reconstruction of Capicua anterior-posterior nuclear localization 25 minutes into nuclear cycle 14 in wild-type embryos from wild-type principal component one (WT), constitutively active Torso embryos from wild-type principal component one (TOR), hyperactive MEK^{E203K} embryos from wild-type principal component one (E203K), and hyperactive MEK^{F53S} embryos from wild-type principal component one (E203K) embryos. b) Statistical analysis of Capicua levels at the anterior, middle, and posterior regions of WT, TOR, E203K, and F53S embryos. Statistical significance was tested using the Kruskal-Wallis test with Dunn's multiple comparisons test. ****: $p<0.0001$. 141

Figure 4.19: Projection of TOR, E203K, and F53S data sets into wild-type vector space. a) Normalized changes in wild-type principal components 1-5 from representing wild-type embryos (black), Torso gain-of-function embryos (red), hyperactive MEK^{E203K} embryos (blue), and hyperactive MEK^{F53S} embryos (green). b) Wild-type spatial modes one through five. Statistical significance was tested using the Kruskal-Wallis test with Dunn's multiple comparisons test. ****: $p<0.0001$. 143

Figure 4.20: RTK and MEK gain-of-function effects on single-cell Capicua dynamics. a) Single-cell Cic-Venus fluorescence traces through nuclear cycle 14. n = 235, 234, 248, and 236 single-cells for WT, TOR, E203K, and F53S embryos, respectively. Blue lines represent single-cell traces and redlines represent population average traces. b) Population average ± SEM single-cell Cic-Venus fluorescence traces for nuclear cycle 14. 145

Figure 4.21: RTK gain-of-function effects on Capicua one phase association model best fit parameters for nuclear cycle 14. Average ± SEM rate constants: 0.227 ± 0.004, 0.253 ± 0.004, 0.089 ± 0.002, 0.116 ± 0.004, and 0.168 ± 0.007 min^{-1} for *cicv/cicv*, *cicv/+*, TOR, E203K, and F53S embryos, respectively. Average ± SEM time constants: 4.8 ± 0.1, 4.2 ± 0.1, 13.0 ± 0.4, 10.9 ± 0.4, and 8.1 ± 0.3 min^{-1} for *cicv/cicv*, *cicv/+*, TOR, E203K, and F53S embryos, respectively. Statistical significance was tested using the Kruskal-Wallis test with Dunn's multiple comparisons test. ****: $p<0.0001$, and ns (not significant): $p>0.05$. n = 256, 235, 234, 248, and 236 single-cells for *cicv/cicv*, *cicv/+*, TOR, E203K, and F53S embryos, respectively. 147

Figure 4.22: Intra- and inter-embryo variability of Capicua nuclear transport. Intra-embryo variation of one phase association model best fit a) rate constant and b) time constant parameters for *cicv*/+, and *cicv*/+;*tor*^{D4021}/+ embryos. Error bars are SEM. n = 27 and 31 embryos for *cicv*/+, and *cicv*/+;*tor*^{D4021}/+, respectively. Statistical significance was tested using the Mann-Whitney test. ****: $p<0.0001$, and **: $p<0.01$. Inter-embryo variation of one phase association model best fit c) rate constant and d) time constant parameters for *cicv*/+, and *cicv*/+;*tor*^{D4021}/+ embryos. Error bars are SEM. n = 4 and 6 experiments for *cicv*/+, and *cicv*/+;*tor*^{D4021}/+, respectively. Statistical significance was tested using the Mann-Whitney test. *: $p<0.05$. 149

Figure B.1: Dorsal-ventral (DV) microfluidic array schematic. a) Overall device layout with main serpentine channel (■), focusing channels (■), and embryo traps and resistance channels (■). b) Zoom-in of boxed region of (a) with dimensions of the embryo trap and resistance channel. 164

Figure B.2: The single-layer anterior-posterior (AP1) array schematic. Top left: Overall device layout with main serpentine channel, and inlet and outlet locations labeled. Bottom: a single row containing 10 embryo traps in the center and individual focusing channels bookending the traps within each row. Top right: Individual trapping unit and focusing channel close up with embryo trap and resistance channels labeled, and dimensions indicated. 165

Figure B.3: The two-layer anterior-posterior (AP2) array schematic. Top left: Overall device layout for the base layer of the device. Bottom left: a single trapping unit of the base layer with important dimensions indicated for the embryo trap and resistance channel. Top right: Overall device layout for the top layer of the device. Bottom right: a single trapping unit of the top layer with important dimensions indicated for the embryo trap and resistance channel. Notice: main difference is in the width of the embryo trap in which the base layer embryo trap is 280 µm wide whereas the top layer embryo trap is 160 µm wide. The top layer is meant to guide embryos into the center of the trap while the base is meant to keep PDMS side walls from interfering with imaging quality. 166

SUMMARY

Developmental robustness refers to the ability of an organism to handle perturbation and still produce the normal phenotype. In the case of embryogenesis, embryos must be able to maintain coordination between the events of embryogenesis, e.g. cellular proliferation and morphogenesis, in the face of environmental changes. Understanding how developmental systems achieve robustness is a key goal of developmental biology. The fruit fly *Drosophila melanogaster* is commonly used as a model of development and developmental genetics owing to *Drosophila*'s high genetic conservation that allows this simple organism to provide insight into human development. *Drosophila* is also amenable to genetic manipulation, and fluorescent imaging enabling direct observation of developmental processes via fluorescent-fusion proteins. So called *in vivo* live imaging is a powerful technique that allows researchers to visualize dynamic processes in real time within a developing organism. However, *in vivo* live imaging is technically challenging due to time-consuming and low-throughput manual manipulations that are required to prepare *Drosophila* embryos for time-lapse microscopy. As a result, large-scale data collection is virtually impossible and prevents researchers from obtaining highly quantitative information regarding live embryo development.

To address this issue, this thesis advances the quantitative imaging toolsets available to biologists by developing and refining microfluidic technologies for high-throughput time-lapse microscopy of live *Drosophila* embryos. Compared to

conventional imaging techniques, significant engineering feats and expansion of microsystem functionality facilitate rapid microscopy of a wide range of biological applications within *Drosophila* development. Simple device design was a major consideration when engineering these microsystems in order to facilitate rapid adoption of these technologies by the biology community. Specifically, a suite of microfluidic devices were developed to enable high-throughput *in vivo* live imaging of *Drosophila* embryos from any possible orientation. As a result of these technological advances, new insight regarding anoxia-induced developmental arrest and recovery, mitotic wave-front propagation dynamics, and the effects of RTK-ERK signaling pathway mutations on downstream signaling kinetics were uncovered and quantitatively characterized.

Moreover, this thesis contributed to the development and integration of data analysis software to complement the rapid microscopy, microfluidic hardware in order to establish a platform for *in vivo* live imaging of a large number of individual *Drosophila* embryos. The platform developed in this thesis has the potential to address several important questions in embryogenesis including identification of the sources of inter-embryo variability, obtaining quantitative data of dynamic processes throughout embryogenesis, and facilitating mechanistic studies of developmental disorder pathology. Finally, the technologies I developed in this dissertation are generalizable, and can be applied to developmental studies of other model organisms as well as quantitatively characterizing developmental responses to other environmental and genetic perturbations found throughout embryogenesis.

CHAPTER 1: INTRODUCTION

1.1: Background

Understanding how biological systems operate macroscopically (e.g. morphogenesis and behavior), and how this is governed by microscopic activities (e.g. gene expression and cell signaling) is a key goal throughout biology. There are many tools available that can be used to address these questions including direct observation of biological processes in living organisms, and to extract meaningful information from what is observed. *In vivo* imaging uses fluorescence microscopy, and in recent years, significant advances in optical sectioning techniques have enabled imaging with high spatiotemporal resolution deep within intact tissues for high-content imaging. In parallel, engineers have been progressing microfluidics technology to enable high-throughput experimentation, and perform tasks that were simply not possible without microfluidic technology. Both high-throughput experimentation and high-content imaging can produce vast amounts of biological imaging data requiring the development of automated image processing and data extraction techniques. As an introduction to this thesis, this chapter highlights recent advances in the areas of: 1) fluorescence microscopy, 2) microfluidic and automation technology, and 3) image analysis software and computer vision as it pertains to developmental biology. I will give particular attention to advances that have been instrumental in progressing studies of the model organism *Drosophila melanogaster*, which was used throughout this thesis, and reviewed in the following

section of this thesis. This chapter also highlights deficiencies that persist in these areas of research, and this thesis aims to provide solutions.

1.2: *Drosophila melanogaster* as a Model for Development

The fruit fly *Drosophila melanogaster* is a commonly used model of genetics and development, and as such has been subject of previous reviews [1, 2]. *Drosophila* is highly accessible genetically, which allows laboratories to house flies with virtually any gene mutant, knock-out, or reporter fusions making genotype-phenotype studies readily available. Furthermore, fruit flies exhibit a short developmental period (i.e. ~24 hours for embryogenesis, and ~10 days from fertilized egg to adult fly), which enables rapid and large-scale developmental studies that are extremely difficult in slower developing organisms such as mice. Fruit fly research has been instrumental in progressing our understanding of a variety of fields of research. As such, work involving *Drosophila* has received the Nobel Prize on four separate occasions demonstrating the significance of research with this simple model organism [3-7].

In 1933, Thomas H. Morgan was awarded the Nobel Prize for his work on the role of chromosomes in heredity. Specifically, this led to the theory that genes are arranged in a linear array known today as chromosomes, and thus provided a physical mechanism for heredity [3]. In the award speech, some of the credit for his accomplishments is credited to the choice of studying *Drosophila melanogaster*. In comparison to other genetic models the fruit fly exhibits a short generation time, which allowed T.H. Morgan to work quickly in comparison to other geneticists at the time. Hermann J. Muller, a student of T.H. Morgan, was interested understanding the role of

mutation in evolution, but was hampered by the slow process for natural mutations to arise. Consequently, H.J. Muller looked for a method to induce mutagenesis, and improve the rate at which gene mutations can be studied. In his search, H.J. Muller discovered that X-ray radiation damages chromosomes and induces genetic mutations [4], was awarded the Nobel Prize in 1946 for this discovery, and formed the foundation for mutagenesis-based genetic screening.

The 1995 Nobel Prize in Physiology and Medicine was awarded to the combination of Christiane Nüsslein-Volhard, Eric F. Wieschaus, and Edward B. Lewis for their collective contributions regarding genetic control of early embryonic development. E.B. Lewis worked to understand the genetic basis for homeotic mutations by studying the "four-winged" fly. In doing so, E.B. Lewis found that a mutation in a gene family he referred to as the bithorax-complex produced the four-winged fly. Furthermore, he elucidated the correlation between gene order in the bithorax-complex and segment order along the body axis [7]. This work formed the basis for *HOX* genes, which have since been shown to be evolutionarily conserved across other organisms including humans [8].

C. Nüsslein-Volhard and E.F. Wieschaus worked together in order to uncover what controls embryogenesis. Utilizing mutagenesis-based screening, the two researchers discovered 15 genes important for controlling segmentation in the early *Drosophila* embryo, and were able to functional classify these genes into 3 groups referred to as gap, pair-rule, and segment-polarity genes [5]. A few years after this work, C. Nüsslein-Volhard published a paper describing the discovery of the morphogen Bicoid (bcd) [9]. The idea of a morphogen, a molecule that acts in a concentration-dependent manner for

pattern formation during embryogenesis, was first proposed by Alan Turing, but no such molecule had been identified previously [10]. Ever since the identification of Bicoid, there has an increase in research determined to identify morphogens, which are now known to be highly conserved through evolution and found in vertebrates including humans [11-15].

The research described above highlights the significance of *Drosophila* research, and yet only represents a small portion of the body of research involving *Drosophila*. Researchers continue to utilize *Drosophila* in order to study a vast array of topics in biology including development [16-18], behavior [19-21], and disease [22-24]. As research involving model organisms such as *Drosophila* progresses, so too do the technologies that are used in those studies in an ever increasing goal of conducting rapid yet precise biological research. The technologies I give particular attention to and highlight in this thesis include: fluorescence microscopy, microfluidics, and computer vision.

1.3: Fluorescence Microscopy for Imaging Development

Fluorescence microscopy, and specifically epifluorescence microscopy, has been the workhorse for imaging-based experiments in biology for hundreds of years. Currently epifluorescence imaging is commonly used, and suitable for addressing many questions in research areas such as behavior, neuroscience, and development. However, epifluorescence microscopy is often insufficient to spatially resolve features deep within the tissues of larger model organisms such as zebrafish and *Drosophila* embryos, or highly diffractive tissues such as cell aggregates. To improve spatial resolution, biologists

turn to optical sectioning techniques such as confocal microscopy [25-28] and light-sheet microscopy [29-34]. Light-sheet microscopy, however, is not compatible with conventional mounting techniques (i.e. glass cover slips cannot be used in light-sheet microscopy), which renders microfluidic integration impossible. Confocal microscopy on the other hand employs conventional mounting techniques and is compatible with microfluidic technologies. As such, confocal microscopy will be the focus of this section.

Confocal microscopy has been around for several decades, and there are many commercially available systems that make this technique one of the most commonly used method of optical sectioning. Confocal microscopy achieves optical sectioning through the use of a pinhole aperture that acts as a spatial filter to remove out-of-focus light and allowing only the in-focus light to pass through to the detector, which is typically a photomultiplier tube. In point scanning confocal microscopy a light source illuminates the whole specimen, and the final image is constructed by scanning the laser across the focal plane to build up the image pixel by pixel. Single-photon confocal microscopy is a powerful tool for acquiring high-resolution images deep within intact tissue, but still has limited imaging depth in highly diffractive tissues such as *Drosophila* embryos. Non-linear optics (NLO), i.e. two-photon excitation, can alleviate some of the scattering issues associated with single-photon excitation, and enable deeper imaging within thick tissues [35].

Many studies have utilized two-photon microscopy, and for brevity sake only a few will be highlighted here. McMahon et al. [36] used two-photon confocal microscopy in order to image ventral furrow formation, collapse, and subsequent mesoderm spreading in live *Drosophila* embryos. Two-photon excitation was used to image these

processes at the anterior-posterior center of the embryo from laterally oriented embryos and track cell movements. In a similar application, Wang et al. [37] used two-photon excitation to monitor epithelial invagination during gastrulation in *Drosophila* embryos. In studies such as these, imaging volumes were limited to a subsection of the *Drosophila* embryo as the biological questions did not require whole embryo information. Studies that require rapid image acquisition, e.g. requiring whole-embryo imaging or monitoring highly dynamic processes, can turn to a faster form of confocal microscopy known as spinning disk.

Spinning disk confocal microscopy improves the image acquisition rate by scanning multiple points simultaneously. Yet, there is still an issue of pinhole cross-talk that limits its use with highly scattering specimens. Recently, Shimozawa et al. [38] took a step in addressing these issues with spinning disk by eliminating pinhole cross-talk. Shimozawa and colleagues used a combination of increasing the inter-pinhole distance, and incorporating two-photon illumination in order to improve the spatial resolution attained during spinning disk confocal microscopy.

1.4: Microfluidics and Automation for Manipulating *Drosophila* Embryos

The use of microfluidic systems in studying biological phenomena has been expanding in recent years, and has been the subject of several reviews [39-41]. These systems offer advantages such as parallelized experimentation and integration of automation tools for high-throughput experimentation. In addition, microfluidic systems can be the enabling technology that allows scientists to perform otherwise impossible experiments to address questions in biology that were difficult to answer. Microfluidic-

enabled experimentation requires integration of software tools in order to: 1) automate microfluidic operation, and 2) automate data mining and extraction methods. The integration of microfluidic hardware and software tools have enabled high-throughput studies in neurobiology [42-48], development [49-57], as well as screening/sorting applications [58-69] in a variety of model organisms including *Caenorhabditis elegans*, *Danio rerio*, and *Drosophila*.

The model organism *Drosophila* can be difficult to handle for tasks such as imaging development and behavior, sorting, and microinjection. To address these limitations, several engineered microsystems have been developed to facilitate and automate tedious tasks that often limit experimental throughput. In addition, microfluidic devices have been created to control the microenvironment in order to spatially (i.e., across individual animals) perturb development. In this section, I review some of the recent advances made in microfluidic systems used for studies of *Drosophila* embryo development. Engineered microfluidics systems have been developed to aid in tasks such as embryo sorting [70, 71], microinjection [72], arraying [73-75], and enabling experimental designs involving the spatiotemporal perturbation of embryo development by altering temperature locally to sections of the embryo [76-78], or concentration of chemical species such as methylmercury chloride [79].

1.4.1: Microfluidic Sorting of Embryos

Drosophila is an excellent model for understanding molecular mechanisms of genetic networks, because of *Drosophila*'s fully mapped genome, and genetic accessibility [80]. There are many essential genes, an estimated 3600 [81], that if

knocked-out cause premature death. In studies aimed at understanding the molecular mechanisms of essential genes, geneticists utilize mutant strains, but the difficulty lies in sorting the 25% homozygous mutants from the rest of the population. Conventional methods require scientists to manually identify embryos of interest and manually isolate them from the rest of the population, which is a time-consuming process. To facilitate this process, Furlong et al. [70] developed a system similar to flow cytometers, which could sort fluorescently-labeled *Drosophila* embryos. This system operates by using fluidics to distribute embryos along a flow path, so that a single embryo will pass through a fluorescence-based detector and sort embryos based on the absence or presence of fluorescence. In this case, Furlong and colleagues employed a magnetically driven valve that would open and close the fluid stream leading to a waste bin. When open, embryos would be sorted to "waste", and when closed embryos would be sorted to "save". The system engineered by Furlong et al. could automatically sort ~15 embryos per second requiring only pipetting of an embryo suspension to the inlet of the device. Today, there are commercially available systems produced by Union Biometrica, known as the Complex Parametric Analyser and Sorter (COPAS) that can be used to sort particles of up to 1,500 µm in diameter allowing its use with sorting *Drosophila* and zebrafish embryos. This system uses absence or presence of fluorescence to sort objects as well, but instead of using a magnetic valve, these systems use an air stream to blow away unwanted embryos before delivery to a multiwell plate. The COPAS system is an example of microfluidic technology that can be commercialized and implemented by other laboratories for high-throughput sorting.

1.4.2: Microfluidics-Assisted Microinjection of Embryos

Microinjection is powerful technique used for the delivery of small molecules such as RNAi into developing embryos; yet it is technically challenging due to tedious hand manipulations required for conventional microinjection. Delubac et al. [72] constructed a microfluidic system with an integrated microinjector for automated microinjection of *Drosophila* embryos. The microfluidic device would automatically retrieve embryos from a reservoir, and deliver embryos to the microinjector by sheath flow. Embryos are punctured with a microneedle by flowing embryos into the microinjector rather than moving the injector into the embryo. A camera at the injection site automatically detects the presence of an embryo, sends a command to the microinjector for injection, and following injection the embryo is unloaded to a collection reservoir solely by fluid flow. Delubac et al. showed the viability of the system by injecting eGFP-expressing embryos with siRNA against eGFP. In this setup, Delubac et al. could inject one embryo every 3-4 seconds (231 injected embryos after 14 minutes) with 90% successful silencing of GFP fluorescence.

1.4.3: Microfluidics-Enabled Spatial Perturbation of Embryos

One of the biggest advantages to utilizing microfluidics is the ability to perform experiments that are extremely difficult, or simply not possible without microfluidic technology. For example, microfluidics-based approaches have allowed precise control of environmental stimuli. Spatially controlling the microenvironment is enabled by physical phenomena that occur at the micron-scale. Fluid flow in micrometer-sized channels is characterized by laminar flow fields as indicated by low Reynold's Number. Laminar flow is described as fluid particles moving in "sheets" next to one another and exhibiting no convective mixing. That means only diffusion exists along the axis perpendicular to

the flow direction. As a result, stable step-changes and stable gradients in concentration or temperature can exist across microfluidic channels.

Lucchetta et al. [76] developed a microfluidic device that can impose a temperature step-change across a single embryo, and found that embryos develop normally when anterior/posterior halves grow at different temperatures. The results suggested that in face of environmental perturbations, a simple reciprocal gradient system is not the mechanism for developmental robustness in anterior-posterior patterning. Lucchetta et al. [78] further used this experimental setup with a *Drosophila* strain expressing a Bicoid-GFP (Bcd) fusion and showed that a precise Bcd gradient is not necessary for normal development. In addition, it is suggested that a simple diffusion-established Bcd gradient could not account for robust anterior-posterior patterning. One of challenges associated with the system developed by Lucchetta et al. [76] is the manual mounting of single embryos within the microfluidic device. Dagani et al. [77] incorporated microfluidic self-assembly in order to eliminate tedious hand placement of embryos within the microfluidic channel.

1.4.4: Microfluidic Arraying of Embryos for Imaging

Conventional methods for imaging *Drosophila* embryos with specific orientations generally requires manual manipulation of individual embryos and chemical-based immobilization via glue. Consequently, these methods are time-consuming and low-throughput [82, 83]. This becomes limiting with regard to studying dorsal-ventral development in the *Drosophila* embryo. Dorsal-ventral patterning in *Drosophila* is one of the most well-understood and studied genetic networks, but is experimentally difficult to

study due to tedious manual manipulation required for end-on imaging. Witzberger *et al.* [84] used confocal microscopy in conjunction with a custom built imaging slide to directly image ventral furrow formation in live *Drosophila* embryos via end-on imaging. The slide consisted of a fabricated well array, in which embryos were placed on either anterior or posterior pole. However, while this method is compatible with live imaging of *Drosophila* embryos; it is technically challenging because it involves the manual placement of embryos into each well. Chung et al. [73, 74] developed a microfluidic embryo trap array that can automatically orient pre-processed, fixed embryos for end-on imaging through the use of passive hydrodynamics. This system allowed orienting of several hundreds of embryos in a matter of minutes, and quantitatively established the dorsal-ventral extents of genes involved in dorsal-ventral patterning [85-88].

While the devices described here provide technological advancements that allow highly parallelized imaging of dorsal-ventral development in *Drosophila* embryos, neither are optimal for high-throughput live imaging of *Drosophila* embryos. Furthermore, neither method was used to provide external stimuli, which could be useful in drug discovery applications and/or uncovering environment-development links. Imaging of the anterior-posterior plane of *Drosophila* embryos was also neglected in these studies, wherein imaging the anterior-posterior plane would allow for investigating many more processes of embryogenesis including, for example, germ band retraction [89, 90] and dorsal closure [26, 91, 92]. As a result, there is a need for improvements in the available microfluidic toolset to allow for high-throughput arraying and imaging of live *Drosophila* embryogenesis.

1.5: Image Analysis Software for Developmental Biology

High-content, high-throughput research in development, and biology in general, depend upon the development of computer software tools for high-throughput data analysis. With advancing fields of fluorescence microscopy and microfluidics-based experimentation, the bottleneck in many cases now shifts to image processing and data extraction. Over the past decade there have been significant developments in the area of open source bioimage processing and analysis software such as Fiji [93], ICY [94], CellProfiler [95], BioImageXD [96], BigDataViewer [97], V3D [98], and CARTA [99] to name a few. There are several great reviews that focus on software for data visualization in biology that we highly recommend for a more in depth review of the subject matter and a more comprehensive list of available software [100-104]. An important consideration in data analysis software is generalizability, which refers to the ease with which a particular software can adapt to different applications. Bioimage analysis software has been developed to facilitate or automate a number of tedious tasks in developmental biology including, for example, cell lineaging [105-108], constructing virtual embryos [109-113], and computer vision-based phenotyping software [42, 114-116].

1.5.1: Automated Cell Lineaging

A major challenge in developmental biology is the imaging and tracking of all cells in entire developing embryos throughout all of embryogenesis. Part of the problem is related to acquiring 4D imaging data with high enough spatiotemporal resolution to see all cell tracks. The other part of the problem has to do with reconstructing cell tracks throughout development. This is conventionally attained by manual annotation, which is a painstakingly slow process. Bao et al. [107] developed STARRYNITE to analyze 4D

confocal imaging data of developing *C. elegans* embryos and construct cell lineage trees up to the 350-cell stage of development in 25 minutes. The invariant cell lineages exhibited in *C. elegans* development allows straightforward identification of the same cell across individuals, and straightforward comparisons of lineage phenotypes. However, this is made more difficult in more complex organisms such as *Drosophila* and zebrafish, which likely exhibit heightened cell lineage variability in addition to the relative increase in embryo size and cell numbers. Recently, Amat et al. [108] developed an open-source computational framework for segmentation and tracking of cell lineages from large-scale fluorescence microscopy images. The generalizability of the software allows analysis of bioimage data sets of several model organisms (e.g. *Drosophila*, zebrafish, and mouse) acquired from a variety of microscopy techniques including confocal and light-sheet. The software is user-friendly requiring only the adjustment of 2 parameters for analyzing all data sets, which allows this type of software to be easily adopted by other laboratories. Cell tracking techniques such as those described here are incredibly useful for understanding embryo development, and is generally a requirement for downstream analyses including, for example, quantification of gene patterning dynamics.

1.5.2: Virtual Embryos

Another challenge for developmental biology is comparing whole-embryo development between individuals. A virtual or digital embryo, which is an idealized, average embryo that can represent all embryos of the same genotype raised in the same environmental condition can be used for this issue. Creating virtual embryos is a challenge in of itself, because of inherent developmental variability exhibited throughout development. Fowlkes et al. [109] constructed a spatiotemporal atlas of gene expression

patterns in the *Drosophila* blastoderm, which was built upon a virtual embryo. By creating a virtual embryo, Fowlkes and colleagues could capture average gene expression patterns by removing inter-embryo variations in morphology, and gene expression. The purpose of this method is to establish gene expression networks, and Fowlkes and colleagues showed that they could recover already known gene interactions from the virtualized map, and predict hundreds more. Murray et al. [117] built upon the STARRYNITE software in order to automatically map spatiotemporal gene patterning throughout *C. elegans* embryogenesis, and enabled comparisons between lineage phenotypes. Virtual Brain Explorer (ViBE-Z) was developed by Ronneberger et al. [111] for automated mapping of gene expression patterns observed in zebrafish larval brains, and can automatically identify anatomical locations for registration. One of the main goals of these projects is to enable direct and easy comparison between embryos to uncover the effects of particular genes, drugs, and environmental conditions on the development of entire embryos. Kobitski et al. [112] constructed a digital zebrafish embryo, and used it to compare the developmental phenotypes between wildtype embryos and mutants. Kobitski and colleagues found that the one-eye pinhead (oep) mutant shows abnormal development several hours prior to any phenotypic alterations can be seen by eye. As illustrated by the above examples, a significant challenge in understanding embryo development stems from an inherent difficulty regarding data visualization. As such, software, and even just visualization methods that are easy to interpret would greatly improve understanding as well as scientific communication regarding embryo development.

1.5.3: Computer Vision for Automated Phenotyping

Interpretation of bioimage data is conventionally performed by manual inspection (i.e. seen by eye) and sufficient in many cases especially when obvious changes in phenotypes are observed. However, experimental results in developmental biology are often noisy, because of inherent developmental variability across individuals of a population. This makes manual data interpretation difficult. In this area, computer vision can be used to extract useful information from bioimage data and "see" what is not easily seen by eye. For more detailed information regarding computer vision in biology readers can refer to the following reviews [118, 119]. Computer vision has been applied to many studies of biology, but has been more extensively used in studies of individual cells and tissues [115, 116, 120]. For example, Yin et al. [114] used support vector machines in a RNAi screen for automated classification of cellular phenotypes, and identification of genetic regulators of cell morphology and the cytoskeleton.

The application of computer vision-based classification and data analysis to multicellular organisms is more limited, and primarily used for automating cell lineaging as outlined above. Recently, Crane et al. [42] integrated computer vision with microfluidics-based screening to perform autonomous genetic screening for genes involved in synaptogenesis during *C. elegans* development. Crane and colleagues developed a computational platform for image segmentation, feature extraction, and animal classification based on extracted features. Computer vision is useful in these cases, because tasks such as whole-animal classification can be performed based on non-obvious phenotypic descriptors. Bioimage classification such as this is ubiquitous in imaging-based studies of biology, and as a result computer-vision based analysis should find widespread use in the near future.

Despite the availability of technologies that can be utilized for common image processing needs in a variety of organisms, the diverse range of biological applications throughout the biology community is often beyond the capabilities of these technologies. Unfortunately, available software are developed to address a specific problem and tend be application specific, requiring alteration for use in other experimental contexts. On top of this, it can be unclear or even impossible for end-users to successfully apply these technologies for specific applications.

1.6: Thesis Contributions and Significance

This thesis provides both biological and engineering contributions to the fields of microfluidics, image processing, and developmental biology. These contributions were designed to address the experimental challenges that limit the throughput of *in vivo* live imaging of *Drosophila* embryos during early embryogenesis. Specifically, the microfluidic hardware developed in this thesis surpasses conventional preparation techniques that were required to prepare live *Drosophila* embryos for time-lapse microscopy thereby enabling rapid *in vivo* live imaging of embryogenesis. Furthermore, the microfluidic technology is capable of orienting *Drosophila* embryos from any view facilitating rapid imaging of any fluorescence-microscopy-compatible biological process *in vivo*. To complement the microfluidic hardware, this thesis developed custom algorithms to enable automatic and unbiased quantitative analysis of developmental rate and nuclear signaling dynamics. The hardware and software technologies developed in this thesis constitute a platform for performing high-throughput *in vivo* live imaging of *Drosophila* embryogenesis and large-scale quantitative analysis.

In addition to engineering enabling technologies, this thesis demonstrates the power of integrated microsystems by studying a variety of biological problems and providing new insight to anoxia-induced developmental arrest, mitotic wave-front propagation dynamics, and the effects of RTK-ERK signaling pathway mutations on downstream signaling kinetics. The biological applications in this thesis demonstrate the potential for these engineered microsystems, but only represent a fraction of the biological applications that can benefit from these technologies. Furthermore, the microfluidic technologies that arose from the work described in this thesis have been distributed and used by non-specialists, thereby exemplifying the potential impact that this thesis presents. Finally, the technologies I developed in this dissertation are generalizable, and can be utilized for quantitative analysis of development in other model organisms thereby expanding the potential impact of this thesis work.

CHAPTER 2: AN OPTIMIZED MICROFLUIDIC ARRAY FOR DORSAL-VENTRAL IMAGING AND PROVIDING PRECISE ENVIRONMENTAL PERTURBATION TO LIVE DROSOPHILA EMBRYOS

This chapter is adapted from a research article entitled "An integrated platform for large-scale data collection and precise perturbation of live *Drosophila* embryos" published in Scientific Reports in 2016 [121].

2.1: Introduction

Embryogenesis is a collection of dynamic processes involving cell division, cell growth and death, collective cell movements, cell shape changes, and gene patterning. *In vivo* live imaging of development allows biologists to directly visualize and understand the fundamental principles governing these highly dynamical processes [36, 56, 122-125]. Recent advances in fluorescence microscopy, in combination with endogenous fluorescent reporters, has made it possible to image whole embryos with single-cell resolution throughout embryogenesis [126-130]. However, inherent inter-embryo variability and low-throughput imaging methods make acquiring statistically meaningful data about embryonic development difficult. To address this issue, a combination of high-throughput experimental methods (for acquiring large imaging data sets [131]) and image processing software (for rapid and standardized automated data extraction [114]) can be used to increase the statistical power of data analysis methods [65].

Previously, we developed a microfluidic device that can array hundreds of embryos for end-on imaging in a matter of minutes [73, 74]. This method was primarily used with pre-processed, fixed embryo samples to quantitatively define the spatial expression distributions of key dorsal-ventral patterning genes [87, 88, 132, 133]. While we showed that it was possible to use the device with live *Drosophila* embryos, we did not fully optimize the device to culture and image *Drosophila* embryos through gastrulation, as well as for even longer culture and observation applications. Furthermore, the previous device was not designed to be compatible with microenvironment perturbations delivered to embryos throughout development [91, 92, 126, 134].

This chapter presents an optimized microfluidic device for arraying live *Drosophila* embryos for parallelized imaging of dorsal-ventral development with the option of subjecting the embryos to rapid and reliable alterations to microenvironments throughout development (Figure 2.1). This allows for otherwise impossible dynamic control of the embryo microenvironment while allowing continuous *in vivo* live imaging of the dorsal-ventral plane in several embryos simultaneously. Furthermore, we have developed an image processing and analysis pipeline for the automated and unbiased measurements of developmental rates on-chip, and I show that embryos develop with similar rates as those found using conventional live imaging techniques. Finally, I use the microfluidic device to investigate the effects of environmental perturbations by controlling oxygen availability to *Drosophila* embryos throughout development to investigate the effects of anoxic conditions on developmental arrest. The microfluidic array was used to create dynamic microenvironments during embryo development and

monitor embryo responses *in vivo*. Specifically, I briefly exposed embryos to anoxic microenvironments and analyzed anoxia-induced developmental arrest and recovery.

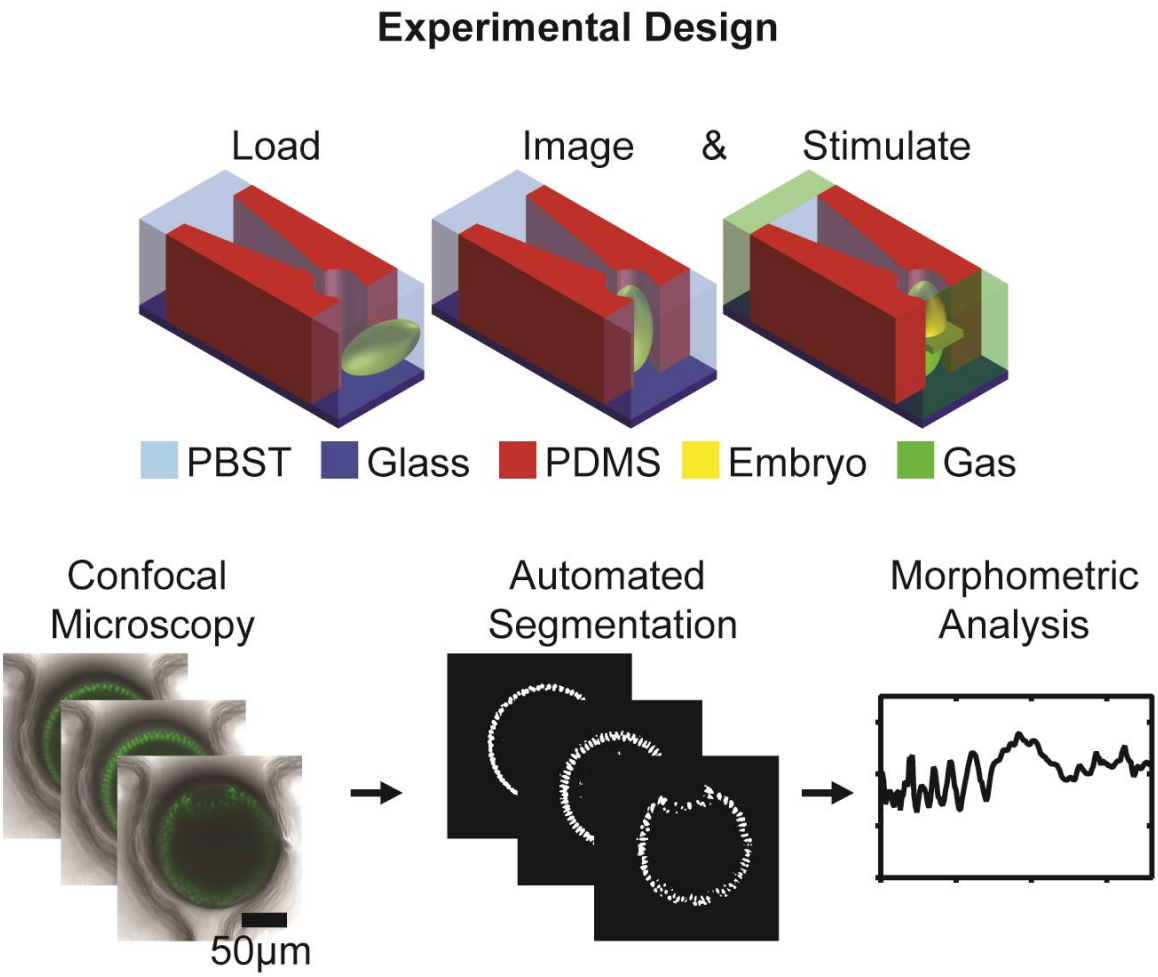

Figure 2.1: Method protocol: Load device with live embryos. *In vivo* live imaging of end-on oriented embryos. Delivery of gas-phase stimuli (in this case humidified nitrogen gas), and continue *in vivo* live imaging developmental responses. Confocal microscopy images of live embryo development are then automatically segmented and used for morphometric analysis and data extraction to analyze developmental responses to stimuli.

2.2: Materials and Methods

2.2.1: Fabrication of the Dorsal-Ventral (DV) Array

Polydimethylsiloxane (PDMS; Dow Corning) microfluidic devices were fabricated using a rapid prototyping technique [135]. Briefly, device layouts were designed in AutoCAD and printed onto high resolution transparencies to create photomasks (CAD Art Services; Appendix B Figure B.1). SU8 2100 photoresist was spin coated onto silicon wafers to a thickness of ~500 μm. The SU8 film was then patterned with a negative relief via standard photolithography and using the previously constructed photomask. The unexposed SU8 is removed via chemical development and the master mold is treated overnight with silane vapor ((tridecafluoro-1,1,2,2-tetrahydrooctyl)-1-trichlorosilane; United Chemical Technologies) to facilitate release of PDMS during replica molding.

PDMS devices are replica molded by first pouring a thin layer of 15:1 PDMS onto the surface of the master mold and allowed to cure for 30 minutes at 75^{o}C. A second layer of 10:1 PDMS is then poured on top and allowed to cure for an additional 3 hours at 75^{o}C. The softer layer allows the embryo traps to flex open under slight positive pressure (~6 psi) during embryo loading while the stiffer layer makes the overall device rigid for handling. Access holes are then punched through the PDMS mold to create device inlet and outlet. The PDMS mold is finally plasma bonded to a glass coverslip to create the fully enclosed microfluidic device (Figure 2.2).

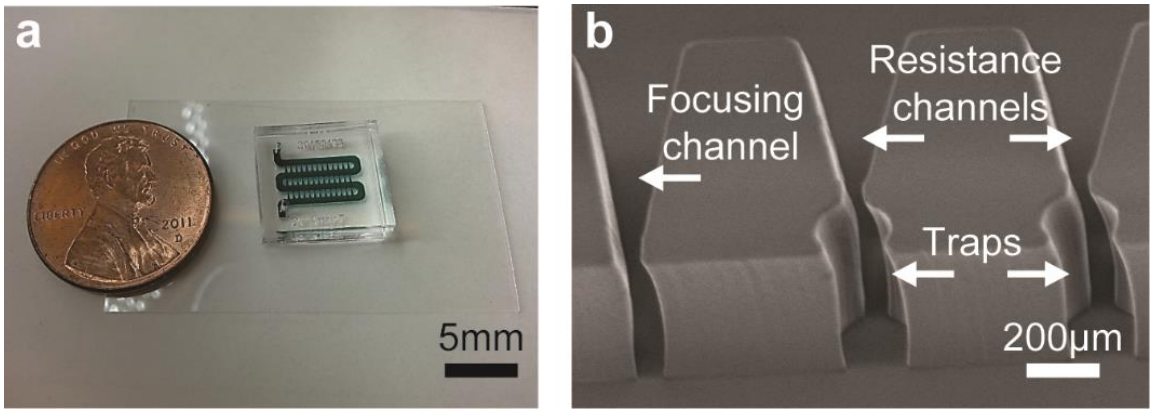

Figure 2.2: Optimized dorsal-ventral live imaging array. a) Fully constructed dorsal-ventral microfluidic array with channels filled with green dye. b) Scanning electron micrograph of embryo traps and focusing channel.

2.2.2: Fly Strains and Embryo Loading

Histone2AV-GFP (Histone-GFP; Bloomington stock center) expressing flies were used to visualize cell migration and quantify cell cycle kinetics. Embryos were prepared for live imaging using standard preparation protocols [136]. Briefly, adult flies were placed over a fresh agar plate for 2 hours at 25^{o}C for embryo synchronization and collection. Chorion membranes were removed from live embryos by soaking in 2.5% sodium hypochlorite (bleach active ingredient; Clorox) for ~1 minute. Embryos were rinsed with 10 ml of deionized water to remove bleach prior to suspending embryos in 15 ml of PBST, which refers to 0.03% Triton X-100 (Sigma Aldrich) in phosphate-buffered saline solution (VWR). PBST was used for device loading as the surfactant helps prevent embryo aggregation and clumping in the microchannels.

PDMS microfluidic devices are mounted on a dissecting microscope for embryo loading. The dissecting scope is preferred for loading as it offers a wide field of view that

allows monitoring for loading errors throughout loading. Devices were primed with PBST to remove air bubbles and coat the PDMS surface with surfactant to help prevent embryo clumping in the microchannels (~5 minutes). Once devices are primed and embryos prepared, embryos were then delivered to the microfluidic device by application of slight positive pressure (~6 psi). After device loading, the device is taken to a confocal microscope for time-lapse confocal microscopy.

2.2.3: Finite Element Modeling of Fluid Dynamics and Oxygen Transport within the DV Array

COMSOL (COMSOL, Inc.) finite element modeling software was utilized to predict the laminar flow patterns and oxygen mass transport within the microfluidic array. We solved for the 2D steady state solution of the incompressible Navier-Stokes equation. The fluid properties are assumed to be equivalent to those of pure water (i.e. density and viscosity). We assumed no slip boundary conditions for all boundaries except inlet and outlet. The inlet superficial velocity was experimentally determined during loading experiments to ~0.285 m/s, and set as the inlet boundary condition. The outlet was set to an open boundary condition with 0 N/m^2 normal stress at the outlet. Temperature was set to 298.15 K in the model.

For mass transport simulation, we constructed a cross section of the microfluidic array that consisted of a top layer of 5-mm thick PDMS, and a bottom layer of 500-μm thick nitrogen gas representing the serpentine channel during anoxia perturbation. The length of the layers were specified as 550 mm and 40 mm to represent the stretched out length of the serpentine channels in our previously designed large array [73] and the

small array described here. We first solved for the 2D steady-state solution of the Navier-Stokes equation. The fluid properties are assumed to be equivalent to those of pure oxygen. We assumed no slip boundary conditions for all boundaries except inlet and outlet. The inlet superficial velocity was experimentally measured during loading experiments to be ~0.285 m/s, and set as the inlet boundary condition. The outlet was set to an open boundary condition with 0 N/m^2 normal stress at the outlet. Temperature was set to 298.15 K. This solution was then fed into the 2D transient model for combined convection and diffusion mass transport. Diffusivity of oxygen in PDMS was set to 3.55 x 10^{-9} m^2/s, while the diffusivity of oxygen in nitrogen was set to 1 x 10^{-5} m^2/s. Initial conditions include 2% oxygen concentration throughout the microfluidic cross section. Boundary conditions include: no flux at bottom of serpentine channel (glass slide), 0% oxygen concentration at device inlet (humidified nitrogen gas), 2% oxygen concentration at PDMS surfaces facing the outside environment, and 10:1 oxygen partition coefficient at the gas:PDMS interface (top of serpentine channel). Ten minutes of operation with a 1-minute time step were solved for to predict oxygen concentrations during anoxia treatment.

2.2.4: Time-Lapse Confocal Microscopy

Imaging was performed on a Zeiss LSM 710 confocal microscope with a Zeiss EC Plan-Neofluar 40x/1.30 oil DIC M27 objective. Embryos were imaged ~80 µm from either anterior or posterior pole. Temperature was maintained at 25ºC throughout imaging via an environmental chamber. Embryos remained within the PBST solution within the array throughout imaging. Images were acquired every 60 seconds for a duration of 3

hours in order to encompass the events leading up to and including the first movements of gastrulation (i.e. cellularization and ventral furrow formation).

Higher resolution imaging was utilized to visually confirm that nuclear cycle phase correlates with the measured "average area of nucleus". Imaging of this type was done utilizing a Zeiss LSM 710 confocal microscope with a Zeiss Plan-Apochromat 63x/1.40 oil DIC M27 objective. Embryos were imaged ~50 µm from either anterior or posterior pole. The temperature was maintained at 25^{o}C throughout imaging via an environmental chamber. Embryos remained within the PBST solution within the array throughout imaging. Images were acquired every 18 seconds for a duration of 2 hours in order to encompass stage 4 of development.

2.2.5: On-Chip Oxygen Manipulation

To manipulate the oxygen levels on-chip, first devices were loaded with embryos and set-up on the confocal microscope for time-lapse microscopy. Once mounted onto the microscope, tubing was connected to the device inlet and outlet such that humidified gas from a gas cylinder can be pumped through the device serpentine channel (Figure 2.3). This was done by connecting gas cylinders of specific gas concentrations to a bubble stone that would bubble the dry gas through deionized water in order to humidify the gas. This was necessary to greatly reduce or eliminate evaporation of the liquid that remained around embryos in the traps and resistance channels as the gas passed through the serpentine channel. The humidified gas would travel to the microfluidic device via a low gas permeable tubing (i.e. polyethylene tubing) at very ~1-3 ml per minute. The low flow rate allowed the gas phase to displace the liquid within in the serpentine channel, but

not within the embryo traps and resistance channels. The gas was allowed to flow through the device for 10 minutes after which the device is flushed with aerated PBST to bring the microenvironment back to normoxia. Imaging continued throughout the experiment and continued for an additional 2 hours after the anoxic exposure.

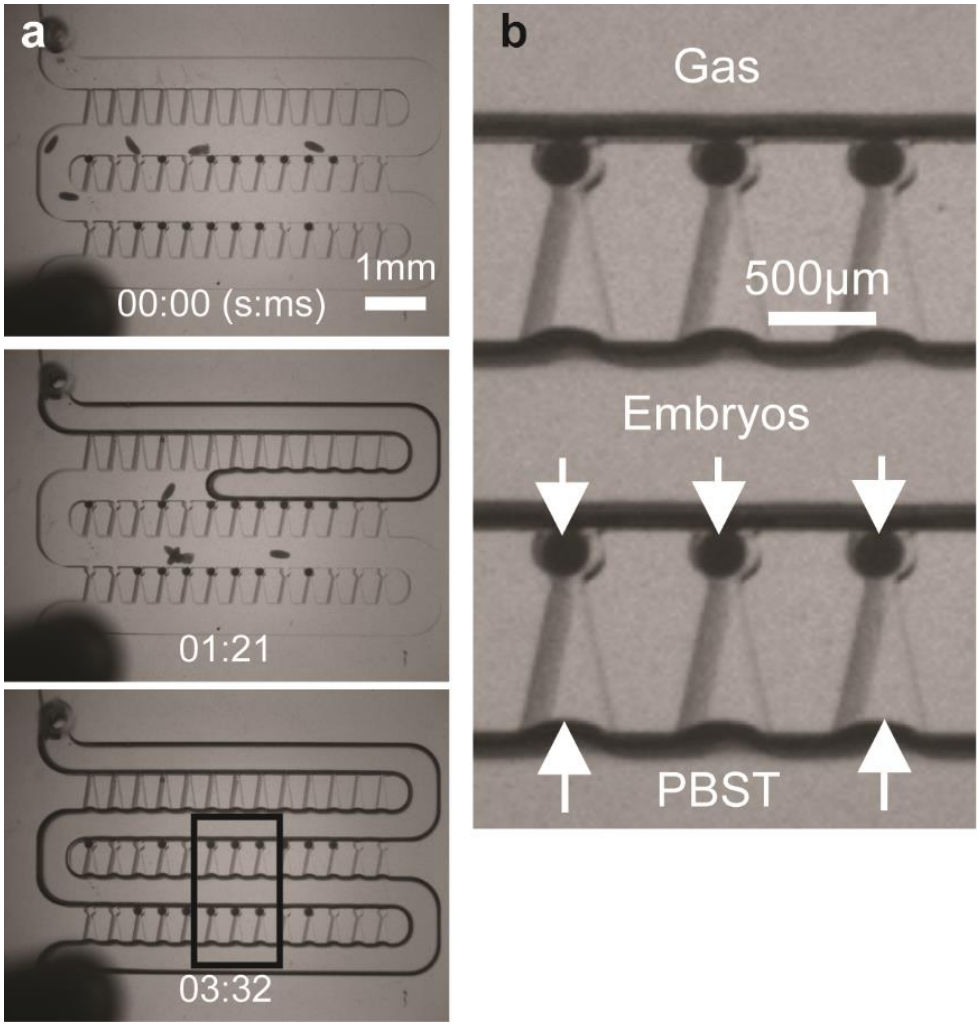

Figure 2.3: Delivery of anoxic gas via serpentine channel. a) Frames from video showing delivery of humidified nitrogen gas to live embryos on-chip. b) Zoom-in of boxed region in (a) indicating embryos remain oriented for end-on imaging with a reservoir of PBST found in resistance channels that keep embryos from drying out during anoxia exposure.

2.2.6: Cell Cycle Kinetics Quantification

Cell cycle kinetics were extracted from the time-lapse images by using a custom built Matlab (Mathworks) program. Briefly, the algorithm uses a combination of relative difference filtering and clustering to identify and segment nuclei from Histone-GFP channels. Once segmented, the algorithm calculates user-defined features about the segmented nuclei including, for example, "average area of a nucleus" (referred to as nuclear area from this point forward). Cell cycle timing is then extracted by examining peak widths in the nuclear area feature trajectory.

2.3: Results

2.3.1: DV Array Optimization for End-On Imaging of Live Embryos

In this chapter, I designed and optimized a microfluidic device as part of a platform for precise environmental perturbation and continuous live imaging of embryo development. Specifically, I aimed to deliver a platform that could display minimal concentration variability across the device in a molecular species that readily diffuses through PDMS. Optimization yielded an embryo array platform with acceptable environmental variations in oxygen concentrations for the investigation of anoxic conditions during *Drosophila* embryo development. As a result, this platform should be highly adaptable and still be optimized for a variety of other biologically relevant environmental perturbation studies on embryos. Furthermore, the throughput of this design is limited by the imaging frequency of state-of-the-art confocal microscopy. Thus, very few live imaging setups would be able to take advantage of embryo capacities larger than this optimized design.

For anoxic studies on *Drosophila* development, precise control of the embryo microenvironment and the ability to dynamically change the oxygen availability around developing embryos is necessary. Beginning with the embryo trap array from previous works, it was expected the larger microfluidic device would prove difficult to accurately control the on-chip oxygen concentration, as oxygen would readily diffuse through the gas-permeable polydimethylsiloxane (PDMS) device along the fluid flow path. I constructed COMSOL finite element models to investigate the combined fluid and mass transport in the previous design. From the model, it was discovered that a significant oxygen concentration gradient would exist across a microfluidic array as large as our previously designed embryo trap array [73] (Figure 2.4). It was therefore necessary to optimize the initial design by reducing the residence time of the perfusate in order to ensure minimal variability of microenvironments experienced by embryos in the array.

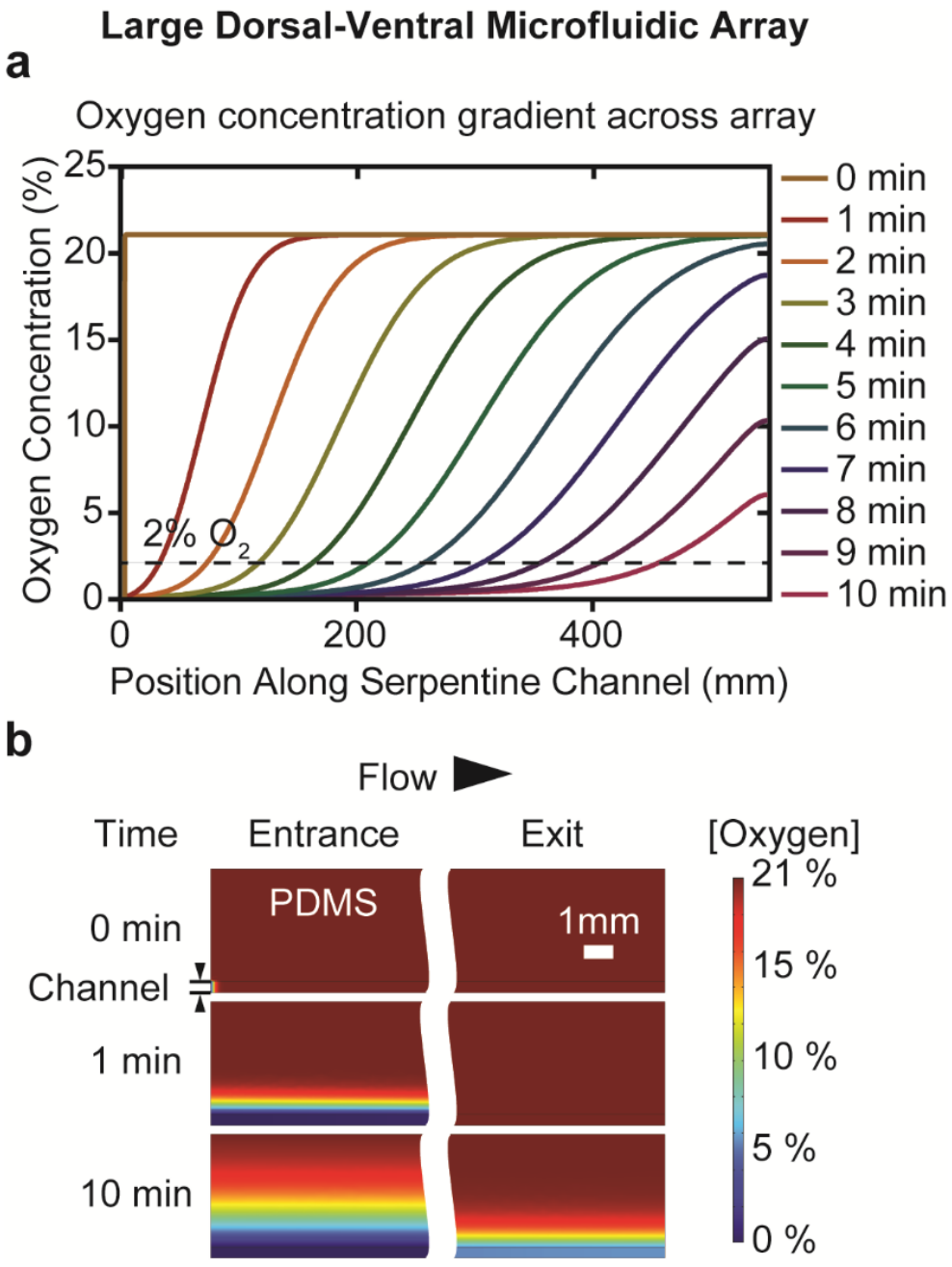

Figure 2.4: COMSOL simulations of combined fluid and mass transport in the original microfluidic array [73]. a) Line plots depicting oxygen concentration along the serpentine channel as a function of time in a microfluidic array with dimensions equivalent to that described by our previous large array. Even after 10 minutes of circulating anoxic gas there is still a significant oxygen concentration gradient along the serpentine channel. b) Surface plots depicting oxygen concentration in the serpentine channel and PDMS at the entrance and exit of the large microfluidic array. Significant oxygen concentration gradient in the serpentine channel from entrance to exit of the large microfluidic array.

It was discovered during optimization that imaging frequency was a major bottleneck in experimental throughput. Relevant observations for morphological changes occur in the dorsal-ventral plane of the embryo at ~80 μm from either the anterior or posterior pole throughout stages 4-6 of development, and relevant morphological changes occur at a temporal resolution of 1 minute. Thus, a minimum imaging rate of 1 frame per second per embryo is necessary to visualize the rapid nuclear cycling dynamics that occurs during stage 4 of embryogenesis. Using these imaging parameters, laser scanning confocal microscopy generally allows imaging of ~20 embryos per experiment. Thus, even if gas permeability were not an issue for a given experimental design, a device as large as the original embryo trap would not have offered any advantages or increases for throughput for live embryo imaging.

For these reasons, the device was miniaturized such that the time-lapse imaging device now contains 22 embryo traps in a 1.7 x 5.5 mm device footprint (Figure 2.5a). Twenty-two traps was selected specifically, because array devices such as this have been shown to reach loading efficiencies of >90%; thus, attaining ~90% loading efficiency, we are then able to array our target goal of 20 embryos for each imaging experiment.

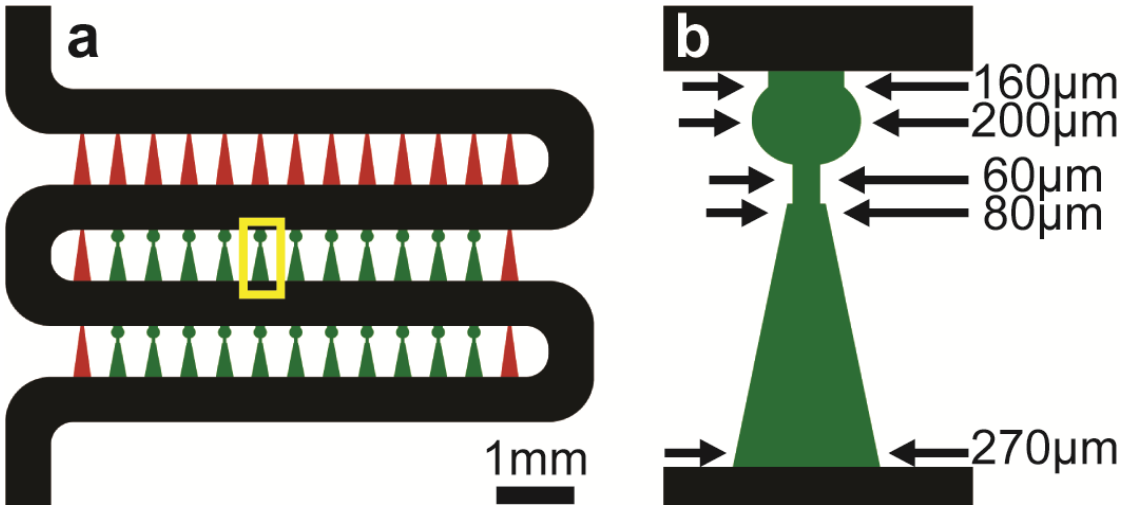

Figure 2.5: Overall layout for the optimized dorsal-ventral live imaging array with main serpentine channel (■), focusing channels (■), and embryo traps and resistance channels (■).b) Zoom-in of boxed region of (a) with dimensions of the embryo trap and resistance channel.

As for environmental variability in the miniaturized design, COMSOL finite element modeling of the DV array indicates that oxygen can be rapidly removed from the serpentine channel and exhibit constant oxygen concentrations within 1 minute of switching to humidified nitrogen gas perfusate (Figure 2.6).

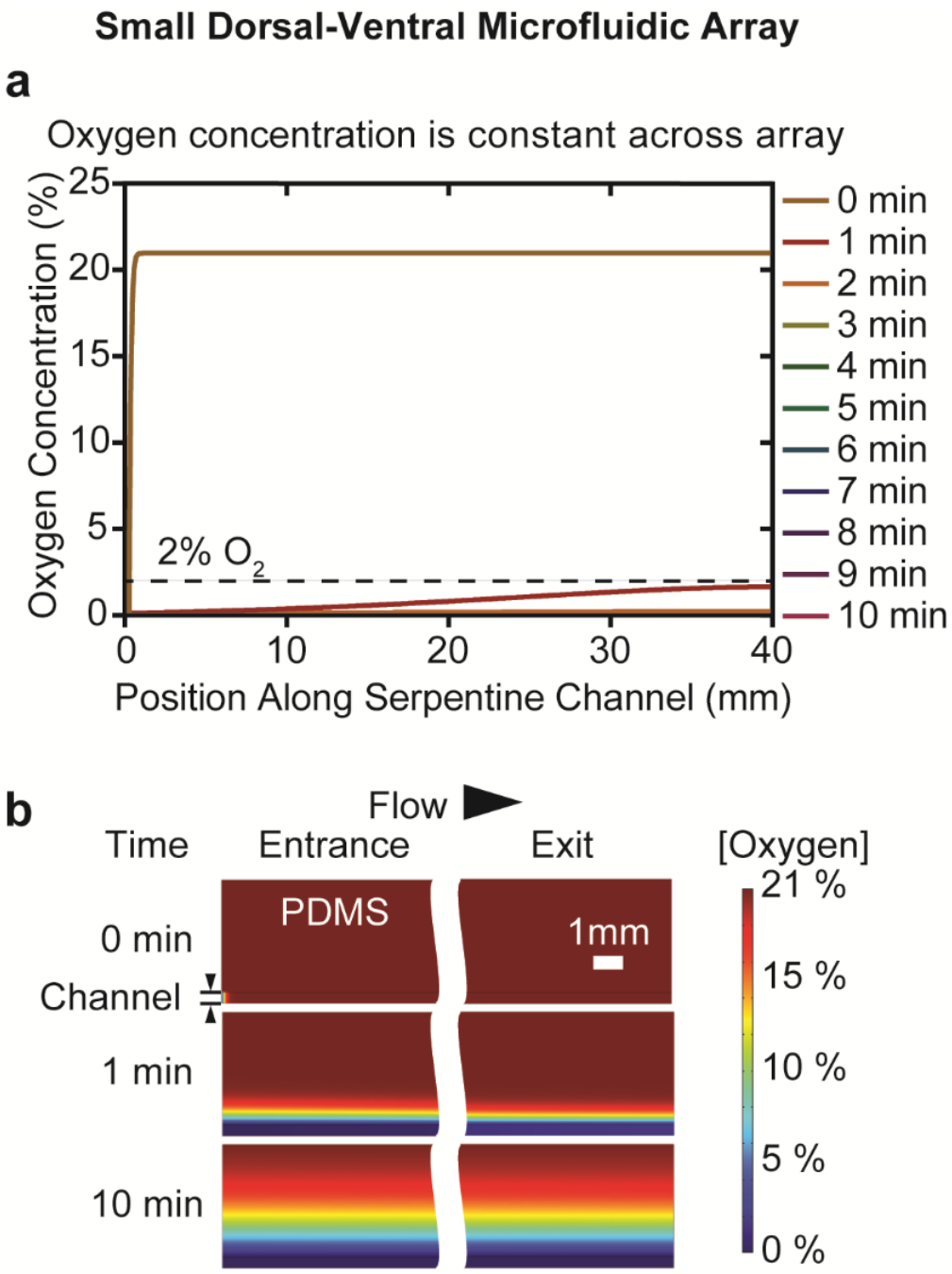

Figure 2.6: COMSOL simulations of combined fluid and mass transport for the optimized dorsal-ventral live imaging array. a) Line plots depicting oxygen concentration along the serpentine channel as a function of time in a microfluidic array with dimensions equivalent to that described in this paper. After 1 minute of circulating anoxic gas there is <2% oxygen present within the serpentine channel, and <0.1% oxygen after 2 minutes. b) Surface plots depicting oxygen concentration in the serpentine channel and PDMS at the entrance and exit of the small microfluidic array. Constant oxygen concentration in the serpentine channel from entrance to exit of the small microfluidic array.

Scaling the embryo array design from an original size footprint of 50 x 17 mm down to the current 1.7 x 5.5 mm footprint was not a trivial process, because the operational principle of the device relies on the balancing of two perpendicular flow fields throughout the device to efficiently capture embryos. The two flow fields that govern efficient embryo capture are 1) the main flow along the larger serpentine channel, and 2) the secondary flow through the embryo traps arrayed along the serpentine channel. Reducing the number of columns (equivalently, traps) along a row in the array decreases the average flow rate through the embryo traps along a given row. As a result, a smaller array of the original trap design exhibited an average loading efficiency of 26 ± 8% (3 experiments with n = 9, 5, and 3 embryos) (Figure 2.7a).

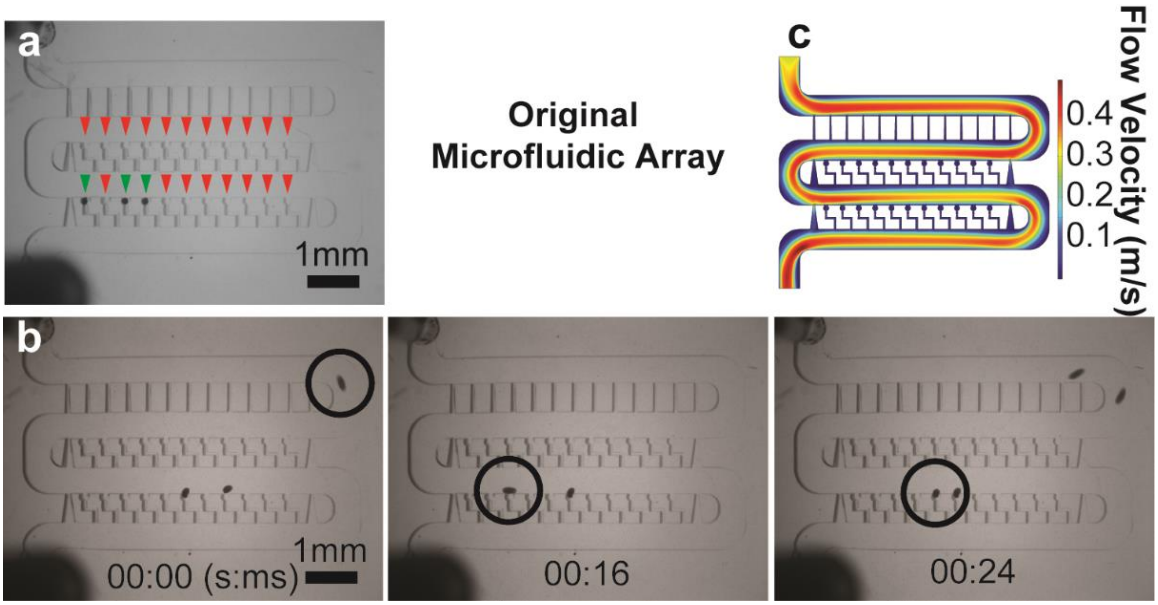

Figure 2.7: Device loading and COMSOL simulation for the original dorsal-ventral microfluidic array [73, 74]. a) Typical device loading for microfluidic array employing previously developed embryo trap, ▼ indicate empty traps, ▼ indicate traps with embryos successfully loaded. b) Frames from live embryo loading in (a) showing embryos do not successfully trap in device. ○ is tracking a single embryo through successful trapping. c) COMSOL simulation of the non-optimized microfluidic array exhibiting Dean flow and high flow velocity in the serpentine channel relative to embryo traps and resistance channels.

This suggests that the ratio of hydraulic resistances between flow through embryo traps and flow along the serpentine channel are improperly balanced in the smaller array. COMSOL finite element modeling and embryo-loading videos indicated that Dean flow [137-139] is achieved in these smaller devices, which successfully placed embryos along the bottom of the serpentine channel near trap entrances; however, the cross-flow through the traps was not strong enough to drive embryos into traps (Figure 2.7b and 2.7c) To address this issue, a redesign of the microfluidic architecture was required to properly balance flow throughout the device and increase loading efficiency.

In order to compensate for the decreased fluid flow through the traps, we aimed to reduce hydraulic resistance of the embryo traps. This was accomplished by first decreasing the length of the resistance channel in the embryo trap unit. However, this did not effectively reduce the hydraulic resistance sufficiently to improve embryo trapping, as average loading efficiency for such design was 64 ± 8% (3 experiments with n = 17, 14, and 11 embryos). We further refined the resistance channel geometry such that the resistance channel tapered from 80 μm wide to 270 um (Figure 2.5b). With this design, loading efficiency improved to 91 ± 3% (3 experiments with n = 21, 20, 19 embryos) (Figure 2.8a and 2.8b). COMSOL simulations confirmed that the flow velocity in the serpentine channel is significantly decreased relative to flow velocity through traps in this design when compared to the original embryo trap design (Figure 2.8c).

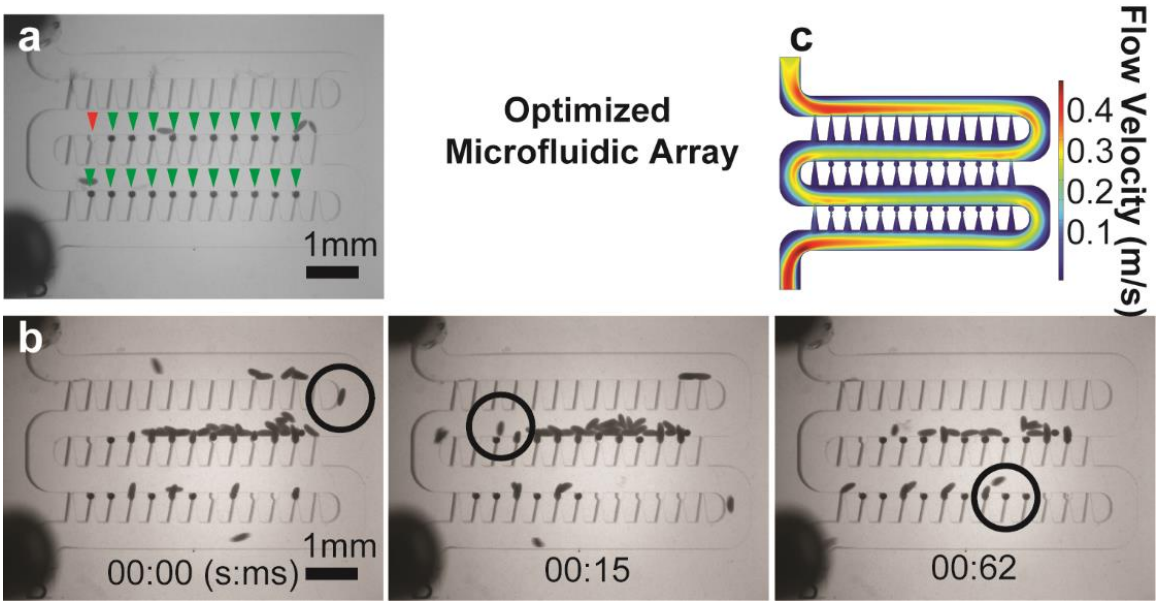

Figure 2.8: Device loading and COMSOL simulation for the optimized dorsal-ventral microfluidic array. a) Typical device loading for optimized microfluidic array. ▼ indicate empty traps, ▼ indicate traps with embryos successfully loaded. b) Frames from live embryo loading in (a) showing embryos successfully trap in device. ○ is tracking a single embryo through successful trapping. c) COMSOL simulation of the optimized microfluidic array exhibiting Dean flow and lower flow velocity in the serpentine channel relative to the non-optimized microfluidic array in Figure 2.7.

It should be noted that although sufficiently high flow rates are desired through the embryo traps, very low hydraulic resistances through embryo traps can result in embryos clogging the serpentine channel and prevent loading of additional traps downstream. Thus, a precise ratio of flow rates through the embryo traps and serpentine channel must be achieved to guide the embryos into the traps, but also allow following embryos to pass occupied traps to the next vacant trap downstream.

An additional design parameter is trap geometry. Optimization of this feature required two major changes. The first regarded the overall size of the trap. The trap is a truncated-cylinder of 500 µm tall and 200 µm in diameter. The diameter of the trap was

expanded from the original 150 μm in order to reduce pressure exerted from the PDMS trap on the embryo, and improve viability of live embryos on-chip. The second major change regards the trap entrance, which was previously designed to be 90 μm wide. This allowed robust trapping such that fluidic connections could be removed and devices could be easily transported from stereomicroscopes, which are preferred for device loading to higher resolution microscopes such as confocal microscopes. However, although the trap does flex upon slight positive pressure during loading, higher pressures are typically required to direct embryos completely into traps of this shape. Both the added pressure and strain imparted on embryos as they squeeze through the trap entrance can have harmful effects on live embryos.

To reduce the strain imparted on developing embryos during device loading, we optimized the trap entrance such that embryos can enter traps readily at 6 psi, which is an acceptable pressure for handling live organisms [52, 65, 140], and yet still be robustly held in traps for long-term imaging without active circulation of media. To do this, traps with various entrance widths were constructed and tested. We found that trap entrances that approach 200 μm do not robustly hold embryos for end-on imaging; once flow is halted, embryos immediately fall out of the traps into the serpentine. Also, traps with entrances of 170-190 μm wide held embryos well in static flow conditions, but could not robustly handle embryos because of problems such as transporting devices from low-resolution microscopes to higher resolution microscopes, or accidental bumping of devices. The widest entrance that exhibited robust embryo handling throughout imaging and resisted other complicating factors was 160 um (Figure 2.5b). Taken together, the

optimized device we developed can robustly orient ~20 live embryos for long-term, end-on imaging in less than 3 minutes.

2.3.2: Embryos Shows Normal Developmental Progression after Trapping in the DV Array

In order to test the compatibility of the device for imaging live *Drosophila* embryos, we first loaded the array and imaged embryo development of Histone-GFP expressing embryos under static conditions in which no active circulation of perfusate was utilized. This is the simplest way to use the device for live imaging. Furthermore, PDMS is gas permeable allowing free diffusion of oxygen from the outside environment toward respiring embryos. Operating with no circulation will allow us to test whether embryos receive sufficient oxygen while developing on-chip, which can be validated by analyzing developmental phenotypes and rates, and comparing with what is known in the literature.

Frames from time-lapse imaging of a Histone-GFP expressing embryo are shown in Figure 2.9. Typically, embryos are stage 3 or younger when these experiments begin, which is characterized by the absence of nuclei at the periphery of the embryo. Cytoplasmic contractions can be seen during these early stages of development in the GFP channels indicating that synchronous divisions are occurring deep within the yolk beyond visibility. Approximately 25 minutes into imaging, nuclei began to appear at the periphery (Figure 2.9), which marks the beginning of stage 4 of embryogenesis. During stage 4, for the next ~45 minutes, the embryo proceeded through 4 synchronous nuclear divisions (Figure 2.9) after which the embryo enters stage 5 of development. Stage 5

lasted ~60 minutes in which the syncytial *Drosophila* embryo becomes cellularized to form the blastula (Figure 2.9). After cellularization, ventral furrow invagination is initiated during stage 6 (Figure 2.9), and invagination completes during stage 7 (Figure 2.9). Finally, the invaginated mesoderm collapses and proceeds through the process of mesoderm spreading during stage 8 of development (Figure 2.9). Qualitatively embryos appear to exhibit normal developmental phenotypes within the microfluidic array, and to further confirm this we quantitatively assess on-chip developmental rates in the following section.

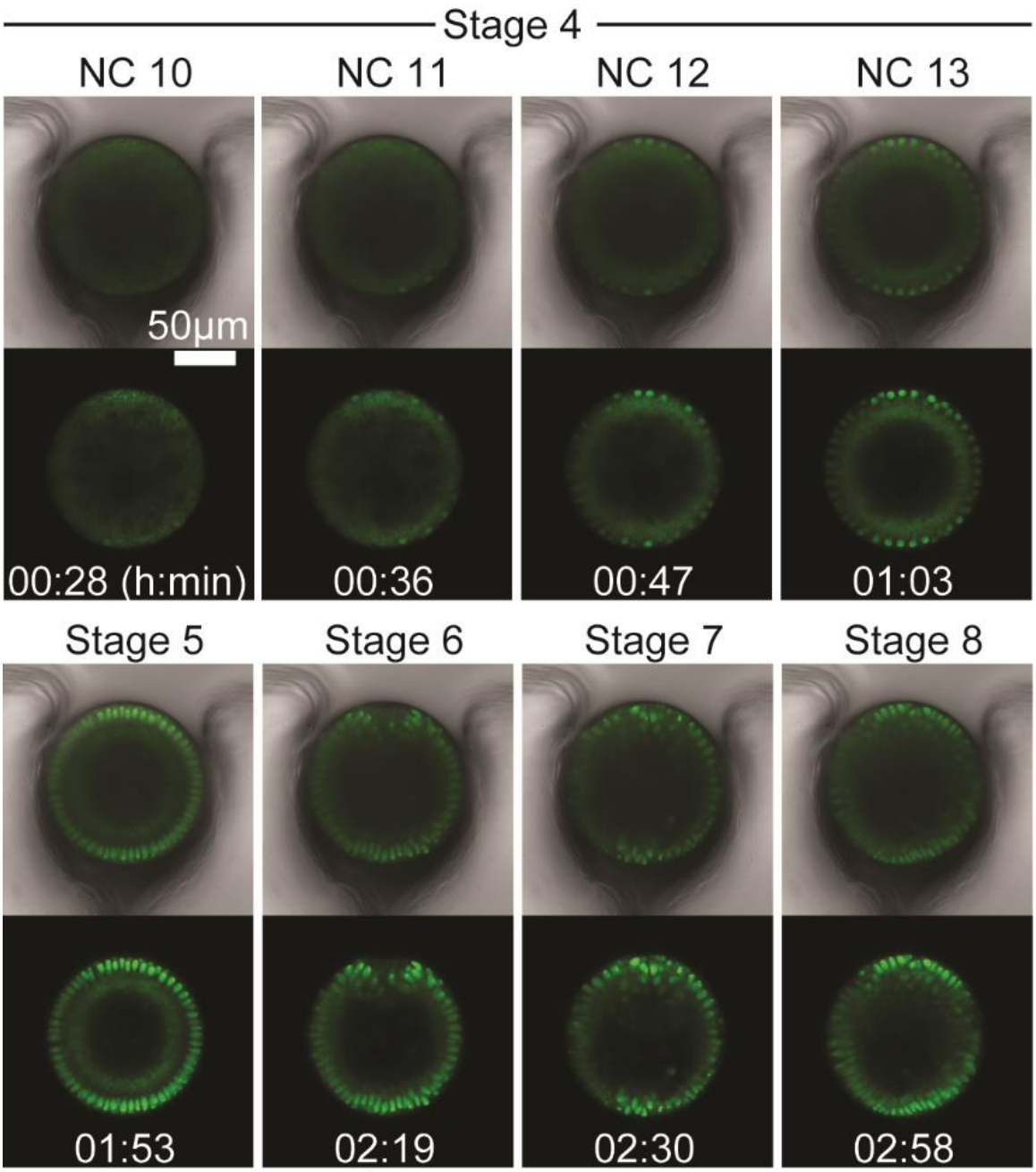

Figure 2.9: Each pair of images are single time points from a time-lapse imaging video of a live developing embryo expressing a Histone-GFP transgene within the microfluidic array. The video was 3 hours in total length, and each time-point is stamped with the time that each event occurred. The time is relative to the start time when the confocal microscope began scanning. Top image is a merge of bright-field and Histone-GFP channels, while the bottom image is only the Histone-GFP channel. From left to right: tope row: nuclear cycle 10, nuclear cycle 11, nuclear cycle 12, nuclear cycle 13; bottom row: stage 5, stage 6, stage 7, and stage 8.

2.3.3: Nuclear Cycle Kinetics Analysis Indicates Embryos Develop at a Normal Rate in the DV Array

With device optimized for live imaging on-chip, we collected imaging data and compared on-chip development to what was reported in the literature. Previously, Foe and Alberts provided quantitative information about nuclear cycle kinetics in the *Drosophila* syncytial blastoderm [136]. We collected similar data by live imaging on-chip and analyzing the nuclear cycle kinetics during embryonic stages 4 and 5. By doing this, we can quantitatively measure developmental rates on-chip and check if normal development is achieved within the microfluidic device.

To complement our high-throughput experimental method developed here, we have also developed automated data-analysis approaches. Specifically, we developed an algorithm for automatic identification and segmentation of fluorescent images. In this case of analyzing nuclear cycle kinetics, segmentation is identifying individual nuclei (by Histone-GFP fluorescence) in time-lapse videos. With the nuclei identified, the program then calculates a library of user-defined features that can be used to extract important information about cell cycle kinetics. A feature we found useful is the "average area of a nucleus" or "nuclear area" for short. When plotted as a function of time, the nuclear area exhibits an oscillatory behavior (Figure 2.10). The peaks and valleys correspond to nuclear cycles 10-13 and stage 5, wherein the peaks correspond to interphase and the valleys correspond to the nuclear division phase. This simple measure allows easy and unbiased identification of nuclear cycling kinetics, and provides an assessment for developmental rate on-chip.

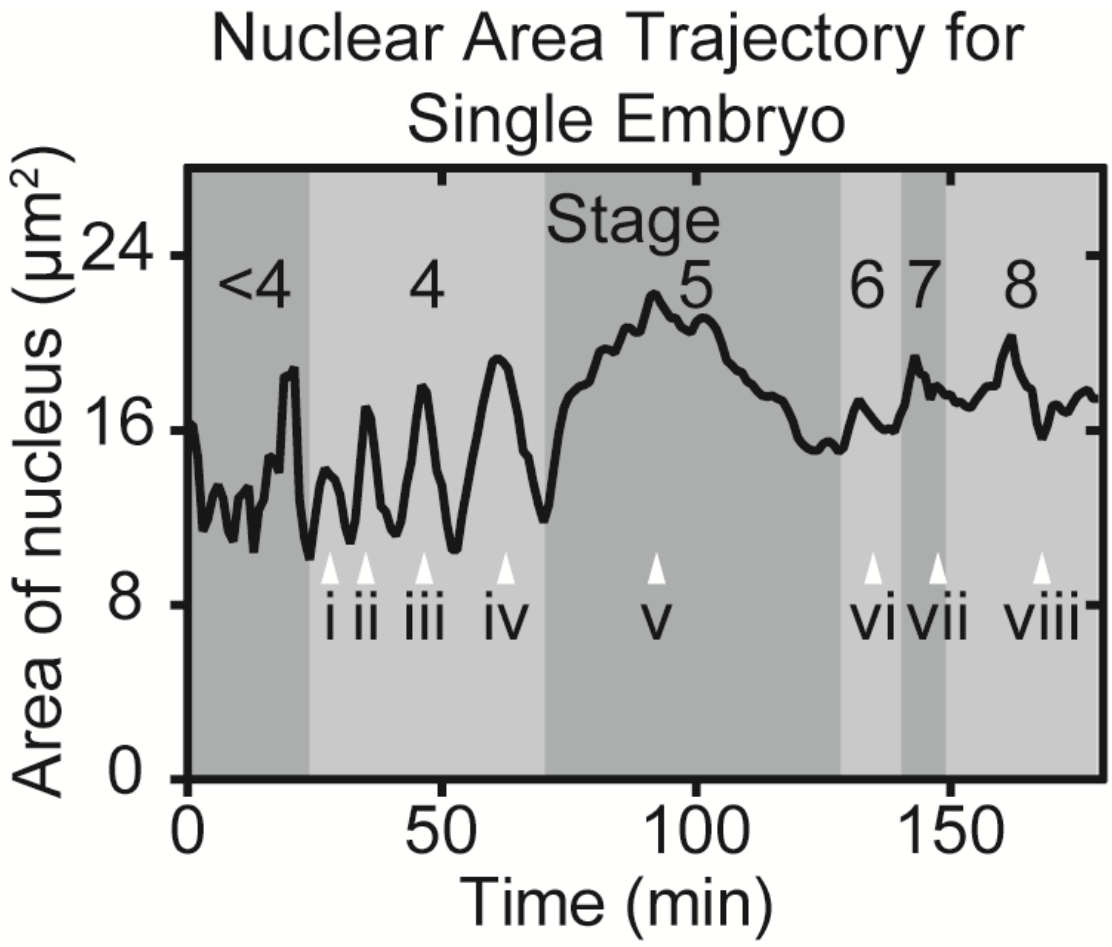

Figure 2.10: The average area of a nucleus trajectory for a single embryo; the same embryo found in Figure 2.9. i-viii indicate the time point at which each image in Figure 2.9 was taken. i) Stage 4, nuclear cycle 10. ii) Stage 4, nuclear cycle 11. iii) Stage 4, nuclear cycle 12. iv) Stage 4, nuclear cycle 13. v) Stage 5. vi) Stage 6. vii) Stage 7. viii) Stage 8.

In order to understand what exactly nuclear area is correlated with, we imaged Histone-GFP expressing embryos using a 63X oil immersion objective and analyzed the videos with the same segmentation algorithm (Figure 2.11a). We infer that the peak maxima are associated with interphase as nuclei exhibit a round morphology with

uniform intensity at these time points (Figure 2.11a and 2.11b). Nuclear area decreases as nuclei progress to prophase as chromosomes begin to condense, which is identified by nuclei exhibiting a more punctate appearance (Figure 2.11a and 2.11b). The decrease in nuclear area continues as chromosomes condense further and align at the nuclear division plane during metaphase (Figure 2.11a and 2.11b). The sister chromatids are segregated during anaphase wherein chromatids can be seen with an elongated morphology (Figure 2.11a and 2.11b). Finally, the nuclear area hits trough minima during telophase as chromosomes are now in a rounded morphology, and still highly condensed prior to chromosome expansion (Figure 2.11a and 2.11b) that occurs during the next interphase (Figure 2.11a and 2.11b). Therefore, the minimum to minimum distance in nuclear area trajectories can be used to extract the length of each nuclear cycle during stage 4 of development, wherein specifically these values are measuring the time from one telophase to the next.

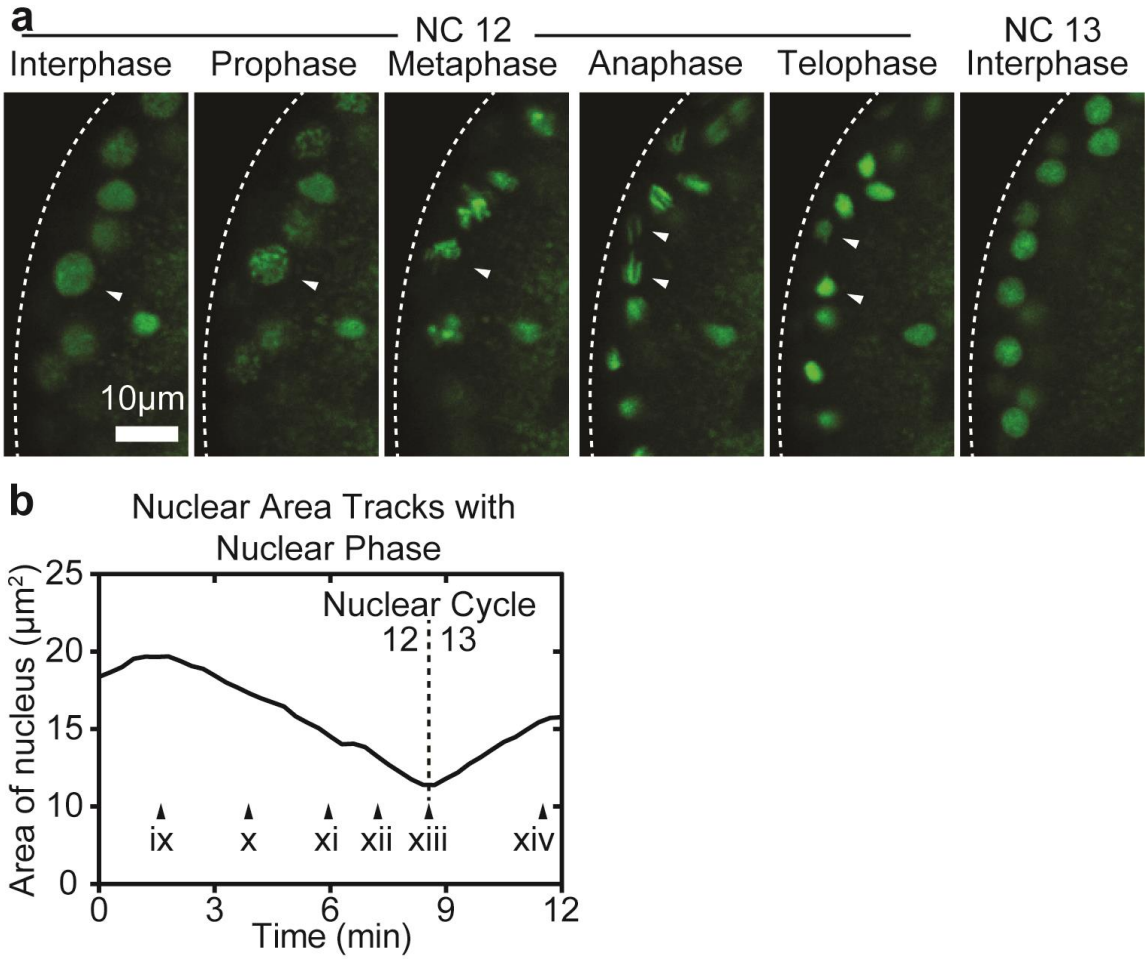

Figure 2.11: High magnification imaging of cell cycle. a) 63X confocal imaging of Histone-GFP expressing embryo and nuclear cycle phases. ▼ indicates the same nuclei proceeding from nuclear cycle 12 interphase to prophase to metaphase to anaphase to telophase. After telophase, the nuclei was lost due to significant z-drift caused by yolk contractions during nuclear cycle 13 interphase. b) Nuclear area trajectory for embryo found in (a). ix-xiv indicate the time point at which each image in (a) was taken. ix) Interphase, nuclear cycle 12. x) Prophase, nuclear cycle 12. xi) Metaphase, nuclear cycle 12. xii) Anaphase, nuclear cycle 12. xiii) Telophase, nuclear cycle 12. xiv) Interphase, nuclear cycle 13.

Recording large numbers of embryo development time-sequences and averaging feature trajectories allows us to establish what average embryos look like when developing in the microfluidic array and compare to the literature. This is helpful when comparing embryo development under different experimental conditions. Because

embryos are not perfectly age-synchronized, videos (and therefore feature trajectories) must first be aligned in the developmental time frame. Here, we used nuclear division 12 as the developmental time point with which to align all videos (i.e. the nuclear division between nuclear cycles 12 and 13). Accurate and unbiased alignment of videos in time is made simple, because the code can easily identify nuclear division 12 as a single time-point by looking for local minima in the nuclear area trajectory. Alignment of videos thus allows us to average feature trajectories in order to establish what an average embryo looks like when developing inside the microfluidic array (Figure 2.12a).

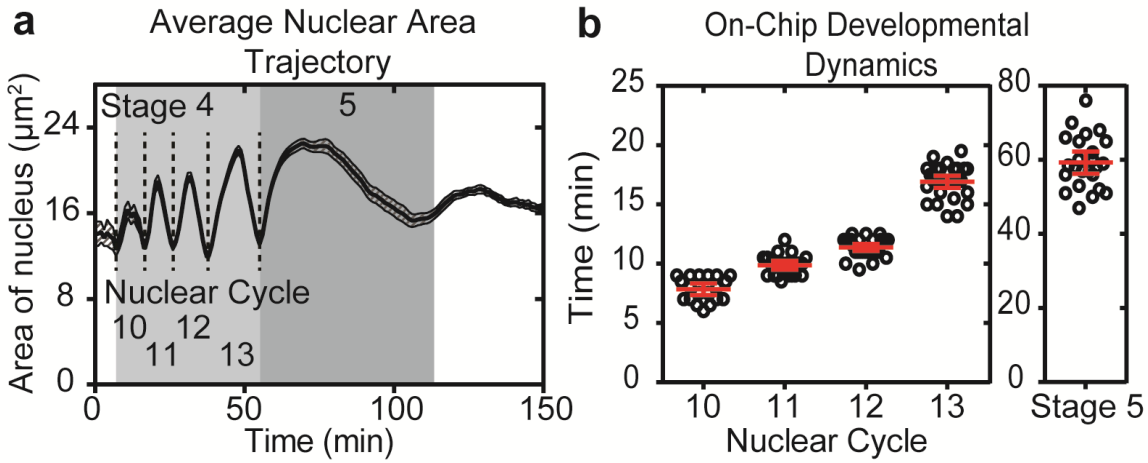

Figure 2.12: Quantifying on-chip developmental dynamics. a) Average nuclear area trajectory ± S.E.M. for embryos developing on-chip exhibits stereotyped oscillations that corresponds with stage 4-5 of development (n = 35 embryos). b) Measured nuclear cycle duration for Histone-GFP expressing embryos developing on-chip as extracted by examining the peak widths found in Figure 2.12. Average ± S.E.M. duration of nuclear cycle 10, 11, 12, 13, and stage 5 are 7.8 ± 0.2 minutes (n = 27 embryos), 9.9 ± 0.2 minutes (n = 32 embryos), 11.4 ± 0.1 minutes (n = 35 embryos), 16.9 ± 0.2 minutes (n = 35 embryos), and 59.3 ± 1.4 minutes (n = 25 embryos), respectively.

The population average (n = 35 embryos from 3 experiments) of the nuclear area trajectory exhibits a stereotyped pattern of 5 peaks that correspond with nuclear cycles 10-14 encompassing stages 4-5 of development. The peak widths are then used to directly extract the duration for each nuclear cycle. The observed duration for nuclear cycles 10, 11, 12, 13 and stage 5 are as follows: 7.8 ± 0.2 minutes (n = 27 embryos), 9.9 ± 0.2 minutes (n = 32 embryos), 11.4 ± 0.1 minutes (n = 35 embryos), 16.9 ± 0.2 minutes (n = 35 embryos), and 59.3 ± 1.4 minutes (n = 25 embryos) (average ± standard error of mean S.E.M.)) (Figure 2.12b), which closely matches with what is known to occur for these stages of development when using more conventional imaging methods [136]. Specifically, we see that the duration for each nuclear cycle increases progressively from one cycle to the next starting at cycle 10. Additionally, the relative increases from cycle to cycle are similar to what is expected; i.e. moderate increases in duration from cycle 10 to 11 to 12, a more substantial increase in the duration of cycle 13, and an even more substantial increase in the duration for stage 5. It is evident that the device can effectively array live embryos in order to collect large imaging data sets for statistical analysis of developmental dynamics.

2.3.4: Effects of Anoxia Exposure are Short-Lived and Delay Overall Development

Embryogenesis in humans and flies alike requires sufficient oxygen availability for normal development [141-144]. Fluctuations in nutrient availability are inescapable, and yet developing embryos must be robust to these changing conditions throughout development. Typically, to directly visualize the effects of oxygen availability on *Drosophila* embryogenesis, experimentalists apply gas with specific oxygen concentrations directly over embryos mounted on a glass slide [145-149]. Responses are

then monitored with *in vivo* live imaging with either differential interference contrast imaging or fluorescent reporters [145, 150]. However, not much work has been done to precisely characterize these responses, which is primarily due to the fact that traditional methods are limited to imaging one or two embryos at a time. This is because embryos must be tediously hand-mounted with embryo glue to prevent embryos from floating away during imaging. Here we apply our method of microfluidic high-throughput live imaging and analysis to quantitatively assess kinetics of anoxia-induced developmental arrest and recovery.

In order to investigate anoxia-induced arrest and recovery, we perturbed development by briefly exposing embryos to anoxia while on-chip. To do this, we delivered anoxic pulses of 10 minutes to embryos on-chip by flowing humidified nitrogen gas through the serpentine channel (Figure 2.3). This method allows for rapid changing of the microenvironment as the entire array can be perfused in less than 4 seconds (Figure 2.3a). It is possible to do so because the PDMS traps securely hold embryos in place despite active perfusion through the microchannels. Furthermore, the surface tension of PBST is strong enough to resist displacement by the gas phase in the traps and resistance channels, which act as a reservoir of water so that embryos do not dry out during anoxia exposure (Figure 2.3b). Finally, this method allows us to directly visualize the dorsal-ventral plane and the morphological responses in the dorsal-ventral plane to anoxia, a feat that to our knowledge has never been accomplished before.

We next analyzed the effects of 10 minute anoxia exposure on nuclear cycle kinetics quantitatively. Embryos that are in nuclear cycle 13 of development when the anoxia exposure occurs exhibit classic signs of anoxia-induced arrest. During metaphase

arrest, nuclei proceed through each phase of the nuclear cycle until metaphase is reached. Under normoxic conditions, nuclei remain in metaphase for ~1-2 minutes (Figure 2.13a). However, under anoxic conditions, nuclei exhibit a hypercondensed morphology (Figure 2.13b). Embryos remain in this arrested state with hypercondensed nuclei throughout the remainder of the anoxia exposure, and continue to be arrested for several minutes after normoxia is re-established in the device (Figure 2.13c). We quantitatively measured that embryos proceeded to anaphase approximately 7.9 ± 0.7 minutes after embryos were returned to normoxia, which is consistent with what was previously observed [145, 150].

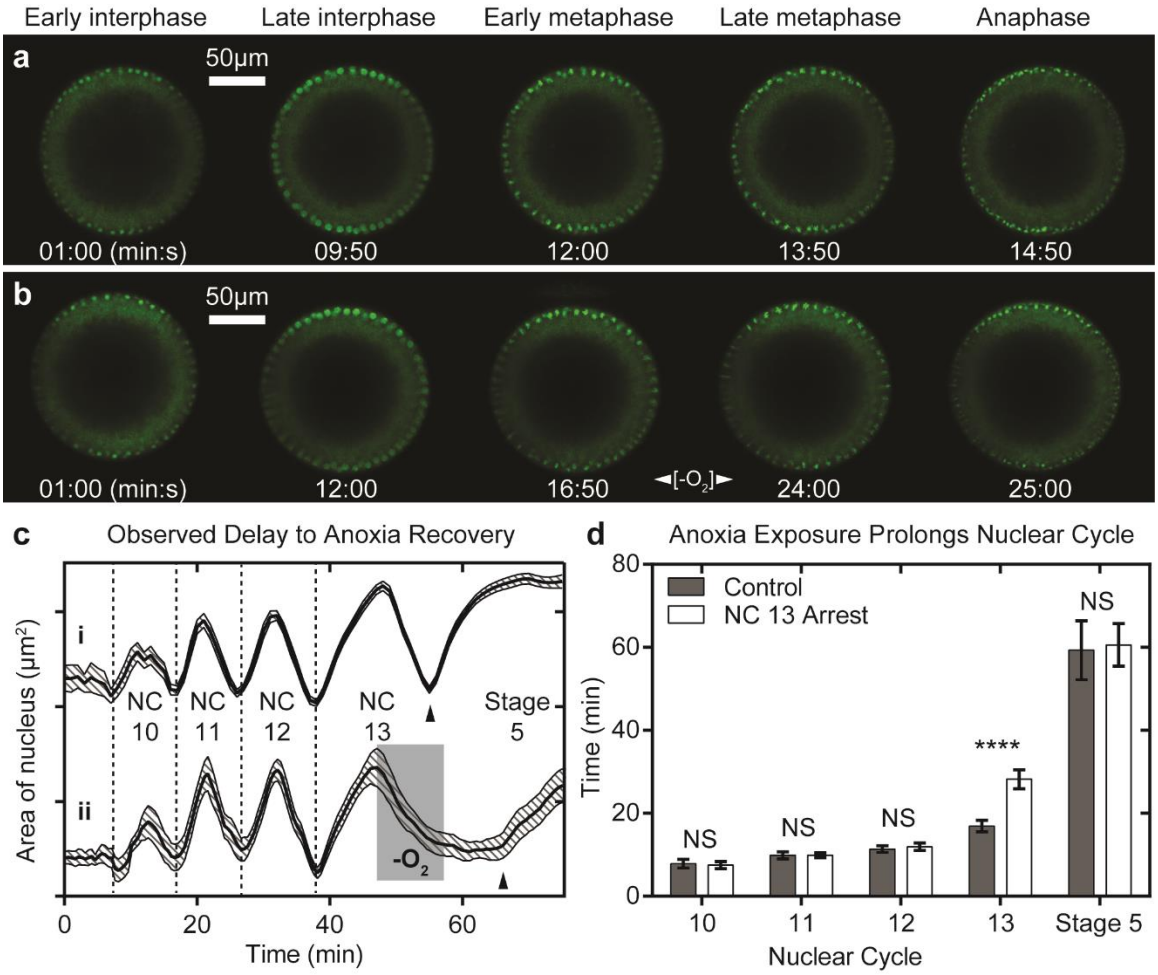

Figure 2.13: Immediate effects of anoxia exposure on embryo development. a) Frames from *in vivo* live imaging a Histone-GFP expressing embryo progressing through nuclear cycle 13 (control). b) Frames from *in vivo* live imaging a Histone-GFP expressing embryo progressing through nuclear cycle 13 that exhibits anoxia-induced metaphase arrest. c) Average ± S.E.M. nuclear area trajectory for embryos grown in (i) normoxia (n = 35 embryos), and (ii) experiencing 10 minutes of anoxia during nuclear cycle 13 (n = 14 embryos). Shaded region in (ii) indicates when anoxia was delivered. Black triangle indicates telophase to interphase 14 transition. d) Average ± S.D. durations for nuclear cycles 10, 11, 12, 13, and stage 5 for embryos grown in normoxia (control, n = 35 embryos), and experiencing 10 minutes of anoxia during nuclear cycle 13 (NC 13 arrest, n = 14 embryos). Nuclear cycles 10-12 and stage 5 durations are not significant (NS) while nuclear cycle 13 is statistically different from control (****$p<0.0001$. T-test).

Because this method allows us to continuously image embryo development throughout anoxia exposure, we can quantitatively measure developmental rates prior to

and after anoxia exposure. By doing this, we find that anoxia-exposed embryos have quantitatively the same nuclear cycle kinetics as control embryos prior to anoxia exposure. This indicates that embryos are viable and developing at normal rates prior to anoxia exposure (Figure 2.13d). This is expected, because prior to anoxia exposure, the on-chip conditions are the same as control groups (i.e., embryos are in non-circulating PBST). Embryos that experienced anoxia during nuclear cycle 13, however, were quantitatively measured to have a nuclear cycle 13 duration of 28.0 ± 0.6 minutes (Figure 2.13d). Therefore, 10 minutes of anoxia exposure during nuclear cycle 13 resulted in an increase of ~11.1 ± 2.3 minutes in the duration of nuclear cycle 13. This suggests that *Drosophila* embryos arrest and recover from anoxia-induced developmental arrest with similar kinetics.

After anoxia exposure, embryos recover from arrest and continue through the next phases of development, in this case, stage 5 cellularization and stage 6 ventral furrow formation. Previously, it has been shown that embryos exhibit decreased viability when exposed to anoxia prior to cellularization [145, 151]. We observed the same effect using our method. Embryos were found to successfully recover from anoxia-induced developmental arrest in nuclear cycle 13 ~64% of the time (i.e. 9 out of 14 embryos recover). Successful recovery was taken as the observation of gastrulation (i.e. ventral furrow formation) after arrested development (Figure 2.14a). Embryos that did not successfully gastrulate after arrested development exhibited atypical morphology (Figure 2.14b). We observed that sister chromatids frequently segregate unsuccessfully from one another after anoxia-induced arrest. This was observed by the presence of Histone-GFP signal being visibly present between two daughter nuclei that eventually fused together.

Many of the nuclei in the field of view appeared to exhibit this same phenotype after anoxia-induced arrest resulting in massive polyploidy and eventually, massive delamination of nuclei from the plasma membrane at the embryo periphery. This suggests that the sensitivity of syncytial embryos to anoxia/hypoxia-induced developmental arrest could be related to massively unsuccessful nuclear divisions prior to cellularization.

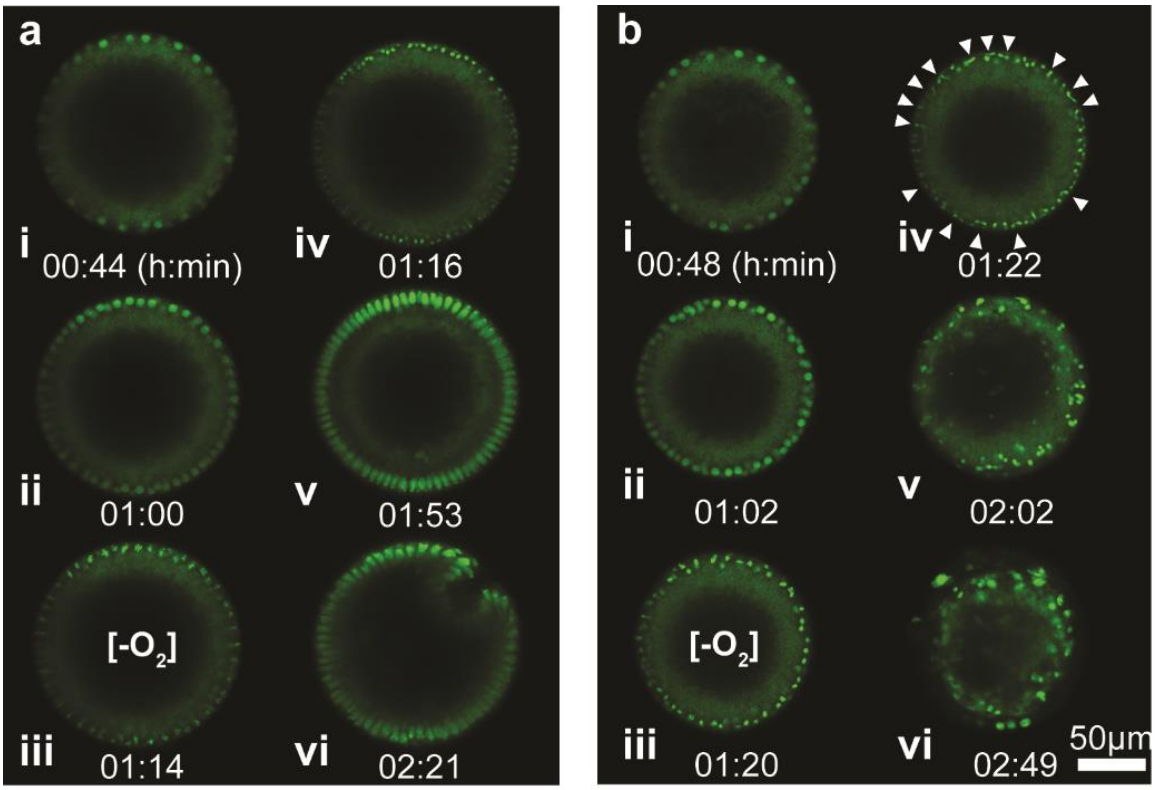

Figure 2.14: Recovery from anoxia-induced developmental arrest. a) Frames from *in vivo* live imaging a Histone-GFP expressing embryo that successfully recovers from anoxia-induced developmental arrest. i) nuclear cycle 12, ii) nuclear cycle 13, iii) nuclear cycle 13 arrest in metaphase, iv) nuclear cycle 13 anaphase-telophase transition, v) stage 5, and vi) ventral furrow formation. b) Frames from *in vivo* live imaging a Histone-GFP expressing embryo that does not recover from anoxia-induced developmental arrest. i) nuclear cycle 12, ii) nuclear cycle 13, iii) nuclear cycle 13 arrest in metaphase, iv) nuclear cycle 13 anaphase-telophase transition (white triangles indicate fused daughter nuclei), and v-vi) nuclear delamination.

Embryos that successfully gastrulate after anoxia-induced arrest exhibit qualitatively normal morphologies in the dorsal-ventral plane (Figure 2.14a). Nuclei extend in the apical-basal direction during cellularization and a typical ventral furrow forms during stages 6 and 7 of development. Relative to the start of stage 4, embryos exhibit a statistically significant delay in ventral furrow formation after anoxia-induced arrest when compared to control embryos (Figure 2.15). The delay in ventral furrow formation was measured to be ~14.1 ± 4.2 minutes, which indicates anoxia-induced arrest results in overall developmental delays. This is a fact that is well-known in the literature. Interestingly however, the duration of stage 5 in anoxia-exposed embryos is measured to be statistically the same as control embryos indicating that embryos proceed with the same developmental rates immediately after recovery (Figure 2.13d). Together, this set of data suggests that the effects of anoxia exposure are immediate, but short-lived.

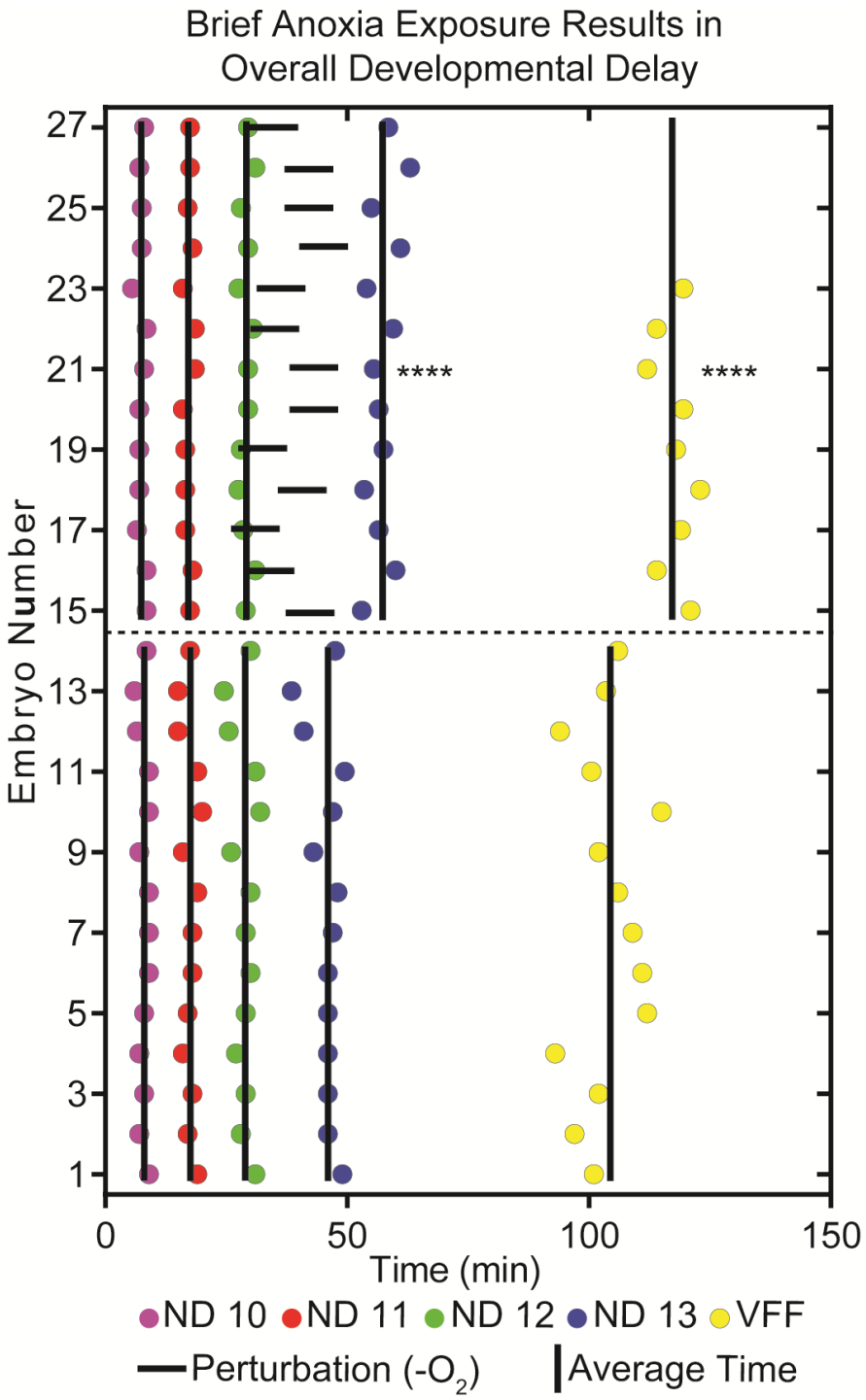

Figure 2.15: Plots showing the timing of milestone events for individual embryos on-chip with population averages for the timing of each event (|). Milestones include nuclear division (ND) 10, 11, 12, and 13, and ventral furrow formation (VFF). Embryos 1-14 are grown entirely in normoxia, and embryos 15-27 are exposed to brief anoxia in nuclear cycle 13 (anoxia indicated by -). The timing of nuclear division 13, and ventral furrow formation are statically different from control (****p<0.0001. T-test).

The phenomena mentioned above is not unique to the specific stage of embryogenesis that we have been exclusively investigating, i.e. nuclear cycle 13. Using our system, we can easily target any stage of interest for environmental perturbation, and we show that *Drosophila* embryos can undergo anoxia-induced developmental arrest during the earlier nuclear cycle 12 and the later nuclear cycle 14 in addition to nuclear cycle 13 (Figure 2.16a). Similarly to what was observed during nuclear cycle 13 arrest, nuclear cycle 12 and 14 arrest show an increase in the amount of time required for an individual embryo to perform each phase of development, while the other surrounding cycles are unaffected, which again indicates that our system can rapidly and robustly switch from normoxia to anoxia and back to normoxia. Furthermore, the phases of development that occur after anoxia-induced developmental arrest appear to align in time between experimental conditions suggesting that arresting in nuclear cycles 12, 13, and 14 simply result in the same amount of developmental delay (Figure 2.16b).

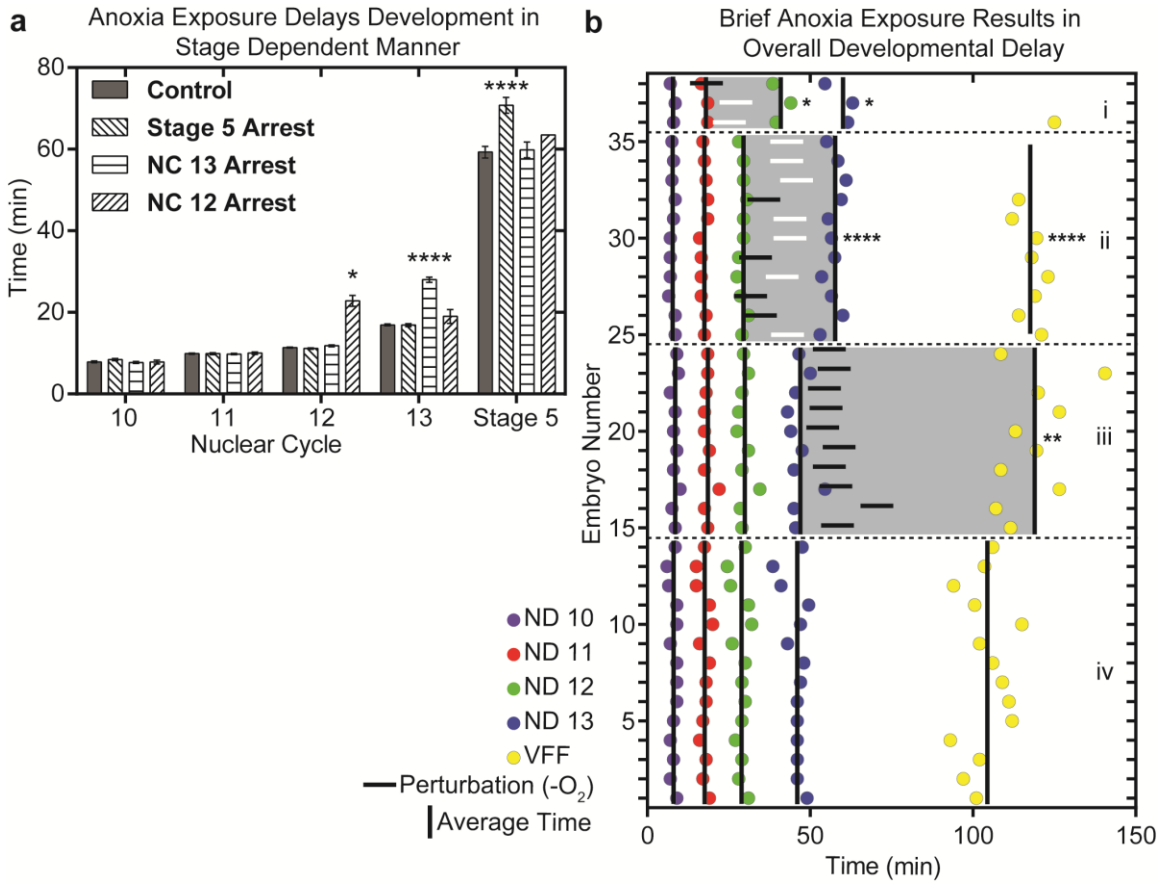

Figure 2.16: Effects of brief anoxia on nuclear cycle kinetics for cycles 12, 13, and 14. a) Average ± S.D. durations for nuclear cycles 10, 11, 12, 13, and stage 5 for embryos grown in normoxia (control, n = 35 embryos), and experiencing 10 minutes of anoxia during nuclear cycle 12 (NC 12 arrest, n = 3 embryos), 13 (NC 13 arrest, n = 14 embryos), and 14 (Stage 5 arrest, n = 17 embryos). Nuclear cycles not experiencing anoxia exhibit durations that are not significant (NS) while nuclear cycles that experience anoxia are statistically different from control (*p<0.05 and ****p<0.0001. T-test). b) Plots showing the timing of milestone events for individual embryos on-chip with population averages for the timing of each event (|). Milestones include nuclear division (ND) 10, 11, 12, and 13, and ventral furrow formation (VFF). Embryos 1-14 are grown entirely in normoxia, embryos 15-24 are exposed to brief anoxia in nuclear cycle 14 (anoxia indicated by -), embryos 25-35 are exposed to brief anoxia in nuclear cycle 13, and embryos 35-38 are exposed to brief anoxia in nuclear cycle 12. The timing of subsequent milestones are statically different from control (*p<0.05, **p<0.01, and ****p<0.0001. T-test).

However, an interesting observation was made for embryos that were arrested during nuclear cycle 14 (i.e. stage 5 of *Drosophila* embryogenesis) as compared to

nuclear cycles 12 and 13: embryos arrested during stage 5 of embryogenesis exhibited exceptionally high viability after anoxia exposure with 17 out the 17 tested embryos exhibiting proper ventral furrow formation whereas only 10 out of the 17 embryos arrested during nuclear cycles 12 and 13 exhibited proper ventral furrow formation. It is known in the literature that *Drosophila* embryos exhibit higher tolerance to anoxia exposure after cellularization [145, 150], but the above observations suggest that *Drosophila* embryos exhibit improved anoxia tolerance during the process of cellularization itself, which to our knowledge was not known prior.

To explain what could be the underlying reason for the improved tolerance to anoxia exposure during stage 5 of *Drosophila* embryogenesis I performed a literature search to acquire a better understanding of what is known to occur during this developmental phase. Stage 5 of *Drosophila* embryogenesis involves the process of cellularization wherein the embryo plasma membrane invaginates around individual nuclei and ends with each nuclei enclosed within individual cell membranes. At the same time, nuclear cycle 14 is significantly longer than the previous 13 nuclear cycles, and lasts longer than stage 5 itself. This means for the duration of stage 5, and for any of the anoxia treatments that all cells were in interphase. Important to note here is that it is well known in the literature that *Drosophila* cells have multiple cell cycle checkpoints and can arrest at different phases of the cell cycle, which includes interphase and metaphase [145, 146, 148]. With the rapid nuclear cycling that occurs prior to stage 5 it is possible that embryos arrested during nuclear cycles 12 and 13 could have arrested during either interphase or metaphase. Upon further investigation, we found that our collection of embryos arrested during nuclear cycles 12 and 13 involve a mixture of embryos that

appeared to arrest at either interphase or metaphase (Figure 2.17). We used morphological differences to make the distinction between interphase and metaphase arrest. As mentioned earlier, embryos arrested during metaphase exhibit hypercondensed nuclei that are aligned at cell division planes for the duration of the anoxia exposure (Figure 2.17b). On the other hand, interphase arrested embryos exhibit a delayed nuclear expansion from the previous nuclear cycle telophase for the duration of the anoxia exposure (Figure 2.17c).

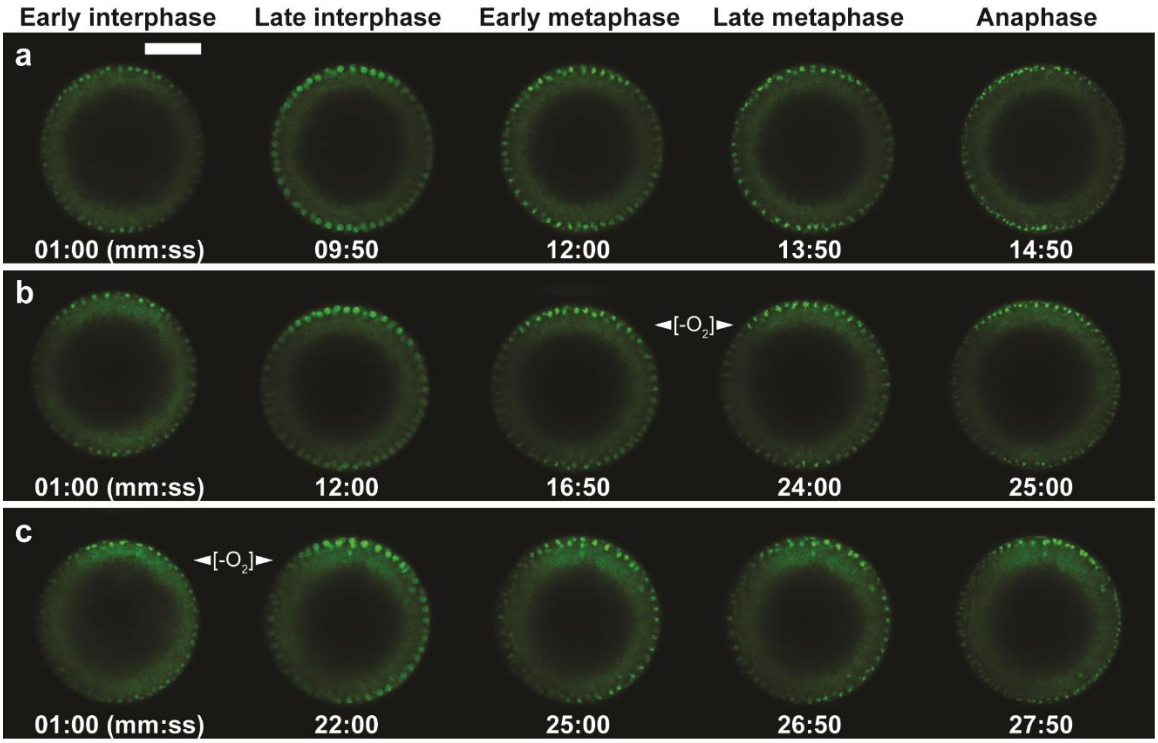

Figure 2.17: Morphological comparison between interphase and metaphase arrest. a) Frames from *in vivo* live imaging a Histone-GFP expressing embryo progressing through nuclear cycle 13 (control). b) Frames from *in vivo* live imaging a Histone-GFP expressing embryo progressing through nuclear cycle 13 that exhibits anoxia-induced metaphase arrest. c) Frames from *in vivo* live imaging a Histone-GFP expressing embryo progressing through nuclear cycle 13 that exhibits anoxia-induced interphase arrest.

Our method of morphometric analysis also shows a difference in the nuclear area trajectories between embryos arrested in either interphase or metaphase, which further confirm the morphological observations listed above (Figure 2.18).

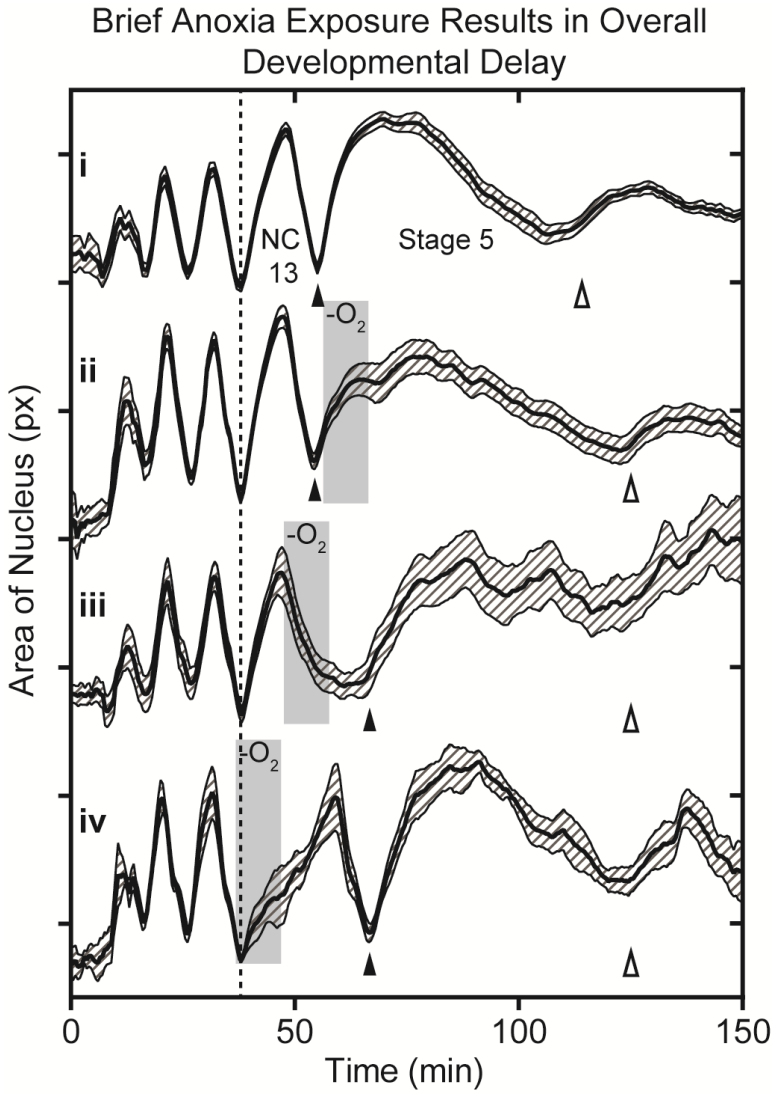

Figure 2.18: Average ± S.E.M. nuclear area trajectory for embryos grown in (i) normoxia (n = 35 embryos), and (ii) experiencing 10 minutes of anoxia during nuclear cycle 14 (n = 17 embryos), nuclear cycle 13 metaphase arrest (n = 8 embryos), and nuclear cycle 13 interphase arrest (n = 6 embryos). Shaded region in (ii-iv) indicates when anoxia was delivered. Closed triangle indicates telophase to interphase 14 transition. Open triangle indicates onset of gastrulation.

This allows us to identify the arrest checkpoint by simply looking at the shape of the nuclear area trajectory of individual embryos with no need to look at the raw imaging data. A summary of the relationship between anoxia-induced developmental arrest checkpoint and viability is presented in Table 2.1. This data suggests that the arrest checkpoint is a major determinant of embryo viability after anoxia-induced arrest. It has been shown previously that the centrosome is sensitive to anoxia, and loses stability during anoxia exposure [149]. This serves as a possible explanation for the observation of poor sister chromatid segregation and subsequent nuclear delamination after metaphase arrest.

Table 2.1: Summary of the observed relationship between anoxia-induced developmental arrest, cell cycle phase arrest checkpoint, and embryo survival after recovery from anoxia-induced developmental arrest

Nuclear Cycle	Total Embryos Arrested in Interphase	Total Embryos to Survive Interphase Arrest	Total Embryos Arrested in Metaphase	Total Embryos to Survive Metaphase Arrest
12	1	0	2	1
13	6	5	8	4
14	17	17	N/A	N/A
Total	24	22	10	5
Survival (%)	92		50	

2.4: Discussion and Conclusions

The combination of endogenous fluorescent reporters and *in vivo* live imaging is a powerful tool for understanding development as it allows biologists to directly visualize dynamic processes in living organisms. Yet, at present it is difficult to uncover the relationship between environmental perturbations and developmental responses *in vivo*, owing to the difficulty of controlling the microenvironment around live specimen. We have shown in this chapter a platform that integrates microfluidics, automated image processing, and data extraction for high-throughput studies of normal developmental processes and responses to environmental perturbations. This system is capable of rapid delivery of external stimuli to arrayed, live embryos for continuous *in vivo* live imaging. By using automated image processing and data extraction algorithms, it was possible to quantitatively measure the responses of developing *Drosophila* embryos to varying oxygen concentration early in embryogenesis, for example.

Our system relies on a simple microfluidic design with no moving parts or active valving that securely and robustly arrays live embryos for *in vivo* live imaging; because there is no need for specialized equipment, it is easy to set up and therefore can be adopted by other laboratories. The design of the DV array allows easy removal of embryos and sterilization of the device after each experiment, such that the device can be used multiple times if desired. Furthermore, with slight modifications, this method can be applied to other models of development including, for example, *C. elegans* and zebrafish to facilitate studies of developmental variability and environmental sensing. The generalizability of this method should enable widespread use and rapid adoption across the fields of developmental biology.

In addition to the experiments shown in this chapter, this method will allow further studies of other developmental systems and how these systems respond to environmental perturbation. Furthermore, our method is applicable to many other applications relevant to teratology, and developmental disorder pathology and treatment. For example, this method is directly applicable to studies interested in less-severe forms of hypoxia [143, 145, 148]. In addition to investigating varying degrees of hypoxia, one could also study known teratogens of unknown pathology to investigate the early embryonic responses to teratogen exposure such as alcohol [152]. Furthermore, this method can be used with disease models including, for example, microcephaly [153], to understand the pathology of early embryonic developmental disorders. Finally, it is also straightforward to apply this method to screening therapeutics aimed at treating teratogen exposure or developmental disorders [154] in a high-throughput manner and enabling quantitative studies throughout developmental biology.

CHAPTER 3: HIGH-THROUGHPUT ARRAYING AND IMAGING OF LATERALLY ORIENTED LIVE DROSOPHILA EMBRYOS

This chapter is adapted from a research article entitled “High-throughput arraying and imaging of laterally oriented live *Drosophila* embryos”, which is currently submitted to Lab on a Chip.

3.1: Introduction

While the device that was developed in the previous chapter was highly useful for studies of dorsal-ventral development it was unable to, however, capture information regarding the anterior-posterior axis. The ability to image along the anterior-posterior axis in a microfluidic array would greatly increase the number of biological processes we can observe, and therefore broaden the applicability of the high-throughput imaging techniques we develop.

In this chapter, we engineered a microfluidic device that can rapidly array live *Drosophila* embryos for high-throughput time-lapse microscopy with a lateral orientation. The device is a simple design that utilizes passive hydrodynamics for efficient and automated trapping of *Drosophila* embryos for parallelized time-lapse imaging of the anterior-posterior axis. We displayed the utility of the device for *in vivo* live imaging by using the device to load, and image live *Drosophila* embryos for up to 3 h of development. The optimized device operates with nearly 90 % loading efficiency, and allows imaging of all anatomical surfaces every time the device is loaded (i.e. dorsal,

ventral, left, and right). We observed complex morphogenesis events that occur at different locations around the developing embryo, quantitatively confirmed that embryos exhibit normal development within the device. Furthermore, we used the device for large-scale, quantitative analysis of mitotic wave-front patterns during early embryogenesis, and use our high-throughput imaging method to establish normal developmental phenotypes. Moreover, the method developed here is generalizable and can be used for *in vivo* live imaging of other developmental processes in *Drosophila* such as germ band retraction [89, 90] or dorsal closure [26, 91, 92] as well as imaging other models of development such as *zebrafish*, and *C. elegans*.

3.2: Materials and Methods

3.2.1: Single-Layer Anterior-Posterior (AP1) Array Fabrication and Preparation

I utilized the same method of rapid prototyping as mentioned in chapter 2 section 2.2.1 of this thesis to fabricate the single-layer AP1 array described in this chapter [135]. Differences in the fabrication protocol are described in this section. Mold fabrication involved a single-layer, photolithographic procedure, and a schematic of the photomask can be found in Appendix B (Figure B.2). The total device height was designed to be 200 µm. In order to achieve the desired layer height we employed the thick photoresist SU-8 2100 (MicroChem Corp.).

To fabricate the master mold with multi-layer thick SU-8 2100, I used a specifically tuned lithographic process. Silicon wafers were dehydrated by baking at 150 ^{o}C for 30 min. The wafer was allowed to cool to room temperature after each bake before proceeding to the next step. To achieve the total device height of 200 µm, I deposited

SU-8 2100 by repeating a single coating sequence twice as each process was tuned to deposit 100 µm of SU-8 2100 each. A 100 µm thick layer of photoresist was deposited with a two-step spinning protocol with the following parameters: step 1) 100 rpm s^{-1} acceleration, 500 rpm spin speed, and 10 s spin duration, and step 2) 300 rpm s^{-1} acceleration, 3000 rpm spin speed, and 30 s spin duration. The resist film was dried by baking at 65 ^{o}C for 5 min and 95 ^{o}C for 20 min. The previous steps were repeated in order to deposit the second layer of photoresist. The photoresist was patterned with the photomask by exposing the film to 365 nm wavelength light with an exposure energy of 500 mJ cm^{-2}. Resist cross-linking was expedited by baking at 65 ^{o}C for 5 min and 95 ^{o}C for 10 min. The uncross-linked resist was removed by soaking in an agitated bath of SU-8 developer (propylene glycol methyl ether acetate, Sigma Aldrich). The mold was then rinsed with isopropyl alcohol, and allowed to air dry. Finally, the mold was exposed to silane vapor ((tridecafluoro-1,1,2,2-tetrahydrooctyl)-1-trichlorosilane; United Chemical Technologies) to facilitate casting ejection during subsequent replica molding processing.

Replica molding PDMS (polydimethylsiloxane, Dow Corning) devices and plasma bonding to glass cover slips followed the same procedure as described in chapter 2 section 2.2.1 of this thesis.

Microfluidic device preparation followed the same protocol described in chapter 2 section 2.2.2 of this thesis while utilizing the single-layer AP array described in this chapter.

3.2.2: *Drosophila* Strains and Embryo Preparation

A *Drosophila* strain expressing a histone-green fluorescent protein fusion (Histone2A-GFP, for short: his-GFP, Bloomington Stock Center) was used as wild type strain throughout this study. Monitoring cell cycle states and cellular behaviors are inferred from imaging his-GFP expression.

Drosophila embryos must be collected and prepared for imaging prior to microfluidic arraying and live imaging on-chip, and followed the same procedure as described in chapter 2 section 2.2.2.

3.2.3: AP1 Array Loading

Microfluidic arraying of *Drosophila* embryos followed the same protocol described in chapter 2 section 2.2.2 of this thesis while utilizing the AP1 array described in this chapter.

For control experiments, we followed a protocol as described by Foe and Alberts [136]. Live embryos were prepared in the same manner as described above. Once prepared, a single live embryo was pipetted onto an open top glass cover slip, and immersed in PBST solution. A single embryo was then imaged in the same manner as described in the following section.

3.2.4: Time-Lapse Confocal Microscopy

Time-lapse microscopy was performed with a Zeiss LSM 710 confocal microscope with a Zeiss Plan-Apochromat 20x/0.8 M27 objective. An environmental chamber maintained a set temperature of 25 ^{o}C throughout imaging. GFP fluorescence was excited via a 488 nm argon laser and emission was detected via a photomultiplier

tube, and transmitted light was detected simultaneously via 488 nm transmission. Embryos remained immersed in PBST solution throughout imaging.

Two different scanning modes were employed depending on the type of data that was desired. A slow scan mode was employed to acquire detailed spatial information about embryo morphogenesis, which involved imaging ~80 μm thick z-stack with 5 μm interval at a frequency of 30 s. Slow scan typically allowed only imaging of a single embryo per experiment with laser scanning confocal microscopy. A fast scan mode was employed for large-scale data collection, which involved imaging a single z-slice ~35 μm from the embryo side at a frequency of 30 s. Fast scan typically allowed imaging of ~20 embryos per experiment with laser scanning confocal microscopy. An imaging frequency of 30 s was employed in both cases to allow tracking of mitotic wave-fronts during stage 4 of development.

3.2.5: Finite Element Modeling of AP1 Array Fluid Dynamics

COMSOL (COMSOL, Inc.) finite element modeling software was utilized for modeling fluid dynamics within the microchannels of the device and setup in the same manner as described in section 2.2.3.

3.3: Results and Discussion

3.3.1: AP1 Design for Arraying Laterally Oriented Embryos

We developed a microfluidic array device in order to image a large number of live *Drosophila* embryos along the anterior-posterior axis in a high-throughput manner. For ease of reference, we will call this device the anterior-posterior array or AP1 array for

short. It is a simple design involving a single PDMS layer consisting of interconnected embryo traps that are meant to laterally orient and securely hold embryos for time-lapse microscopy (Figure 3.1).

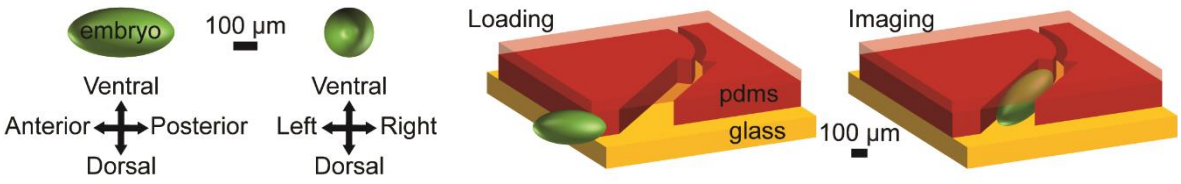

Figure 3.1: 3D representation of a *Drosophila* embryo loading into a single embryo trap in the AP1 array for time-lapse imaging. Trap geometry dictates that embryos enter the trap laterally with the anterior-posterior axis running along the length of the trap.

Embryos are delivered to the device as a liquid suspension through a single inlet that first introduces embryos to the main serpentine channel. From the serpentine channel, embryos are transported throughout the device and through the action of passive hydrodynamics will enter an embryo trap. This process proceeds automatically, and continuously until all traps or a majority of the traps are occupied by a single embryo. Single embryo trapping is achieved by closely matching the trapping channel dimensions to that of the dimensions of a single embryo (Figure 3.2a). Embryos that do not enter an embryo trap are carried by the loading solution through the serpentine channel to the outlet at the end of the device. The microchannels were designed to be ~200 µm tall to allow embryos to freely flow through the microchannels during loading, but also restrict embryos to orient laterally within embryo traps (Figure 3.2b). The device was designed to densely pack embryos into a confined area in order to minimize stage translation time as

the imaging throughput is limited by the speed of the microscope, and the desired imaging frequency of 30 s. The overall device size is therefore ~16 mm x ~14 mm and the imaging area occupied by embryos within the device is ~8 mm x ~3 mm (Figure 3.2c).

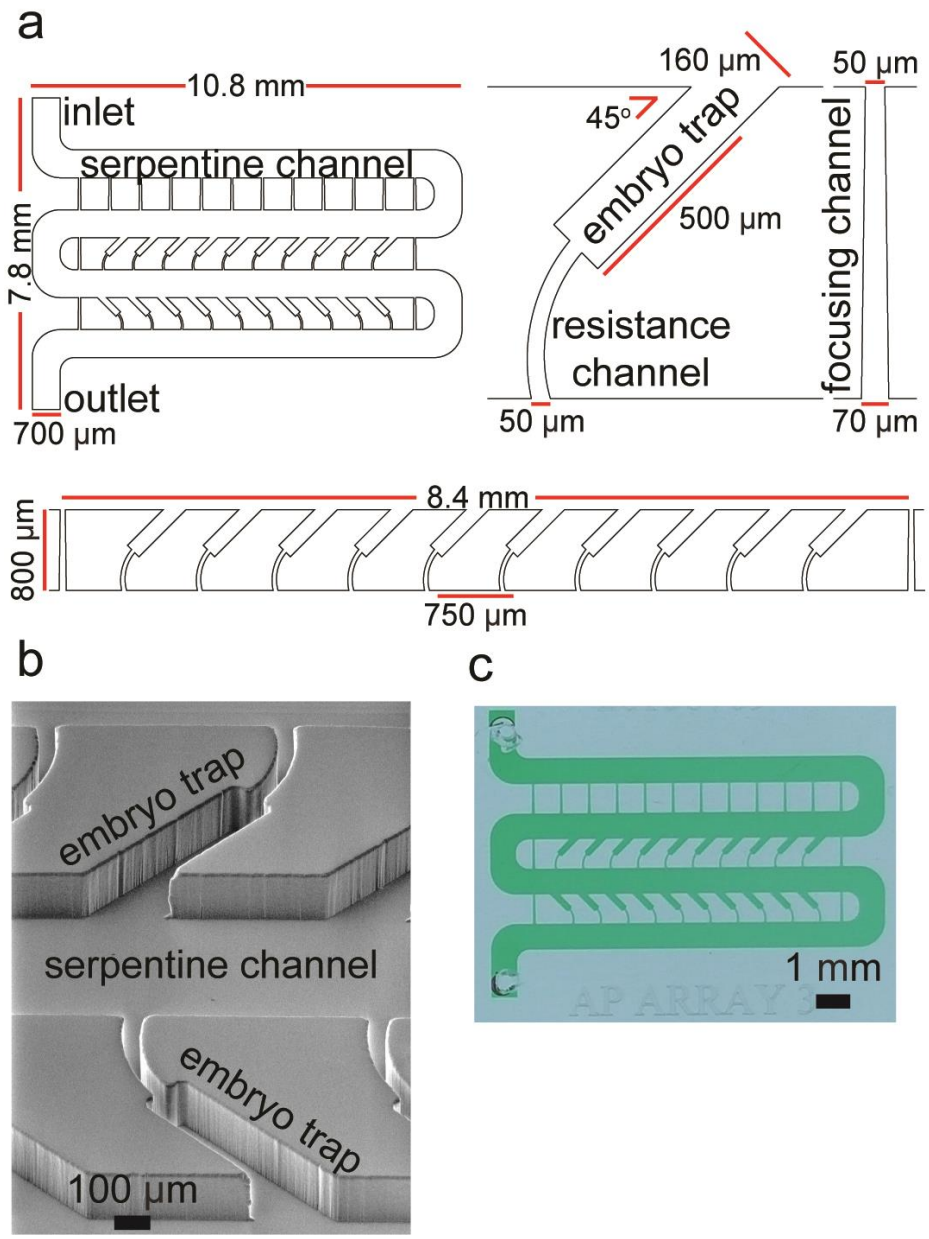

Figure 3.2: The optimized AP1 array. a) Overall device layout with dimensions consisting of 4 individual units: serpentine channel, focusing channels (x16), embryo traps (x20), and resistance channels (x20). Embryos enter the device through the inlet to the serpentine channel at the top of the device. Embryos travel along the serpentine until they encounter an embryo trap, at which cross-flow through focusing channels, embryo traps, and resistance channels drive embryos into embryo traps. Once all traps are occupied by a single embryo, remaining embryos are carried by the serpentine to the device outlet at the bottom of the device. b) Scanning electron micrograph of PDMS mold showing two embryo traps in two different rows connected by the serpentine channel. c) Optical micrograph of entire microfluidic array device with channels filled green dye.

3.3.2: AP1 Facilitates Simple and Efficent Arraying of Laterally Oriented Embryos

The microchannel manifold design of the device allows for rapid and simple arraying of *Drosophila* embryos (Figure 3.3). The device design was inspired by our work in chapter 2 with the DV array as well as previous work that developed similar arrays for trapping *C. elegans* [140] and single-cells [155]. On top of the simplistic design, manifold type arrays operate in a deterministic manner that allow devices to be constructed with high-density. In other words, these devices can trap many specimen within a small area, which is important in reducing stage translation time during time-lapse microscopy, and therefore increase the amount of specimen that can be imaged in parallel. The deterministic operation of manifold type arrays is contrasted with other previously developed arrays, which trap in a stochastic manner [156]. Stochastic arrays are simple to operate; however, the trapping mechanisms typically requires traps to be sparsely spaced, and therefore decreases the density of the array and the total amount of embryos that can be trapped within a single device. Trapping mechanisms other than passive hydrodynamics have been developed, but generally require more complex chip design and external components [157-160]. Operation of a manifold type array is simple as it requires no active parts such as on-chip valving, and only requires a pressure source to deliver embryo suspensions to the chip. The simple operation and high-density trapping offered by the manifold type array developed in this thesis chapter should allow rapid adoption of this technology by non-specialists, and thereby increase the impact of this technology.

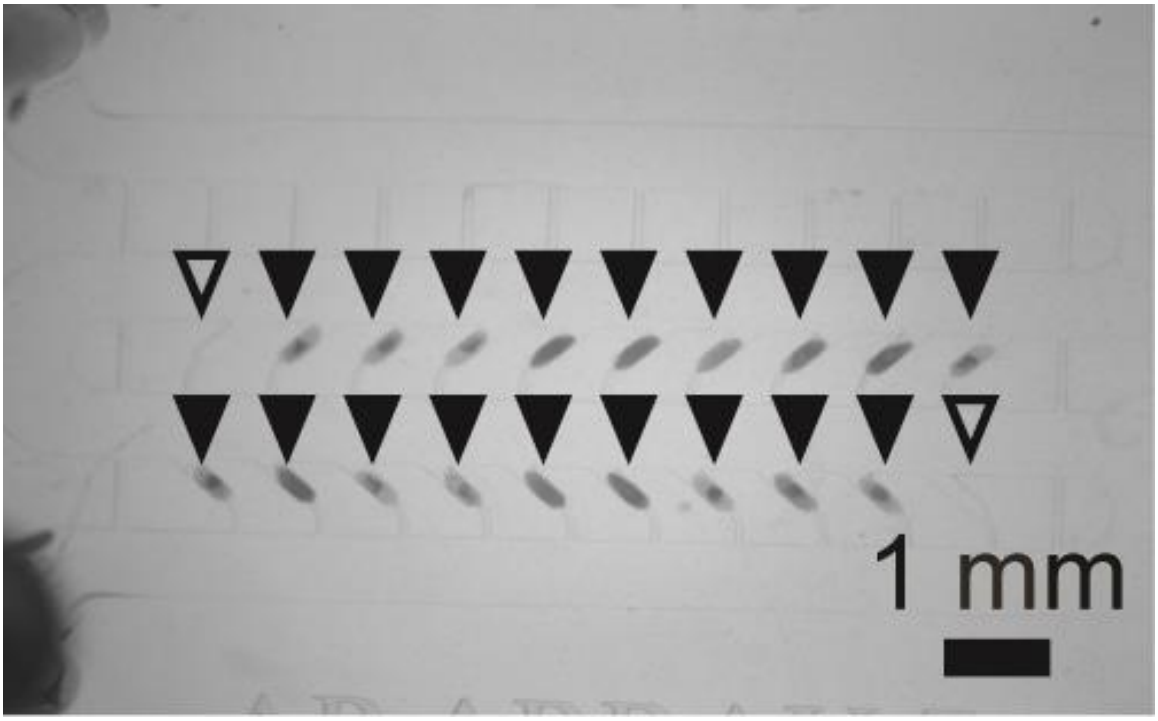

Figure 3.3: Efficient trapping and arraying of lateral oriented *Drosophila* embryos via the optimized AP1 array. Typical loading results are depicted in this figure wherein filled triangles indicate traps with embryos successfully loaded while open triangles indicate empty traps with no embryo loaded.

Operation of manifold type devices such as the device design here depend upon optimized fluidic resistances throughout the microchannels for efficient trapping. The starting point for the design of the AP1 array began with the optimized dorsal-ventral array designed from chapter 2 of this thesis. As such, an initial design of the AP1 array consisted of wide, tapered focusing channels which were employed to decrease fluidic resistance in the direction perpendicular to the serpentine channel and increase trapping efficiency (compare Figure 3.4a and Figure 3.4b).

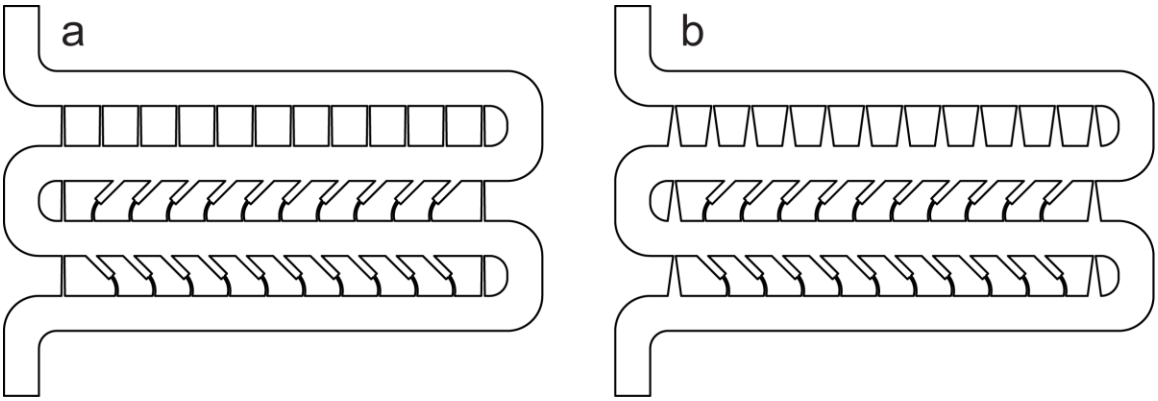

Figure 3.4: Comparison of the optimized design and an initial design of the AP1 array. a) The optimized AP1 array with narrow focusing channels (see top row). b) An initial design of the AP1 array that closely mimicked the optimized dorsal-ventral array from Chapter 2. As such, this initial design employed wide tapering focusing channels (see top row).

However, the operation of such a device resulted in rapid clogging within the serpentine channel (Figure 3.5a). COMSOL simulations indicated that flow through the serpentine channel significantly drops at the turn from the first row to the second row, which is consistent with where embryos begin clogging in the initial design (Figure 3.5a). We therefore increased the fluidic resistance of the focusing channels by significantly narrowing the focusing channels (Figure 3.4a). COMSOL simulations indicated that for this design fluid flow throughout the serpentine channel is uniform (Figure 3.5 b). Operation of the optimized device geometry resulted in devices that do not clog, and exhibit an average loading efficiency of 87 ± 6 % (Figure 3.5b). The rapid, yet simple arraying of live *Drosophila* embryos with this device enables high-throughput, large-scale imaging of embryogenesis, and thus opens the door for quantitative analysis of morphogenesis and development.

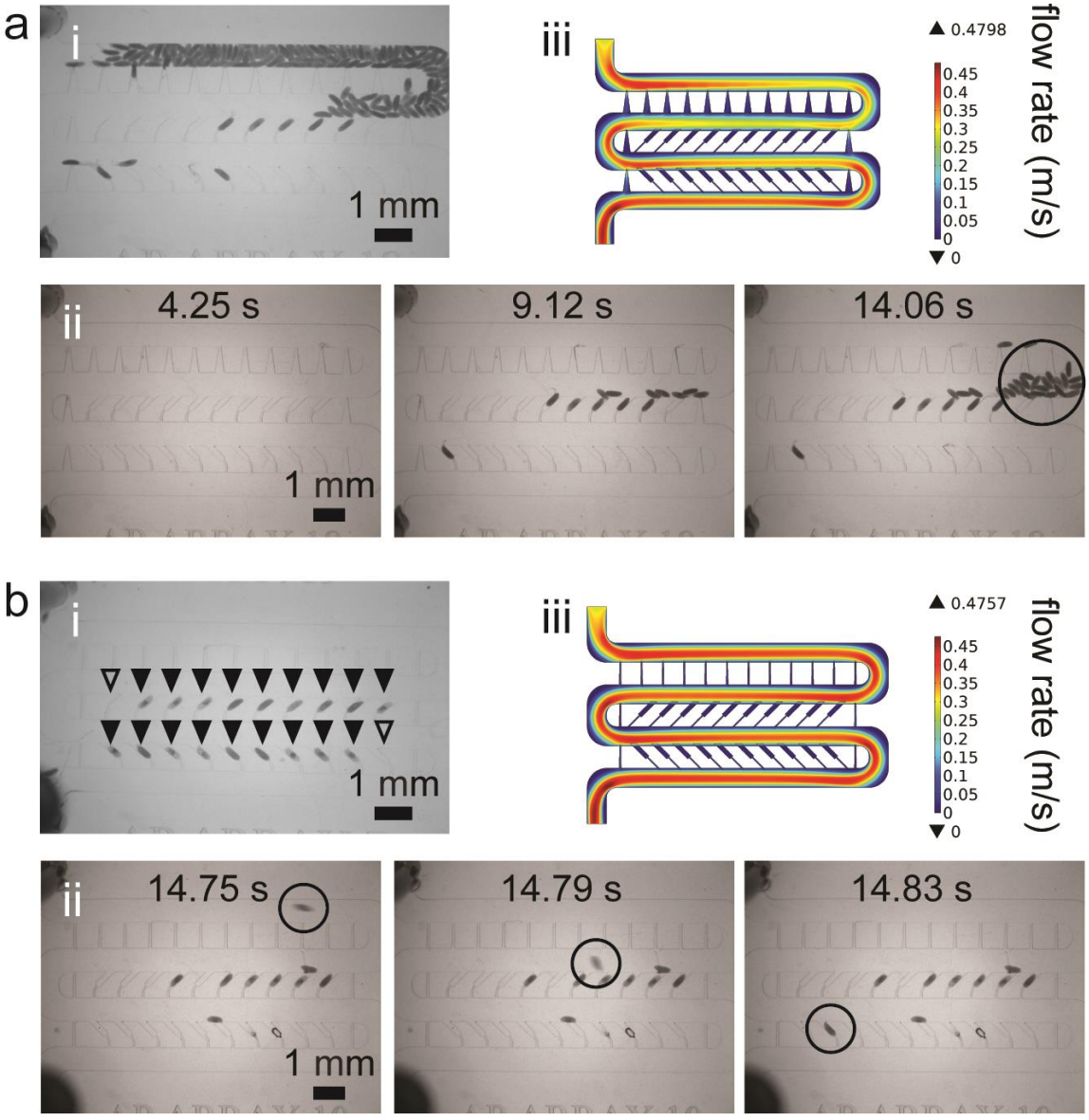

Figure 3.5: The importance of microfluidic design architecture and trapping efficiency. Device loading experiments and COMSOL simulations for a) an initial device design and b) the optimized device design. i) Typical loading results. Filled triangles- traps with embryos successfully loaded, open triangles- empty traps with no embryo loaded. The optimized device exhibits an average loading efficiency of 87 ± 6 %, while the initial device clogged within the serpentine channel every time. ii) Time-lapse optical micrographs of embryo loading. Open circle in a.ii indicates the nascent clog that resulted in a.i, while the open circle in b.ii tracks a single embryo from device entry to successful loading. iii) COMSOL simulations of flow rate through the microchannels. The initial design exhibits a decreased flow rate within the serpentine in transitioning from the first row to the second row, which is consistent with clog location in loading experiments, while the optimized device exhibits uniform flow rate throughout the serpentine channel.

3.3.3: AP1 Arraying Allows All Dorsal-Ventral Orientations to be Viewed On-Chip Simultaneously

The goal for the microfluidic device is to rapidly and robustly array live *Drosophila* embryos for high-throughput lateral imaging (i.e. along the anterior-posterior axis). We had no prior preference as to which side of the embryo is imaged through (i.e. dorsal, ventral, left, or right), because during stage 4-5 of embryogenesis *Drosophila* embryos are essentially symmetric about the dorsal-ventral and left-right axes. However, specialized studies interested in specific biological processes would necessarily have a preference as to what side of the embryo is visible. We therefore characterized the dorsal-ventral orientation preference of arrayed embryos within the device. To do this, we loaded devices with live embryos, and monitored *in vivo* development of histone-GFP expressing embryos from stage 6 of embryogenesis and beyond. Stage 6 marks the onset of gastrulation, in which embryos begin to show obvious morphological differences around the dorsal-ventral axis (Figure 3.6). From the dorsal view, germ band elongation as well as transverse furrow formation can be easily monitored (Figure 3.6a). From the lateral view, germ band elongation can also be monitored in addition to cephalic furrow formation (Figure 3.6b). From the ventral view, ventral furrow formation as well as stomodeal invagination can be visualized (Figure 3.6c).

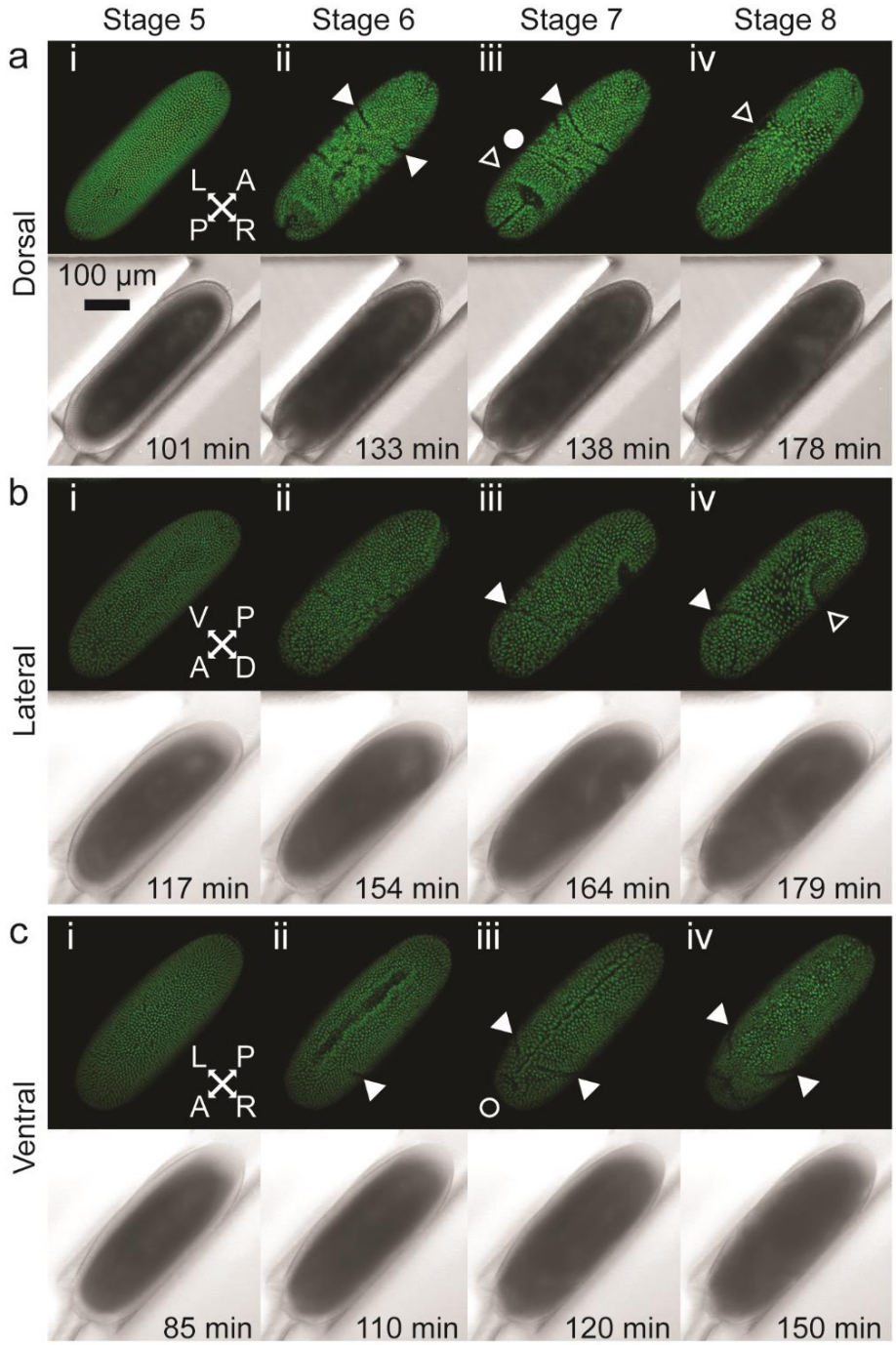

Figure 3.6: Imaging morphogenesis and embryo orientation. Maximum intensity projection time-lapse confocal microscopy images of his-GFP expressing embryos from a) dorsal, b) lateral, and c) ventral sides. Anatomical axes are indicated in i) by: A- anterior, P- posterior, D- dorsal, V- ventral, L- left, and R- right. Filled triangle- cephalic furrow, open triangle- pole cell migration, filled circle- transverse furrow invagination, open circle- stomodeal invagination. Ventral furrow formation is visible in c.ii as a wide groove along a majority of the anterior-posterior axis. Time is relative to the start time on the confocal microscope.

Based on these experiments it is established that the device operates essentially with a random dorsal-ventral (DV) orientation (Figure 3.7a). The random DV orientation preference of this device makes the device highly useful for any application, because the device is expected to load embryos of all orientations every time. This does come at a cost however, because if a particular orientation is preferred, then only a fraction of the embryos will be useful within a given device. However, this shortcoming can be easily overcome through simple scaling, and increasing the overall size of the device to accompany more traps, and therefore allow high-throughput arraying of lateral oriented embryos with specific DV orientations. In addition to the random dorsal-ventral orientation preference, we also observed a strong preference for embryos to enter traps with the posterior pole first (Figure 3.7b). A slight asymmetry in embryo shape along the anterior-posterior axis is likely related this phenomena. Specifically, the posterior half of the embryo is typically wider than the anterior half as the widest part of the dorsal-ventral axis is more posteriorly located. However, how the asymmetry in embryo shape produces the posterior pole first loading preference is unclear.

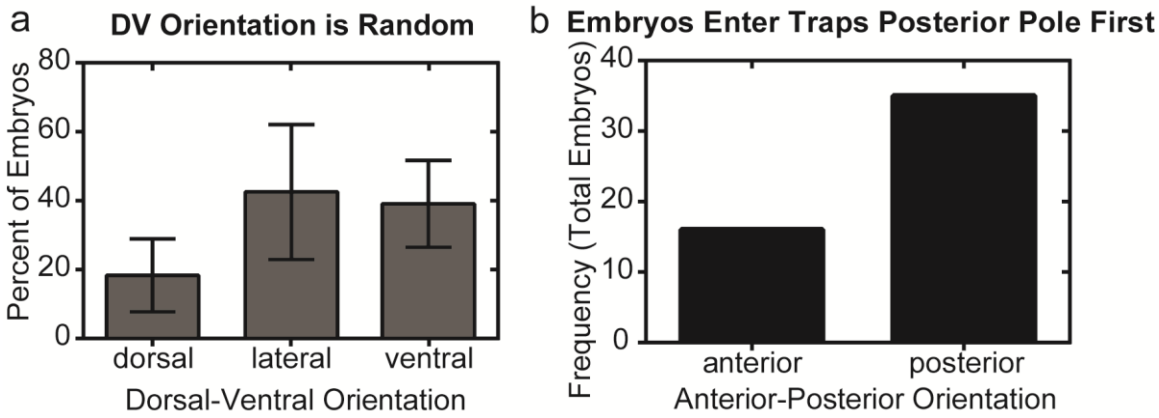

Figure 3.7: Embryo orientation preference for the AP1 array. a) The dorsal-ventral orientation of laterally oriented embryos within the AP1 array. Error bars are standard deviation. b) The anterior-posterior orientation of laterally oriented embryos within the AP1 array. The anterior-posterior orientation refers to which pole enters the trap first.

3.3.4: Microfluidic Arraying Does Not Affect Nuclear Cycling Dynamics

Upon fertilization, the newly formed *Drosophila* embryo proceeds through 9 rounds of synchronous nuclear divisions near the center of the embryo within the yolk. After which, at the start of nuclear cycle 10 and marking the start of stage 4 of *Drosophila* embryogenesis nuclei will migrate toward the periphery, and assemble in a monolayer under the common plasma membrane (Figure 3.8a). Subsequently, nuclei proceed through 4 nearly synchronous nuclear divisions before cellularization (Figure 3.8). It is known that these 4 nuclear divisions proceed with highly reproducible kinetics, and therefore can be utilized as a measure of developmental viability.

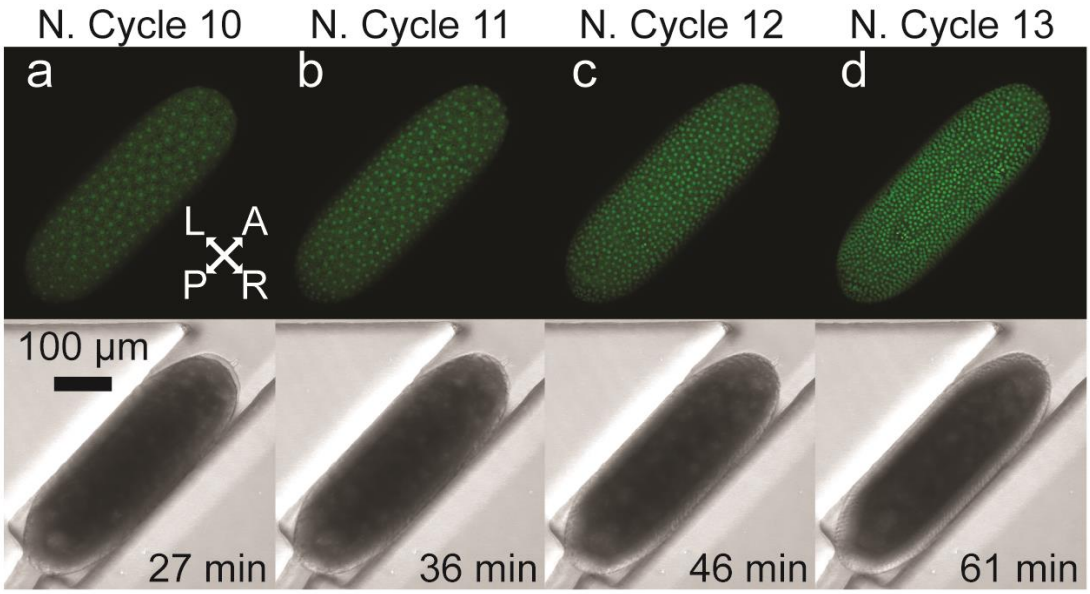

Figure 3.8: Maximum intensity projection time-lapse confocal microscopy images of a stage 4 his-GFP expressing embryo with the green channel on top and the transmitted light channel on bottom. Nuclear cycles a) 10, b) 11, c) 12, and d) 13 are depicted. Anatomical axes are indicated in a) by: A- anterior, P- posterior, L- left, and R- right. Time is relative to the start time on the confocal microscope.

In order to assess the viability of microfluidic arrayed *Drosophila* embryos, we quantified the nuclear cycling kinetics of microfluidic arrayed *Drosophila* embryos and compare them to appropriate controls (Figure 3.9). The control for these experiments closely match the imaging protocol as developed by Foe and Alberts [136]. Briefly, embryos are chemically dechorionated with bleach as described in section 3.2.3. After which a single embryo is placed on an open top glass slide, immersed with PBST, and imaged via time-lapse confocal microscopy. Under these conditions, embryos exhibit nuclear cycle durations (mean ± standard error of the mean) of 8.1 ± 0.4 min, 10.1 ± 0.3 min, 12.2 ± 0.4 min, and 17.8 ± 0.7 min for nuclear cycles 10, 11, 12 and 13, respectively (Figure 3.9). These numbers closely match those found in the literature [136]. Microfluidic arrayed embryos experience a similar preparation procedure as described in

section 3.2.3. Embryos arrayed in this optimized lateral imaging device exhibit nuclear cycle durations of 7.8 ± 0.2 min, 9.6 ± 0.1 min, 11.1 ± 0.2 min, and 16.8 ± 0.3 min for nuclear cycles 10, 11, 12 and 13, respectively (Figure 3.9). The durations for each nuclear cycle is not statistically different ($p > 0.05$) between conditions based on a student's T-test. This is further confirmed by comparing these nuclear cycle kinetics to those attained by imaging embryos in our previously described end-on imaging device [121] (DV array condition), in which all nuclear cycle durations are not statistically different ($p > 0.05$) between conditions based on a student's T-test (Figure 3.9). These results indicate that microfluidic arraying does not affect nuclear cycling kinetics, and embryos proceed with expected developmental rates on-chip.

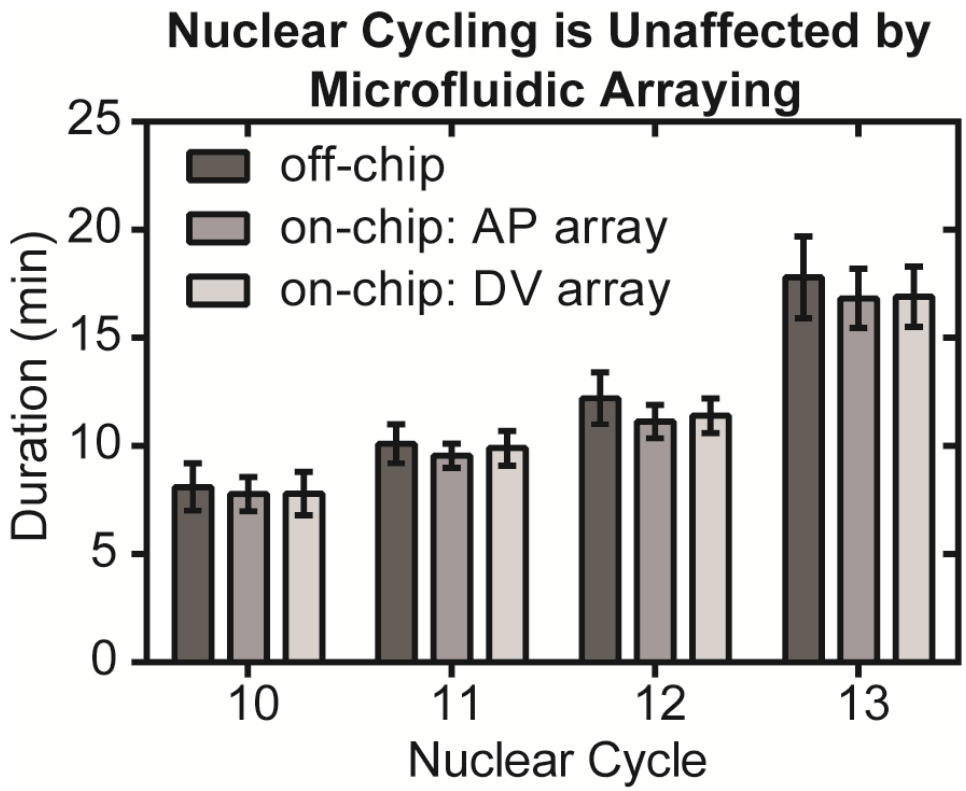

Figure 3.9: Nuclear cycle durations for his-GFP expressing embryos in control conditions (off-chip), within the optimized lateral array device (on-chip: AP1 array), and within the dorsal-ventral array that previously described in Chapter 2 of this thesis (on-chip: DV array). The durations are averages with standard deviation error bars. n = 7, 24, and 30 embryos for off-chip, AP1 array, and DV array conditions, respectively. All nuclear cycle durations are not statistically different between experimental conditions based on a student's T-test ($p > 0.05$).

3.3.5: Two Simultaneous Mitotic Wave-fronts is More Commonly Observed than a Single Mitotic Wave-front

Nuclear cycling throughout stage 4 of *Drosophila* embryogenesis is well known to proceed metasynchronously, in which divisions can be visualized as a wave-front propagating along the anterior-posterior axis [136]. The existence of two distinct mitotic wave-front patterns is also well documented [136]. In one scenario, two mitotic wave-fronts initiate simultaneously with one originating near the anterior pole and the other

originating near the posterior pole, which both propagate along the anterior-posterior axis until the two wave-fronts meet at the anterior-posterior middle of the embryo (Figure 3.10a). The second scenario involves a single mitotic wave-front that initiates at either anterior or posterior pole, propagates along the entire anterior-posterior axis, and terminates at the opposite pole (Figure 3.10b). However, it is unclear which scenario takes place during the normal development. The difficulty with assessing this problem is related to low-throughput conventional imaging methods that typically restrict sample sizes to a few embryos.

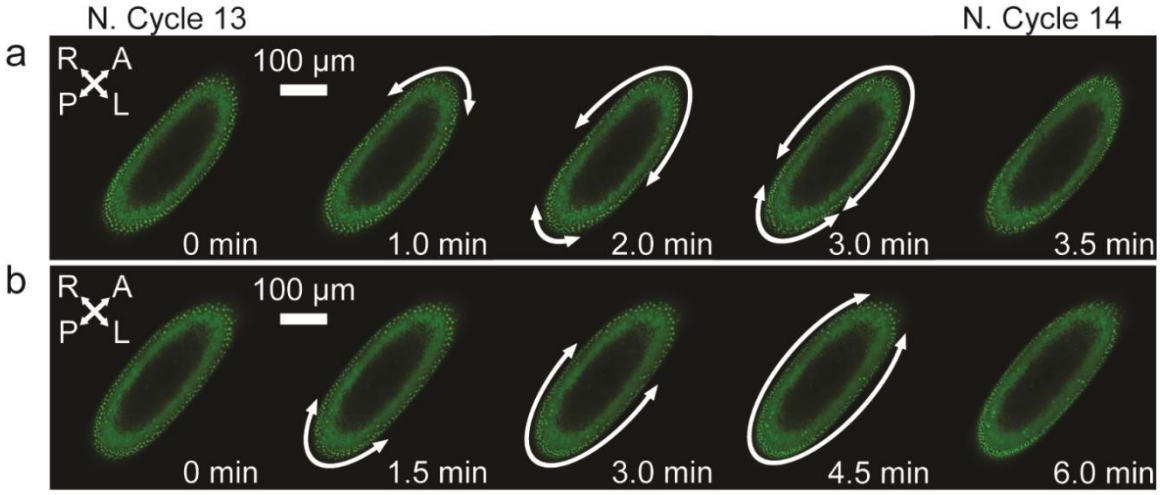

Figure 3.10: Mitotic wave-front phenotypes. Single z-slice time-lapse confocal microscopy images of two his-GFP expressing embryos exhibiting either a) two mitotic wave-fronts, or b) one mitotic wave-front during nuclear division 13. White arrows indicating cells that have transitioned from metaphase to anaphase. Anatomical axes are indicated in by: A- anterior, P- posterior, L- left, and R- right while imaging through the ventral side of the embryo. Time is relative to the first frame in which all cells are in metaphase just prior to mitotic wave-front initiation.

In order to investigate mitotic wave-front patterns we utilized our engineered, high-throughput microfluidic device to perform large-scale imaging of stage 4 *Drosophila* embryos. We limited our analysis of mitotic wave-fronts to nuclear division 13 occurring between nuclear cycle 13 and 14, and marking the transition from stage 4 to stage 5 of *Drosophila* embryogenesis. This simplification was made, because mitotic wave-front patterns are known to remain constant between nuclear cycles for a given embryo [136]. We observed the existence of two wave-fronts (Figure 3.10a) and one wave-front (Figure 3.10b) during our experiments. The far majority of embryos exhibited two mitotic wave-fronts (n = 42 embryos) while only a handful of embryos exhibited one mitotic wave-front (n = 5 embryos) (Figure 3.11). All 5 embryos that exhibited one mitotic wave-front also exhibited developmental abnormalities such as asynchronous divisions during cellularization. This along with the fact that two mitotic wave-fronts are more frequently observed (~90 %, 42 out of 47 embryos exhibiting two wave-fronts) suggests that the normal case is two simultaneous mitotic wave-fronts initiating at both anterior and posterior poles.

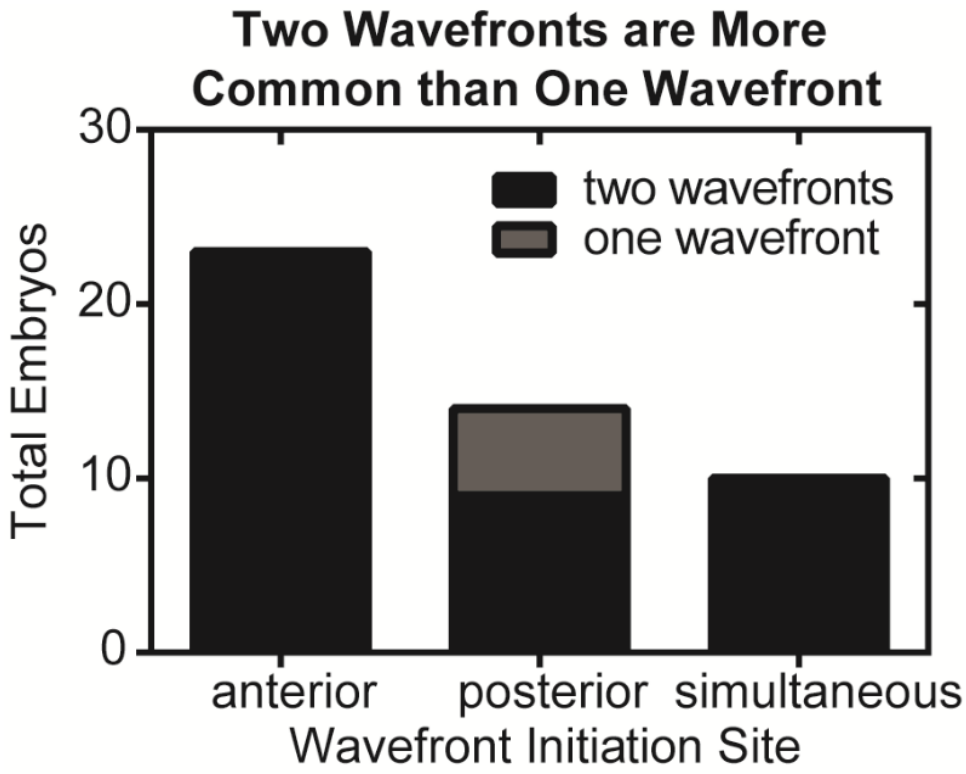

Figure 3.11: Wave-front count for all imaged embryos with the indicated pole at which the mitotic wave-front initiated. For embryos exhibiting two wave-fronts, the wave-front initiation site refers to the pole at which the first wave-front appeared if a temporal delay in wave-front initiation was observed. If no delay between two wave-fronts was observed then those embryos are labeled "simultaneous".

The underlying mechanism regulating the metasynchrony of the stage 4 mitotic divisions is still not well understood. The existence of two distinct mitotic wave-front patterns is interesting, and it is also not well understood how the two patterns relate to each other. To understand how these two wave-front patterns compare we quantitatively assessed characteristics regarding wave-front propagation dynamics. We first established a characteristic time scale for all cells to transition from metaphase to anaphase. This was done by identifying the time it takes for all cells to proceed through the metaphase to anaphase transition. We found that embryos with two mitotic wave-fronts require 2.45 ±

0.13 min (average ± standard error of the mean, n = 42) for all cells to proceed from metaphase to anaphase, while embryos with a single mitotic wave-front require 4.60 ± 0.43 min (n = 5) (Figure 3.12a). It is unknown whether wave-fronts in embryos exhibiting a single or two mitotic wave-fronts propagate with the same speed. We therefore calculated wave-front speed, and found that the average individual wave-front in embryos exhibiting two wave-fronts propagates at 98.7 ± 6.2 μm/min (average ± standard error of the mean, n =42), while the wave-front in embryos exhibiting a single mitotic wave-front propagates at 92.8 ± 7.9 μm/min (n = 5) (Figure 3.12b). These values are within expectation based on what is known in the literature [136, 161]. Furthermore, this result suggests that the wave-front propagation speed is independent of the number of mitotic wave-fronts propagating at a given time ($p>0.05$, T-test). Interestingly, this suggests that the underlying mechanism for metasynchronous nuclear divisions, whether be it chemical or mechanical signaling, or a combination, is the same for both occurrences.

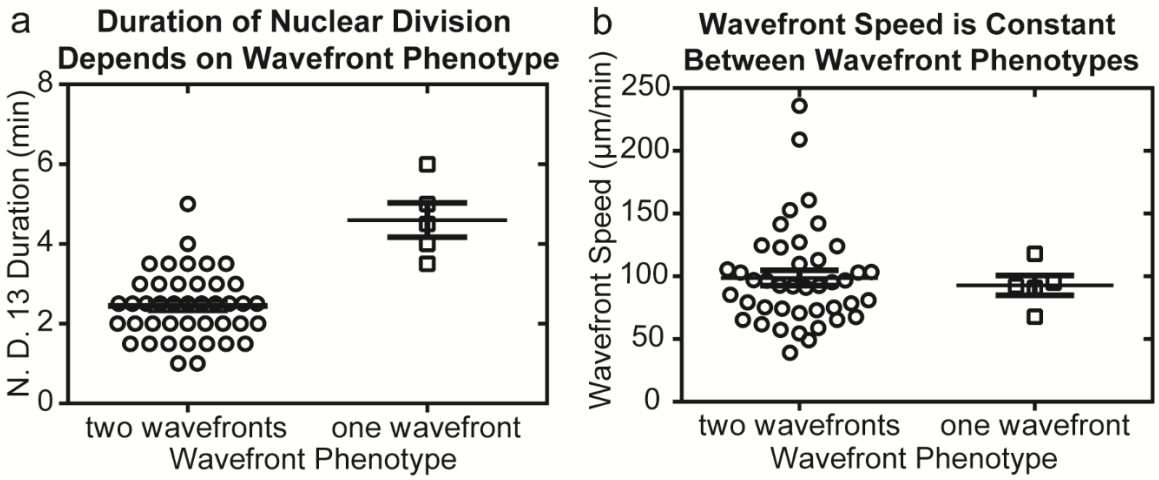

Figure 3.12: Quantitative analysis of wave-front propagation properties. a) Measured duration for all cells to transition from metaphase to anaphase for embryos exhibiting two wave-fronts and one wave-front. Average ± standard error of the mean indicated by whiskers. b) Measured speed of mitotic wave-fronts for embryos exhibiting two wave-fronts and one wave-front. Average ± standard error of the mean indicated by whiskers. Mitotic wave-front speeds for embryos exhibiting one of two wave-fronts are not statistically different from each other based on a student's T-test ($p > 0.05$).

The initiation of two mitotic wave-fronts is known to occur simultaneously or with a temporal delay between anterior and posterior poles [136], but which is the case for normal development is unknown. We observed both cases in our imaging experiments, wherein the existence of a temporal delay between mitotic wave-front initiation (n = 32 embryos) occurred more frequently than simultaneous initiation (n = 10 embryos) (Figure 3.11). Those exhibiting a delay between poles more often initiated first at the anterior pole (n = 23 embryos) rather than the posterior pole (n = 9 embryos) (Figure 3.11). From our imaging data, we could calculate the temporal delay between mitotic wave-front initiations. The delay in mitotic wave-front initiation was was calculated as anterior initiation time minus posterior initiation time (Figure 3.13). We found an average delay of 0.36 ± 0.74 min (average ± standard deviation) (Figure 3.13).

From this data, we cannot conclude with absolute certainty what, if any single phenotype, is expected to be “normal”. The data at hand merely provides an expectation for that the anterior pole mitotic wave-front initiating first, which is followed by posterior pole mitotic wave-front initiating to occur more frequently. This data raises interesting questions regarding mitotic wave-front initiation. Specifically, what regulates the initiation? How is the initiation site established? Higher imaging frequency, and other molecular markers such as centrosomal-fluorophore fusions could aid in answering this question. In addition, longer term tracking of embryos into adulthood could also provide more information regarding the long term consequences of mitotic wave-front phenotype on health outcomes for individual embryos. However, that scale of experimentation was not the goal of this thesis chapter.

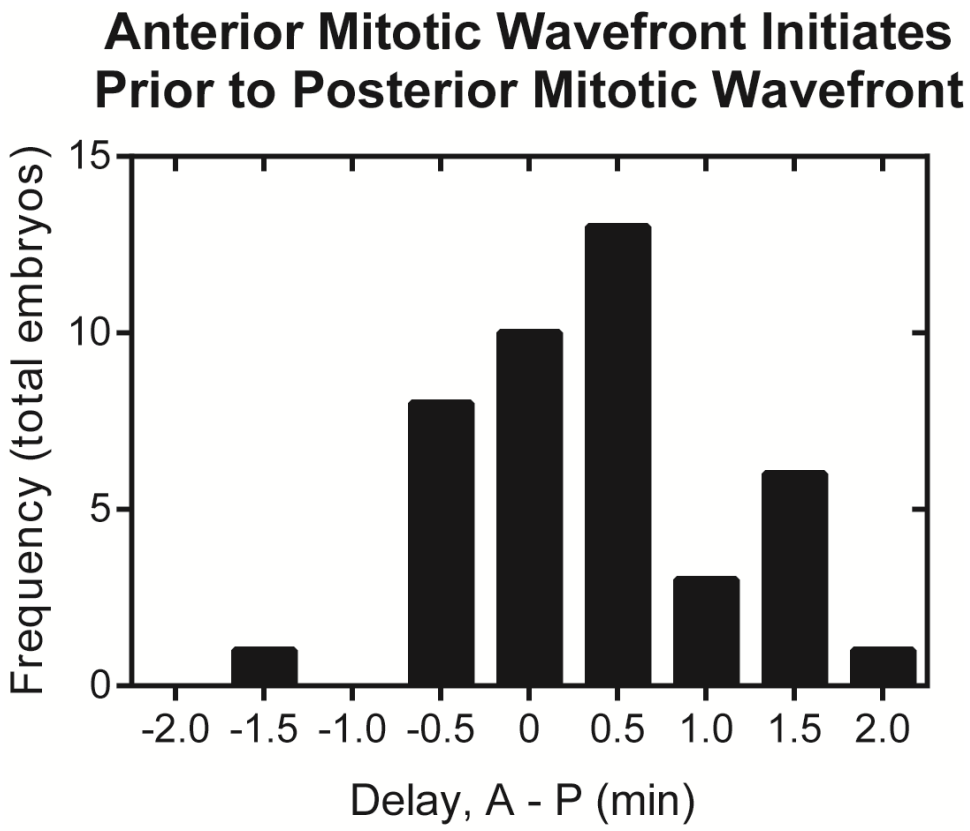

Figure 3.13: Measured temporal delay in mitotic wave-front initiation for embryos exhibiting two wave-fronts. Delay is calculated as posterior minus anterior initiation times. Positive values indicate anterior wave-front appeared first, and negative values indicate posterior wave-front appeared first.

3.3.6: Effect of Nuclear Cycle Number on Mitotic Wave-front Properties

Previous work by other labs have indicated that mitotic wave-front propagation dynamics is not independent of nuclear cycle [161]. It is unclear why mitotic wave-front dynamics changes with each nuclear cycle, but it is believed to be related to nuclei number affecting mitotic wave-front signaling propagation. A quantitative understanding of mitotic wave-front propagation dynamics throughout stage 4 of *Drosophila* embryogenesis would be instrumental in the development of a mechanistic understanding of mitotic wave-front propagation and elucidating the connection to nuclear cycle

number. We therefore quantitatively characterized mitotic wave-front propagation dynamics for nuclear cycles 10-13, which encompass all of stage 4 of *Drosophila* embryogenesis. It has been noted in the literature that embryos maintain one or two mitotic wave-fronts all throughout stage 4 of embryogenesis [136]. We observed the same phenomenon using our high-throughput imaging method.

In order to assess wave-front kinetics throughout stage 4 of embryogenesis, we performed the same analysis from above on the 3 other nuclear cycles that comprise stage 4 of *Drosophila* embryogenesis. We first established the characteristic time scale for all cells to transition from metaphase to anaphase for nuclear cycles 10-13. From this, we observe that embryos exhibit a trend of increasing timescales for the propagation of metaphase to anaphase transition across the embryo from nuclear cycle 10 to nuclear cycle 13 (for simplicity, we refer to this process as the nuclear division phase or simply" nuclear division") (Figure 3.14a). We measured the duration for each of the nuclear division phases from cycle to cycle to be: 1.11 ± 0.08 (n = 34 embryos), 1.50 ± 0.09 (n = 38 embryos), 2.28 ± 0.12 (n = 42 embryos), and 2.68 ± 0.15 min (n = 47 embryos) for nuclear cycles 10, 11, 12, and 13, respectively. Correspondingly, mitotic wave-front speed decreases from nuclear cycle 10 to 13 (Figure 3.14b). We measured the mitotic wave-front speeds from cycle to cycle to be: 243.5 ± 17.4 (n = 34 embryos), 169.6 ± 7.3 (n = 38 embryos), 110.1 ± 4.8 (n = 42 embryos), and 98.0 ± 5.5 μm/min (n = 47 embryos) for nuclear cycles 10, 11, 12, and 13, respectively. These observations are consistent with what has been noted in the literature [136, 161].

The existence of a sub-population of embryos exhibiting extremely fast moving wave-fronts in nuclear cycle 10 was observed (Figure 3.14b). The 6 embryos that were

measured as exhibiting a nuclear cycle 10 wave-front speed of ~400-500 μm/min (Figure 3.14b) are the same 6 embryos that were measured as having a nuclear division 10 duration of 0.5 min^{-1} (Figure 3.14a). In other words, the mitotic wave-front was observed to propagate across the entire anterior-posterior length of the embryo in two frames. As a result, the mathematical calculation for mitotic wave-front speed cannot be as accurate as there is not enough temporal resolution in the data, and results in a noticeable error in calculating mitotic wave-front speed. This is purely an artifact that is produced by the imaging frequency employed during this study, which can be corrected by using a higher temporal resolution in the imaging experiments (sacrificing the total number of embryos that can be imaged simultaneously). While imaging every 30 s provides enough temporal resolution to make accurate measurements during nuclear cycle 13, this imaging frequency is insufficient during nuclear cycle 10, because of the great speed with which nuclear cycle 10 mitotic wave-fronts propagate. Using the data at hand, all embryos would be classified as exhibiting one mitotic wave-front in nuclear cycle 10, but it is believed that this is purely an artifact of the imaging frequency used in this study.

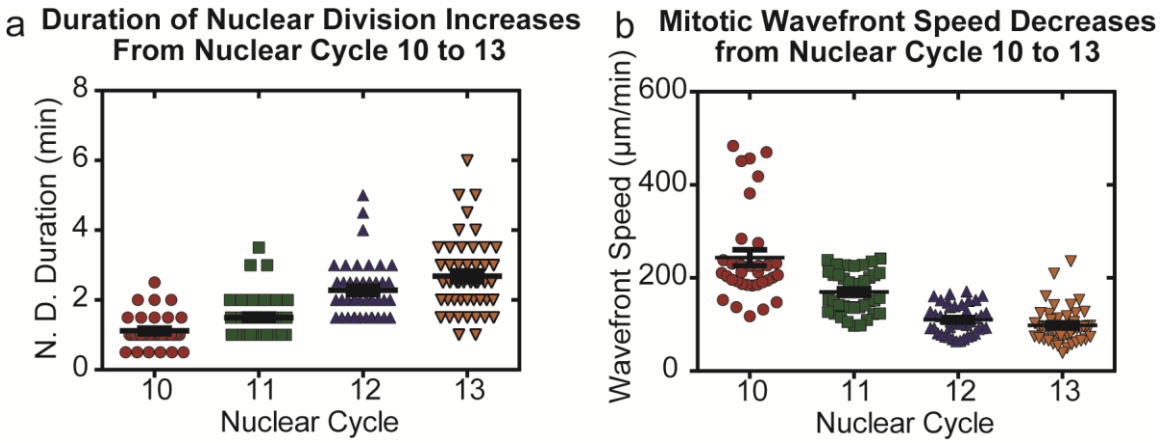

Figure 3.14: Wave-front propagation properties as a function of nuclear cycles 10-13. a) Measured duration for all cells to transition from metaphase to anaphase for all embryos. Average ± standard error of the mean indicated by whiskers. Nuclear division durations were measured at 1.11 ± 0.08 (n = 34 embryos), 1.50 ± 0.09 (n = 38 embryos), 2.28 ± 0.12 (n = 42 embryos), and 2.68 ± 0.15 min (n = 47 embryos) for nuclear cycles 10, 11, 12, and 13, respectively. b) Measured speed of mitotic wave-fronts for all embryos. Average ± standard error of the mean indicated by whiskers. Wave-front speeds were measured at 243.5 ± 17.4 (n = 34 embryos), 169.6 ± 7.3 (n = 38 embryos), 110.1 ± 4.8 (n = 42 embryos), and 98.0 ± 5.5 µm/min (n = 47 embryos) for nuclear cycles 10, 11, 12, and 13, respectively.

The existence of a sub-population of embryos that exhibit relatively elongated nuclear division durations was observed (Figure 3.14a). With our previous knowledge of embryos exhibiting two distinct mitotic wave-front phenotypes, we decided to look at these same properties, while taking into consideration the mitotic wave-front phenotype that was observed for nuclear cycle 13. Separating embryos based on the observed nuclear cycle 13 mitotic wave-front phenotype, we find that embryos exhibiting one mitotic wave-front exhibit a longer nuclear division phase for all nuclear cycles of stage 4 (Figure 3.15a). For two mitotic wave-fronts, the nuclear division duration was measured as 0.98 ± 0.06 (n = 29 embryos), 1.31 ± 0.06 (n = 33 embryos), 2.09 ± 0.08 (n = 37 embryos), and 2.45 ± 0.13 min (n = 42 embryos) for nuclear cycles 10, 11, 12, and 13,

respectively. In comparison, for one mitotic wave-front, the nuclear division duration was measured as 1.90 ± 0.18 (n = 5 embryos), 2.70 ± 0.30 (n = 5 embryos), 3.70 ± 0.51 (n = 5 embryos), and 4.60 ± 0.43 min (n = 5 embryos) for nuclear cycles 10, 11, 12, and 13, respectively. All of these values are statistically different from their counterparts based on a student's T-test ($p<0.0001$ for all nuclear cycles). However, similar to what we have noted before, the mitotic wave-front speeds do not differ in a statistically meaningful way based on a student's T-test ($p>0.05$ for all nuclear cycles) (Figure 3.15b). For two mitotic wave-fronts, the mitotic wave-front speed was measured as 246 ± 20 (n = 29 embryos), 170 ± 8 (n = 33 embryos), 108 ± 5 (n = 37 embryos), and 98 ± 6 μm/min (n = 42 embryos) for nuclear cycles 10, 11, 12, and 13, respectively. The mitotic wave-front speed for embryos exhibiting one mitotic wave-front was measured to be 227 ± 24 (n = 5 embryos), 162 ± 20 (n = 5 embryos), 122 ± 18 (n = 5 embryos), and 92 ± 8 min (n = 5 embryos) for nuclear cycles 10, 11, 12, and 13, respectively. This further confirms the notion that mitotic wave-fronts propagate at the same speed regardless of the number of mitotic wave-fronts that are observed in a given embryo. This is of course under the assumption that embryos maintain mitotic wave-front phenotypes throughout stage 4 of *Drosophila* embryogenesis.

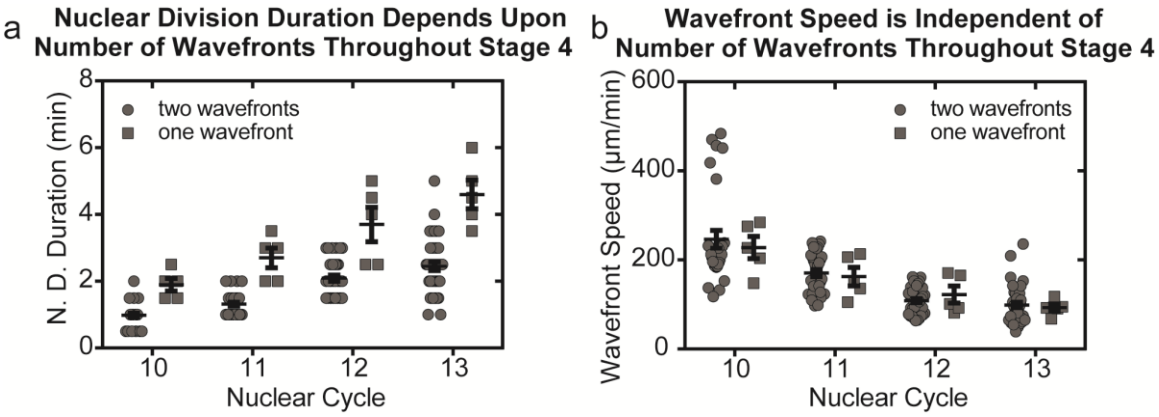

Figure 3.15: Wave-front propagation properties as a function of nuclear cycles 10-13 for embryos exhibiting one or two mitotic wave-fronts during nuclear cycle 13. a) Measured duration for all cells to transition from metaphase to anaphase for all embryos. Average ± standard error of the mean indicated by whiskers. For two wave-fronts, nuclear division durations were measured at 0.98 ± 0.06 (n = 29 embryos), 1.31 ± 0.06 (n = 33 embryos), 2.09 ± 0.08 (n = 37 embryos), and 2.45 ± 0.13 min (n = 42 embryos) for nuclear cycles 10, 11, 12, and 13, respectively. For one wave-front, nuclear division durations were measured at 1.90 ± 0.18 (n = 5 embryos), 2.70 ± 0.30 (n = 5 embryos), 3.70 ± 0.51 (n = 5 embryos), and 4.60 ± 0.43 min (n = 5 embryos) for nuclear cycles 10, 11, 12, and 13, respectively. b) Measured speed of mitotic wave-fronts for all embryos. Average ± standard error of the mean indicated by whiskers. For two wave-fronts, wave-front speeds were measured at 246 ± 20 (n = 29 embryos), 170 ± 8 (n = 33 embryos), 108 ± 5 (n = 37 embryos), and 98 ± 6 μm/min (n = 42 embryos) for nuclear cycles 10, 11, 12, and 13, respectively. For one wave-front, 227 ± 24 (n = 5 embryos), 162 ± 20 (n = 5 embryos), 122 ± 18 (n = 5 embryos), and 92 ± 8 min (n = 5 embryos) for nuclear cycles 10, 11, 12, and 13, respectively.

While further experiments and evidence are needed to understand the mitotic wave-front phenotypes, we demonstrated in this section the ability to obtain quantitative data in a rather simple and straightforward way by using the engineered microfluidic tools. As has been mentioned throughout this chapter as well as in chapter 2 of this thesis, the measurements we have been making have been observed before using conventional low-throughput imaging methods. Here, through the use of microfluidics we can perform large-scale imaging of live *Drosophila* embryogenesis that was not used previously, which allows us to make quantitative measures about the biological processes under

observation. This is evident when one compares the measurements made on mitotic wave-front speed to that of a previous paper that made the exact same measurements about mitotic wave-front speed. Idema et al. [161] used conventional live imaging techniques that limited the sample size to 5 embryos total, wherein 3 embryos were imaged on one day while 2 embryos were imaged on a separate day. In those two data sets, Idema et al. found a large variation between the two days, and could not reconcile the differences as these were ideally replicated experiments and should have produced similar results. The first observation is that our measurements of average mitotic wave-front speed for cycles 10-13 are in between the two data sets reported by Idema et al (Figure 3.16). Furthermore, the data sets reported by Idema et al. are among the spread of the measurements made in this thesis chapter (Figure 3.16). Therefore, we hypothesize that the apparent discrepancy between data sets reported by Idema et al. can be attributed to day-to-day to variation, or even biological noise. Reconciling this discrepancy was made possible by making quantitative measurements that was enabled by the large sample sizes that we can achieve with the microfluidics-enabled high-throughput imaging methods we have developed in this thesis.

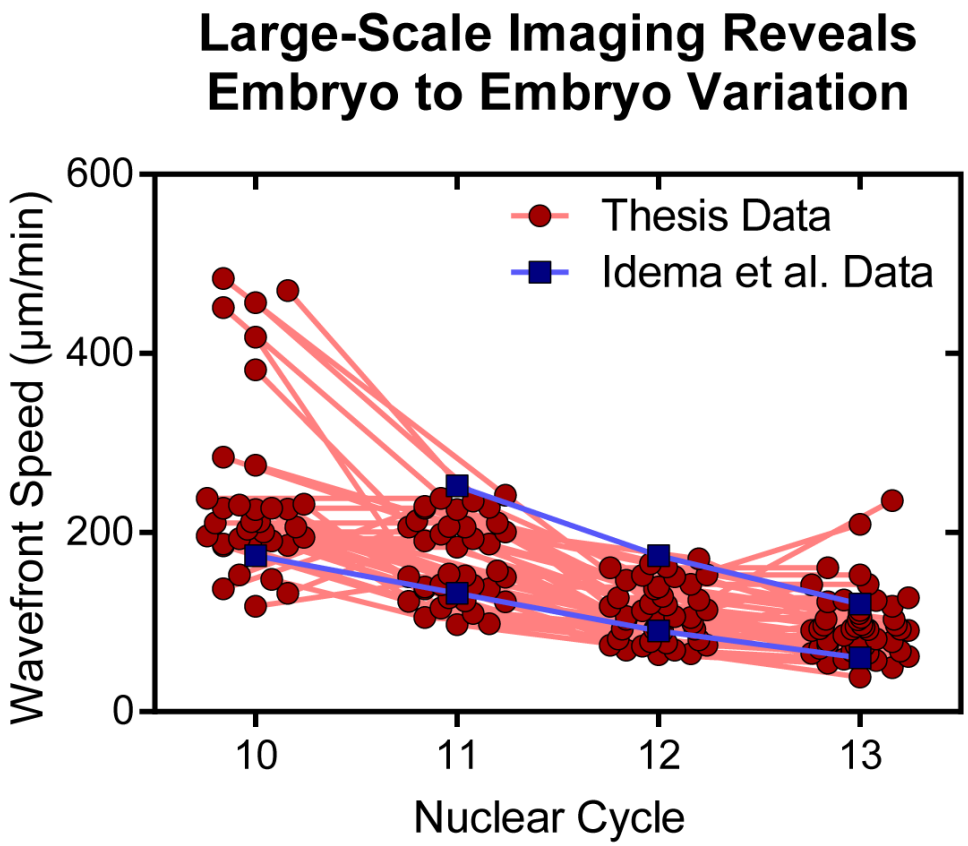

Figure 3.16: Comparison of mitotic wave-front speed as collected in this thesis and by the work of Idema et al. Thesis Data refers to individual embryo data collected in this thesis using our microfluidics-enabled high-throughput imaging technique. Idema et al. Data refers to data set averages for 3 and 2 embryos collected on separate days.

3.4: Conclusion

In vivo live imaging is a powerful technique for visualizing and understanding dynamic processes across the fields of biology including developmental biology. Yet, time-lapse imaging is technically difficult to perform in a high-throughput manner with model organisms such as the *Drosophila* embryo. In this chapter, we developed a microfluidic device for high-throughput arraying of lateral oriented live *Drosophila* embryos for massively parallel time-lapse microscopy. The device is simple in design

and therefore simple to use to facilitate the rapid adoption of this technology by non-specialists. While not explored in depth in this chapter, the device can be used to look at other stages of *Drosophila* embryogenesis as well as longer term imaging applications. Furthermore, with simple scaling the device should be applicable to other model organisms thereby increasing the devices impact throughout biology.

The method developed in this chapter greatly improves our ability to image *Drosophila* embryogenesis in a high-throughput manner, and takes a step toward quantitative biology. However, it should be noted that all of the analysis in this chapter was performed by hand through manual inspection, and as such required significant person-hours to complete. The next step in truly providing high-throughput techniques for quantitative biology in analyzing dynamic phenotypes requires the development of automated analysis software. The goal of the next chapter in this thesis attempts to tackle this problem for a different biological application, At the end of the following chapter, we will have developed a complete method for quantitative biology that employs both microfluidics and computer vision, and use it to statistically compare dynamic intercellular phenotypes of early *Drosophila* embryogenesis.

CHAPTER 4: STATISTICAL COMPARISON OF INTERCELLULAR DYNAMICS VIA MICROFLUIDICS AND COMPUTER VISION

4.1: Introduction

Receptor tyrosine kinase (RTK) signaling is well known to be used multiple times throughout development across many organisms [162-164]. In the stage 4 *Drosophila* embryo, the ligand Trunk (trk) is activated at the poles and binds the RTK receptor Torso (tor) [165]. Torso binding sets off a signaling cascade involving extracellular signal-regulated kinase (ERK) [166], which typically results in the phosphorylation of nuclear factors thereby affecting the expression of target genes [167, 168]. Capicua (cic), a well-known transcriptional repressor, has been shown to be a downstream target of RTK-ERK signaling in the early embryo [87, 169]. It has additionally been shown that mutations in RTK signaling affect the nucleocytoplasmic partitioning of Capicua in the early embryo [170]. However, quantitative information of Capicua spatiotemporal signaling patterns is currently lacking, which is primarily a result of low-throughput conventional live imaging techniques. Additionally, there has been increased interest in understanding how mutations in the Ras-MAPK (mitogen-activated protein kinase) signaling pathway affect development to produce an array of developmental disorders [171-173]. A detailed understanding of Capicua dynamics could be the first step toward understanding how mutations in Ras-MAPK signaling affect downstream target gene spatiotemporal expression patterns during early embryogenesis.

In this chapter, I addressed some of technological gaps that currently limit the ability to collect large-scale, quantitative information regarding intercellular signaling dynamics during embryogenesis. Specifically, this chapter presents an optimized microfluidic device for arraying live *Drosophila* embryos for parallelized imaging of anterior-posterior development at the embryo midsection. To complement the high-throughput imaging device, I additionally developed an image processing and analysis strategy for the automated and unbiased measurements of dynamic intercellular phenotypes during *Drosophila* embryogenesis. The integrated platform consisting of the microfluidic device and image processing software was used to quantitatively measure spatiotemporal patterns of the transcription factor Capicua within the *Drosophila* blastoderm. Furthermore, I used this engineered microsystem to investigate the effects of environmental and genetic perturbations on Capicua dynamics. Specifically, we were interested in understanding how temperature and mutations in upstream RTK-ERK signaling affected Capicua dynamics.

4.2: Materials and Methods

4.2.1: Fabrication of the Two-Layer Anterior-Posterior (AP2) Array

I utilized the same method of rapid prototyping as mentioned in chapter 2 section 2.2.1 of this thesis to fabricate the two-layer AP2 array described in this chapter [135]. Deviations from the fabrication protocol are described in this section. Mold fabrication involved a two-layer, photolithographic procedure to pattern two distinct layers with two different photomasks which can be found in Appendix B (Figure B.3). Each layer was

designed to be 100 µm tall for a total device height of 200 µm. In order to achieve the desired layer heights we employed the thick photoresist SU-8 2100 (MicroChem Corp.).

To fabricate the master mold with multi-layer thick SU-8 2100, I used a specifically tuned lithographic process as described in section 3.2.1. However, in between each photoresist deposition sequence, I patterned individual layers with two different photomasks by exposing the film to 365 nm wavelength light with an exposure energy of 240 mJ cm^{-2}. The rest of the protocol follows the exact same procedure as described in section 3.2.1.

Replica molding PDMS (polydimethylsiloxane, Dow Corning) devices and plasma bonding to glass cover slips followed the same procedure as described in chapter 2 section 2.2.1 of this thesis.

4.2.2: Three-Dimensional Finite Element Modeling of AP2 Array Fluid Dynamics

Finite element modeling was performed via COMSOL Multiphysics® 4.3b Modeling Software (COMSOL, Inc.). For simplification, a single trapping unit was modeled consisting of an embryo trap, resistance channel, and one turn of the main serpentine channel. The three-dimensional (3D) steady-state incompressible Navier-Stokes equation was solved for in order to visualize flow patterns through the microfluidic traps. Boundary conditions include an inlet superficial velocity that was experimentally estimated to be on the order of 0.1 m/s, an assumed outlet condition of atmospheric pressure, and no slip along channel surfaces. Fluid properties were assumed to be equivalent to pure water. Temperature was set to 298 K within the device.

4.2.3: *Drosophila melanogaster* Strains and Embryo Preparation

A *Drosophila melanogaster* strain that is homozygous for Capicua-Venus (Cic-Venus) fusion protein transgene (*cicv/cicv*) was used to study the effects of culture temperature on Capicua dynamics and generously provided by Stanislav Y. Shvartsman. In order to investigate the effects of RTK-ERK signaling on Capicua dynamics we utilized the following fly strains: *cicv/+* (flies carrying one copy of the *cic-venus* transgene and otherwise wildtype), *cicv/+;tor*^{D4021}*/+* (flies carrying one copy of the *cic-venus* transgene with a heterozygous *torso* gain-of-function mutation) [170], *cicv/+,MEK*^{E203K}*/+* (flies carrying one copy of the *cic-venus* transgene with a heterozygous *Dsor1* (*Drosophila* MEK) hyperactive mutation), and *cicv/+,MEK*^{F53S}*/+* (flies carrying one copy of the *cic-venus* transgene with a heterozygous *Dsor1* (*Drosophila* MEK) hyperactive mutation), which were constructed by Yogesh Goyal. The four genotypes will be referred to as *wt*, *tor*, *E203K*, and *F53S*, respectively, throughout the rest of the thesis for simplicity. Adult flies and eggs were maintained and processed with established protocols for live imaging [136].

Drosophila embryos were collected and prepared for imaging prior to microfluidic arraying and live imaging on-chip, following the same procedure as described in chapter 2 section 2.2.2.

4.2.4: AP2 Arraying of Embryos for Time-Lapse Microscopy

Microfluidic device preparation and arraying of *Drosophila* embryos followed the same protocol described in chapter 2 section 2.2.2 of this thesis while utilizing the two-layer AP2 array described in this chapter.

Time-lapse confocal microscopy was performed in a similar manner as described in chapter 3 section 3.2.4 of this thesis. Differences between the conditions utilized in this chapter and those utilized in chapter 3 section 3.2.4 are discussed here: A 514 nm argon laser was used for capturing Cic-Venus fluorescence while 514 nm transmission was used for capturing transmitted light images simultaneously. Embryos were imaged in the anterior-posterior plane at the embryo midsection with a frequency of 2 min^{-1} for 3 h. The temperature was maintained through the use of an environmental chamber during imaging. Temperatures used in this study include 25, 27.5, and 30 ºC, and are noted where appropriate.

4.2.5: Algorithm for Quantifying Single-Cell Gene Expression Dynamics

Image processing was done using a combination of ImageJ and Matlab™ R2015a software with custom code. The built-in straighten tool in ImageJ was utilized to straighten the egg surface such that the monolayer of nuclei in the *Drosophila* blastoderm were arranged in a straight line from anterior to posterior. This was the only step performed in ImageJ and the output was subsequently processed in Matlab. Filtering and object removal was based on built-in Matlab functions including, for example, regionprops, and was an extension of our previous work on the development of relative difference filtering and clustering (RDFC) that was utilized in chapter 2 of this thesis [174].

4.3: Results and Discussion

4.3.1: Development of the AP2 Array

For this study, it was important to acquire images in a plane parallel to the anterior-posterior axis at a depth near the middle of the embryo (here referred to as the mid-section). In chapter 3 of this thesis, I developed a microfluidic trap array (AP1) for high-throughput imaging of laterally oriented live *Drosophila* embryos that could be utilized in this study [175]. However, the relatively small traps in the AP1 array can produce optical aberrations that become more apparent when imaging near embryo mid-section (Figure 4.1). The close proximity of the trap walls to regions of the embryo caused those regions of the embryo to appear less fluorescent. Consequently, the microfluidic array needed to be redesigned to allow aberration-free imaging at the embryo mid-section.

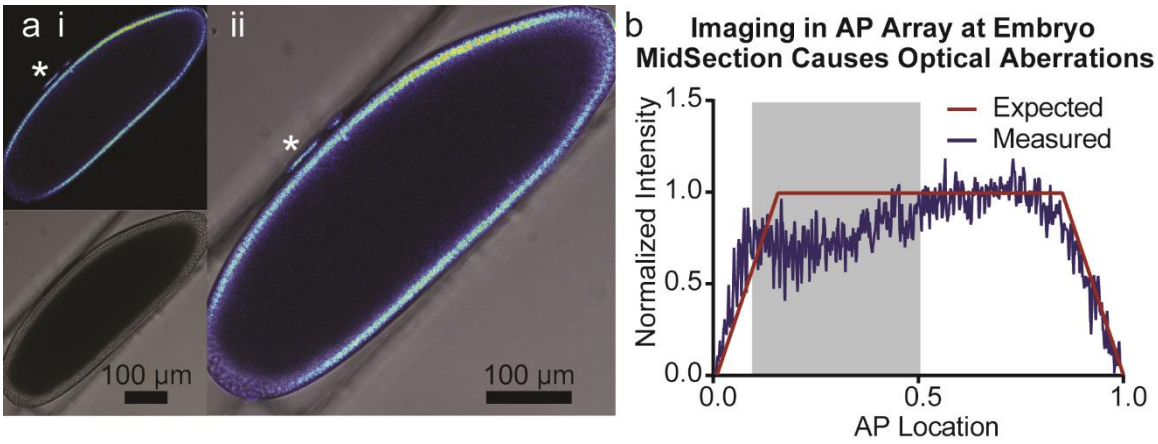

Figure 4.1: Single-layer AP1 array introduces optical aberrations when imaging at embryo mid-section. a) Optical confocal micrographs at the mid-section of a Cic-Venus expressing embryo within the single layer AP1 array described in chapter 3. i) Cic-Venus channel (top) and transmitted light channel (bottom). * indicates visible Cic-Venus reflection in PDMS sidewalls. ii) Merge of Cic-Venus and transmitted light channels. * indicates visible Cic-Venus reflection in PDMS sidewalls. b) Intensity plot along the ventral epithelium in which PDMS sidewalls induce optical aberration (top side of embryo in (a)). Gray box indicates the area of the epithelium that is artificially dimmed due to PDMS sidewall interference.

To improve image quality near the embryo mid-section, the trap was designed with a wide base and a narrow top (Figure 4.2). The wide base allows aberration-free imaging of the *Drosophila* embryos near the mid-section as trap walls no longer contact the embryo surface, while the narrow top centers embryos within the trap and away from trap walls (Figure 4.2).

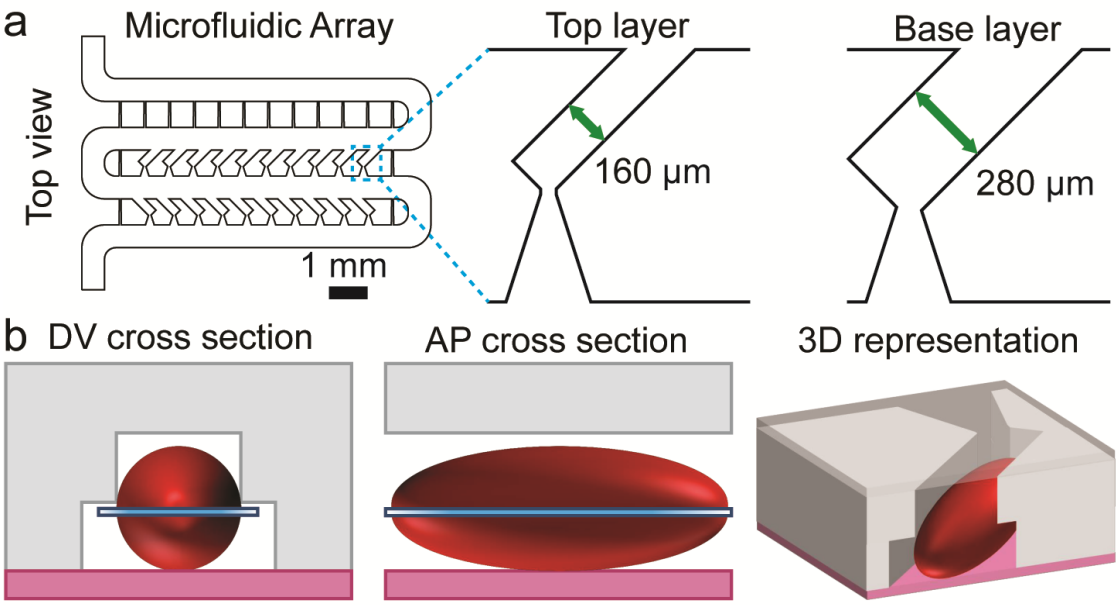

Figure 4.2: Two-layer AP2 microfluidic array schematic. a) Left: Overall device layout from a top-down view depicting the main serpentine channel, focusing channels, embryo traps and resistance channels. Right: Close up of embryo trap design in both the top layer that guides embryos to the center of the trap, and the base layer wherein the imaging plane is located for time-lapse confocal microscopy. b) Left: Dorsal-ventral cross-section of an embryo (red) in the trap with imaging plane (blue) indicated. PDMS (gray) and glass cover slips (pink) are also depicted. Center: Anterior-posterior cross-section of an embryo in the trap with imaging plane indicated. Right: Three-dimensional perspective of an embryo in the trap.

This design change was expected to affect overall trapping efficiency of the array. Experimentally, the redesigned trap produced an average trapping efficiency of 58% (n = 6 experiments), whereas the previously designed AP1 array could trap with ~90% efficiency (Figure 4.3a). Low trapping efficiency is the result of improper balancing of fluid transport along the serpentine channel and through traps. Three-dimensional finite element modeling of fluid dynamics via COMSOL was used to predict fluid transport within the microfluidic device and identify designs with potential to improve trapping efficiency (Figure 4.3). The optimized design involved a significant widening of the resistance channel in order to increase fluid transport through the traps (Fig 4.3b), and produced an average trapping efficiency of 98% (n = 3 experiments) (Figure 4.3b). The optimized design was then used for highly parallelized lateral imaging of *Drosophila* embryogenesis to enable quantitative analysis of Cic-Venus signaling dynamics in the *Drosophila* blastoderm.

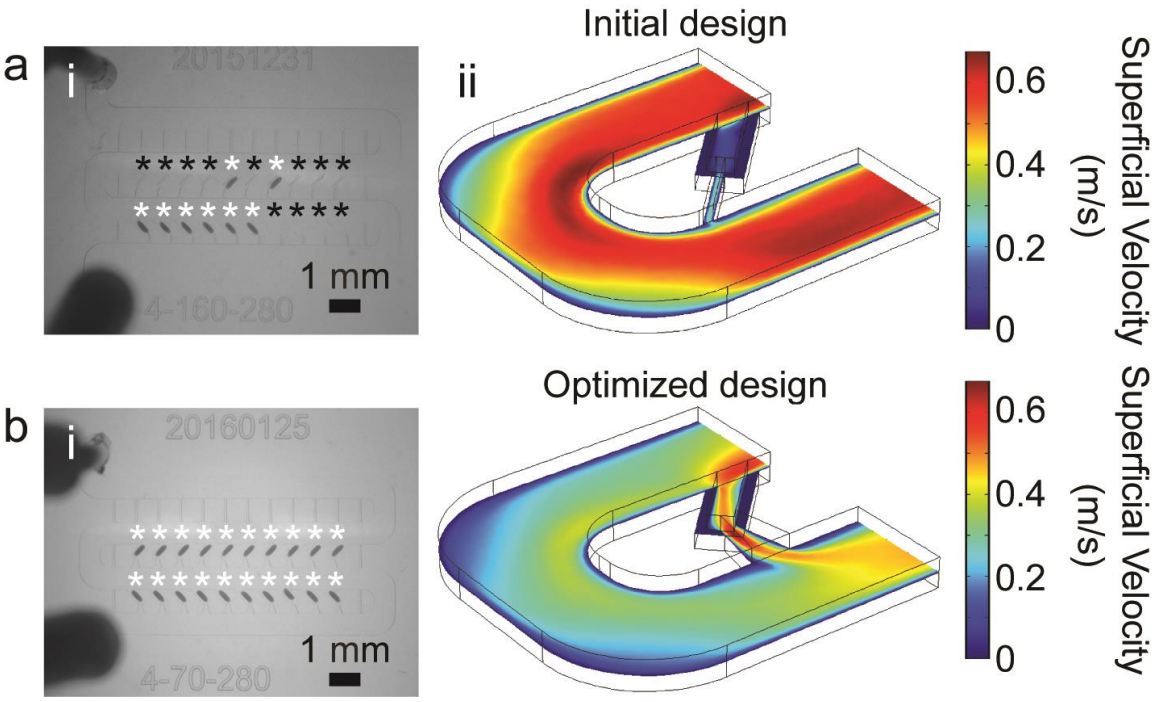

Figure 4.3: Array loading and COMSOL simulation results. a) Initial design that simply incorporates a wide base in the trapping unit to the optimized single-layer AP1 array from chapter 3. i) Typical loading results for the initial design with an average trapping efficiency of 58% (n = 6 experiments). White asterisks indicate traps with embryos successfully loaded while black asterisks indicate empty traps. ii) Surface plots of superficial velocity at channel mid-plane from COMSOL three-dimensional finite element modeling. Most fluid follows the serpentine channel in this design. b) Optimized two-layer AP2 array design. i) Typical loading results for the optimized design with an average trapping efficiency of 98% (n = 3 experiments). White asterisks indicate traps with embryos successfully loaded while black asterisks indicate empty traps. ii) Surface plots of superficial velocity at channel mid-plane from COMSOL three-dimensional finite element modeling. Most fluid is diverted to the embryo trap in this design.

4.3.2: Construction of Capicua Spatiotemporal Patterning Heat-maps

The microfluidic array enabled high-throughput imaging of live *Drosophila* embryos. Representative frames from time-lapse imaging of Cic-Venus dynamics suggest embryos develop as expected within the microfluidic array (Figure 4.4). During *Drosophila* embryogenesis, RTK signaling is active at the poles during stage 4. RTK

signaling results in the phosphorylation of Capicua, which alters the nucleocytoplasmic partitioning of Capicua. When RTK signaling is inactive, Capicua remains in a dephosphorylated, active state that allows Capicua to enter the nucleus and repress target gene expression. Active RTK signaling phosphorylates Capicua to inactivate the transcriptional repressor, which ultimately results in Capicua translocation to the cytoplasm wherein Capicua is degraded and Capicua target genes become de-repressed. As a result, Capicua exhibits a spatial pattern along the anterior-posterior axis that inversely correlates with RTK signaling along the anterior-posterior axis (Figure 4.4). Specifically, Capicua levels are low at the poles and elevated toward the embryo mid-body, wherein Capicua levels are uniform throughout the central ~50% of the anterior-posterior axis. The area of uniform Capicua levels near the anterior-posterior center is a result of low and uniform levels of RTK signaling in that region [87, 176]. The Capicua anterior-posterior spatial pattern persists throughout stages 4 and 5 of embryogenesis. It is important to note that the anterior-posterior pattern of Capicua is identical around the dorsal-ventral axis allowing the anterior-posterior Capicua gradient to be visible from any dorsal-ventral orientation during stages 4 and 5 of embryogenesis.

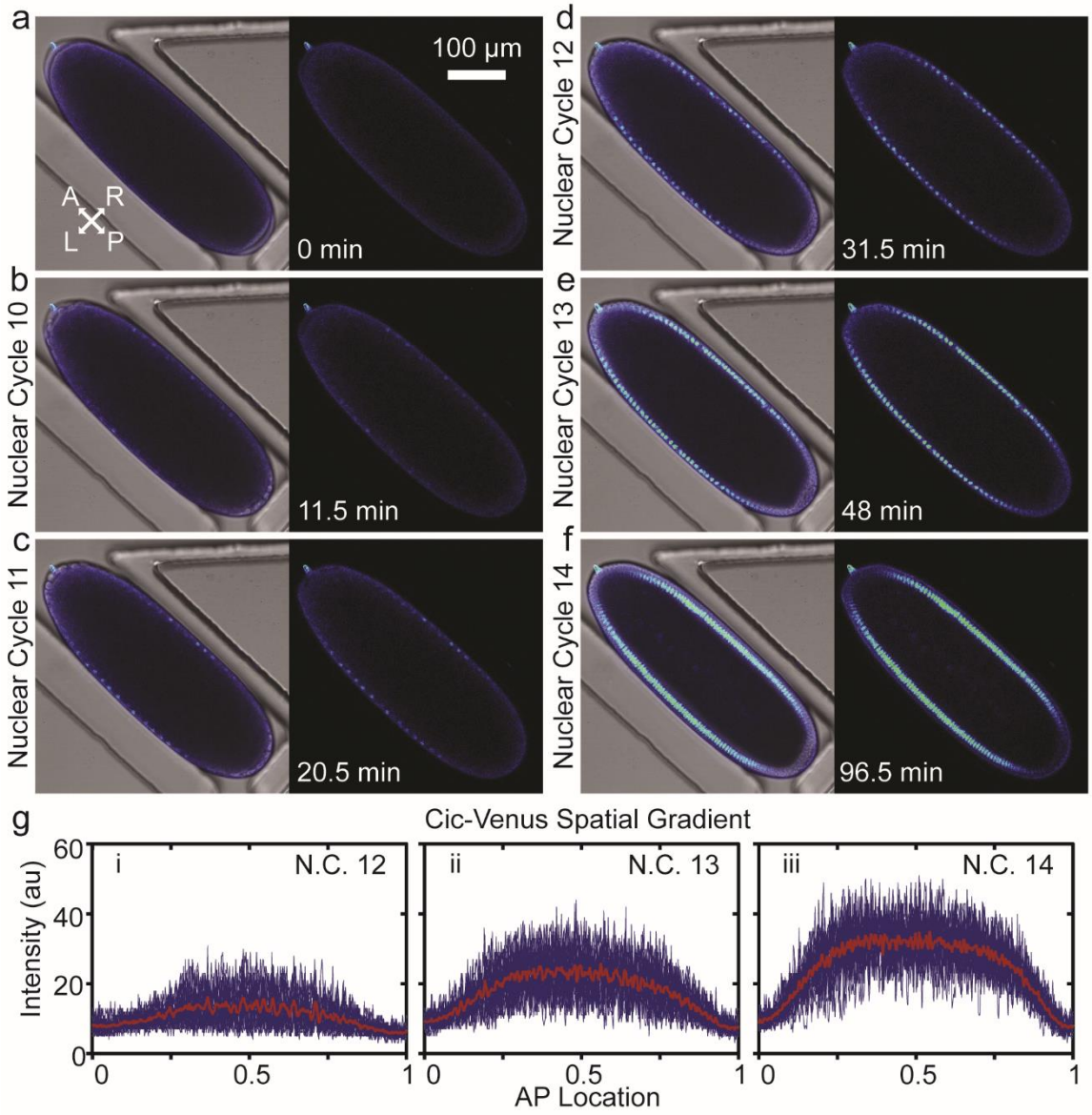

Figure 4.4: Cic-Venus spatial distribution. a-f) Time-lapse confocal microscopy optical micrographs depicting an embryo that is homozygous for *cic-venus* transgene. Left images are merges of the Cic-Venus and transmitted light channels while right images are from the Cic-Venus channel only. Time is relative to imaging start time. a) imaging start point, b-e) stage 4 of embryogenesis with nuclear cycles b) 10, c) 11, d) 12, and e) 13, and f) stage 5 of embryogenesis with nuclear cycle 14. g) Cic-Venus anterior-posterior (0-1) spatial gradient during nuclear cycle i) 12, ii) 13, and iii) 14. Individual embryo spatial gradients are blue line plots with the population average in red. n = 22 embryos.

While the spatial patterns regarding RTK signaling and Capicua are well studied for specific stages of development, the temporal patterns or signaling kinetics have been studied to a lesser degree. A lack of kinetic data regarding these signaling systems can be attributed to time consuming, conventional preparation techniques for time-lapse imaging of *Drosophila* embryogenesis. To our knowledge, the only paper that measured Capicua signaling dynamics throughout stages 4 and 5 of embryogenesis acquired data from a single embryo [170]. Using our method of high-throughput microscopy, we wanted to construct a large data set of Capicua dynamics in order to investigate the effects of genetic and environmental perturbation on Capicua dynamics that are statistically meaningful.

Our method of high-throughput microscopy typically produced just under 4000 images per experiment. Therefore, automating image processing and analysis became a requisite in this study to prevent a bottleneck at this step from limiting throughput. Preprocessing steps were taken to prepare the raw imaging data for subsequent automated analysis. This involved re-mapping the four-dimensional raw imaging data to three-dimensional representations (Figure 4.5). This was initially born out of an attempt to improve data visualization, and eventually became an important tool for analyzing signaling dynamics in this study. First, raw imaging data is imported into ImageJ to isolate two individual gradients per embryo with the built-in ImageJ function Straighten (Figure 4.5a and Figure 4.5b). Gradients are cropped in such a way that the vertical dimension is always the anterior-posterior location with anterior at the top of the image, and the horizontal dimension is the apical-basal location (Figure 4.5b). The cropped imaging data is then imported to Matlab wherein the two-dimensional gradient (each

image in Figure 4.5b) is reduced to a single line-plot at every time-point by taking the maximum at every anterior-posterior spatial location (vertical dimension in Figure 4.5b). The assumption here is that the maximum value in the apical-basal direction would generally be found within a nucleus during interphase of the cell cycle and represent Cic-Venus nuclear levels while during the division phase of the cell cycle this value would represent Cic-Venus cytoplasmic levels. Finally, the anterior-posterior line-plots are stacked in a heat-map representation so that the anterior-posterior spatiotemporal patterning for a single embryo gradient can be visualized in one image (Figure 4.5c). The re-mapped imaging data plots the anterior-posterior location along the vertical dimension, time along the horizontal dimension, and Cic-Venus intensity by color. Re-mapping of the raw imaging data is done twice per embryo on both “left” and “right” segments of the blastoderm. This re-mapped imaging data is the basis for the rest of the analysis performed in this thesis chapter.

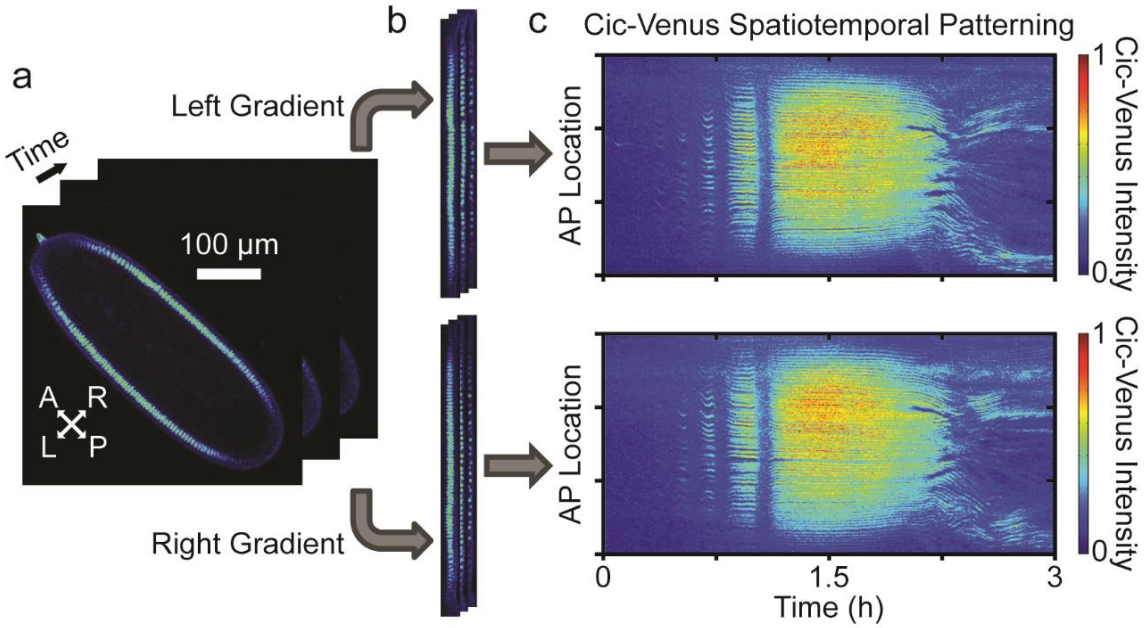

Figure 4.5: Re-mapping of the four-dimensional imaging data to three-dimensional representations. a) Raw four-dimensional imaging data of a single Cic-Venus expressing embryo including 360 images per embryo. b) Imaging data from (a) are imported to ImageJ, cropped, and straightened with the built-in ImageJ function Straighten to produce 360 gradient images for a total of 720 images. The vertical dimension represents the anterior-posterior direction, and the horizontal direction represents the apical-basal direction. c) Imaging data from (b) are imported to Matlab and reduced to a single Cic-Venus line-plot by taking the maximum along the vertical anterior-posterior direction of each image and stacked in a heat-map representation of Cic-Venus spatiotemporal dynamics.

4.3.3: Quantifying Developmental Dynamics

One of the first goals we set out to accomplish here was to establish a baseline for Cic-Venus dynamics in our wild-type control embryos. Here, when referring to wild-type control we are referring to strains that do not possess mutations that alter the natural function of the gene product. However, wild-type embryos in this study still possess the *cic-venus* transgene, which we assume functions equivalently to natural Capicua. Important to note that there were two wild-type control strains used in this study. One

wild-type control was homozygous for the *cic-venus* transgene (*cicv/cicv*) and was used when investigating the effects of culture temperature on Capicua dynamics, while the second wild-type control was heterozygous for the *cic-venus* transgene (*cicv/+*) and was used when investigating the effects of mutations in the upstream RTK-ERK signaling pathway on Capicua dynamics. The heterozygous wild-type control embryos were necessary controls, because embryos possessing mutations in the RTK-ERK signaling pathway were also heterozygous for the *cic-venus* transgene. Performing experiments in this manner kept Cic-Venus dosages constant within groups to be compared and allowed any observed differences between conditions to be solely attributed to the experimental variable (i.e. either temperature or RTK-ERK mutation).

As previously mentioned, one of our main goals was to understand how changes in the upstream RTK-ERK signaling pathway affects Capicua dynamics. From previous work, it is known that the level of RTK signaling at the anterior-posterior center of the embryo is uniform during stages 4 and 5 of *Drosophila* embryogenesis [170]. It is also known that mutations such as the *torso* gain-of-function mutation used here decreases RTK signaling at the poles, and increases RTK signaling at the anterior-posterior middle of the embryo while maintaining the uniform field of RTK signaling at the anterior-posterior center region of the embryo. We therefore restricted analysis to the central 50% of the anterior-posterior axis as this region exhibits uniform levels of RTK signaling, and Capicua activity. In this way, each cell within this region of the embryo is expected to function similarly, and we assume can be utilized as independent measurements of Cic-Venus dynamics.

One of the first steps was identifying the stages of interest, and in this case those included stages 4 and 5 of *Drosophila* embryogenesis, which include nuclear cycles 10-14. Visual inspection of the Cic-Venus spatiotemporal pattern heat-maps identified stereotyped patterns that correlate with different phases of embryogenesis. Prior to nuclear cycle 10, a uniform and low signal is detected throughout the anterior-posterior axis of the embryo as no nuclei are present at the embryo surface (Figure 4.6). At the onset of nuclear cycle 10 and stage 4 of embryogenesis, nuclei migrate to the embryo plasma membrane all around the embryo surface. However, nuclei are only visible near the anterior-posterior center as low levels of RTK signaling allows Capicua to enter nuclei in this region and provide contrast necessary to visualize distinct nuclei. Nuclei proceed through 4 rounds of synchronous and rapid nuclear divisions during the rest of stage 4 of embryogenesis. Each nuclear cycle is visible and most obvious toward the anterior-posterior center of the embryo as high levels of Cic-Venus intensity correspond to individual nuclei. Nuclei are lost in between each nuclear cycle as nuclei divide and disperse Cic-Venus into the cytoplasm. During each nuclear cycle Cic-Venus migrates into the nucleus and progressively increases the intensity within nuclei. At the onset of nuclear cycle 14 and stage 5 of embryogenesis, Cic-Venus migrate into nuclei and maintain high levels of Cic-Venus for a majority of stage 5 and continues until the embryo exits stage 5 of embryogenesis (Figure 4.6). After stage 5, major morphogenetic movements occur including cephalic furrow formation, which marks the onset of gastrulation.

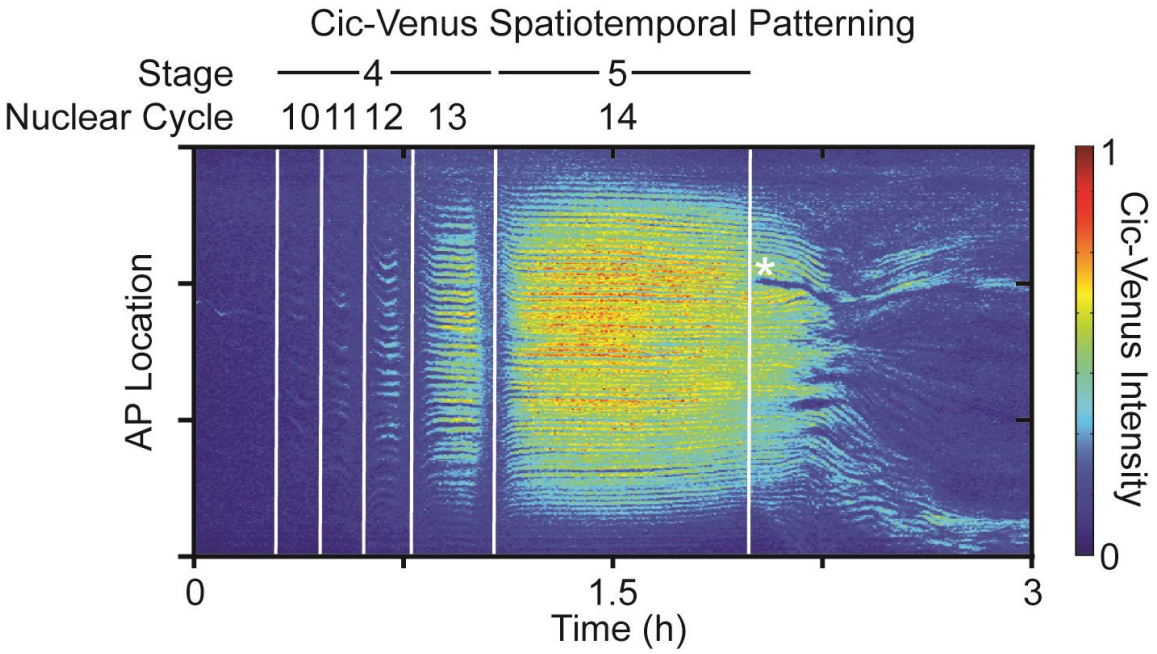

Figure 4.6: A detailed illustration highlighting the timing of *Drosophila* embryogenesis upon the Capicua spatiotemporal patterning heat-maps described earlier. Prior to stage 4, no nuclei are visible as they are located deep within the egg yolk. During stage 4, nuclei become visible and proceed through 4 synchronous nuclear cycles, specifically, nuclear cycles 10-13. Onset of nuclear cycle 14 marks the onset of stage 5. Exit of stage 5 is marked by major morphogenic movements including cephalic furrow formation at the onset of gastrulation. Asterisk indicates cephalic furrow.

Automated Staging of Drosophila Embryos Using Capicua Spatiotemporal Heat-maps

In order to automatically identify stages 4 and 5 of embryogenesis, we averaged Cic-Venus intensity within the anterior-posterior central region of the embryo for each time point to further reduce the Cic-Venus spatiotemporal pattern heat-maps to a line-plot and refer to this plot as average Cic-Venus fluorescence (Figure 4.7a). An oscillating pattern is clearly visible and visual inspection indicates that each peak corresponds with a specific nuclear cycle (Figure 4.7a). This was expected as similar measurements have been made before with this specific *Drosophila* strain [170] as well as strains expressing His-GFP as described in chapter 2 of this thesis [121]. The built-in function findpeaks in

Matlab enabled automatic identification of each peak location, and when used with the inverse of the line-plot identified valley locations. The most useful criterion that enables automated identification of specific nuclear cycles is the built-in feature MinPeakProminence, which calculates the vertical drop of a local maximum. For the vast majority of videos a single value for MinPeakProminence could identify peaks and valleys associated with the nuclear cycles of interest. Specifically, a value of 0.7 was used for a majority of embryogenesis videos, while a minority of videos needed slight adjustment in either direction to accurately identify nuclear cycles of interest.

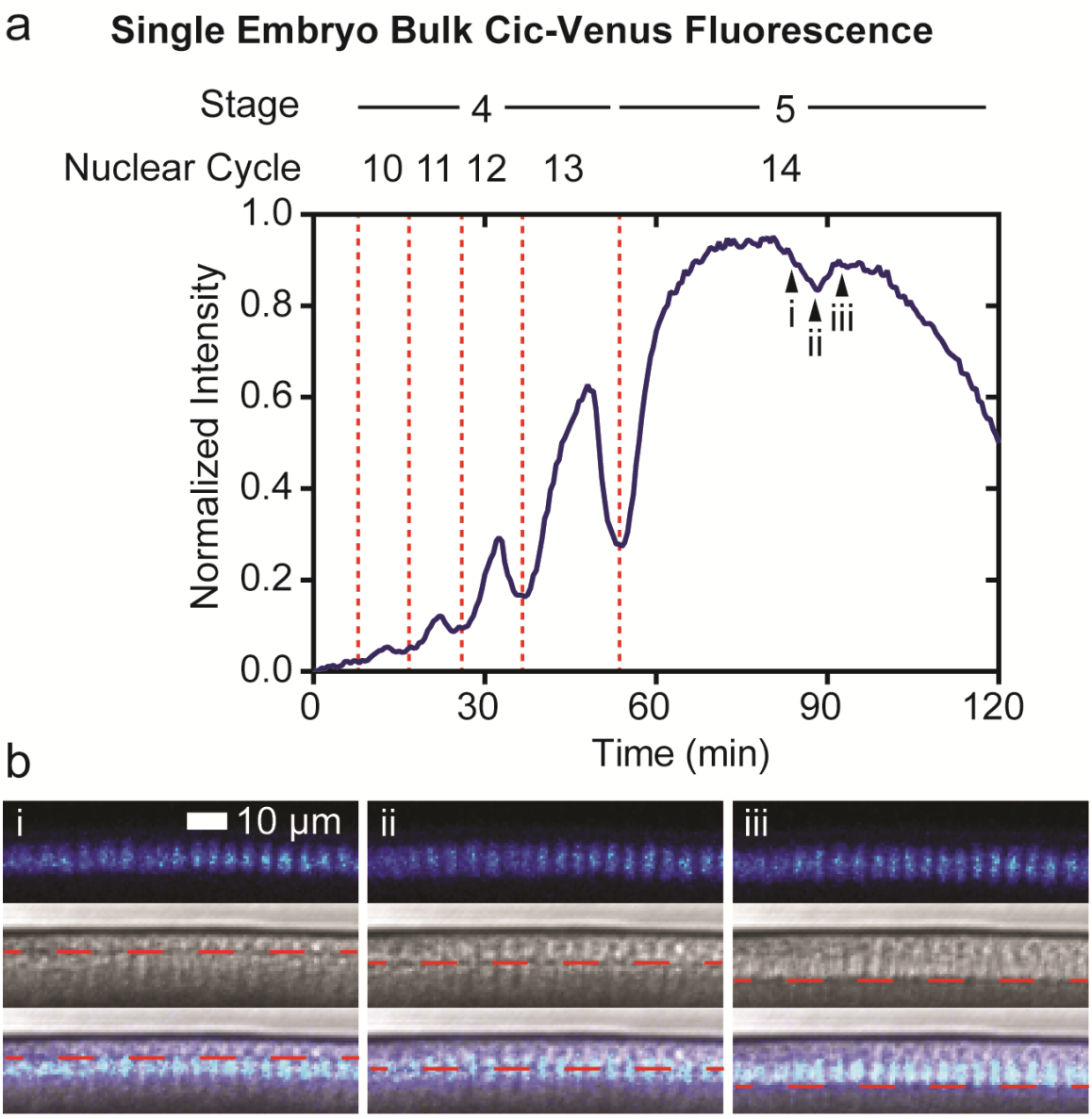

Figure 4.7: a) Single embryo average Cic-Venus fluorescence. Dotted red lines represent transitions between nuclear cycles (division phase). Nuclear localization of Cic-Venus increases from cycle to cycle as indicated by increasing Cic-Venus intensity. b) Confocal micrographs of embryo surface with Cic-Venus channel (top), transmitted light (middle), and merge (bottom). i-iii) Optical micrographs that correlate with (i-iii) in (a): i) 5 minutes before observed minimum in Cic-Venus intensity. ii) Exact time of observed minimum in Cic-Venus intensity. iii) 5 minutes after observed minimum in Cic-Venus intensity. Dotted red lines are tracking furrow canal migration.

Unexpectedly, a prominent minimum within nuclear cycle 14 was observed (Figure 4.7a). Upon further review, the minimum seems to be biologically significant as it appears to be associated with the process of furrow canal migration (FCM). To elaborate, during stage 5 of *Drosophila* embryogenesis, nuclei are located just under the common plasma membrane of the embryo, which at this point of development is considered a syncytium or a single cell with multiple nuclei. During stage 5, the common plasma membrane furrows and invaginates around individual nuclei. This invagination process continues with the furrow canal migrating basally toward the embryo center, so that at the end of stage 5 every nucleus is enclosed by independent cell membranes. This overall process, and designation for stage 5 of *Drosophila* embryogenesis, is referred to as cellularization. Furrow canal migration was observed via transmitted light illumination, and allowed us to connect FCM to the measured dimming of Cic-Venus intensity in nuclear cycle 14 (Figure 4.7b). However, the data at hand only suggests a potential causal-link between FCM and Cic-Venus dimming during nuclear cycle 14. Furthermore, even if FCM is the cause for the observed dimming in Cic-Venus intensity in nuclear cycle 14, it is unclear if the observed lowering in intensity is indicative of general transport of Cic-Venus proteins out of the nucleus, or if the observed lowering in intensity is an optical artifact caused by the furrow canal itself. If the former, then this suggests a path to further investigate what the downstream consequences of FCM-induced Cic-Venus export from the nucleus, and whether this process results in Capicua target gene derepression.

Temporal Alignment of Videos to Facilitate Population-Level Comparative Analysis

Once the nuclear cycle locations in time were identified we could align individual embryo trajectories to establish population average Cic-Venus dynamics and investigate embryo-to-embryo variability in average Cic-Venus fluorescence. Specifically, the location identified as the transition from nuclear cycle 13 to 14 was utilized to align videos. From this data, it was observed that there is embryo-to-embryo variability in average Cic-Venus fluorescence; however, the overall trend of the curves appears highly stereotyped (Figure 4.8a). Variation in overall Cic-Venus fluorescent intensity was expected as embryos are expected to display variations in overall amounts of Cic-Venus. Normalization in order to account for embryo-to-embryo variability in Cic-Venus production showed that average Cic-Venus dynamics is highly reproducible across embryos (Figure 4.8b). Robust identification of nuclear cycles 12, and 13 and 14 was possible with this method, and as such we limited our analysis to these nuclear cycles. Furthermore, the observed dimming of Cic-Venus during nuclear cycle 14 is highly reproducible across embryos, and provided a unique marker for identifying the onset of furrow canal migration (Figure 4.8). Additionally, it is observed that Cic-Venus nuclear localization exhibits increased variability after onset of furrow canal migration (Figure 4.8b). This is expected as it is known that the dorsal-ventral patterning system utilizes RTK signaling pathways to spatially pattern the dorsal-ventral axis, and as such will differentially affect Capicua nuclear localization around the dorsal-ventral axis [87]. As a result, we limited our analysis of Cic-Venus dynamics in nuclear cycle 14 to the early phase of nuclear cycle 14 marked by the onset of furrow canal migration.

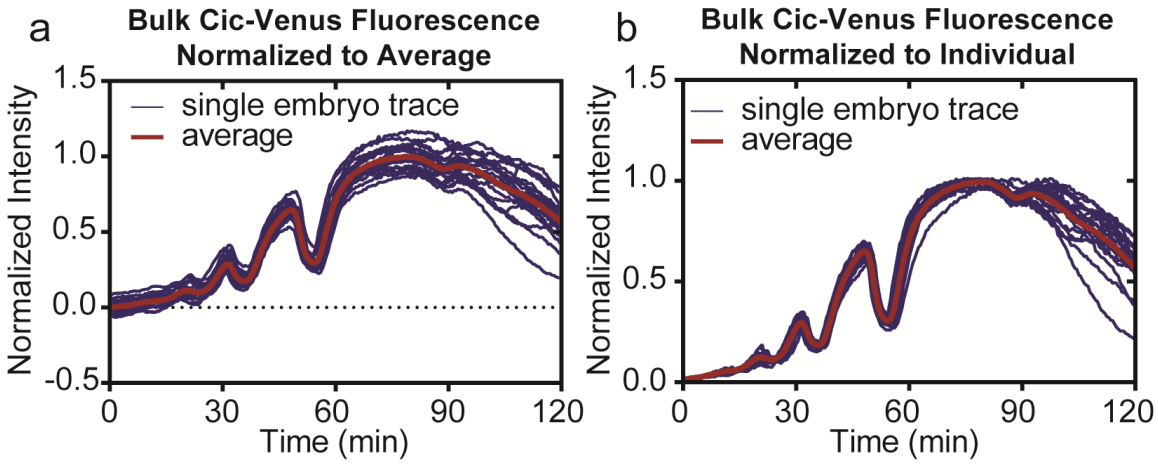

Figure 4.8: a) Average Cic-Venus fluorescence normalized to average. Individual embryo traces (blue lines) are normalized by subtracting the population average minimum (red line) and dividing by the difference of the population average maximum and population average minimum. (n = 20 embryos). b) Average Cic-Venus fluorescence normalized to individual. Individual embryo traces (blue lines) are normalized by subtracting the individual trace minimum (red line) and dividing by the difference of the individual trace maximum and individual trace minimum. (n = 20 embryos).

Quantification of Nuclear Cycle Dynamics

One of the main goals of this research was to investigate the effects of environmental and genetic perturbation on development and, more specifically, Capicua signaling dynamics. In order to provide a basis for the subsequent comparative analysis, we established a library of measurements that describe Capicua dynamics. From the average Cic-Venus fluorescence curves encompassing onset of nuclear cycle 12 to onset of FCM, we quantified the relative timing of developmental milestones in reference to nuclear cycle 11 nuclear division, which included: nuclear cycle 12 Cic-Venus peak (NC12 peak, nuclear cycle 12 nuclear division (NC12 division), nuclear cycle 13 Cic-Venus peak (NC13 peak), nuclear cycle 13 nuclear division (NC13 division), nuclear cycle 14 Cic-Venus peak (NC14 peak), and onset of furrow canal migration (FCM)

(Figure 4.9a). The population average ± standard error of the mean (SEM) were measured as 7.6 ± 0.1 (n = 71 embryos), 12.3 ± 0.1 (n = 71 embryos), 24.5 ± 0.2 (n = 71 embryos), 31.2 ± 0.2 (n = 71 embryos), 54.5 ± 0.5 (n = 70 embryos), and 65.2 ± 0.4 min (n = 66 embryos) for NC12 peak, NC12 division, NC13 peak, NC13 division, NC14 peak, and FCM, respectively. From this data, we also calculated the duration of nuclear cycles 12 and 13, and find the average ± SEM were 12.3 ± 0.1 (n = 71 embryos) and 18.8 ± 0.2 min (n = 73 embryos), respectively (Figure 4.9b). The durations of nuclear cycles 12 and 13 closely match values measured for other *Drosophila* strains using conventional live imaging techniques [136] as well as other microfluidic live imaging formats [121, 175]. Additionally, the measured duration of nuclear cycle 14 onset to FCM of 34.1 ± 0.3 min (n = 68 embryos) correlates well with what is known about furrow canal migration, and together with the measured nuclear cycle durations indicates the homozygous *cic-venus* strain develops at an expected rate within the microfluidic array. The measures made here provide a basis for comparison when investigating the effects of environmental and genetic perturbation on the dynamics of Capicua nucleocytoplasmic transport.

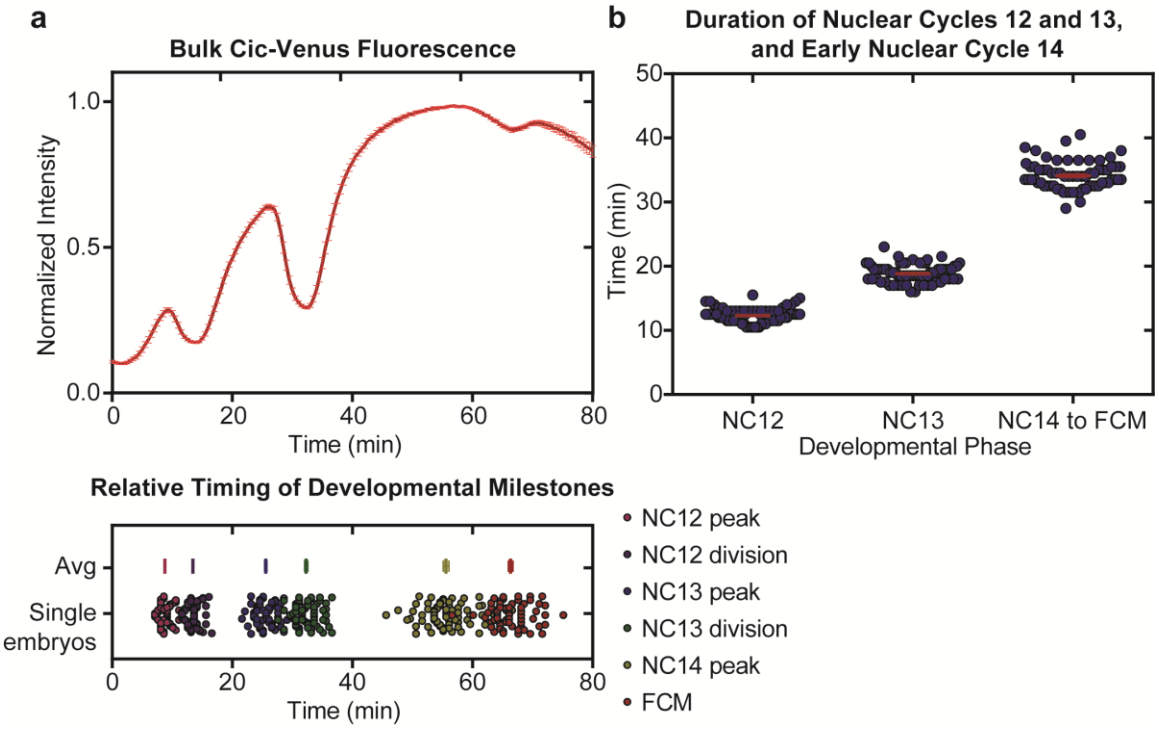

Figure 4.9: Timing of developmental milestones. a) Relative timing of developmental milestones. Top: Average ± SEM average Cic-Venus fluorescence curve from nuclear cycle 11 division to FCM (n = 30 embryos). Bottom: Measured relative timing of developmental milestones for individual embryos with population average ± SEM indicated for nuclear cycle 12 Cic-Venus peak intensity (NC12 peak), nuclear cycle 12 nuclear division (NC12 division, nuclear cycle 13 Cic-Venus peak intensity (NC13 peak), nuclear cycle 13 nuclear division (NC13 division), nuclear cycle 14 Cic-Venus peak intensity (NC14 peak), and furrow canal migration (FCM). Time zero represents nuclear cycle 11 division. Horizontal axes in top and bottom graphs are aligned to illustrate connection between Cic-Venus fluorescence traces and features. b) Quantified durations of nuclear cycles 12 (NC12) and 13 (NC13), and nuclear cycle 14 to onset of furrow canal migration (NC14 to FCM). Red lines represent population averages ± SEM.

Identification and Segmentation of Individual Cells through Time

The features described above quantify overall timing of development within an individual embryo, but do not completely describe Capicua signaling dynamics. We were also interested in quantifying the nucleocytoplasmic shuttling rate of Capicua, and in order to quantify this feature in a meaningful way we needed to analyze individual cells

within an embryo. As described earlier, the average Cic-Venus fluorescence curves ignore cell-to-cell variability, because all locations, both inter- and extra-cellular, within the central 50% of the anterior-posterior axis were averaged together. As a result, the fluorescence intensity in the average Cic-Venus fluorescence curves were not expected to represent a value that is equivalent to the average fluorescence intensity of single cells.

In order to identify single-cell Cic-Venus traces throughout time we referred back to the Cic-Venus spatiotemporal patterning heat-maps constructs in section 4.3.2 of this thesis. Here, I focus on constructing single-cell Cic-Venus traces for nuclear cycle 14. The process started by cropping the heat-map to isolate nuclear cycle 14 (Figure 4.10a). I utilized nuclear division 13 and furrow canal migration as markers to identify the onset of nuclear cycle 14. The relative difference filter developed by Charles Zhao and utilized in chapter 2 of this thesis was implemented here and utilized to segment cell locations within the Cic-Venus spatiotemporal heat-map (Figure 4.10b). Following a similar procedure as utilized in chapter 2, the built-in Matlab function Regionprops was employed to quantify morphological features to describe each segmented objects. The built-in Matlab feature Area, which calculates the number of pixels an object is comprised of, was useful in removing unwanted objects that are easily distinguished from cells based on Area (Figure 4.10c). Additionally, as we are interested in studying single-cell dynamics of cells within the central 50% of the anterior-posterior axis, the built-in Matlab feature Centroid, which identifies the *x*-*y* pixel location of an objects centroid (in this case, *y* represents the anterior-posterior location), unwanted objects outside of this region could also be removed from the analysis based on the Centroid. After these

processing steps, the desired single-cells are properly segmented in a black and white image (Figure 4.10c).

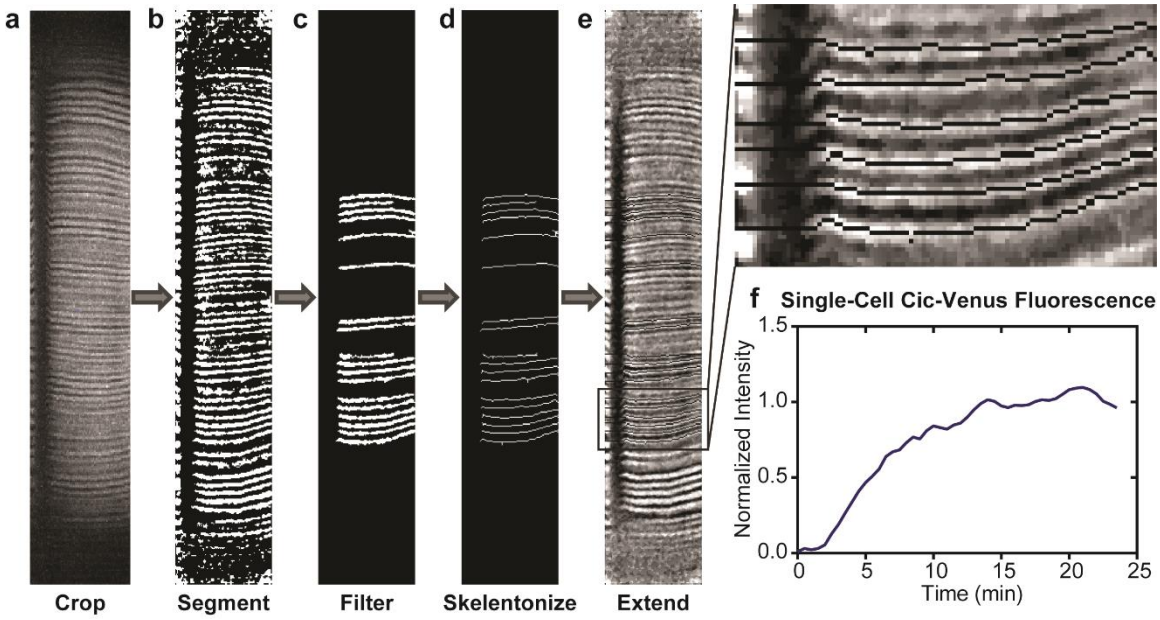

Figure 4.10: Image processing flow chart for measuring single-cell Cic-Venus fluorescence. a) The Cic-Venus spatiotemporal patterning heat-map was cropped to isolate the developmental phase of interest. Time frame to crop was determined based on the average Cic-Venus fluorescence curves. Nuclear cycle 14 is depicted here. b) Cropped image from (a) is segmented using the relative difference filter developed by Charles Zhao. c) Objects in the segmented image from (b) were filtered based on morphological parameters from the built-in Matlab function Regionprops. d) Filtered objects from (c) were skelentonized using Matlab built-in function Bwmorph, and subsequently smoothed. e) Skeletonized objects from (d) are extended forward and backward in time (left and right) to construct full length cell path throughout nuclear cycle 14. f) Sample single-cell Cic-Venus fluorescence trace through nuclear cycle 14.

After individual cells were identified, the next step in the process used the cell location within the Cic-Venus spatiotemporal patterning heat-map to track the cell location through time and anterior-posterior location. In order to do this, the algorithm

first employed the built-in Matlab function Bwmorph, which performs a set of morphological operations, and the morphological operation skel to skelentonize identified cell segments (Figure 4.10d). This was followed by application of custom built smoothing algorithms in order to reduce the skeletonized object to a single pixel in the vertical dimension of the image (i.e. the anterior-posterior location), which represents the center of the cell in space along the anterior-posterior axis.

Last step was to finish constructing cell paths through each nuclear cycle. The previous steps were based on the initial cell segmentation when implementing the relative difference filtering method. This process can only identify cells when Cic-Venus levels are high to provide enough contrast for segmentation. As a result, cells were lost during the division phases when nuclear intensity was at the same level as the cytoplasm. In order to complete the nuclear traces, we simply extended the first identified nuclear region ahead in time and the last identified nuclear region back in time for each cell (Figure 4.10e). Approximating nuclear locations in this manner is based upon the assumption that nuclei do not move significant distances along the anterior-posterior direction.

At this point, the anterior-posterior locations for all identified cells have been identified through time and space, and these paths were used as a mask to evaluate Cic-Venus levels within each nucleus based on intensity. To do this, the algorithm averages over a 5 pixel window centered on the identified cell location for each time point, which corresponds to 4.6 μm in our microscopy setup. At this point in the algorithm, we have established single-cell nuclear levels of Capicua throughout time (Figure 4.10f), which allowed us to quantify features describing Capicua nuclear import.

Quantification of Single-Cell Capicua Nucleocytoplasmic Shuttling Rate

Utilizing the above procedure, we extracted single-cell Cic-Venus traces throughout nuclear cycle 14 for 256 single cells (Figure 4.11a). Single-cell traces were fit to exponential one-phase association equation in order to establish rate and time constants describing single-cell Cic-Venus kinetics in nuclear cycle 14 (Figure 4.11b):

$$I = I_o + (I_{max} - I_o) * (1 - e^{-K*t})$$

where I = intensity at time t, I_o = intensity at time zero, I_{max} = maximum intensity, K = rate constant, and t = time. While fitting the above model to nuclear cycles 13 and 14 well, it became increasingly difficult to adequately fit the equation to nuclear cycle 12. A far majority of single-cell traces failed to converge during model fitting, and is believed to be caused by a combination of low signal-to-noise, and too few experimental data points per cell during nuclear cycle 12. As a result, we limited this analysis to nuclear cycles 13 and 14. In doing so, we measured the average ± standard error of the mean (SEM) for the model rate constant to be 0.207 ± 0.006 and 0.210 ± 0.004 min^{-1} for nuclear cycles 13 and 14, respectively (Figure 4.11c). It was found that the means of the rate constants are not statistically different between nuclear cycles 13 and 14 (Mann-Whitney test, $p>0.05$, n = 244 and n = 256 single-cells for cycles 13 and 14, respectively), which is consistent with what was known about upstream RTK signaling during these phases of development. Specifically, within this region of the embryo, it has been shown that RTK signaling is consistently low through stages 4 and 5 of *Drosophila* embryogenesis [87, 176], and as such provides the expectation that Capicua nucleocytoplasmic shuttling would be unchanging through these phases of development.

Furthermore, we measured the average ± SEM for the model time constant to be 6.0 ± 0.2 and 5.2 ± 0.1 min for nuclear cycles 13 and 14, respectively (Figure 4.11c). It was similarly found that the means of the time constants are not statistically different between nuclear cycles 13 and 14 (Mann-Whitney test, $p>0.05$, n = 244 and n = 256 single-cells for cycles 13 and 14, respectively). This further suggests that nucleocytoplasmic shuttling is unchanging within the central 50% of the anterior-posterior axis through stages 4 and 5 of development. While these differences, or lack thereof, between nuclear cycles are interesting the more significant aspect is these values provide a baseline for comparison when investigating the effects of environmental and genetic perturbation on Capicua dynamics in the following sections.

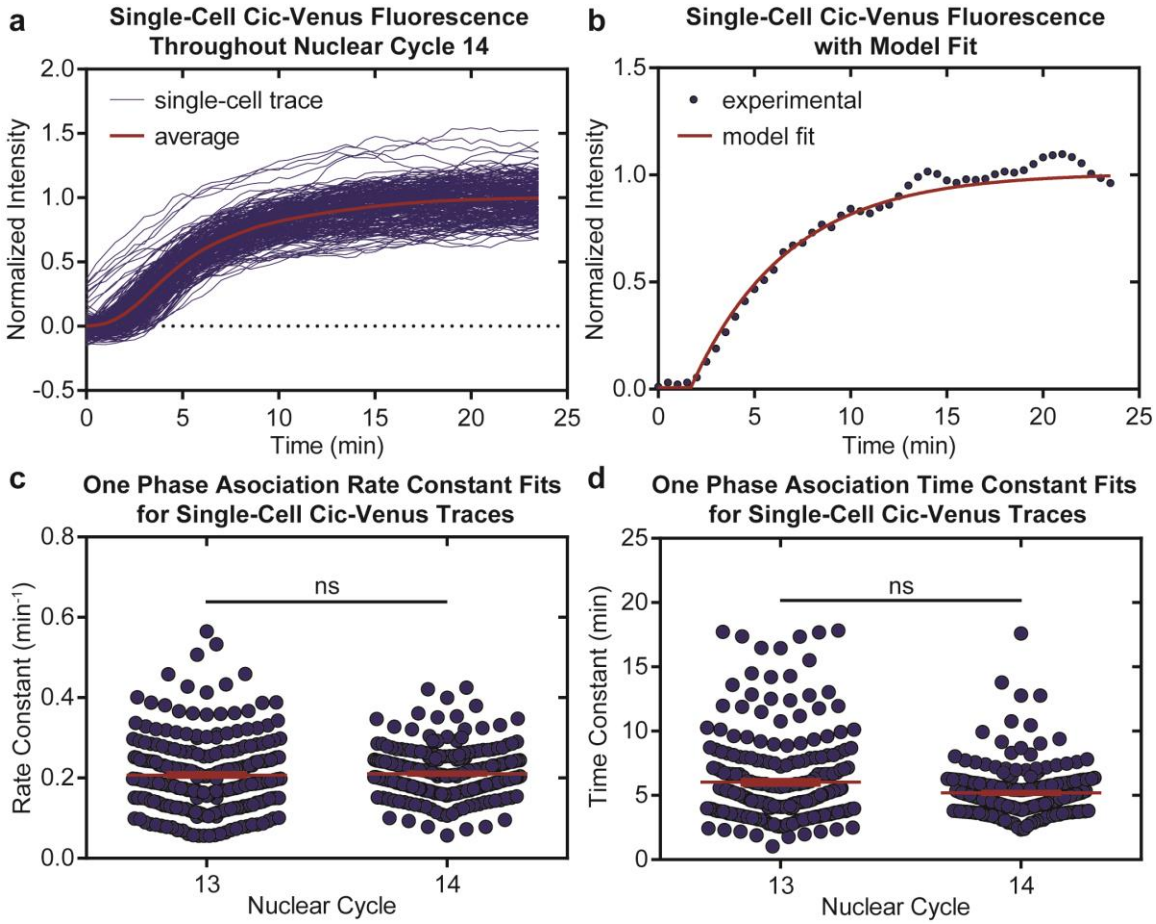

Figure 4.11: Capicua nucleocytoplasmic shuttling kinetics. a) Single-cell Cic-Venus traces for early nuclear cycle 14 (n = 256 single-cells). Blue lines represent single-cell traces and red line represents the population average trace. b) Fitting single-cell Cic-Venus traces to one phase association equation. Blue circles represent experimental trace for a single-cell and red line represents best fit model prediction. c) One phase association rate constant fits for single-cell Cic-Venus traces in nuclear cycles 13 and 14. Blue circles represent single-cell fits and red line represents population average ± SEM. Measured average ± SEM rate constants of 0.207 ± 0.006 and 0.210 ± 0.004 min^{-1} for nuclear cycles 13 and 14, respectively (Mann Whitney test, $p>0.05$, n = 244 and n = 256 single-cells for cycles 13 and 14, respectively). d) One phase association time constant fits for single-cell Cic-Venus traces in nuclear cycles 13 and 14. Blue circles represent single-cell fits and red line represents population average ± SEM. Measured average ± SEM time constants of be 6.0 ± 0.2 and 5.2 ± 0.1 min for nuclear cycles 13 and 14, respectively (Mann Whitney test, $p>0.05$, n = 244 and n = 256 single-cells for cycles 13 and 14, respectively).

4.3.4: Effects of Developmental Dynamics by Culture Temperature

Temperature has long been known as a strong external factor that affects developmental dynamics. Generally, increased temperature results in increased metabolism and increases the rate of development. *Drosophila* embryogenesis has also been shown to be affected by temperature in this way [177]. From this we could establish an expectation for how temperature might affect Cic-Venus dynamics. Therefore, temperature effects served as a model system to establish if our method could adequately quantify differences in Cic-Venus dynamics as the result of a perturbation whether it be environmental (i.e. temperature) or genetic (mutations in RTK-ERK signaling). Regarding temperature effects, we hypothesize that an increase in culture temperature would result in increased Capicua nucleocytoplasmic shuttling rates.

To investigate the effects of temperature on Cic-Venus dynamics we arrayed and imaged *cic-venus* homozygous embryos in a temperature controlled environment at 25, 27.5, and 30 ^{o}C. Utilizing the same processing method as described above, we constructed average Cic-Venus traces from the onset of nuclear cycle 12 to furrow canal migration (FCM) (Figure 4.12a). Population averages were measured and plotted on the same graph for the three temperatures investigated here (Figure 4.12b). Finally, the timing of developmental milestones were extracted from average Cic-Venus fluorescence traces and plotted as a function of temperature (Figure 4.12c). As expected, we observed an overall increase in developmental rates with increasing temperature. Furthermore, while it was observed that the timing of developmental events contracts from 25 to 27.5 to 30 ^{o}C, it was also observed when comparing the timing of developmental events between 25 and 27.5 ^{o}C, and 27.5 and 30 ^{o}C that the relative contraction in event timing decreases. While temperature is generally known to increase developmental rate, this

suggests that temperature will not indefinitely increase developmental rate with indefinite increases in temperature. This is consistent with what was observed by Kuntz et al. when investigating overall timing of *Drosophila* embryogenesis across several temperatures and several *Drosophila* species [177]. While Kuntz et al. focused on timing of morphological changes in embryo development, here we have shown that kinetics of gene patterning follows a similar temperature dependence.

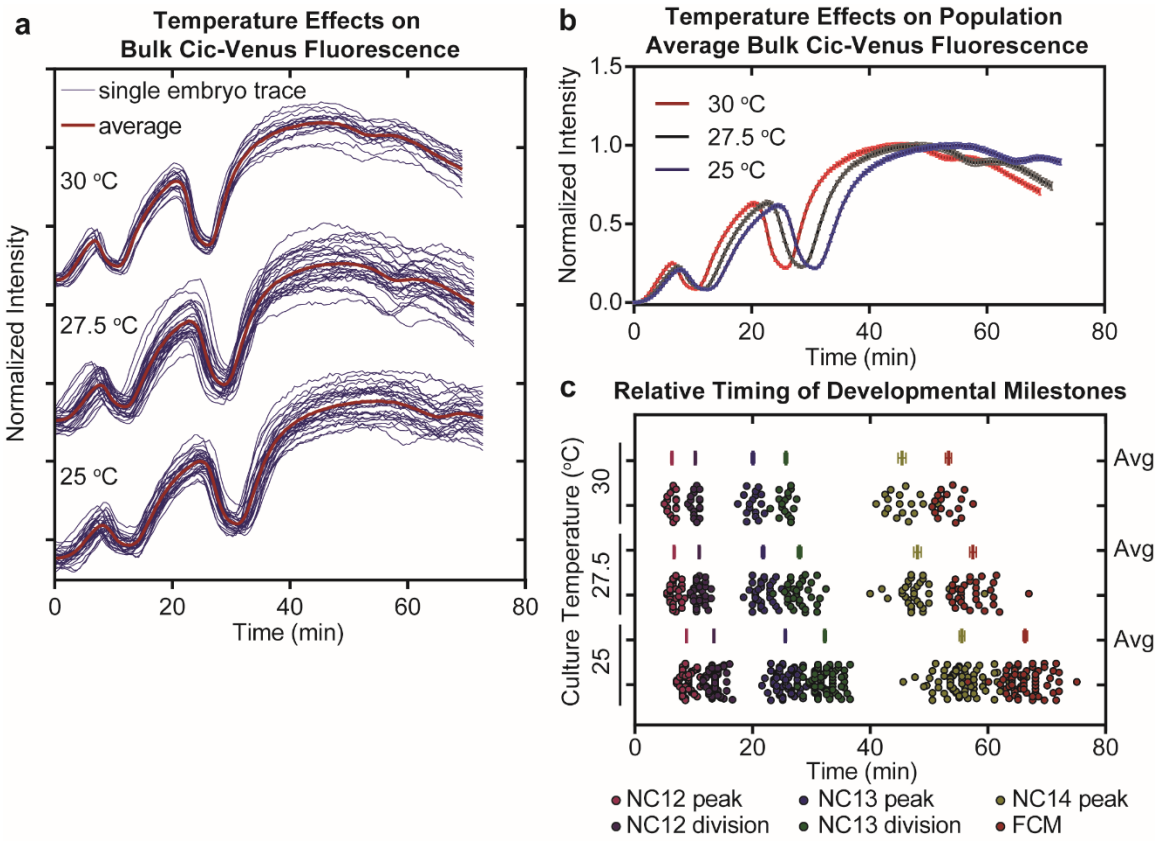

Figure 4.12: Temperature effects on average Capicua dynamics. a) Average Cic-Venus fluorescence through nuclear cycles 12-14 as a function of temperature. n = 30, 32, and 18 embryos for 25, 27.5, and 30 ºC, respectively. Blue lines represent individual embryo traces and redlines represent population average traces. b) Population average average Cic-Venus fluorescence traces from (a). Error bars are standard error of the mean (SEM). c) Relative cumulative timing of Cic-Venus developmental milestones as a function of temperature. Time is relative to the onset of nuclear cycle 12. Milestones include: Cic-Venus peak intensity for nuclear cycle 12 (pink, NC12 peak), nuclear cycle 12 nuclear division (purple, NC12 division), Cic-Venus peak intensity for nuclear cycle 13 (blue, NC13 peak), nuclear cycle 14 nuclear division (green, NC13 division), Cic-Venus peak intensity for nuclear cycle 14 (yellow, NC14 peak), and furrow canal migration (red, FCM). Dots are individual embryos while line and error bars represent average ± SEM.

Uniform Scaling of Nuclear Cycle Kinetics by Rearing Temperature

From this data, we measured the effects of temperature on nuclear cycle duration for nuclear cycles 12, and 13, and the duration for onset of nuclear cycle 14 to furrow

canal migration (FCM) (Figure 4.13). An overall decrease in cycle duration was observed when increasing temperature from 25 to 30 ^{o}C. However, the relative decrease in cycle duration was found to decrease when comparing the differences between 25 and 27.5 ^{o}C with 27.5 and 30 ^{o}C further suggesting the dampening of temperature effects at elevated temperatures. However, the Kruskal-Wallis test with Dunn's multiple comparisons test found the differences between nearly all the cycle durations at the temperatures investigated here to be statistically significant from each other suggesting that for this particular *Drosophila* strain that these developmental phases are still contracting beyond 27.5 ^{o}C (Figure 4.13a). This observation is further confirmed by analyzing the scaled duration for these nuclear cycles, which when tested by the Kruskal-Wallis with Dunn's multiple comparisons test shows that all nuclear cycles tested scale uniformly with temperature increases from 25 to 30 ^{o}C (Figure 4.13b).

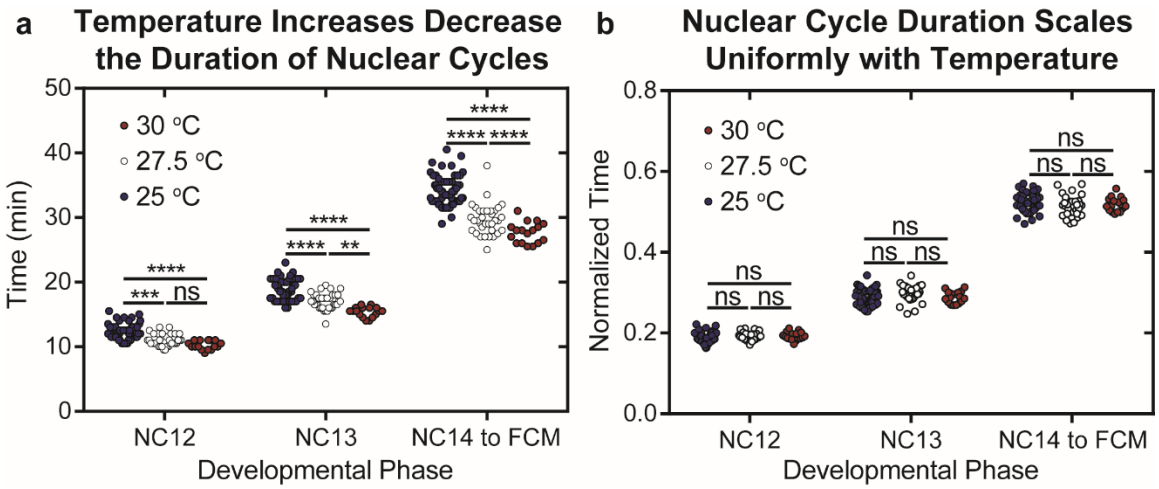

Figure 4.13: Temperature effects on nuclear cycle duration for nuclear cycles 12, 13, and early nuclear cycle 14 encompassing onset of nuclear cycle 14 to furrow canal migration (FCM). a) Measured cycle durations for embryos grown at 25, 27.5 and 30 ºC. b) Measured scaled cycle durations for embryos grown at 25, 27.5, and 30 ºC. Cycle durations are scaled for each embryo by the total duration measured for nuclear cycle 12 onset to FCM. n = 30, 32, and 18 embryos for 25, 27.5, and 30 ºC, respectively. Statistical significance was tested using the Kruskal-Wallis test with Dunn's multiple comparisons test. ****: $p<0.0001$, ***: $p<0.001$, **: $p<0.01$, and ns (not significant): $p>0.05$.

Non-Uniform Scaling of Capicua Nucleocytoplasmic Shuttling by Rearing Temperature

To investigate the effects of temperature on Capicua nucleocytoplasmic shuttling, we utilized the single-cell analysis pipeline described above. Using this method, 512 single-cell Cic-Venus traces were extracted from imaging embryos at 25, 27.5, and 30 ºC for a total of 1536 single-cell measurements (Figure 4.14a and 4.14b). Generally, it was observed that single-cell Cic-Venus traces contracted with increases in temperature for both nuclear cycles investigated here. These shape changes were quantified by fitting experimental data to the one phase association equation (Figure 4.14c and 4.14d).

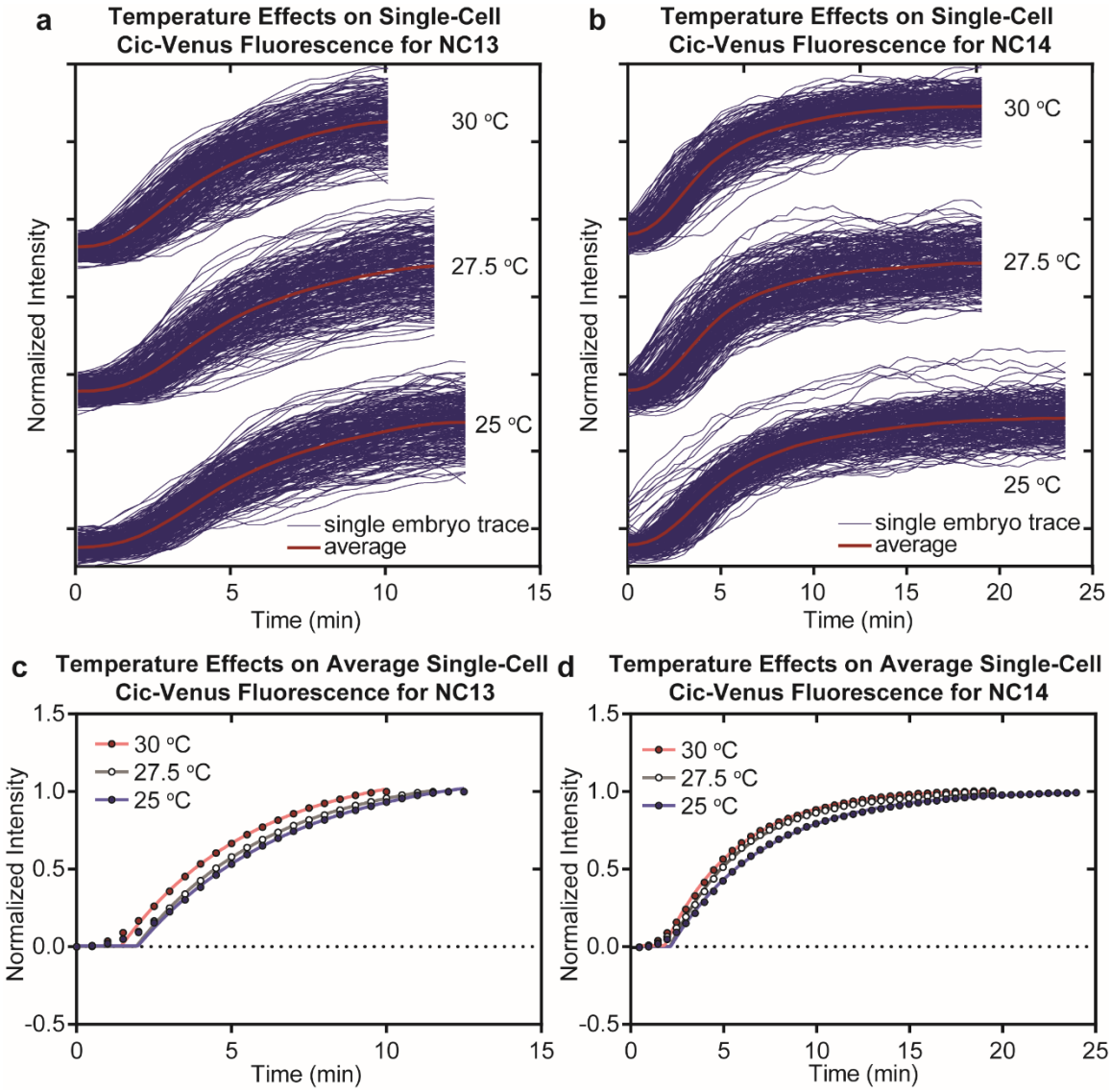

Figure 4.14: Temperature effects on single-cell Capicua dynamics. Single-cell Cic-Venus fluorescence traces through nuclear cycle a) 13 and b) 14 as a function of temperature. n = 256 cells for 25, 27.5, and 30 ºC, respectively. Blue lines represent single-cell traces and red lines represent population average traces. Population average single-cell Cic-Venus fluorescence traces for nuclear cycle c) 13 and d) 14. Dots represent experimental data of population average single-cell Cic-Venus fluorescence while lines represent one phase association model best fits.

The best fit model parameters for both rate and time constants for all single-cell traces within nuclear cycles 13 and 14 for all temperatures are summarized in Figure 4.15. The

observed trends were similar for both nuclear cycle 13 and 14. Specifically, Capicua rate constants increased from 25 to 27.5 ^{o}C and slightly increased/unchanged from 27.5 to 30 ^{o}C (Figure 4.15a and 4.15b). Correspondingly, Capicua time constants decreased from 25 to 27.5 ^{o}C and slightly decreased/unchanged from 27.5 to 30 ^{o}C (Figure 4.15c and 4.15d). These observations further suggest the dampening of temperature effects at elevated temperatures. These observations were further confirmed using the Kruskal-Wallis test with Dunn's multiple comparisons test, which found the differences between 25 and 27.5 ^{o}C were statistically significant ($p<0.01$ for nuclear cycle 13 and $p<0.0001$ for nuclear cycle 14) while the differences between 27.5 and 30 ^{o}C were not statistically significant ($p>0.05$) for all nuclear cycles investigated. This is in contrast to the earlier finding that nuclear cycle dynamics were uniformly scaled by temperature changes between 25 and 30 ^{o}C. Furthermore, this result is in contrast to the earlier expectation regarding temperature effects on Capicua nucleocytoplasmic shuttling. Under the assumption that Capicua transport into the nucleus is purely diffusion, then Capicua nuclear influx would be expected to increase with temperature. However, based on one phase association best fit parameters for the rate constant, which we assume represents Capicua nuclear import rate, increases with temperature, but exhibits dampening at elevated temperatures. This suggests that Capicua transport into the nucleus is either not pure diffusion-based transport or under regulation of a global timer as first suggested by Kuntz et al. [177].

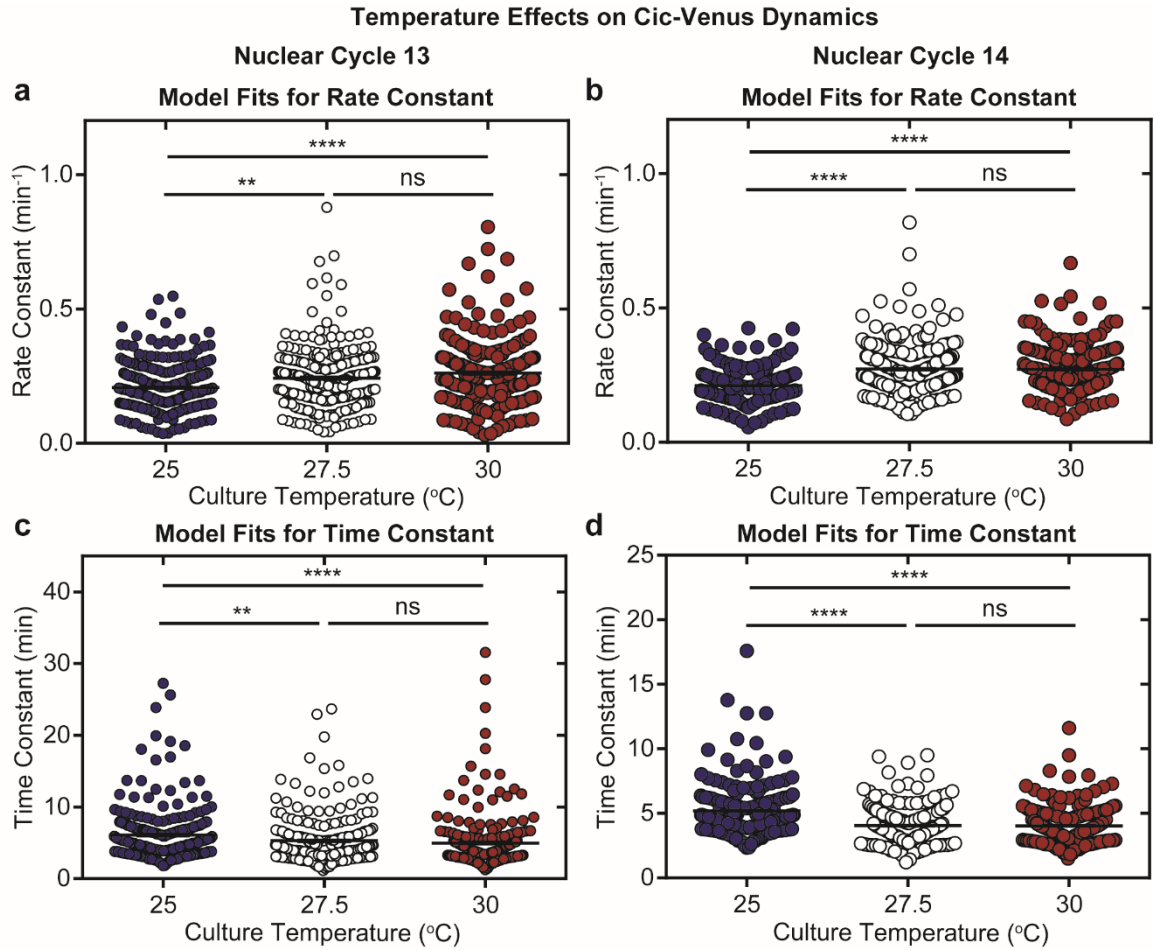

Figure 4.15: Temperature effects on single-cell Cic-Venus one phase association model best fit parameters for nuclear cycles 13 (a and c), and 14 (b and d). n = 256 single-cells for 25, 27.5, and 30 ^{o}C, respectively. Average ± SEM rate constants for nuclear cycle 13: 0.207 ± 0.006, 0.2423 ± 0.007, and 0.261 ± 0.008 min^{-1} at 25, 27.5 and 30 ^{o}C. Average ± SEM rate constants for nuclear cycle 14: 0.210 ± 0.003, 0.272 ± 0.006, and 0.272 ± 0.005 min^{-1} at 25, 27.5 and 30 ^{o}C. Average ± SEM time constants for nuclear cycle 13: 6.1 ± 0.2, 5.3 ± 0.2, and 5.0 ± 0.2 min at 25, 27.5 and 30 ^{o}C. Average ± SEM time constants for nuclear cycle 14: 5.2 ± 0.1, 4.1 ± 0.1, and 4.0 ± 0.1min at 25, 27.5 and 30 ^{o}C. Statistical significance was tested using the Kruskal-Wallis test with Dunn's multiple comparisons test. ****: $p<0.0001$, **:$p<0.01$, and ns (not significant): $p>0.05$.

4.3.5: Effects of RTK Gain-of-Function on Capicua Signaling Dynamics

It is well known the biological systems utilize an array of signaling pathways to transmit messages between and within cells, which are used many times over throughout

development. The RTK-ERK signaling pathway is well-known to be used multiple times throughout development. RTK-ERK signaling is also highly conserved across the animal kingdom from simple organisms such as the fly to highly complex organisms including humans [162-164]. Interestingly, mutations in molecules involved in this signal transduction pathway have been linked to human diseases such as Neurofibromatosis type 1 and Cardio-facio-cutaneous syndrome [171-173]. Consequently, there has been increased interest in understanding how mutations in the RTK-ERK signaling pathway affect development to produce an array of developmental disorders known as RASopathies. The transcriptional repressor Capicua is a well-known target of RTK-ERK signaling in the early *Drosophila* embryo [169]. Here, we were interested in understanding how Capicua spatiotemporal expression patterns and signaling dynamics are affected by mutations in RTK-ERK signaling pathway.

Constitutively Active RTK Differentially Affects Capicua Spatiotemporal Patterning along the Anterior-Posterior Axis

To investigate the effects of RTK-ERK mutations on Cic-Venus dynamics we arrayed and imaged *cicv*/+ (WT), *cicv*/+;tor^{D4021}/+ (TOR), *cicv*/+;MEK^{E203K}/+ (E203K), and *cicv*/+;MEK^{F53S}/+ (F53S) embryos in a temperature controlled environment at 25 ^{o}C. MEK mutants were specifically used in this study, because of the known association of these mutations with human diseases. E203K is associated with human cancers, specifically melanoma, while F53S is associated with human developmental disorders, specifically Cardio-facio-cutaneous syndrome, a RASopathy. Utilizing the same processing method as described above, we constructed Capicua spatiotemporal patterning heat-maps for two hours of embryogenesis centered at nuclear division 13 (Figure 4.16).

In this manner, the constructed heat-maps depict Capicua nuclear localization dynamics through stages 4 (approximately the first hour) and 5 (approximately the second hour) of *Drosophila* embryogenesis. The *cicv/+* embryos follow a similar trend as the *cicv/cicv* embryos utilized in the previous sections; however, with lower absolute intensity, which was expected to accompany the decrease in copy number of the *cic-venus* transgene between the two strains (Figure 4.16a and 4.6). Previous work had shown that the TOR gain-of-function mutation differentially affects RTK-dependent ERK signaling in the early *Drosophila* embryo. Specifically, ERK signaling increases within the anterior-posterior center of the embryo while ERK signaling decreases at both the anterior and posterior pole regions [170]. Based on these observations, one would expect that Capicua nuclear localization would decrease within the central region and increase within the pole regions of the embryo. The spatiotemporal patterning heat-map seems to exhibit this expectation as it appears that Cic-Venus intensity increases within the pole regions of embryo of the *cicv/+;tor*^{D4021}*/+* embryos (Figure 4.16b). This observation is further confirmed by calculating the ratio of the two genotype spatiotemporal heat-maps (Figure 4.16c). The measured Cic-Venus is clearly increased at the poles exhibiting a ratio greater than one and decreased within the central region of the embryo exhibiting a ratio less than one.

The results suggest that the absolute levels of Capicua within nuclei are strongly altered during *Drosophila* embryogenesis. An interesting question would be how changes in the absolute levels of the transcription factor Capicua effects the expression patterns of downstream target genes? One would expect increased/decreased levels of Capicua to have a profound effect on embryo patterning. Interestingly, it appears that Capicua is

more strongly localized at the poles of the embryo throughout stage 5 and much of stage 4 of *Drosophila* embryogenesis suggesting that the effects of this mutation potentially manifest much earlier in development than the stages observed in this study.

The high-dimensionality of the data represented in the Capicua spatiotemporal patterning heatmaps makes it rather difficult to compare Capicua patterning across multiple genotypes. Here we showed a comparison between two genotypes and the goal is to compare with many more. To simply this comparison, we turned to principal component analysis in the next section to reduce the dimensionality of these data sets, and facilitate simple comparisons in Capicua patterning between different genetic backgrounds.

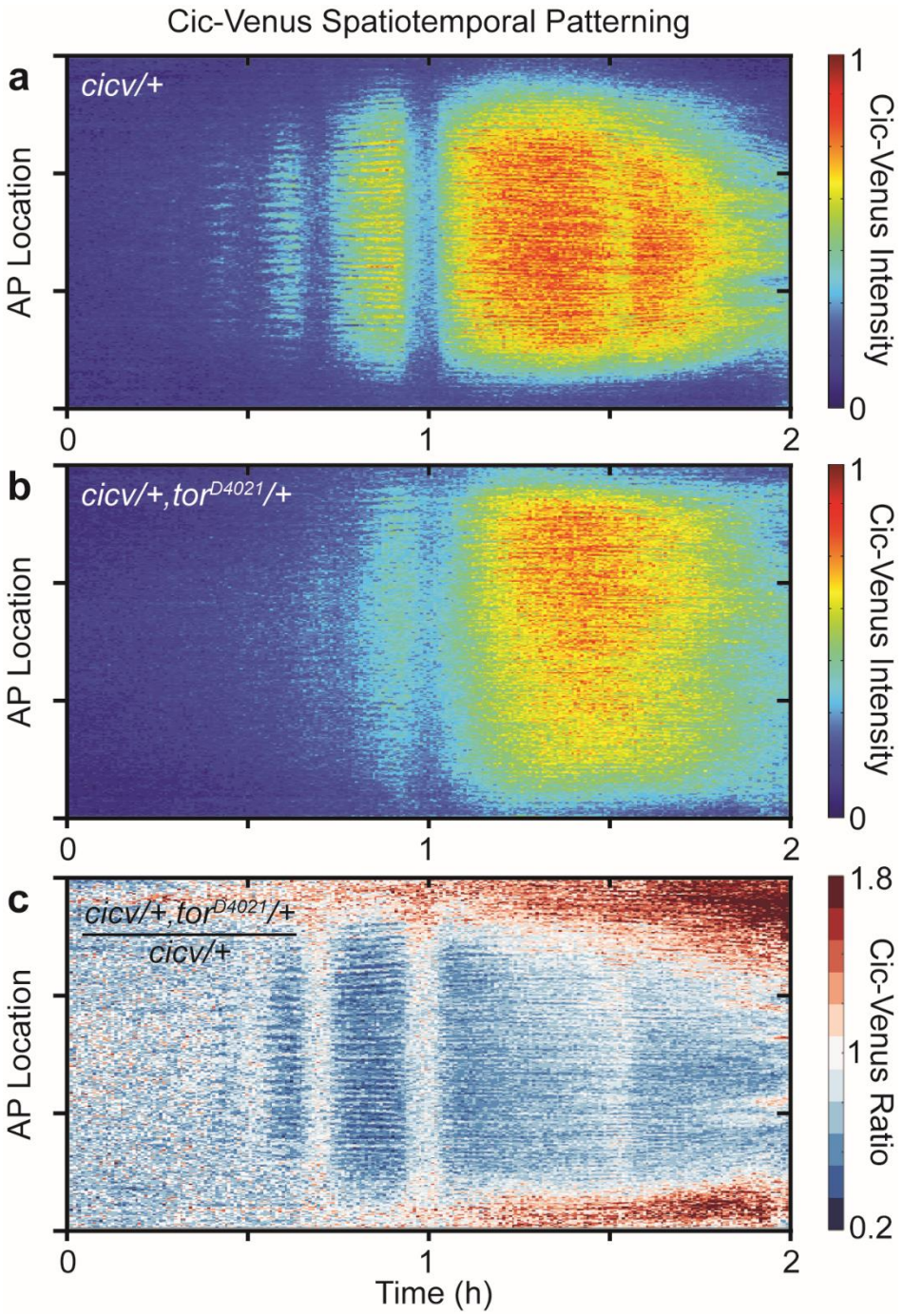

Figure 4.16: Spatiotemporal patterning of Cic-Venus for a) *cicv*/+ (wild-type control), and *cicv*/+,*tor*^{D4021}/+ embryos. Heat-maps are centered at nuclear division 13 (hour 1). Heat-maps are individually normalized to the maximum intensity within the heat-map. Each heat-map is the average of 3 individual embryos. Color represents the normalized Cic-Venus intensity. c) The ratio of the heat-maps found in (a) and (b). Color represents the ratio value, wherein values greater than one indicate higher levels of Capicua in the mutant relative to wild-type, and values less than one indicate lower levels of Capicua in the mutant relative to wild-type.

Dimensionality Reduction to Facilitate Comparative Analysis of Capicua Spatiotemporal Patterning Changes by RTK Gain-of-Function

For simplicity, we utilized principal component analysis in order to reduce the dimensionality of the high-dimensional Capicua space-time dynamics [178]. We hypothesized that the data represented in Figure 4.16a could simply be represented by a small set of spatial modes and time-dependent amplitudes. Furthermore, the spatial modes and time-dependent amplitudes would provide a simple data set to compare the effects of RTK-ERK mutations on Capicua spatiotemporal patterning. Perhaps unsurprisingly, the Capicua spatiotemporal heat-maps data set could be largely reduced to a single principal component wild-type embryos as the first principal component captures greater than 85% of the variance (Figure 4.17a). Each subsequent principal component captures less than 1% of the variance each, suggesting all other principal components capture noise in wild-type Capicua dynamics. The dominant spatial mode appears to represent Capicua anterior-posterior nuclear localization differences (Figure 4.17b). Associated with the dominant spatial modes are time-dependent amplitudes (Figure 4.17c). Strikingly, the time-dependent amplitudes for wild-type embryos closely resembles the average Cic-Venus Fluorescence curves from Figure 4.7. This suggests that the information gathered previously could be captured with principal component analysis without any knowledge about how the system operates *a priori*. Furthermore, the Capicua spatial gradient can be simply represented by two sets of vectors consisting of the single spatial mode and time-dependent amplitudes during stages 4 and 5 of embryogenesis.

This is confirmed by reconstructing Capicua spatiotemporal patterning and comparing to raw heatmaps (Figure 4.17d).

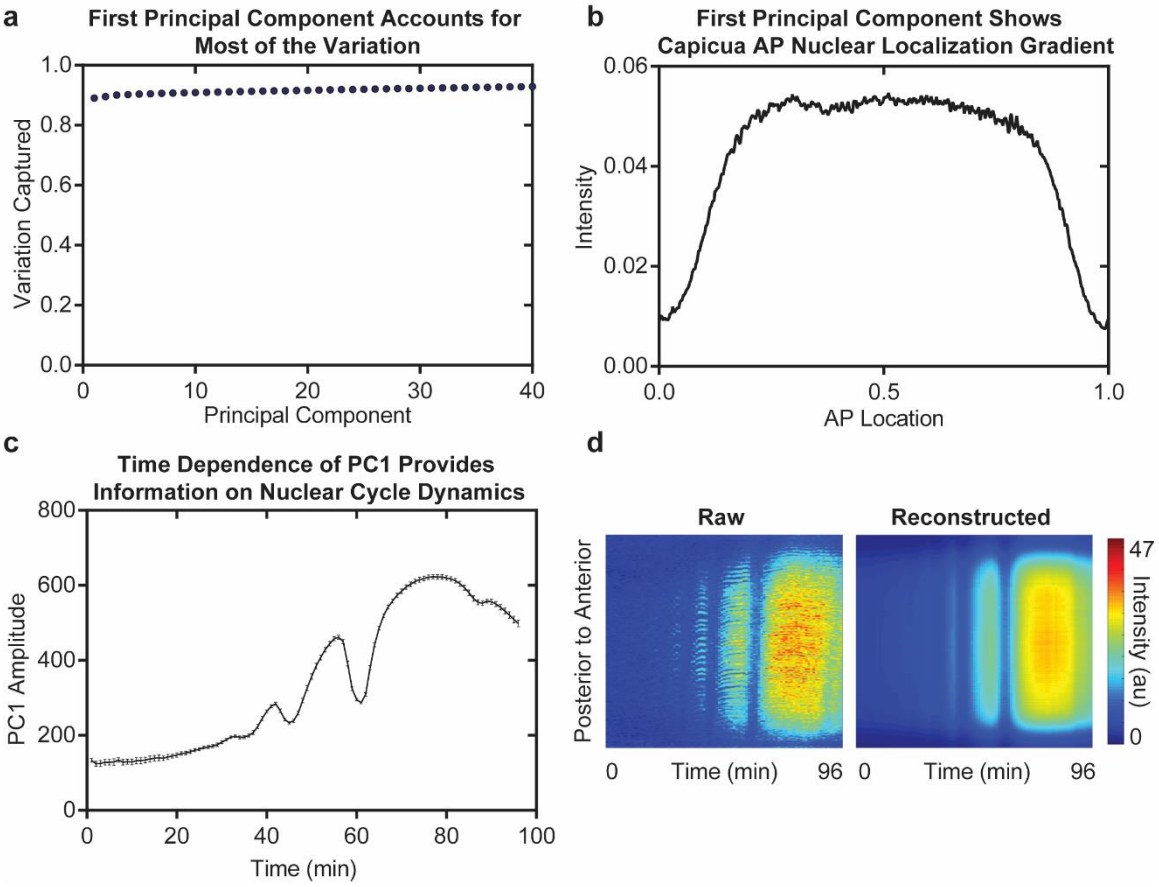

Figure 4.17: Principal Component Analysis of Capicua Spatiotemporal Dynamics. a) Measure of variance captured by the first 40 principal components for *cicv*/+ embryos. b) Dominant spatial modes describing Capicua anterior-posterior nuclear in *cicv*/+ embryos. c) Time-dependent amplitudes of the first principal components for *cicv*/+ embryos. d) Comparing raw Capicua spatiotemporal patterning heatmap for a single WT embryo with the reconstructed Capicua spatiotemporal patterning heatmap using principal component 1 and the associated time-dependent amplitudes.

Capicua anterior-posterior nuclear localization 25 minutes into nuclear cycle 14 is simply reconstructed by scaling the dominant spatial mode by time-dependent amplitude

associated with nuclear cycle 14 peak time (Figure 4.18a). Reconstruction indicates that Capicua signaling within the midbody is dampened between WT, and all other mutant genotype embryos including TOR, E203K, and F53S. Furthermore, Capicua nuclear localization at both the anterior and posterior poles are elevated in TOR, E203K, and F53S embryos. These results are consistent with what we observed in the capicua spatiotemporal heat-maps in Figure 4.16. Reconstruction of Capicua anterior-posterior nuclear localization for all embryos in the data set allowed us to statistical compare Capicua levels within the different regions of embryos between the 4 genotypes (Figure 4.18b). The Kruskal-Wallis with Dunn's multiple comparisons test indicate that Capicua levels are significantly decreased within the embryo midbody, and statistically increased at the poles of the embryo in TOR, E203K, and F53S embryos ($p<0.0001$).

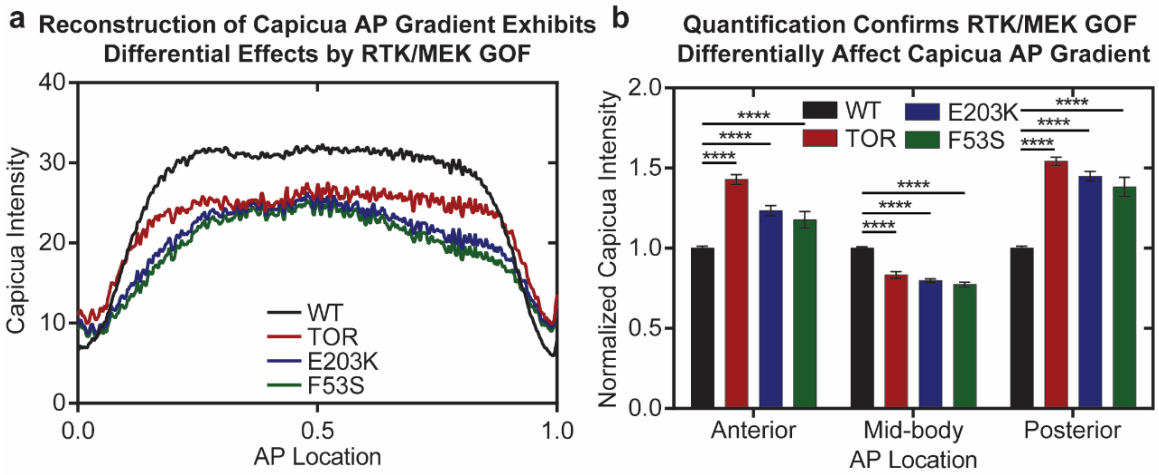

Figure 4.18: Reconstruction and Analysis of Capicua Spatial Patterning. a) Reconstruction of Capicua anterior-posterior nuclear localization 25 minutes into nuclear cycle 14 in wild-type embryos from wild-type principal component one (WT), constitutively active Torso embryos from wild-type principal component one (TOR), hyperactive MEK^{E203K} embryos from wild-type principal component one (E203K), and hyperactive MEK^{F53S} embryos from wild-type principal component one (E203K) embryos. b) Statistical analysis of Capicua levels at the anterior, middle, and posterior regions of WT, TOR, E203K, and F53S embryos. Statistical significance was tested using the Kruskal-Wallis test with Dunn's multiple comparisons test. ****: $p<0.0001$.

Principal component analysis can be utilized to ask how the mutant data gathered here "fits" into wild-type vector space. Simply put, this asks how the time-dependent amplitudes of wild-type principal components scale in order to represent mutant spatiotemporal Capicua dynamics. For example, it is expected that wild-type principal component one amplitudes would be scaled down in order to represent the TOR, E203K, and F53S data sets. This is exactly what happens as principal component one decreases from wild-type to TOR, E203K, and F53S embryos. While principal components beyond principal component one appears to represent noise in the wild-type data set, there is potential that these lower level principal components might have true meaning in other genetic backgrounds. For example, spatial mode two is significantly increased in TOR

embryos (Figure 4.19a). Visual inspection indicates that the wild-type spatial mode two captures differences in Capicua nuclear localization along the anterior-posterior axis (Figure 4.19b). Wild-type Capicua gradient is not expected to show significant anterior-posterior differences as the Capicua gradient exhibits high symmetry along the anterior-posterior axis. As a result, principal component two accounts for less than 1% of the variation in wild-type data, and also exhibits a mean value near zero further suggesting a strong symmetry along the anterior-posterior axis in wild-type embryos. However, in order to represent Torso gain-of-function data, wild-type principal component two magnitude increases, and exhibits a non-zero mean. This, together with the spatial mode, suggests Torso gain-of-function embryos exhibit a strong anterior to posterior asymmetry with elevated levels occurring more anteriorly. We know this to be the case, but the significance of this application of PCA is this information can be acquired without any knowledge of the details regarding Torso gain-of-function embryo data *a priori*.

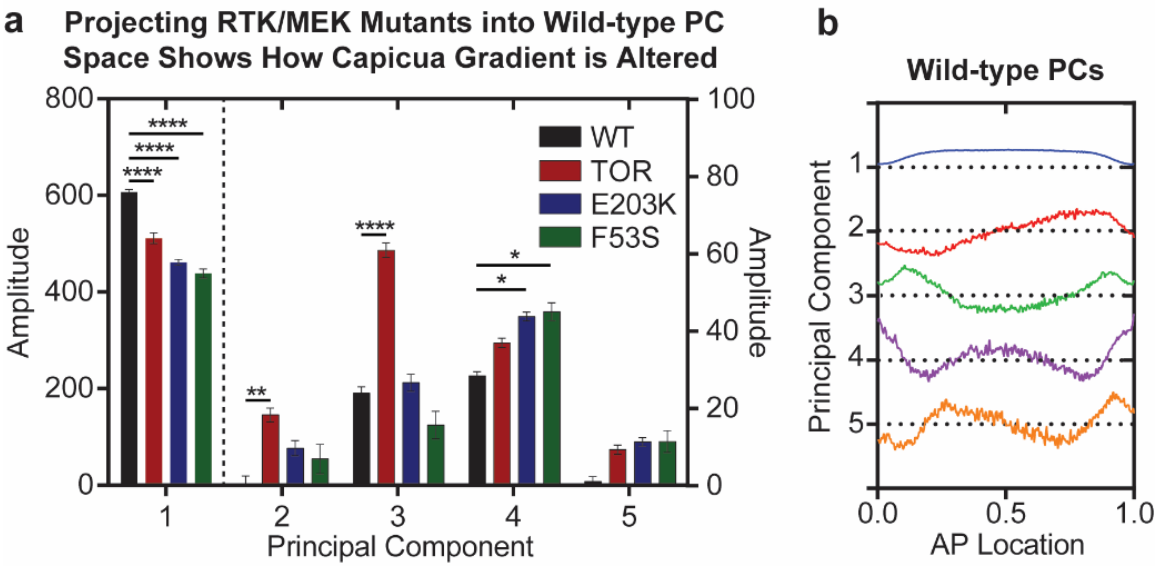

Figure 4.19: Projection of TOR, E203K, and F53S data sets into wild-type vector space. a) Normalized changes in wild-type principal components 1-5 from representing wild-type embryos (black), Torso gain-of-function embryos (red), hyperactive MEK^{E203K} embryos (blue), and hyperactive MEK^{F53S} embryos (green). b) Wild-type spatial modes one through five. Statistical significance was tested using the Kruskal-Wallis test with Dunn's multiple comparisons test. ****: $p<0.0001$.

Previous work showed that the same Torso gain-of-function mutation used in this study surprisingly resulted in increased extracellular regulated kinase (ERK) signaling within the anterior-posterior middle, but decreased ERK signaling at the poles as assayed by dpERK antibody staining [170]. Here, I used *in vivo* live imaging and found that the downstream target, Capicua, exhibits the exact expected result in all three regions of the embryo based on what was known to occur to upstream ERK signaling. Important to note here, is our approach of *in vivo* live imaging could be executed and analyzed within 1 day, whereas the antibody staining-based approached used in previous work would require 4-5 days to execute and analyze; highlighting the significance of the methods I have developed throughout this thesis. Furthermore, inherent to the technique used in this

thesis, I can collect data that is simply not possible using antibody staining-based approaches. Specifically, in the next section I investigated the effects of RTK gain-of-function on Capicua nucleocytoplasmic shuttling rates.

RTK Gain-of-Function Decreases Capicua Nucleocytoplasmic Shuttling at Midbody

To investigate the effects of upstream mutations in RTK-ERK signaling on Capicua nucleocytoplasmic shuttling, we utilized the single-cell analysis pipeline described above. Using this method, 235, 234, 248, and 236 single-cell Cic-Venus traces at the onset of nuclear cycle 14 were extracted from imaging WT, TOR, E203K, and F53S embryos at 25 ^{o}C for a total of 953 single-cell measurements (Figure 4.20a). Population average traces for quantified for each genotype and plotted together for simple visual comparison (Figure 4.20b). Generally, it was observed that single-cell Cic-Venus traces became prolonged in the RTK gain-of-function mutation embryos. This is most evident when one compares the population average trace wherein TOR, E203K, and F53S embryos reach peak Cic-Venus intensity approximately 5 min after wild-type embryos (Figure 4.20b). These shape changes were quantified by fitting experimental data to the exponential model equation described previously.

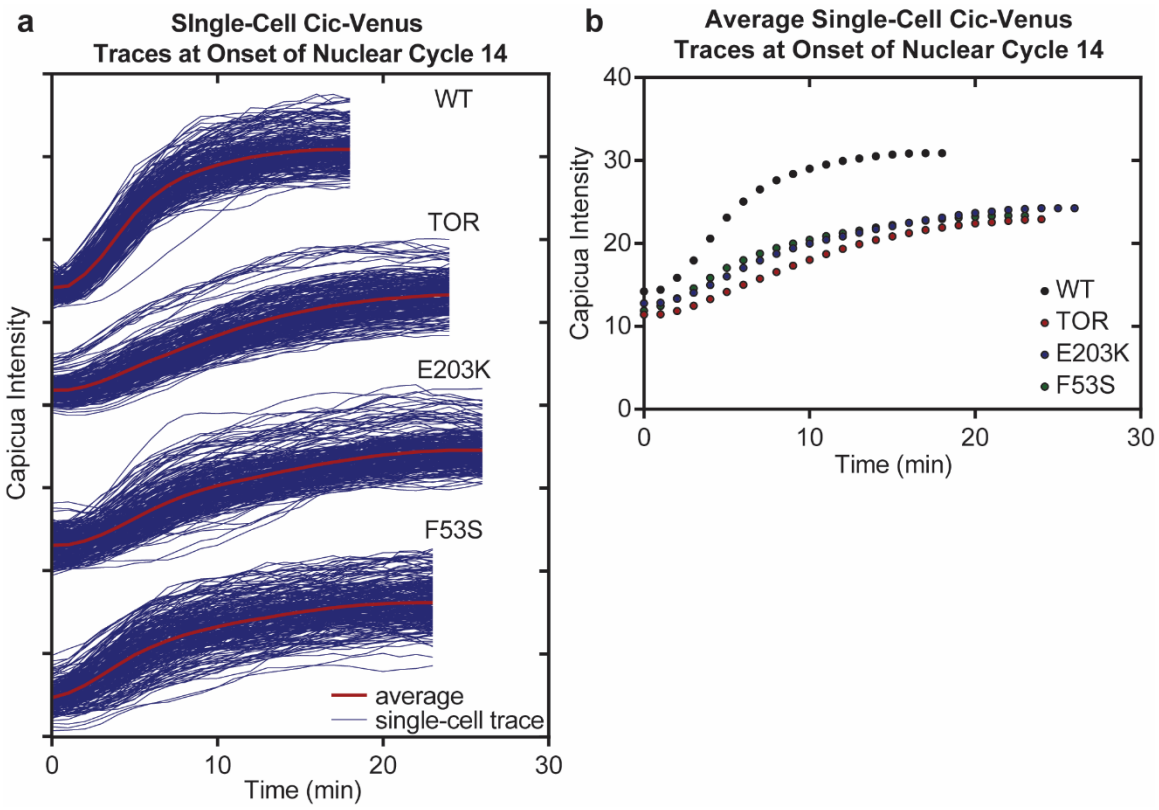

Figure 4.20: RTK and MEK gain-of-function effects on single-cell Capicua dynamics. a) Single-cell Cic-Venus fluorescence traces through nuclear cycle 14. n = 235, 234, 248, and 236 single-cells for WT, TOR, E203K, and F53S embryos, respectively. Blue lines represent single-cell traces and redlines represent population average traces. b) Population average ± SEM single-cell Cic-Venus fluorescence traces for nuclear cycle 14.

The best fit model parameters for both rate and time constants for all single-cell traces within nuclear cycle 14 for all genotypes investigated are summarized in Figure 4.21. It was observed that Capicua rate constants decreased from wild-type embryos to TOR, E203K, and F53S embryos (Figure 4.21a). Correspondingly, Capicua time constants increased from wild-type embryos to TOR, E203K, and F53S embryos (Figure 4.21b). For TOR embryos, these observations are consistent with what was previously known about how constitutively active Torso affects Capicua nucleocytoplasmic partitioning

[170]. Furthermore, we confirmed the significance of these measurements by using the Kruskal-Wallis test with Dunn's multiple comparisons test, which found the differences between WT embryos and all mutant embryos to be statistically significant ($p<0.0001$). Importantly, it was also found that the differences between homozygous and heterozygous Cic-Venus (i.e. *cicv/cicv* and *cicv/+*) embryos were not statistically significant ($p>0.05$) indicating that our method for measuring Capicua kinetics is not affected by absolute levels of Cic-Venus. This result indicates that the observed differences between wild-type embryos and embryos expressing the RTK gain-of-function mutations are not an artifact of inherent differences of absolute levels of Cic-Venus. These results suggest that the TOR, E203K, and F53S mutations studied in this thesis affect both the absolute levels and temporal kinetics of the transcription factor Capicua. The downstream consequences of the observed changes in Capicua spatiotemporal patterning, and decoupling the concentration and kinetic effects is an interesting future direction for this study.

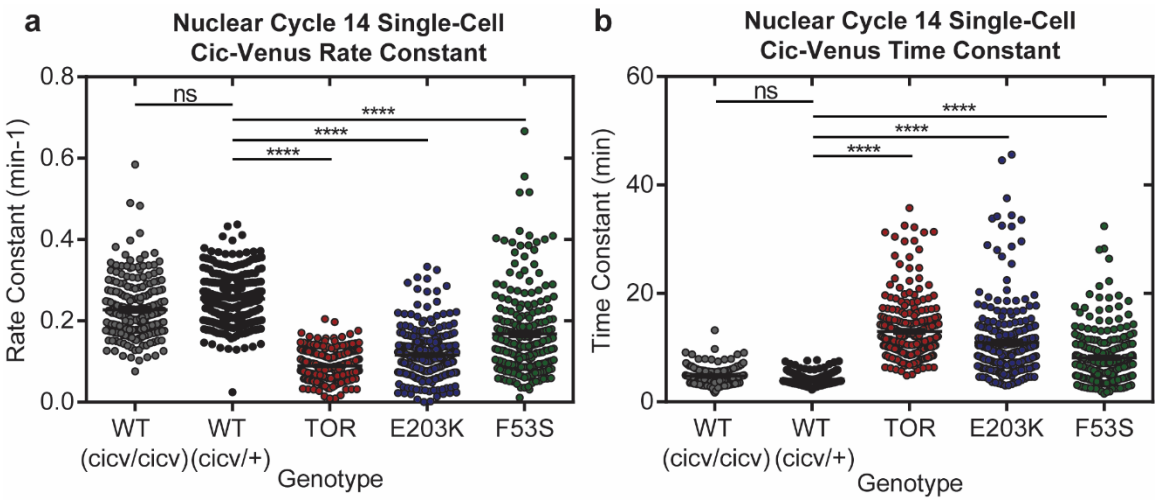

Figure 4.21: RTK gain-of-function effects on Capicua one phase association model best fit parameters for nuclear cycle 14. Average ± SEM rate constants: 0.227 ± 0.004, 0.253 ± 0.004, 0.089 ± 0.002, 0.116 ± 0.004, and 0.168 ± 0.007 min^{-1} for *cicv/cicv*, *cicv/+*, TOR, E203K, and F53S embryos, respectively. Average ± SEM time constants: 4.8 ± 0.1, 4.2 ± 0.1, 13.0 ± 0.4, 10.9 ± 0.4, and 8.1 ± 0.3 min^{-1} for *cicv/cicv*, *cicv/+*, TOR, E203K, and F53S embryos, respectively. Statistical significance was tested using the Kruskal-Wallis test with Dunn's multiple comparisons test. ****: $p<0.0001$, and ns (not significant): $p>0.05$. n = 256, 235, 234, 248, and 236 single-cells for *cicv/cicv*, *cicv/+*, TOR, E203K, and F53S embryos, respectively.

RTK Gain-of-Function Increases Variability of Capicua Nucleocytoplasmic Shuttling

To investigate the effects of RTK-ERK mutations on the variability of downstream Capicua kinetics, I quantified coefficients of variation for both measured Capicua rate and time constants during nuclear cycle 14. Coefficient of variation was calculated two ways in order to assess intra-embryo variability as well as inter-embryo variability. Specifically, intra-embryo variability refers to variation in single-cell measurements within a given embryo while inter-embryo variability refers to variation in average embryo measurements within a population. It was observed that intra-embryo variability increased from wild-type embryos to embryos possessing the RTK gain-of-

function mutation for the best fit rate and time constants of Capicua nuclear transport kinetics (Figure 4.22a and 4.22b). The differences were found to be statistically significant based upon the Mann-Whitney test for the rate constant ($p<0.01$) and time constant ($p<0.0001$). Moreover, it was observed that inter-embryo variability increased from wild-type embryos to embryos possessing the RTK gain-of-function mutation for the best fit rate and time constants (Figure 4.22c and 4.22d). The differences were found to be statistically significant based upon the Mann-Whitney test for both rate and time constants ($p<0.05$). These results suggest that the Torso gain-of-function mutation increases the variability of Capicua transport kinetics within a given embryo as well as across a population of embryos when one compares these values for those of wild-type embryos. One could ask: What are the consequences of the observed increase in the variability of Capicua dynamics? How does the increased variability of Capicua dynamics affect downstream gene expression patterns? Are the patterns affected in space and/or time? Is the variability of the patterns affected? Answers to these questions would provide insight to feedback/feedforward mechanisms regulating this gene network. Such feedback/feedforward mechanisms are known to be used throughout development, and findings regarding this system could be widely applicable to other gene networks within *Drosophila* and higher organisms including humans.

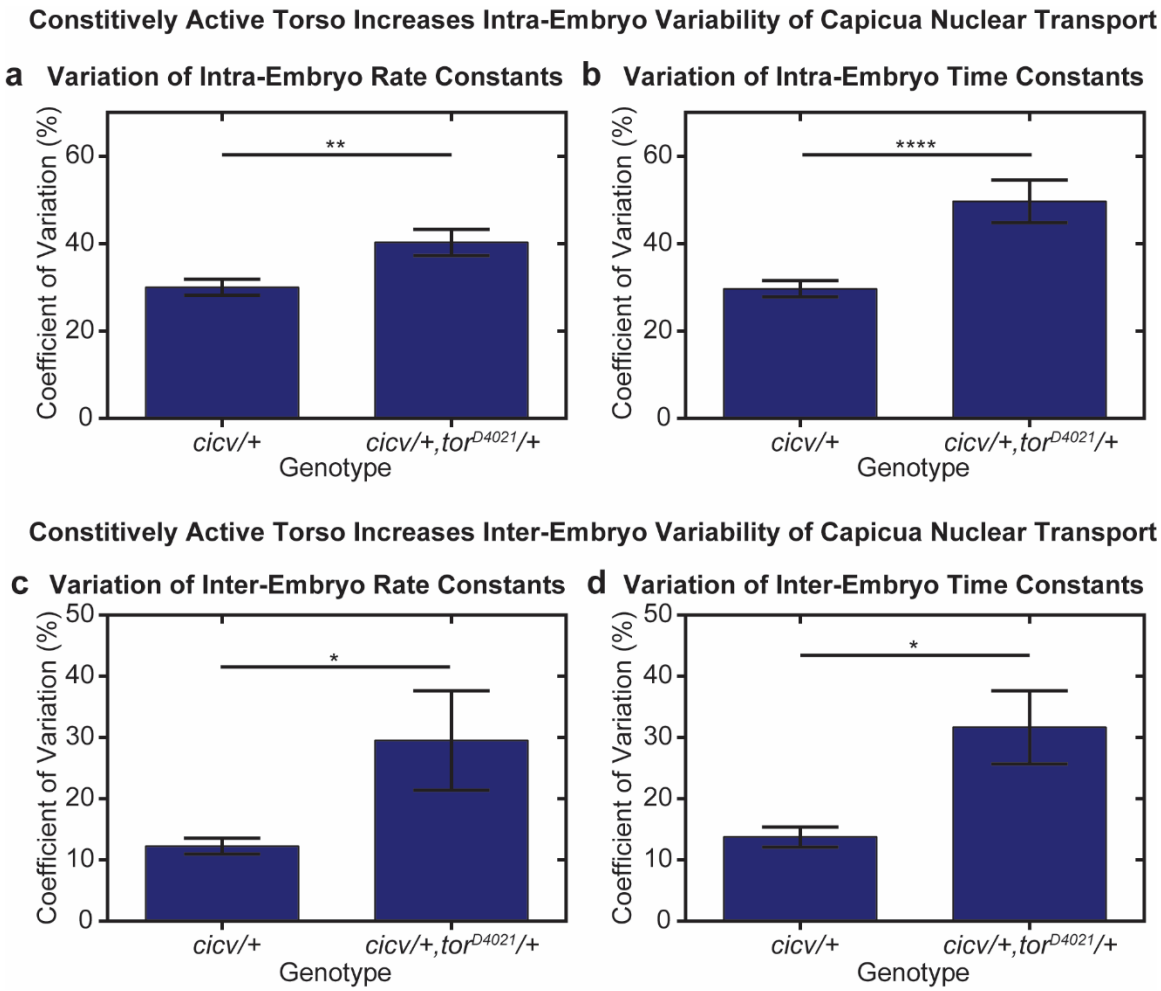

Figure 4.22: Intra- and inter-embryo variability of Capicua nuclear transport. Intra-embryo variation of one phase association model best fit a) rate constant and b) time constant parameters for *cicv*/+, and *cicv*/+;*tor*^{D4021}/+ embryos. Error bars are SEM. n = 27 and 31 embryos for *cicv*/+, and *cicv*/+;*tor*^{D4021}/+, respectively. Statistical significance was tested using the Mann-Whitney test. ****: $p<0.0001$, and **: $p<0.01$. Inter-embryo variation of one phase association model best fit c) rate constant and d) time constant parameters for *cicv*/+, and *cicv*/+;*tor*^{D4021}/+ embryos. Error bars are SEM. n = 4 and 6 experiments for *cicv*/+, and *cicv*/+;*tor*^{D4021}/+, respectively. Statistical significance was tested using the Mann-Whitney test. *: $p<0.05$.

4.4: Conclusion

In this chapter, I developed microfluidic and computer vision-based tools to address some of technological gaps that currently limit the ability to collect large-scale,

quantitative intercellular signaling dynamics during embryogenesis. Specifically, I engineered an optimized microfluidic chip that is capable of rapidly arraying live *Drosophila* embryos for parallelized imaging of anterior-posterior (AP) development at the embryo midsection. The development of the so-called AP2 array improved upon conventional, time-consuming techniques used to prepare live *Drosophila* embryos for time-lapse microscopy. The ability to collect large-scale imaging data made it necessary to rapidly analyze imaging data sets in order to prevent data analysis from bottlenecking this process. Therefore, to complement the AP2 array, I developed an image processing and analysis pipeline for the automatic and unbiased measurements of dynamic intercellular phenotypes during *Drosophila* embryogenesis. The integrated platform consisting of the microfluidic device and image processing software was used with fluorescence confocal microscopy to quantitatively measure spatiotemporal patterns of the transcription factor Capicua within the *Drosophila* blastoderm. The data obtained here provided detailed information regarding the nuclear localization gradient of Capicua along the anterior-posterior axis throughout early embryogenesis.

Using the tools I developed, I investigated the effects of environmental and genetic perturbations on Capicua dynamics. Specifically, we were interested in understanding how temperature affected Capicua dynamics. Consistent with previous work, we found that the timing of developmental phases scales uniformly with temperature. However, Capicua nuclear transport did not exhibit uniform scaling across the temperatures investigated in this thesis. We found that Capicua obtained a maximal nuclear import rate at 27.5 ^{o}C with no further increase in import rate with increased temperature. This suggests that Capicua transport is not a pure diffusion-based problem,

or under the regulation of a previously proposed global timer. The discontinuity between uniform scaling of developmental timing and non-uniform scaling of Capicua transport regarding temperature effects suggests these two phenomena are not under control of a single regulator.

Additionally, we were interested in understanding how mutations in upstream RTK-ERK signaling affected Capicua dynamics. We quantitatively assessed and found that RTK-MEK gain-of-function mutations differentially affected the Capicua nuclear localization gradient along the anterior-posterior axis. Furthermore, we found that these mutations affected Capicua nuclear localization throughout stages 4 and 5 of embryogenesis, which suggests the effects of these mutations actually manifest earlier than the stages of development investigated in this thesis. Consistent with previous work, we found that RTK gain-of-function affected the kinetics of Capicua nucleocytoplasmic shuttling, wherein Capicua nuclear import was significantly decreased from wild-type embryos within the midbody of the embryo. However, the tools I developed and used here allowed large-scale data collection and quantitative analysis of these dynamic phenotypes. In addition, we found that mutations investigated here produced increased variability within single-embryos and across a population of embryos in terms of Capicua kinetics. This information could provide insight to the feedback/feedforward genetic networks used in this system to produce the spatiotemporal patterns of Capicua and downstream target genes.

The tools developed in this chapter were designed for simplicity in order to facilitate rapid adoption of this technology by non-specialists. (1) The microfluidic device was designed with a single inlet and outlet, and no active parts; (2) positive pressure

necessary to deliver embryos to the device can be simply provided by a thumb-driven syringe; (3) the analysis algorithm developed in this chapter was designed for ease as well. Specifically, the algorithm constructs a spatiotemporal map of gene expression that is simply segmented to identify cell locations throughout time and space. In general, the simplicity of the developed tools allow this system to be highly generalizable, which can be applied to other developmental systems including, for example, zebrafish and *C. elegans*, thereby increasing the potential impact these technologies have throughout biology.

CHAPTER 5: CONCLUSION

5.1: Thesis Contributions

This thesis provides both biological and engineering contributions to the fields of microfluidics, image processing, and developmental biology. These contributions were designed to address the experimental challenges that limit the throughput of *in vivo* live imaging of *Drosophila* embryos during early embryogenesis. Specifically, I developed a platform for large-scale imaging of the dorsal-ventral plane, providing environmental perturbation, and analyzing *Drosophila* embryogenesis (chapter 2). To improve information content of imaging data, I developed a microfluidic device for highly parallelized imaging of the anterior-posterior plane in live *Drosophila* embryos (chapter 3). And finally, I further developed the microfluidic- and computer vision-based technologies I developed in chapters 2 and 3 to enable statistical comparison of intercellular phenotypes during *Drosophila* embryogenesis in response to environmental and genetic perturbation (chapter 4). In addition to engineering enabling technologies, this thesis demonstrates the power of integrated microsystems by studying a variety of biological problems and providing new insight to embryo development in general and developmental responses to genetic and environmental perturbation. Furthermore, the microfluidic technologies that arose from the work described in this thesis have been distributed and used by non-specialists, thereby exemplifying the potential impact that this thesis presents.

In chapter 2, I developed a platform that integrates microfluidics, automated image processing, and data extraction for high-throughput studies of normal developmental processes and responses to environmental perturbations. This system is capable of rapid delivery of external stimuli to arrayed, live embryos for continuous *in vivo* live imaging. To our knowledge, no such technology existed prior to this thesis for the specific application of studying the developmental responses of *Drosophila* embryos. I also developed automated image processing and data extraction algorithms to quantitatively measure developmental responses of *Drosophila* embryos to dynamic environmental stimuli. The large-scale data that I was able to collect and analyze with these technologies provided insight to differential response dynamics of individual embryos to anoxic environments. Specifically, our data suggested that the early *Drosophila* embryo is sensitive to anoxia-induced developmental arrest in a cell cycle specific manner, wherein interphase cell states tolerate anoxia-induced development arrest more readily than division phase cell states including, more specifically, metaphase. We proposed the differential sensitivity of interphase vs. metaphase nuclei to anoxia-induced developmental arrest can account for observed differences in embryo viability post-anoxia treatment.

In chapter 3, I developed a microfluidic device for high-throughput arraying of lateral oriented live *Drosophila* embryos for massively parallel time-lapse microscopy. To our knowledge, no such technology existed prior to this thesis that could rapidly array *Drosophila* embryos for high-throughput microscopy of the anterior-posterior axis (AP1 array). I showed that the AP1 array can be used to look at many stages of *Drosophila* embryogenesis when performing long term imaging. The method of high-throughput

microscopy allowed me to collect large-scale imaging data in order to quantitatively assess developmental dynamics within the early *Drosophila* embryo. I specifically used the AP1 array to quantitatively assess mitotic wave-front dynamics, and found that a majority of embryos exhibit two simultaneously propagating mitotic wave-fronts that initiate at both the anterior and posterior poles of the embryo, while a portion of the population exhibit a single mitotic wave-front that initiates at either the anterior or the posterior pole. Consistent with previous work, I showed that mitotic wave-front speed decreases throughout stage 4 of *Drosophila* embryogenesis. The large-scale data I collected showed that individual embryo measurements of mitotic wave-front speed show significant variability that can account for the differences in mitotic wave-front reported in the literature. Furthermore, I for the first time showed that mitotic wave-front speed is independent of the number of mitotic wave-fronts observed throughout stage 4 of *Drosophila* embryogenesis. From my data, we proposed that the mechanism governing mitotic wave-front propagation is utilized in both embryos exhibiting a single mitotic wave-front and two mitotic wave-fronts.

In chapter 4, I developed microfluidic and computer vision-based tools to address some of technological gaps that currently limit the ability to collect large-scale, quantitative intercellular signaling dynamics in embryogenesis. To complement the AP2 array, I developed an image processing and analysis pipeline for the automatic and unbiased measurements of dynamic intercellular phenotypes during *Drosophila* embryogenesis. The integrated platform consisting of the microfluidic device and image processing software was used to quantitatively measure spatiotemporal patterns of the transcription factor Capicua within the *Drosophila* blastoderm. The data obtained here

provided detailed information regarding the nuclear localization gradient of Capicua along the anterior-posterior axis throughout early embryogenesis. Furthermore, the system allowed for rapid experimentation to investigate the effects of temperature as well as genetic mutations in upstream signaling pathways on Capicua signaling. The integrated microsystem allowed for large-scale data collection that showed, for the first time, that *Drosophila* embryogenesis scales uniformly with temperature, but intercellular signaling dynamics scales non-uniformly with temperature. Furthermore, genetic mutations in the highly conserved RTK-ERK signaling pathway more strongly affects downstream signaling of nuclear factors relative to temperature effects. The biological data collected in chapter 4 lays the groundwork necessary for mechanistic studies aimed at uncovering the effects of RTK-ERK mutations and the manifestation of RTK-ERK-related developmental disorders.

The goal of this thesis was to develop technologies that could broadly impact experimental data collection and analysis throughout biology. While I developed a variety of tools that incorporated microfluidic and computer-vision-based technologies, the prevailing concept throughout all the tools developed here was “simplicity”. Simplicity is what I believe to be the key to developing enabling technologies throughout many different fields of research. Simplicity is what allows technologies to be successfully used by non-specialists in a short time frame. The microfluidic technologies developed in this thesis employed simple designs to efficiently trap live *Drosophila* embryos for rapid time-lapse microscopy. The image analysis algorithms developed in this thesis utilized simple approaches to automatically identify single-cells in space and track through time. The simplicity of the developed approaches should also enable these

technologies to be easily adapted to other developmental systems. These goals have been successfully achieved at it should be noted that these technologies have been distributed and utilized by non-specialists from other academic institutions throughout this thesis.

5.2: Future Directions

The previous section summarized the significant impacts the microfluidic and computer-vision-based technologies that I developed in this thesis has already had in understanding a variety of developmental phenomena found in *Drosophila* embryogenesis. Specifically, these technologies facilitated quantitative studies of anoxia-induced developmental arrest and recovery, mitotic wave-front propagation dynamics, and developmental signaling kinetics. More generally, I developed microfluidic and computer-vision-based technologies that enable high-throughput *in vivo* live imaging and quantitative analysis. Many studies throughout biological research depend upon the ability to gather *in vivo* imaging data with subsequent analysis and interpretation. Therefore, it is my hope that the studies in this thesis merely represent the tip of the iceberg for the studies that could benefit from the technologies developed in this thesis.

Improvements to our microfluidic-based method of environmental perturbation, as found in chapter 2, can be made. Most notably, the action of delivering environmental cues was manually controlled. This method required users to actively monitor and participate in the execution of these experiments. Truly autonomous experimentation would require the development of automation software that can be pre-programed to run a particular experimental design, and automatically deliver environmental stimuli. Such

systems have been developed and successfully employed by other researchers indicating the feasibility of such a system for these tasks.

The microfluidic technologies I developed throughout thesis allow for high-throughput microscopy of developing *Drosophila* embryos from essentially all possible orientations. I expect researchers that use fluorescence microscopy to study an aspect of *Drosophila* embryogenesis including, for example, germ band extension and retraction, dorsal closure, and head involution to benefit from the microfluidic devices developed in this thesis. These technologies should also be generally applicable to other models of development by simple scaling of these devices. In addition to pure observation-based studies, these devices can be utilized to probe development in a more active way as exemplified by chapter 2, and 4 of this thesis. In addition to the experiments shown in this thesis, the engineered microsystems will allow studies of other developmental systems and how these systems respond to external perturbation. Besides investigating anoxia-induced developmental arrest and recovery, one could study known teratogens of unknown pathology to investigate the early embryonic responses to teratogen exposure including, for example, alcohol. It is also straightforward to use these microsystems to screen therapeutics aimed at treating teratogen exposure.

In addition to external perturbation, one could incorporate established genetic models of developmental diseases in order to study disease pathology in a highly quantitative manner through large-scale data collection that is enabled by the technologies developed in this thesis. For example, a disease model for microcephaly could potentially be utilized with the dorsal-ventral array for large-scale imaging of head development from an end-on orientation and potentially provide new insight to disease

onset and progression. The genetic mutants investigated specifically in this thesis in chapter 4 are expected to provide mechanistic insight to the pathology of an array of developmental disorders known as RASopathies. This would require more detailed single-cell information of signaling molecules such as Capicua all along the anterior-posterior axis.

The algorithm for single-cell analysis I developed in this thesis depended upon the ability to segment individual nuclei based on Capicua-Venus expression. While this method served well for investigating individual cells with relatively high Capicua levels, the developed method would exhibit poor performance in identifying cells with low levels of Capicua or any other signaling molecule of interest. Development of new reagents that incorporate endogenous reporters to identify nuclei would allow for this method to identify all cells independent of the relative levels of the signaling molecule of interest. However, of a nuclear reporter should be beneficial for all cells as we expect to enable more robust identification of all cells throughout time. For example, the cells studied in chapter 4 with high levels of Capicua can only be identified when Capicua levels are high enough to provide contrast against the cytoplasm. Since Capicua is actively transported into and out of the nucleus between nuclear cycles, individual cells are lost during and around mitosis. It is only when enough Capicua is transported into the nucleus that single-cells can be identified and tracked. I expect a nuclear reporter to mitigate this issue for this study as well as other studies interested in nuclear signaling kinetics.

APPENDIX A: PUBLICATIONS AND OTHER SCIENTIFIC ACTIVITY

A.1: Accepted/Published Manuscripts

T.J. Levario, et al. “An integrated platform for large-scale data collection and precise perturbation of live *Drosophila* embryos.” Scientific Reports (accepted January 19, 2016).

T.J. Levario, et al. “Microfluidics for high-throughput quantitative studies of early development.” In review at Annual Review of Biomedical Engineering (accepted November 30, 2015).

D.E. White, J.B. Sylvester, M.A. Kinney, T.J. Levario, et al. “Quantitative multivariate analysis of dynamic multicellular morphogenic trajectories.” Integrative Biology. 7, 825-833 (2015).

B. Lim, C.J. Dsilva, T.J. Levario, et al. “Dynamics of inductive ERK signaling in the *Drosophila* embryo.” Current Biology. 25, 1784-1790 (2015).

B. Lim, C.J. Dsilva, T.J. Levario, et al. “Ups and downs of ERK activation in embryos.” AIChE 2014 Annual Meeting Conference Paper (2014).

M. Wiehn, T.J. Levario, et al. “Adsorption of short-chain alcohols by hydrophobic silica aerogels.” Industrial & Engineering Chemistry Research. 52, 18379-18385 (2013).

T.J. Levario, et al. “Microfluidic trap array for massively parallel imaging of *Drosophila* embryos.” Nature Protocols 8, 721-736 (2013).

T.J. Levario, et al. “Rapid adsorption of alcohol biofuels by high surface area mesoporous carbons.” Microporous and Mesoporous Materials. 148, 107-114 (2012).

A.2: Manuscripts in Review or in Preparation

T.J. Levario, et al. “Microfluidics and image processing-enabled quantification of single-cell gene expression dynamics in *Drosophila* embryos.” In preparation (expected submission to Integrative Biology in April, 2016).

T.J. Levario, et al. “Arraying and high-throughput imaging of laterally oriented live *Drosophila* embryos.” In review at Lab on a Chip (submitted April 13, 2016).

C. Zhao, A. Kniss, T.J. Levario, et al. “Rapid and simple quantitative phenotyping of fluorescently-labeled biological systems with relative difference filtering and clustering.” In review at Nature Communications (submitted October 12, 2015).

A.3: Conference Presentations

T.J. Levario and H. Lu. “Development of microfluidic and automation tools for high-throughput microscopy and analysis of embryogenesis.” Oral presentation, School of Chemical & Biomolecular Engineering Ziegler Award Winners Lecture, Atlanta, 2015.

T.J. Levario et al. “Microfluidic and automation tools for large-scale high-content imaging and morphometric analysis.” Oral presentation, 56th Annual Drosophila Research Conference, Chicago, 2015.

T.J. Levario and H. Lu. “Microfluidic embryo well array for parallelized end-on imaging and microinjection.” Oral presentation, AIChE Annual Meeting, Atlanta, 2014.

T.J. Levario et al. “Towards multi-angle microscopy: FEP-PDMS hybrid device for enhanced fluorescence imaging.” Poster presentation, The 18th International Conference on Miniaturized Systems for Chemistry and Life Sciences, San Antonio, 2014.

T.J. Levario et al. “Microfluidic culturing for studying morphogenesis and gastrulation in live *Drosophila* embryos.” Poster presentation, 55th Annual Drosophila Research Conference, San Diego, 2014.

T.J. Levario et al. “Microfluidics and image processing for time-resolved measurements of gene expression dynamics during *Drosophila* embryogenesis.” Poster presentation, Georgia Tech Research and Innovation Conference, Atlanta, 2014.

T.J. Levario & D.R. Nielsen. (2010) “Application of adsorbent aerogels for biofuel recovery.” Poster presentation, Society of Mexican-American Engineers and Scientists 36th Annual Symposium, Anaheim, 2010.

J Ding, T.J. Levario, et al. “Microfluidic platform and image processing technique to quantitatively determine *Drosophila* embryo age.” Poster presentation, Air Products Undergraduate Research Symposium, Atlanta, 2014.

J Ding, T.J. Levario, et al. “Design of a microfluidic-based platform for spatially controlled drug treatment in cichlid early development.” Poster presentation, AIChE 2014 Southern Student Regional Conference, San Juan, 2014.

J Ding, T.J. Levario, et al. “Design of a microfluidic-based platform for spatially controlled drug treatment in cichlid early development.” Poster presentation, Air Products Undergraduate Research Symposium, Atlanta, 2013.

J Ding, T.J. Levario, et al. “Design of a microfluidic-based platform for spatially controlled drug treatment in cichlid early development.” Poster presentation, 8th Annual GT Undergraduate Research Opportunities Program Symposium, Atlanta, 2013.

APPENDIX B: PHOTOMASK DESIGNS

B.1: Photomask for Chapter 2 Single-Layer Dorsal-Ventral (DV) Array

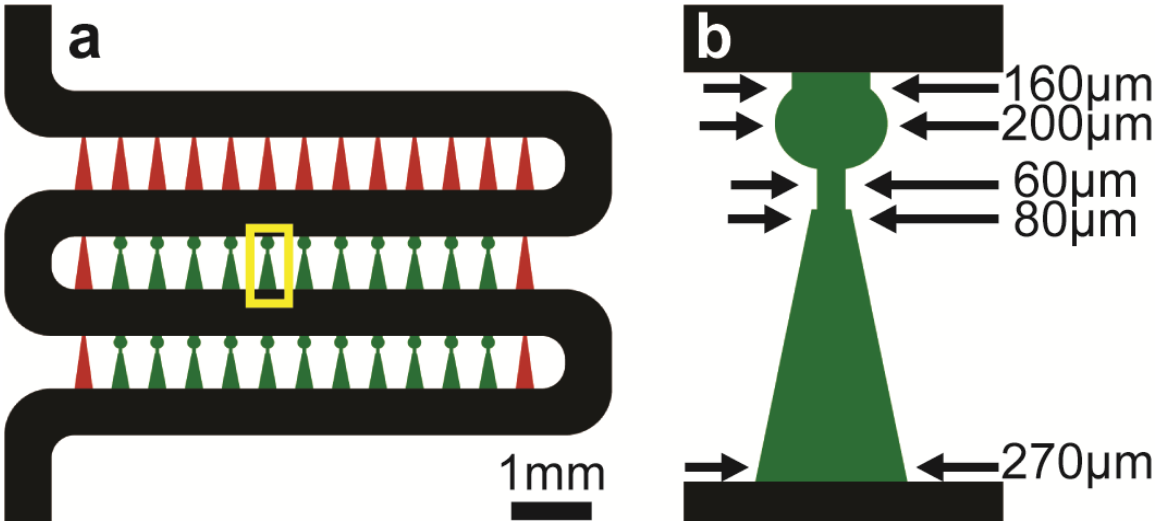

Figure B.1: Dorsal-ventral (DV) microfluidic array schematic. a) Overall device layout with main serpentine channel (■), focusing channels (■), and embryo traps and resistance channels (■). b) Zoom-in of boxed region of (a) with dimensions of the embryo trap and resistance channel.

B.2: Photomask for Chapter 3 Single-Layer Anterior-Posterior (AP1) Array

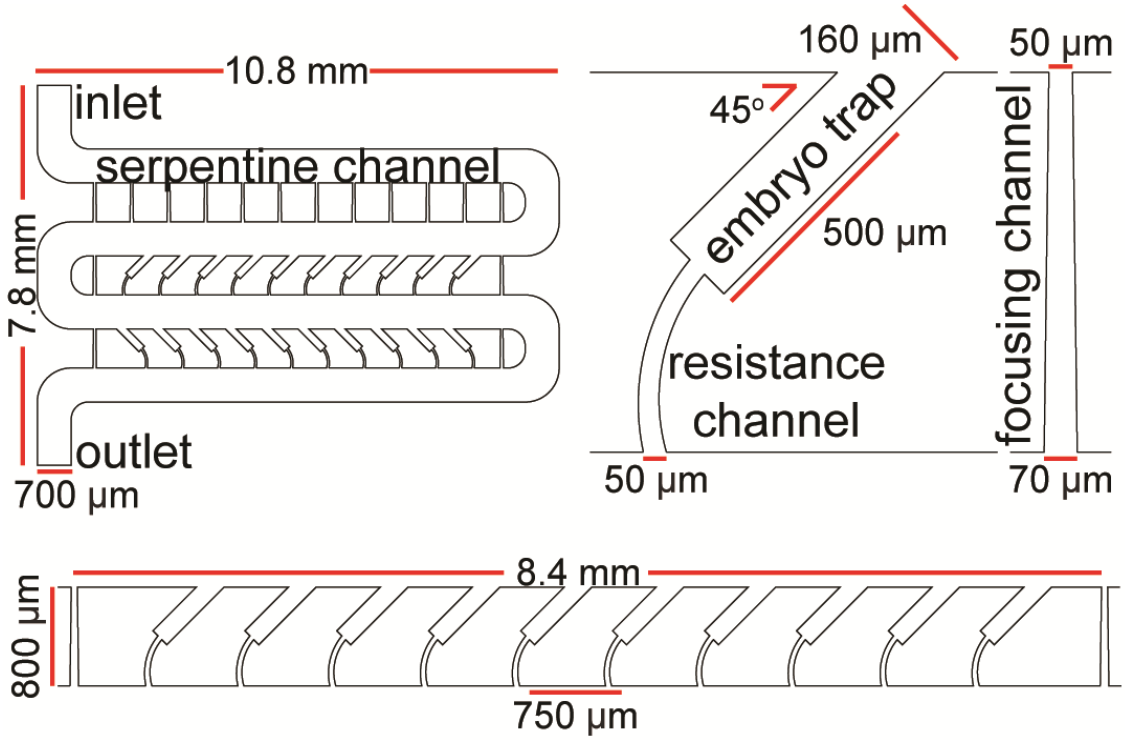

Figure B.2: The single-layer anterior-posterior (AP1) array schematic. Top left: Overall device layout with main serpentine channel, and inlet and outlet locations labeled. Bottom: a single row containing 10 embryo traps in the center and individual focusing channels bookending the traps within each row. Top right: Individual trapping unit and focusing channel close up with embryo trap and resistance channels labeled, and dimensions indicated.

B.3: Photomask for Chapter 4 Two-Layer Anterior-Posterior (AP2) Array

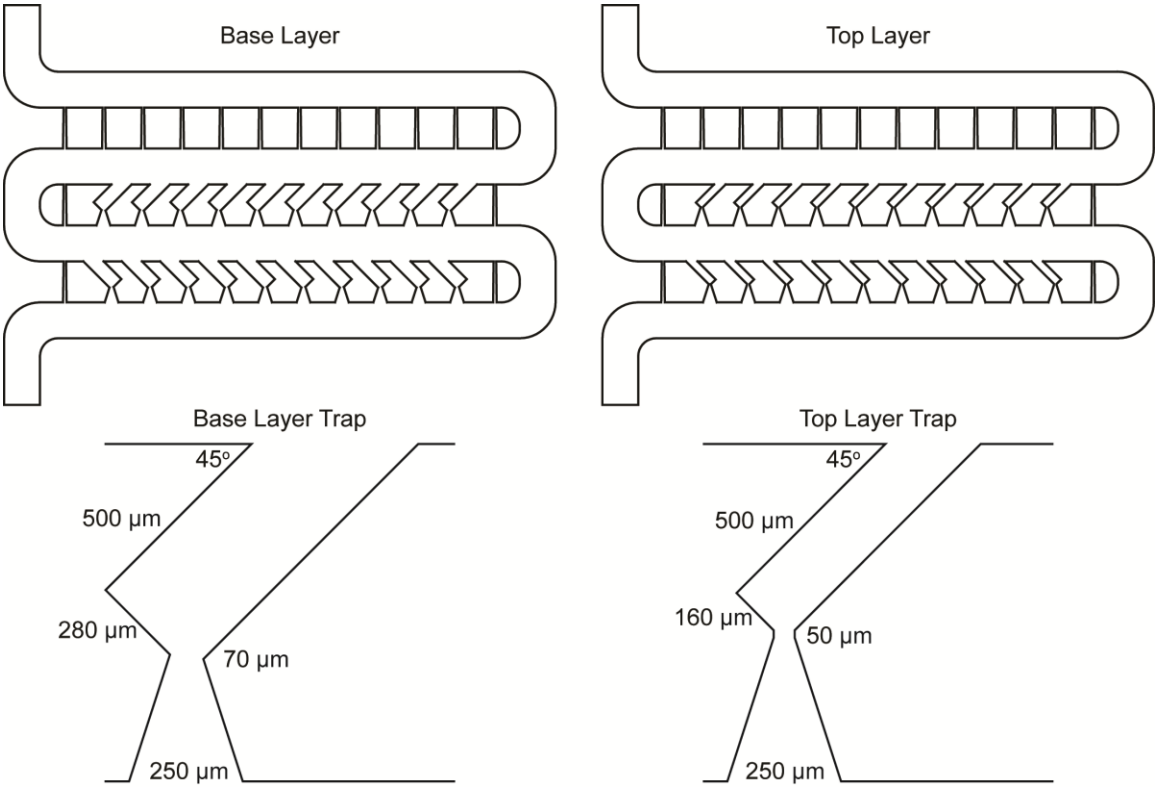

Figure B.3: The two-layer anterior-posterior (AP2) array schematic. Top left: Overall device layout for the base layer of the device. Bottom left: a single trapping unit of the base layer with important dimensions indicated for the embryo trap and resistance channel. Top right: Overall device layout for the top layer of the device. Bottom right: a single trapping unit of the top layer with important dimensions indicated for the embryo trap and resistance channel. Notice: main difference is in the width of the embryo trap in which the base layer embryo trap is 280 µm wide whereas the top layer embryo trap is 160 µm wide. The top layer is meant to guide embryos into the center of the trap while the base is meant to keep PDMS side walls from interfering with imaging quality.

APPENDIX C: MATLAB CODE FOR QUANTIFYING NUCLEAR CYCLING DYNAMICS

```
close all

direc='C:\Users\Tom\Documents\MATLAB\test';


fileList=dir(direc);
fileList = fileList(~[fileList.isdir]);
index=0;

%get order
fileindex=[];
indexes=[];
while index<numel(fileList) %for each image
        index=index+1;
        if ~strcmp(fileList(index).name(end-2:end),'tif')
            continue
        end

         indexstr = regexp(fileList(index).name(1:end-
3),'b\d+','match');
          fileindex(end+1)=str2double(indexstr{1}(1));

        indexes(end+1)=index; %#ok<SAGROW>
end
[~,sorter]=sort(fileindex);
indexes=indexes(sorter);


nuclengths=zeros(1,length(indexes));
nucareas=zeros(1,length(indexes));
nucnumber=zeros(1,length(indexes));
timetable=zeros(1,length(indexes));
timetable2=zeros(1,length(indexes));
nucminoraxislength=zeros(1,length(indexes));
filtpix=zeros(1,length(indexes));
notfiltpix=zeros(1,length(indexes));
middist=zeros(1,length(indexes));
circarea=zeros(1,length(indexes));

for x=1:numel(indexes) %for each image
    index=indexes(x);
    time2=tic;
    image=imread([direc '\' fileList(index).name]);

    time1=tic;
    filtimage=medfilt2(image);
```

```
    closeBW=filtimage>max(filtimage(:))*0.1;

    meanimage=imfilter(filtimage,ones(50,50)/2500,'replicate');
    normimage=(filtimage-meanimage)./meanimage; %last part prevents 0
things frmo turning into INF in the image
    normimage(isnan(normimage))=0;
    normimage(~closeBW)=0;

    %saving thresholded image file
    threshimage=normimage>0.1; %thrsehold for object
    timetable(x)=toc(time1);


    %find nuclei
    oldstats = regionprops(threshimage,
'Centroid','Area','Solidity','PixelList','MajorAxisLength','Perimeter',
'MinorAxisLength');

stats=oldstats([oldstats.Area]>5&[oldstats.Area]<75&[oldstats.Solidity]
>0.7);
     secImSyn=zeros(size(image));

%     regenerate synapse image after processing
    for xx=1:length(stats)
        for y=1:size(stats(xx).PixelList,1)

secImSyn(stats(xx).PixelList(y,2),stats(xx).PixelList(y,1))=1;
        end
    end

%     timetable(x)=toc;
     tempMaj=[stats.MajorAxisLength];
     tempMin=[stats.MinorAxisLength];
    nuclengths(x)=mean(tempMaj);
    nucareas(x)=mean([stats.Area]);
    nucnumber(x)=numel(stats);
    nucminoraxislength(x)=mean(tempMin);
    filtpix(x)=numel(oldstats)-numel(stats);


    %savingfiles
    imwrite(normimage,[direc '\' fileList(index).name(1:end-3)
'_normimage.png'],'PNG')
    imwrite(threshimage,[direc '\' fileList(index).name(1:end-3)
'_threshimage.png'],'PNG')
    imwrite(secImSyn,[direc '\' fileList(index).name(1:end-3)
'_Binary.png'],'PNG')
    circarea(x)=sum(closeBW(:));
    centstats = regionprops(closeBW, 'Centroid','Area');

    [~,maxI]=max([centstats.Area]);
    centroid=centstats(maxI).Centroid; %NOTE: this is reverse order of
the standard matlab matrix order (that is, this is column first)
```

```
    %get distances from middle
    clusdis=NaN*ones(1,numel(stats));
    for xx=1:numel(stats)
        clusdis(xx)=sqrt((stats(xx).Centroid(1)-
centroid(1)).^2+(stats(xx).Centroid(2)-centroid(2)).^2);
    end
    middist(x)=mean(clusdis);
    timetable2(x)=toc(time2);
end
```

APPENDIX D: MATLAB CODE FOR SINGLE-CELL MEASUREMENTS OF CAPICUA DYNAMICS

```
clear
clc

direc='D:\cicvcroppedvideos new\20160424TL\sca\20160424TL21';

fileList=dir(direc);
fileList=fileList(~[fileList.isdir]); %removes ghost files

fileindex=[];
indexes=[];
index=0;

inucleicounter=0;

%% construct and save heatmaps for single-cell analysis in...
%     subsequent sections

while index<numel(fileList) %for each image
        index=index+1;
        if ~strcmp(fileList(index).name(end-2:end),'tif')
            continue
        end

        indexstr = regexp(fileList(index).name(1:end-
4),'2\d+','match');
        fileindex(end+1)=str2double(indexstr{1}(1));

        indexes(end+1)=index; %#ok<SAGROW>
end
[~,sorter]=sort(fileindex);
indexes=indexes(sorter);

for x=1:numel(indexes) %for each time-series videos
    index=indexes(x);
    time2=tic;

    for X1=1:180 %
        image(:,:,X1)=imread([direc '\' fileList(index).name],X1);
    end

    v=squeeze(max(image));

    save([direc '\' fileList(index).name(1:end-4) 'heatmap.mat'],'v');

    start=150;
```

```
    finish=350;
    for X2=start:finish
        vcrop(X2-start+1,:)=v(X2,:);
    end

    vcropmean=mean(vcrop);
    vcropmeaninv=1.01*max(vcropmean)-vcropmean;

    timeplotmatrix(x,:)=vcropmean;

    clearvars image v

    timetable2(x)=toc(time2);

end

timeplotmean=mean(timeplotmatrix);
timeplotmeaninv=1.01*max(timeplotmean)-timeplotmean;

[iapks,ialocs,iaw,iap]=findpeaks(timeplotmean);
[iaipks,iailocs,iaiw,iaip]=findpeaks(timeplotmeaninv);

[ipks,ilocs,iw,ip]=findpeaks(timeplotmean,'MinPeakProminence',2,'NPeaks
'...
    ,3);
[iipks,iilocs,iiw,iip]=findpeaks(timeplotmeaninv,'MinPeakProminence',.5
,...
    'MinPeakHeight',1.36,'NPeaks',4,'MinPeakDistance',1);

for X3=1:numel(iilocs)
        X4=iilocs(X3);
        iipks(X3)=timeplotmean(X4);
end

%figure
plot(timeplotmean)

%save([direc '\' fileList(index).name(1:end-5) ...
%    '_singleembryointensityvstime.mat'],'timeplotmean');

ilocs
iilocs


%% single-cell analysis

ifileList=dir(direc);
ifileList=ifileList(~[ifileList.isdir]); %removes ghost files

ifileindex=[];
iindexes=[];
iindex=0;
```

```
while iindex<numel(ifileList) %for each image
        iindex=iindex+1;
        if ~strcmp(ifileList(iindex).name(end-2:end),'mat')
            continue
        end

        indexstr = regexp(ifileList(iindex).name(1:end-
4),'2\d+','match');
        ifileindex(end+1)=str2double(indexstr{1}(1));

        iindexes(end+1)=iindex; %#ok<SAGROW>
end
[~,sorter]=sort(ifileindex);
iindexes=iindexes(sorter);
inucleitotal=1;

for igradient=1:numel(iindexes) %for each image
    iindex=iindexes(igradient);
    A=load([direc '\' ifileList(iindex).name]);
    A=[A(1,1).v];

    istart14=iilocs(3)-9;
    ifinish14=iilocs(3)+39;
    for iNC14=istart14:ifinish14
        rgNC14(:,iNC14-istart14+1)=A(:,iNC14);
    end


    %save([direc '\' ifileList(iindex).name(1:end-11) 'NC13.mat'],...
    %    'rgNC13');

    hmap2=HeatMap(rgNC14,'Colormap',jet,'Symmetric',false);
    %figure
    %plot(hmap2)
    iindex=indexes(igradient);
    itime2=tic;
    rgimage=double(rgNC14);

    time1=tic;
    rgfiltimage=medfilt2(rgimage);
    rgcloseBW=rgfiltimage>max(rgfiltimage(:))*0.1;

    rgmeanimage=imfilter(rgfiltimage,ones(55,30)/2500,'replicate');...
        %used for relative difference filtering and clustering
    figure
    imshow(rgmeanimage);
    rgnormimage=(rgfiltimage-rgmeanimage)./rgmeanimage; ...
        %last part prevents 0 things frmo turning into INF in the image
    rgnormimage(isnan(rgnormimage))=0;
    rgnormimage(~rgcloseBW)=0;

    %saving thresholded image file
    rgthreshimage=rgnormimage>0.68; %thrsehold for object
    figure
    imshow(rgthreshimage)
```

```
    rgtimetable(igradient)=toc(time1);

    oldstats = regionprops(rgthreshimage,
'Centroid','Area','Solidity',...
        'PixelList','MajorAxisLength','Perimeter','MinorAxisLength');
    stats=oldstats([oldstats.Area]>50&[oldstats.Area]<200&...
        [oldstats.MajorAxisLength]>10&[oldstats.MinorAxisLength]<9);

    [irthreshimage icthreshimage]=size(rgthreshimage);
    rgA=[stats.Centroid];
    rgAnew=[];
    icounterrowcentroid=1;
    for irowcentroid=1:2:length(rgA)
        rgAnew(icounterrowcentroid)=rgA(irowcentroid);
        icounterrowcentroid=icounterrowcentroid+1;
    end
    icountercolumncentroid=1;
    rgBnew=[];
    for icolumncentroid=2:2:length(rgA)
        rgBnew(icountercolumncentroid)=rgA(icolumncentroid);
        icountercolumncentroid=icountercolumncentroid+1;
    end

stats=stats([rgAnew]>0.25*icthreshimage&[rgAnew]<0.75*icthreshimage...
       &[rgBnew]>0.25*irthreshimage&[rgBnew]<0.75*irthreshimage);
    rgsecImSyn=zeros(size(rgimage));

    %generate binary image of nuclei traces
    for ibinary1=1:length(stats)
        for ibinary2=1:size(stats(ibinary1).PixelList,1)
            rgsecImSyn(stats(ibinary1).PixelList(ibinary2,2),...
                stats(ibinary1).PixelList(ibinary2,1))=1;
        end
    end
    figure
    imshow(rgsecImSyn)

    rgnucleiskel=imfill(rgsecImSyn);
    rgnucleiskel=bwmorph(rgnucleiskel,'spur');
    rgnucleiskel=bwmorph(rgnucleiskel,'skel',Inf);...
        %skelentonized single-cell trace
    figure
    imshow(rgnucleiskel)

    nucleiskelstats = regionprops(rgnucleiskel, 'Centroid','Area',...
        'Solidity','PixelList','MajorAxisLength','Perimeter',...
        'MinorAxisLength');

    %% generate nuclear traces based on known nuclear regions from
above
    for itimeandspacevector=1:length(nucleiskelstats)

        initialize=[0];
        icountertimevector=0;
        for itimevector=1:...
```

```
                length(nucleiskelstats(itimeandspacevector).PixelList)
            if nucleiskelstats(itimeandspacevector)...
                    .PixelList(itimevector)~=initialize
                icountertimevector=icountertimevector+1;
            end
            rgtimevector(icountertimevector,itimeandspacevector)=...
                nucleiskelstats(itimeandspacevector)...
                .PixelList(itimevector);
            initialize=nucleiskelstats(itimeandspacevector)...
                .PixelList(itimevector);
        end

        rgtimevector=squeeze(rgtimevector);

        initialize=[0];
        icounterspacevector=0;
        for
ispacevector=1:length(nucleiskelstats(itimeandspacevector)...
                .PixelList)
            if nucleiskelstats(itimeandspacevector)...
                    .PixelList(ispacevector)~=initialize
                icounterspacevector=icounterspacevector+1;
            end
            rgspacevectormatrix(icounterspacevector,ispacevector,...
                itimeandspacevector)=...
                nucleiskelstats(itimeandspacevector)...
                .PixelList(ispacevector+...

length(nucleiskelstats(itimeandspacevector).PixelList));
            initialize=nucleiskelstats(itimeandspacevector)...
                .PixelList(ispacevector);
        end

        %deals with branching in skel
        rgspacevectormatrix;
        rgspacevectormatrixsum=sum(rgspacevectormatrix,2);
        rgspacevectorbins=rgspacevectormatrix~=0;
        rgspacevectorbins=sum(rgspacevectorbins,2);
        rgspacevector=squeeze(round(rgspacevectormatrixsum...
            ./rgspacevectorbins));
        rgspacevector(isnan(rgspacevector))=0;
    end

    [irspacevector icspacevector]=size(rgspacevector);

    %this for loop deals with adding time forward and backward in time
for
    %each nuclear trace
    for iappend=1:icspacevector
        rgTold=rgtimevector(:,iappend);
        rgSold=rgspacevector(:,iappend);

        for iappendsplit=1:length(rgTold)
            if rgTold(iappendsplit) < 1
                break
            end
```

```
            rgT(iappendsplit)=rgTold(iappendsplit);
            rgS(iappendsplit)=rgSold(iappendsplit);
        end

        rgappendFT=[];
        rgappendFS=[];
        %append beginning for time
        for iappendF=1:rgT(1)-1
            rgappendFT(iappendF)=iappendF;
            rgappendFS(iappendF)=rgSold(1);
        end
        rgT=[rgappendFT rgT];
        rgS=[rgappendFS rgS];

        rgappendLT=[];
        rgappendLS=[];
        %append ending for time
        irT=length(rgT);
        icounterappendL=1;
        for iappendL=rgT(irT)+1:icthreshimage
            rgappendLT(icounterappendL)=iappendL;
            rgappendLS(icounterappendL)=rgS(irT);
            icounterappendL=icounterappendL+1;
        end
        rgT=transpose([rgT rgappendLT]);
        rgS=transpose([rgS rgappendLS]);
        rgTnew(:,iappend)=rgT;
        rgSnew(:,iappend)=rgS;

        clearvars rgT rgS rgappendLT rgappendLS rgappendFT
rgappendFS...
            rgSold rgTold iappendsplit
    end
    rgTreshape=reshape(rgTnew,[],1);
    rgSreshape=reshape(rgSnew,[],1);

    %% extracting nuclear intensities along nuclear traces from above
    rgimage=rgimage;
    [irrgimage, icrgimage]=size(rgimage);
    [irSnew, icSnew]=size(rgSnew);
    figure
    hold on

    for inuclei=1:icSnew %for each nucleus

        inuclei;

        for itime=1:irSnew %for each time point

            itime;

            icounterbandwidth=1;
            for ibandwidth=rgSnew(itime,inuclei)-
3:rgSnew(itime,inuclei)+3
```

```
            rgnucleiband(icounterbandwidth,itime)=...
                rgimage(ibandwidth,itime);
            icounterbandwidth=icounterbandwidth+1;

        end

    end

    rgintensitymean(:,inuclei)=mean(rgnucleiband);

    %smooth rgnucleiband
    [irrgintensitymean, icrgintensitymean]=size(rgintensitymean);
    icountersmooth=1;
    for ismooth=3:irrgintensitymean-2

        rgintensitymeansmooth(icountersmooth)=...
            (rgintensitymean(ismooth,inuclei)+...
            rgintensitymean(ismooth-1,inuclei)+...
            rgintensitymean(ismooth+1,inuclei)+...
            rgintensitymean(ismooth-2,inuclei)+...
            rgintensitymean(ismooth+2,inuclei))/5;
        icountersmooth=icountersmooth+1;

    end

    %identify posterior-midbody-anterior location of nuclei
    if nucleiskelstats(inuclei).Centroid(2)<=(1/4)*irrgimage
        iPMA=1;
    end
    if nucleiskelstats(inuclei).Centroid(2)<=(3/4)*irrgimage &&...
            nucleiskelstats(inuclei).Centroid(2)>=(1/4)*irrgimage
        iPMA=2;
        plot(rgintensitymeansmooth)
        legend('1','2','3','4')
    end
    if nucleiskelstats(inuclei).Centroid(2)>=(3/4)*irrgimage
        iPMA=3;
    end

    rgsinglenucleusintensitytrace(:,inuclei)=rgintensitymeansmooth;
    rgsinglenucleusintensitytracePMA(:,inucleitotal)=...
        rgintensitymeansmooth;
    inucleitotal=inucleitotal+1;

end

%% generate image that shows nuclei traces overlaid with heatmap
rgTreshape=reshape(rgTnew,[],1);
rgSreshape=reshape(rgSnew,[],1);

traces=rgnormimage;
for itraces=1:length(rgTreshape)
    traces(rgSreshape(itraces),rgTreshape(itraces))=0;
end
figure
```

```
    imshow(traces)

    %% saving files for individual gradients
    %{
    imwrite(rgnormimage,[direc '\' fileList(iindex).name(1:end-4)...
        '_normimage.png'],'PNG')
    imwrite(rgthreshimage,[direc '\' fileList(iindex).name(1:end-4)...
        '_threshimage.png'],'PNG')
    imwrite(rgsecImSyn,[direc '\' fileList(iindex).name(1:end-4)...
        '_Binary.png'],'PNG')
    imwrite(rgnucleiskel,[direc '\' fileList(iindex).name(1:end-4)...
        '_nucleiskel.png'],'PNG')
    imwrite(traces,[direc '\' fileList(iindex).name(1:end-4)...
        '_traces.png'],'PNG')

    save([direc '\' fileList(iindex).name(1:end-4)...
        '_singlenucleusintensitytrace.mat'],...
        'rgsinglenucleusintensitytrace')
    %}
    %% Clock
    timetable2(igradient)=toc(itime2);

    %% to prevent variables for one nucleus to interfere with
another...
    %because of size changes in variables.

    clearvars rgspacevector rgspacevectorbins rgspacevectormatrix ...
        rgspacevectormatrixsum rgtimevector rgintensitymeansmooth ...
        oldstats nucleiskelstats ivalleylocs ivalleyp ivalleypks ...
        ivalleyw rgAnew rgBnew rgcloseBW rgduration rgfalltime ...
        rgfiltimage rgimage rgintensitymean rgintensitymeansmooth ...
        rgintensitymeansmoothcollectall rgintensitymeansmoothinv ...
        rgmeanimage rgminintensity rgnormimage rgnucleiband ...
        rgmaxintensity rgnucleiskel rgrisetime rgsecImSyn rgSnew ...
        rgSreshape rgthreshimage rgtimetable rgTnew rgTreshape traces
...
        rgA rgsinglenucleusintensitytrace
rgsinglenucleusintensitytraceP...
        rgsinglenucleusintensitytraceM rgsinglenucleusintensitytraceA
...
        rgNC12 rgNC13 rgNC14

end
```

REFERENCES

[1] Campos-Ortega, J.A. and V. Hartenstein, The embryonic development of Drosophila melanogaster. 2nd edition. ed. xvii, 405 pages.

[2] Bate, M. and A. Martinez Arias, The Development of Drosophila melanogaster. 2 volumes (x, 1,558 pages).

[3] Morgan, T.H., Sex limited inheritance in Drosophila. **Science**, 1910. 32(1): p. 120-122.

[4] Muller, H.J., Artificial Transmutation of the Gene. **Science**, 1927. 66(1699): p. 84-7.

[5] Nussleinvolhard, C. and E. Wieschaus, Mutations Affecting Segment Number and Polarity in Drosophila. **Nature**, 1980. 287(5785): p. 795-801.

[6] Lemaitre, B., E. Nicolas, L. Michaut, J.M. Reichhart, and J.A. Hoffmann, The dorsoventral regulatory gene cassette spatzle/Toll/cactus controls the potent antifungal response in Drosophila adults. **Cell**, 1996. 86(6): p. 973-983.

[7] Lewis, E.B., A gene complex controlling segmentation in Drosophila. **Nature**, 1978. 276(5688): p. 565-70.

[8] Burke, A.C., C.E. Nelson, B.A. Morgan, and C. Tabin, Hox genes and the evolution of vertebrate axial morphology. **Development**, 1995. 121(2): p. 333-46.

[9] Driever, W. and C. Nussleinvolhard, The Bicoid Protein Determines Position in the Drosophila Embryo in a Concentration-Dependent Manner. **Cell**, 1988. 54(1): p. 95-104.

[10] Turing, A.M., The Chemical Basis of Morphogenesis. **Philosophical Transactions of the Royal Society of London Series B-Biological Sciences**, 1952. 237(641): p. 37-72.

[11] Wilson, P.A., G. Lagna, A. Suzuki, and A. HemmatiBrivanlou, Concentration-dependent patterning of the Xenopus ectoderm by BMP4 and its signal transducer smad1. **Development**, 1997. 124(16): p. 3177-3184.

[12] Marti, E., D.A. Bumcrot, R. Takada, and A.P. Mcmahon, Requirement of 19k Form of Sonic Hedgehog for Induction of Distinct Ventral Cell-Types in Cns Explants. **Nature**, 1995. 375(6529): p. 322-325.

[13] Nellen, D., R. Burke, G. Struhl, and K. Basler, Direct and long-range action of a DPP morphogen gradient. **Cell**, 1996. 85(3): p. 357-368.

[14] Rock, F.L., G. Hardiman, J.C. Timans, R.A. Kastelein, and J.F. Bazan, A family of human receptors structurally related to Drosophila Toll. **Proceedings of the National Academy of Sciences of the United States of America**, 1998. 95(2): p. 588-593.

[15] Giguere, V., E.S. Ong, P. Segui, and R.M. Evans, Identification of a Receptor for the Morphogen Retinoic Acid. **Nature**, 1987. 330(6149): p. 624-629.

[16] Strigini, M. and S.M. Cohen, Wingless gradient formation in the Drosophila wing. **Current Biology**, 2000. 10(6): p. 293-300.

[17] Dong, J.X., et al., Elucidation of a universal size-control mechanism in Drosophila and mammals. **Cell**, 2007. 130(6): p. 1120-1133.

[18] Graveley, B.R., et al., The developmental transcriptome of Drosophila melanogaster. **Nature**, 2011. 471(7339): p. 473-479.

[19] Krashes, M.J., A.C. Keene, B. Leung, J.D. Armstrong, and S. Waddell, Sequential use of mushroom body neuron subsets during Drosophila odor memory processing. **Neuron**, 2007. 53(1): p. 103-115.

[20] Ceriani, M.F., J.B. Hogenesch, M. Yanovsky, S. Panda, M. Straume, and S.A. Kay, Genome-wide expression analysis in Drosophila reveals genes controlling circadian behavior. **Journal of Neuroscience**, 2002. 22(21): p. 9305-9319.

[21] Stockinger, P., D. Kvitsiani, S. Rotkopf, L. Tirian, and B.J. Dickson, Neural circuitry that governs Drosophila male courtship behavior. **Cell**, 2005. 121(5): p. 795-807.

[22] Feany, M.B. and W.W. Bender, A Drosophila model of Parkinson's disease. **Nature**, 2000. 404(6776): p. 394-398.

[23] Crowther, D.C., K.J. Kinghorn, E. Miranda, R. Page, J.A. Curry, F.A.I. Duthie, D.C. Gubb, and D.A. Lomas, Intraneuronal A beta, non-amyloid aggregates and neurodegeneration in a Drosophila model of Alzheimer's disease. **Neuroscience**, 2005. 132(1): p. 123-135.

[24] Watson, M.R., R.D. Lagow, K.X. Xu, B. Zhang, and N.M. Bonini, A Drosophila model for amyotrophic lateral sclerosis reveals motor neuron damage by human SOD1. **Journal of Biological Chemistry**, 2008. 283(36): p. 24972-24981.

[25] Teleman, A.A. and S.M. Cohen, Dpp gradient formation in the Drosophila wing imaginal disc. **Cell**, 2000. 103(6): p. 971-980.

[26] Kiehart, D.P., C.G. Galbraith, K.A. Edwards, W.L. Rickoll, and R.A. Montague, Multiple forces contribute to cell sheet morphogenesis for dorsal closure in Drosophila. **Journal of Cell Biology**, 2000. 149(2): p. 471-490.

[27] Gong, Y., C.H. Mo, and S.E. Fraser, Planar cell polarity signalling controls cell division orientation during zebrafish gastrulation. **Nature**, 2004. 430(7000): p. 689-693.

[28] Patel, M.R., E.K. Lehrman, V.Y. Poon, J.G. Crump, M. Zhen, C.I. Bargmann, and K. Shen, Hierarchical assembly of presynaptic components in defined C. elegans synapses. **Nature Neuroscience**, 2006. 9(12): p. 1488-1498.

[29] Verveer, P.J., J. Swoger, F. Pampaloni, K. Greger, M. Marcello, and E.H.K. Stelzer, High-resolution three-dimensional imaging of large specimens with light sheet-based microscopy. **Nature Methods**, 2007. 4(4): p. 311-313.

[30] Zanacchi, F.C., Z. Lavagnino, M.P. Donnorso, A. Del Bue, L. Furia, M. Faretta, and A. Diaspro, Live-cell 3D super-resolution imaging in thick biological samples. **Nature Methods**, 2011. 8(12): p. 1047-+.

[31] Hagerling, R., et al., A novel multistep mechanism for initial lymphangiogenesis in mouse embryos based on ultramicroscopy. **Embo Journal**, 2013. 32(5): p. 629-644.

[32] Ahrens, M.B., M.B. Orger, D.N. Robson, J.M. Li, and P.J. Keller, Whole-brain functional imaging at cellular resolution using light-sheet microscopy. **Nature Methods**, 2013. 10(5): p. 413-+.

[33] Reeves, G.T., N. Trisnadi, T.V. Truong, M. Nahmad, S. Katz, and A. Stathopoulos, Dorsal-Ventral Gene Expression in the Drosophila Embryo Reflects the Dynamics and Precision of the Dorsal Nuclear Gradient. **Developmental Cell**, 2012. 22(3): p. 544-557.

[34] Keller, P.J., A.D. Schmidt, A. Santella, K. Khairy, Z.R. Bao, J. Wittbrodt, and E.H.K. Stelzer, Fast, high-contrast imaging of animal development with scanned light sheet-based structured-illumination microscopy. **Nature Methods**, 2010. 7(8): p. 637-U55.

[35] Denk, W., J.H. Strickler, and W.W. Webb, Two-photon laser scanning fluorescence microscopy. **Science**, 1990. 248(4951): p. 73-6.

[36] McMahon, A., W. Supatto, S.E. Fraser, and A. Stathopoulos, Dynamic Analyses of Drosophila Gastrulation Provide Insights into Collective Cell Migration. **Science**, 2008. 322(5907): p. 1546-1550.

[37] Wang, Y.C., Z. Khan, and E.F. Wieschaus, Distinct Rap1 Activity States Control the Extent of Epithelial Invagination via alpha-Catenin. **Developmental Cell**, 2013. 25(3): p. 299-309.

[38] Shimozawa, T., et al., Improving spinning disk confocal microscopy by preventing pinhole cross-talk for intravital imaging. **Proceedings of the National Academy of Sciences of the United States of America**, 2013. 110(9): p. 3399-3404.

[39] Whitesides, G.M., E. Ostuni, S. Takayama, X.Y. Jiang, and D.E. Ingber, Soft lithography in biology and biochemistry. **Annual Review of Biomedical Engineering**, 2001. 3: p. 335-373.

[40] Beebe, D.J., G.A. Mensing, and G.M. Walker, Physics and applications of microfluidics in biology. **Annual Review of Biomedical Engineering**, 2002. 4: p. 261-286.

[41] El-Ali, J., P.K. Sorger, and K.F. Jensen, Cells on chips. **Nature**, 2006. 442(7101): p. 403-411.

[42] Crane, M.M., J.N. Stirman, C.Y. Ou, P.T. Kurshan, J.M. Rehg, K. Shen, and H. Lu, Autonomous screening of C-elegans identifies genes implicated in synaptogenesis. **Nature Methods**, 2012. 9(10): p. 977-+.

[43] Caceres, I.D., N. Valmas, M.A. Hilliard, and H. Lu, Laterally Orienting C. elegans Using Geometry at Microscale for High-Throughput Visual Screens in Neurodegeneration and Neuronal Development Studies. **Plos One**, 2012. 7(4).

[44] Guo, S.X., F. Bourgeois, T. Chokshi, N.J. Durr, M.A. Hilliard, N. Chronis, and A. Ben-Yakar, Femtosecond laser nanoaxotomy lab-on-achip for in vivo nerve regeneration studies. **Nature Methods**, 2008. 5(6): p. 531-533.

[45] Gokce, S.K., S.X. Guo, N. Ghorashian, W.N. Everett, T. Jarrell, A. Kottek, A.C. Bovik, and A. Ben-Yakar, A Fully Automated Microfluidic Femtosecond Laser Axotomy Platform for Nerve Regeneration Studies in C. elegans. **Plos One**, 2014. 9(12).

[46] Samara, C., C.B. Rohde, C.L. Gilleland, S. Norton, S.J. Haggarty, and M.F. Yanik, Large-scale in vivo femtosecond laser neurosurgery screen reveals small-molecule enhancer of regeneration. **Proceedings of the National Academy of Sciences of the United States of America**, 2010. 107(43): p. 18342-18347.

[47] Lin, X.D., S.Q. Wang, X.D. Yu, Z.G. Liu, F. Wang, W.T. Li, S.H. Cheng, Q.Y. Dai, and P. Shi, High-throughput mapping of brain-wide activity in awake and drug-responsive vertebrates. **Lab on a Chip**, 2015. 15(3): p. 680-689.

[48] Chronis, N., M. Zimmer, and C.I. Bargmann, Microfluidics for in vivo imaging of neuronal and behavioral activity in Caenorhabditis elegans. **Nature Methods**, 2007. 4(9): p. 727-731.

[49] Khoshmanesh, K., N. Kiss, S. Nahavandi, C.W. Evans, J.M. Cooper, D.E. Williams, and D. Wlodkowic, Trapping and imaging of micron-sized embryos using dielectrophoresis. **Electrophoresis**, 2011. 32(22): p. 3129-3132.

[50] Cornaglia, M., L. Mouchiroud, A. Marette, S. Narasimhan, T. Lehnert, V. Jovaisaite, J. Auwerx, and M.A.M. Gijs, An automated microfluidic platform for C-elegans embryo arraying, phenotyping, and long-term live imaging. **Scientific Reports**, 2015. 5.

[51] Krajniak, J. and H. Lu, Long-term high-resolution imaging and culture of C. elegans in chip-gel hybrid microfluidic device for developmental studies. **Lab on a Chip**, 2010. 10(14): p. 1862-1868.

[52] Krajniak, J., Y. Hao, H.Y. Mak, and H. Lu, CLIP-continuous live imaging platform for direct observation of C. elegans physiological processes. **Lab on a Chip**, 2013. 13(15): p. 2963-2971.

[53] Hulme, S.E., S.S. Shevkoplyas, A.P. McGuigan, J. Apfeld, W. Fontana, and G.M. Whitesides, Lifespan-on-a-chip: microfluidic chambers for performing lifelong observation of C. elegans. **Lab on a Chip**, 2010. 10(5): p. 589-597.

[54] Nghe, P., S. Boulineau, S. Gude, P. Recouvreux, J.S. van Zon, and S.J. Tans, Microfabricated Polyacrylamide Devices for the Controlled Culture of Growing Cells and Developing Organisms. **Plos One**, 2013. 8(9).

[55] Yu, C.C., D.M. Raizen, and C. Fang-Yen, Multi-well imaging of development and behavior in Caenorhabditis elegans. **Journal of Neuroscience Methods**, 2014. 223: p. 35-39.

[56] Behrndt, M., G. Salbreux, P. Campinho, R. Hauschild, F. Oswald, J. Roensch, S.W. Grill, and C.P. Heisenberg, Forces Driving Epithelial Spreading in Zebrafish Gastrulation. **Science**, 2012. 338(6104): p. 257-260.

[57] Wielhouwer, E.M., et al., Zebrafish embryo development in a microfluidic flow-through system. **Lab on a Chip**, 2011. 11(10): p. 1815-1824.

[58] Yang, F., Z.G. Chen, J.B. Pan, X.C. Li, J. Feng, and H. Yang, An integrated microfluidic array system for evaluating toxicity and teratogenicity of drugs on embryonic zebrafish developmental dynamics. **Biomicrofluidics**, 2011. 5(2).

[59] Choudhury, D., D. van Noort, C. Iliescu, B.X. Zheng, K.L. Poon, S. Korzh, V. Korzh, and H. Yu, Fish and Chips: a microfluidic perfusion platform for monitoring zebrafish development. **Lab on a Chip**, 2012. 12(5): p. 892-900.

[60] Bischel, L.L., B.R. Mader, J.M. Green, A. Huttenlocher, and D.J. Beebe, Zebrafish Entrapment By Restriction Array (ZEBRA) device: a low-cost, agarose-free zebrafish mounting technique for automated imaging. **Lab on a Chip**, 2013. 13(9): p. 1732-1736.

[61] Zheng, C.H., H.W. Zhou, X.X. Liu, Y.H. Pang, B. Zhang, and Y.Y. Huang, Fish in chips: an automated microfluidic device to study drug dynamics in vivo using zebrafish embryos. **Chemical Communications**, 2014. 50(8): p. 981-984.

[62] Li, Y.B., F. Yang, Z.G. Chen, L.J. Shi, B.B. Zhang, J.B. Pan, X.C. Li, D.P. Sun, and H.Z. Yang, Zebrafish on a Chip: A Novel Platform for Real-Time Monitoring of Drug-Induced Developmental Toxicity. **Plos One**, 2014. 9(4).

[63] Li, Y.B., X.J. Yang, Z.G. Chen, B.B. Zhang, J.B. Pan, X.C. Li, F. Yang, and D.P. Sun, Comparative toxicity of lead (Pb2+), copper (Cu2+), and mixtures of lead and copper to zebrafish embryos on a microfluidic chip. **Biomicrofluidics**, 2015. 9(2).

[64] Rohde, C.B., F. Zeng, R. Gonzalez-Rubio, M. Angel, and M.F. Yanik, Microfluidic system for on-chip high-throughput whole-animal sorting and screening at subcellular resolution. **Proceedings of the National Academy of Sciences of the United States of America**, 2007. 104(35): p. 13891-13895.

[65] Chung, K.H., M.M. Crane, and H. Lu, Automated on-chip rapid microscopy, phenotyping and sorting of C. elegans. **Nature Methods**, 2008. 5(7): p. 637-643.

[66] Ai, X.N., W.P. Zhuo, Q.L. Liang, P.T. McGrath, and H. Lu, A high-throughput device for size based separation of C-elegans developmental stages. **Lab on a Chip**, 2014. 14(10): p. 1746-1752.

[67] Aubry, G., M. Zhan, and H. Lu, Hydrogel-droplet microfluidic platform for high-resolution imaging and sorting of early larval Caenorhabditis elegans. **Lab on a Chip**, 2015. 15(6): p. 1424-1431.

[68] Wen, H., Y. Yu, G.L. Zhu, L. Jiang, and J.H. Qin, A droplet microchip with substance exchange capability for the developmental study of C-elegans. **Lab on a Chip**, 2015. 15(8): p. 1905-1911.

[69] Pardo-Martin, C., A. Allalou, J. Medina, P.M. Eimon, C. Wahlby, and M.F. Yanik, High-throughput hyperdimensional vertebrate phenotyping. **Nature Communications**, 2013. 4.

[70] Furlong, E.E.M., D. Profitt, and M.P. Scott, Automated sorting of live transgenic embryos. **Nature Biotechnology**, 2001. 19(2): p. 153-156.

[71] Chen, C.C., S. Zappe, O. Sahin, X.J. Zhang, M. Fish, M. Scott, and O. Solgaard, Design and operation of a microfluidic sorter for Drosophila embryos. **Sensors and Actuators B-Chemical**, 2004. 102(1): p. 59-66.

[72] Delubac, D., C.B. Highley, M. Witzberger-Krajcovic, J.C. Ayoob, E.C. Furbee, J.S. Minden, and S. Zappe, Microfluidic system with integrated microinjector for automated Drosophila embryo injection. **Lab on a Chip**, 2012. 12(22): p. 4911-4919.

[73] Chung, K., Y. Kim, J.S. Kanodia, E. Gong, S.Y. Shvartsman, and H. Lu, A microfluidic array for large-scale ordering and orientation of embryos. **Nature Methods**, 2011. 8(2): p. 171-U103.

[74] Levario, T.J., M. Zhan, B. Lim, S.Y. Shvartsman, and H. Lu, Microfluidic trap array for massively parallel imaging of Drosophila embryos. **Nature Protocols**, 2013. 8(4): p. 721-736.

[75] Bernstein, R.W., X.J. Zhang, S. Zappe, M. Fish, M. Scott, and O. Solgaard, Characterization of drosophila embryos immobilized by fluidic microassembly. **Boston Transducers'03: Digest of Technical Papers, Vols 1 and 2**, 2003: p. 987-990.

[76] Lucchetta, E.M., J.H. Lee, L.A. Fu, N.H. Patel, and R.F. Ismagilov, Dynamics of Drosophila embryonic patterning network perturbed in space and time using microfluidics. **Nature**, 2005. 434(7037): p. 1134-1138.

[77] Dagani, G.T., K. Monzo, J.R. Fakhoury, C.C. Chen, J.C. Sisson, and X.J. Zhang, Microfluidic self-assembly of live Drosophila embryos for versatile high-throughput analysis of embryonic morphogenesis. **Biomedical Microdevices**, 2007. 9(5): p. 681-694.

[78] Lucchetta, E.M., M.E. Vincent, and R.F. Ismagilov, A Precise Bicoid Gradient Is Nonessential during Cycles 11-13 for Precise Patterning in the Drosophila Blastoderm. **Plos One**, 2008. 3(11).

[79] McGorty, R., H. Liu, D. Kamiyama, Z.Q. Dong, S. Guo, and B. Huang, Open-top selective plane illumination microscope for conventionally mounted specimens. **Optics Express**, 2015. 23(12): p. 16142-16153.

[80] Adams, M.D., et al., The genome sequence of Drosophila melanogaster. **Science**, 2000. 287(5461): p. 2185-2195.

[81] Spradling, A.C., D. Stern, A. Beaton, E.J. Rhem, T. Laverty, N. Mozden, S. Misra, and G.M. Rubin, The Berkeley Drosophila Genome Project gene disruption project: Single P-element insertions mutating 25% of vital drosophila genes. **Genetics**, 1999. 153(1): p. 135-177.

[82] Mason, F.M., M. Tworoger, and A.C. Martin, Apical domain polarization localizes actin-myosin activity to drive ratchet-like apical constriction. **Nature Cell Biology**, 2013. 15(8): p. 926-U358.

[83] Gelbart, M.A., B. He, A.C. Martin, S.Y. Thiberge, E.F. Wieschaus, and M. Kaschube, Volume conservation principle involved in cell lengthening and nucleus movement during tissue morphogenesis. **Proceedings of the National Academy of Sciences of the United States of America**, 2012. 109(47): p. 19298-19303.

[84] Witzberger, M.M., J.A.J. Fitzpatrick, J.C. Crowley, and J.S. Minden, End-on Imaging: A New Perspective on Dorsoventral Development in Drosophila Embryos. **Developmental Dynamics**, 2008. 237(11): p. 3252-3259.

[85] Dsilva, C.J., B.Y. Lim, H. Lu, A. Singer, I.G. Kevrekidis, and S.Y. Shvartsman, Temporal ordering and registration of images in studies of developmental dynamics. **Development**, 2015. 142(9): p. 1717-1724.

[86] Lim, B., C.J. Dsilva, T.J. Levario, H. Lu, T. Schupbach, I.G. Kevrekidis, and S.Y. Shvartsman, Dynamics of Inductive ERK Signaling in the Drosophila Embryo. **Current Biology**, 2015. 25(13): p. 1784-1790.

[87] Lim, B., N. Samper, H. Lu, C. Rushlow, G. Jimenez, and S.Y. Shvartsman, Kinetics of gene derepression by ERK signaling. **Proceedings of the National Academy of Sciences of the United States of America**, 2013. 110(25): p. 10330-10335.

[88] Kim, Y., M.J. Andreu, B. Lim, K. Chung, M. Terayama, G. Jimenez, C.A. Berg, H. Lu, and S.Y. Shvartsman, Gene Regulation by MAPK Substrate Competition. **Developmental Cell**, 2011. 20(6): p. 880-887.

[89] Schock, F. and N. Perrimon, Retraction of the Drosophila germ band requires cell-matrix interaction. **Genes & Development**, 2003. 17(5): p. 597-602.

[90] Lynch, H.E., S.M. Crews, B. Rosenthal, E. Kim, R. Gish, K. Echiverri, and S. Hutson, Cellular mechanics of germ band retraction in Drosophila. **Developmental Biology**, 2013. 384(2): p. 205-213.

[91] Saias, L., J. Swoger, A. D'Angelo, P. Hayes, J. Colombelli, J. Sharpe, G. Salbreux, and J. Solon, Decrease in Cell Volume Generates Contractile Forces Driving Dorsal Closure. **Developmental Cell**, 2015. 33(5): p. 611-621.

[92] Zulueta-Coarasa, T., M. Tamada, E.J. Lee, and R. Fernandez-Gonzalez, Automated multidimensional image analysis reveals a role for Abl in embryonic wound repair. **Development**, 2014. 141(14): p. 2901-2911.

[93] Schindelin, J., et al., Fiji: an open-source platform for biological-image analysis. **Nature Methods**, 2012. 9(7): p. 676-682.

[94] de Chaumont, F., et al., Icy: an open bioimage informatics platform for extended reproducible research. **Nature Methods**, 2012. 9(7): p. 690-696.

[95] Carpenter, A.E., et al., CellProfiler: image analysis software for identifying and quantifying cell phenotypes. **Genome Biology**, 2006. 7(10).

[96] Kankaanpaa, P., L. Paavolainen, S. Tiitta, M. Karjalainen, J. Paivarinne, J. Nieminen, V. Marjomaki, J. Heino, and D.J. White, BioImageXD: an open, general-purpose and high-throughput image-processing platform. **Nature Methods**, 2012. 9(7): p. 683-689.

[97] Pietzsch, T., S. Saalfeld, S. Preibisch, and P. Tomancak, BigDataViewer: visualization and processing for large image data sets. **Nature Methods**, 2015. 12(6): p. 481-483.

[98] Peng, H.C., Z.C. Ruan, F.H. Long, J.H. Simpson, and E.W. Myers, V3D enables real-time 3D visualization and quantitative analysis of large-scale biological image data sets. **Nature Biotechnology**, 2010. 28(4): p. 348-U75.

[99] Kutsuna, N., T. Higaki, S. Matsunaga, T. Otsuki, M. Yamaguchi, H. Fujii, and S. Hasezawa, Active learning framework with iterative clustering for bioimage classification. **Nature Communications**, 2012. 3.

[100] Walter, T., et al., Visualization of image data from cells to organisms. **Nature Methods**, 2010. 7(3): p. S26-S41.

[101] Luengo-Oroz, M.A., M.J. Ledesma-Carbayo, N. Peyrieras, and A. Santos, Image analysis for understanding embryo development: a bridge from microscopy to biological insights. **Current Opinion in Genetics & Development**, 2011. 21(5): p. 630-637.

[102] Eliceiri, K.W., et al., Biological imaging software tools. **Nature Methods**, 2012. 9(7): p. 697-710.

[103] Hamilton, N.A., Open Source Tools for Fluorescent Imaging. **Imaging and Spectroscopic Analysis of Living Cells: Optical and Spectroscopic Techniques**, 2012. 504: p. 393-417.

[104] Jug, F., T. Pietzsch, S. Preibisch, and P. Tomancak, Bioimage Informatics in the context of Drosophila research. **Methods**, 2014. 68(1): p. 60-73.

[105] Khan, Z., Y.C. Wang, E.F. Wieschaus, and M. Kaschube, Quantitative 4D analyses of epithelial folding during Drosophila gastrulation. **Development**, 2014. 141(14): p. 2895-2900.

[106] Peng, H.C., F.F. Long, J. Zhou, G. Leung, M.B. Eisen, and E.W. Myers, Automatic image analysis for gene expression patterns of fly embryos. **Bmc Cell Biology**, 2007. 8.

[107] Bao, Z.R., J.I. Murray, T. Boyle, S.L. Ooi, M.J. Sandel, and R.H. Waterston, Automated cell lineage tracing in Caenorhabditis elegans. **Proceedings of the National Academy of Sciences of the United States of America**, 2006. 103(8): p. 2707-2712.

[108] Amat, F., W. Lemon, D.P. Mossing, K. McDole, Y. Wan, K. Branson, E.W. Myers, and P.J. Keller, Fast, accurate reconstruction of cell Lineages from Large-scale fluorescence microscopy data. **Nature Methods**, 2014. 11(9): p. 951-958.

[109] Fowlkes, C.C., et al., A quantitative spatiotemporal atlas of gene expression in the Drosophila blastoderm. **Cell**, 2008. 133(2): p. 364-374.

[110] Fowlkes, C.C., et al., A Conserved Developmental Patterning Network Produces Quantitatively Different Output in Multiple Species of Drosophila. **Plos Genetics**, 2011. 7(10).

[111] Ronneberger, O., et al., ViBE-Z: a framework for 3D virtual colocalization analysis in zebrafish larval brains. **Nature Methods**, 2012. 9(7): p. 735-U316.

[112] Kobitski, A.Y., et al., An ensemble-averaged, cell density-based digital model of zebrafish embryo development derived from light-sheet microscopy data with single-cell resolution. **Scientific Reports**, 2015. 5.

[113] Kaplan, T., X.Y. Li, P.J. Sabo, S. Thomas, J.A. Stamatoyannopoulos, M.D. Biggin, and M.B. Eisen, Quantitative Models of the Mechanisms That Control Genome-Wide Patterns of Transcription Factor Binding during Early Drosophila Development. **Plos Genetics**, 2011. 7(2).

[114] Yin, Z., et al., A screen for morphological complexity identifies regulators of switch-like transitions between discrete cell shapes. **Nature Cell Biology**, 2013. 15(7): p. 860-+.

[115] Collinet, C., et al., Systems survey of endocytosis by multiparametric image analysis. **Nature**, 2010. 464(7286): p. 243-U123.

[116] Liberali, P., B. Snijder, and L. Pelkmans, A Hierarchical Map of Regulatory Genetic Interactions in Membrane Trafficking. **Cell**, 2014. 157(6): p. 1473-1487.

[117] Murray, J.I., Z. Bao, T.J. Boyle, M.E. Boeck, B.L. Mericle, T.J. Nicholas, Z. Zhao, M.J. Sandel, and R.H. Waterston, Automated analysis of embryonic gene expression with cellular resolution in C-elegans. **Nature Methods**, 2008. 5(8): p. 703-709.

[118] Danuser, G., Computer Vision in Cell Biology. **Cell**, 2011. 147(5): p. 973-978.

[119] Sommer, C. and D.W. Gerlich, Machine learning in cell biology - teaching computers to recognize phenotypes. **Journal of Cell Science**, 2013. 126(24): p. 5529-5539.

[120] Zhong, Q., A.G. Busetto, J.P. Fededa, J.M. Buhmann, and D.W. Gerlich, Unsupervised modeling of cell morphology dynamics for time-lapse microscopy. **Nature Methods**, 2012. 9(7): p. 711-U267.

[121] Levario, T.J., C. Zhao, T. Rouse, S.Y. Shvartsman, and H. Lu, An integrated platform for large-scale data collection and precise perturbation of live Drosophila embryos. **Scientific Reports**, 2016. 6.

[122] Wang, Y.C., Z. Khan, M. Kaschube, and E.F. Wieschaus, Differential positioning of adherens junctions is associated with initiation of epithelial folding. **Nature**, 2012. 484(7394): p. 390-393.

[123] Ohki, K., S. Chung, Y.H. Ch'ng, P. Kara, and R.C. Reid, Functional imaging with cellular resolution reveals precise micro-architecture in visual cortex. **Nature**, 2005. 433(7026): p. 597-603.

[124] Chen, T.W., et al., Ultrasensitive fluorescent proteins for imaging neuronal activity. **Nature**, 2013. 499(7458): p. 295-+.

[125] Kerr, R., V. Lev-Ram, G. Baird, P. Vincent, R.Y. Tsien, and W.R. Schafer, Optical imaging of calcium transients in neurons and pharyngeal muscle of C-elegans. **Neuron**, 2000. 26(3): p. 583-594.

[126] Tomer, R., K. Khairy, F. Amat, and P.J. Keller, Quantitative high-speed imaging of entire developing embryos with simultaneous multiview light-sheet microscopy. **Nature Methods**, 2012. 9(7): p. 755-U181.

[127] Krzic, U., S. Gunther, T.E. Saunders, S.J. Streichan, and L. Hufnagel, Multiview light-sheet microscope for rapid in toto imaging. **Nature Methods**, 2012. 9(7): p. 730-U304.

[128] Keller, P.J., Imaging Morphogenesis: Technological Advances and Biological Insights. **Science**, 2013. 340(6137): p. 1184-+.

[129] Scherf, N. and J. Huisken, The smart and gentle microscope. **Nature Biotechnology**, 2015. 33(8): p. 815-818.

[130] Bassi, A., B. Schmid, and J. Huisken, Optical tomography complements light sheet microscopy for in toto imaging of zebrafish development. **Development**, 2015. 142(5): p. 1016-1020.

[131] Chingozha, L., M. Zhan, C. Zhu, and H. Lu, A Generalizable, Tunable Microfluidic Platform for Delivering Fast Temporally Varying Chemical Signals to Probe Single-Cell Response Dynamics. **Analytical Chemistry**, 2014. 86(20): p. 10138-10147.

[132] Kanodia, J.S., Y. Kim, R. Tomer, Z. Khan, K.H. Chung, J.D. Storey, H. Lu, P.J. Keller, and S.Y. Shvartsman, A computational statistics approach for estimating the spatial range of morphogen gradients. **Development**, 2011. 138(22): p. 4867-4874.

[133] Lim, B., C.J. Dsilva, T.J. Levario, H. Lu, T. Schupbach, I.G. Kevrekidis, and S.Y. Shvartsman, Dynamics of Inductive ERK Signaling in the Drosophila Embryo. **Curr Biol**, 2015. 25(13): p. 1784-90.

[134] Ellis, S.J., et al., Talin Autoinhibition Is Required for Morphogenesis. **Current Biology**, 2013. 23(18): p. 1825-1833.

[135] Duffy, D.C., J.C. McDonald, O.J.A. Schueller, and G.M. Whitesides, Rapid prototyping of microfluidic systems in poly(dimethylsiloxane). **Analytical Chemistry**, 1998. 70(23): p. 4974-4984.

[136] Foe, V.E. and B.M. Alberts, Studies of Nuclear and Cytoplasmic Behavior during the 5 Mitotic-Cycles That Precede Gastrulation in Drosophila Embryogenesis. **Journal of Cell Science**, 1983. 61(May): p. 31-70.

[137] Berger, S.A., L. Talbot, and L.S. Yao, Flow in Curved Pipes. **Annual Review of Fluid Mechanics**, 1983. 15: p. 461-512.

[138] Di Carlo, D., D. Irimia, R.G. Tompkins, and M. Toner, Continuous inertial focusing, ordering, and separation of particles in microchannels. **Proceedings of the National Academy of Sciences of the United States of America**, 2007. 104(48): p. 18892-18897.

[139] Bhagat, A.A.S., S.S. Kuntaegowdanahalli, and I. Papautsky, Continuous particle separation in spiral microchannels using dean flows and differential migration. **Lab on a Chip**, 2008. 8(11): p. 1906-1914.

[140] Lee, H., S.A. Kim, S. Coakley, P. Mugno, M. Hammarlund, M.A. Hilliard, and H. Lu, A multi-channel device for high-density target-selective stimulation and long-term monitoring of cells and subcellular features in C. elegans. **Lab on a Chip**, 2014. 14(23): p. 4513-4522.

[141] Genbacev, O., R. Joslin, C.H. Damsky, B.M. Polliotti, and S.J. Fisher, Hypoxia alters early gestation human cytotrophoblast differentiation/invasion in vitro and models the placental defects that occur in preeclampsia. **J Clin Invest**, 1996. 97(2): p. 540-50.

[142] Wingrove, J.A. and P.H. O'Farrell, Nitric oxide contributes to behavioral, cellular, and developmental responses to low oxygen in Drosophila. **Cell**, 1999. 98(1): p. 105-14.

[143] Simon, M.C. and B. Keith, The role of oxygen availability in embryonic development and stem cell function. **Nat Rev Mol Cell Biol**, 2008. 9(4): p. 285-96.

[144] Dunwoodie, S.L., The role of hypoxia in development of the Mammalian embryo. **Dev Cell**, 2009. 17(6): p. 755-73.

[145] DiGregorio, P.J., J.A. Ubersax, and P.H. O'Farrell, Hypoxia and nitric oxide induce a rapid, reversible cell cycle arrest of the drosophila syncytial divisions. **Journal of Biological Chemistry**, 2001. 276(3): p. 1930-1937.

[146] Douglas, R.M., T. Xu, and G.G. Haddad, Cell cycle progression and cell division are sensitive to hypoxia in Drosophila melanogaster embryos. **American Journal of Physiology-Regulatory Integrative and Comparative Physiology**, 2001. 280(5): p. R1555-R1563.

[147] Fischer, M.G., S. Heeger, U. Hacker, and C.F. Lehner, The mitotic arrest in response to hypoxia and of polar bodies during early embryogenesis requires Drosophila Mps1. **Current Biology**, 2004. 14(22): p. 2019-2024.

[148] Douglas, R.M., R. Farahani, P. Morcillo, A. Kanaan, T. Xu, and G.G. Haddad, Hypoxia induces major effects on cell cycle kinetics and protein expression in Drosophila melanogaster embryos. **Am J Physiol Regul Integr Comp Physiol**, 2005. 288(2): p. R511-21.

[149] Pandey, R., S. Heeger, and C.F. Lehner, Rapid effects of acute anoxia on spindle kinetochore interactions activate the mitotic spindle checkpoint. **Journal of Cell Science**, 2007. 120(16): p. 2807-2818.

[150] Foe, V.E. and B.M. Alberts, Reversible Chromosome Condensation Induced in Drosophila Embryos by Anoxia - Visualization of Interphase Nuclear-Organization. **Journal of Cell Biology**, 1985. 100(5): p. 1623-1636.

[151] Teodoro, R.O. and P.H. O'Farrell, Nitric oxide-induced suspended animation promotes survival during hypoxia. **Embo Journal**, 2003. 22(3): p. 580-587.

[152] McClure, K.D., R.L. French, and U. Heberlein, A Drosophila model for fetal alcohol syndrome disorders: role for the insulin pathway. **Disease Models & Mechanisms**, 2011. 4(3): p. 335-346.

[153] Rujano, M.A., L. Sanchez-Pulido, C. Pennetier, G. le Dez, and R. Basto, The microcephaly protein Asp regulates neuroepithelium morphogenesis by controlling the spatial distribution of myosin II. **Nature Cell Biology**, 2013. 15(11): p. 1294-U87.

[154] Pandey, U.B. and C.D. Nichols, Human Disease Models in Drosophila melanogaster and the Role of the Fly in Therapeutic Drug Discovery. **Pharmacological Reviews**, 2011. 63(2): p. 411-436.

[155] Chung, K.H., C.A. Rivet, M.L. Kemp, and H. Lu, Imaging Single-Cell Signaling Dynamics with a Deterministic High-Density Single-Cell Trap Array. **Analytical Chemistry**, 2011. 83(18): p. 7044-7052.

[156] Skelley, A.M., O. Kirak, H. Suh, R. Jaenisch, and J. Voldman, Microfluidic control of cell pairing and fusion. **Nature Methods**, 2009. 6(2): p. 147-152.

[157] Voldman, J., M.L. Gray, M. Toner, and M.A. Schmidt, A microfabrication-based dynamic array cytometer. **Analytical Chemistry**, 2002. 74(16): p. 3984-3990.

[158] Taff, B.M. and J. Voldman, A scalable addressable positive-dielectrophoretic cell-sorting array. **Analytical Chemistry**, 2005. 77(24): p. 7976-7983.

[159] Irimia, D. and M. Toner, Cell handling using microstructured membranes. **Lab on a Chip**, 2006. 6(3): p. 345-352.

[160] Wheeler, A.R., W.R. Throndset, R.J. Whelan, A.M. Leach, R.N. Zare, Y.H. Liao, K. Farrell, I.D. Manger, and A. Daridon, Microfluidic device for single-cell analysis. **Analytical Chemistry**, 2003. 75(14): p. 3581-3586.

[161] Idema, T., J.O. Dubuis, L. Kang, M.L. Manning, P.C. Nelson, T.C. Lubensky, and A.J. Liu, The Syncytial Drosophila Embryo as a Mechanically Excitable Medium. **Plos One**, 2013. 8(10).

[162] Marshall, C.J., Specificity of Receptor Tyrosine Kinase Signaling - Transient Versus Sustained Extracellular Signal-Regulated Kinase Activation. **Cell**, 1995. 80(2): p. 179-185.

[163] Hubbard, S.R. and W.T. Miller, Receptor tyrosine kinases: mechanisms of activation and signaling. **Current Opinion in Cell Biology**, 2007. 19(2): p. 117-123.

[164] Schlessinger, J., Cell signaling by receptor tyrosine kinases. **Cell**, 2000. 103(2): p. 211-225.

[165] Li, W.X., Functions and mechanisms of receptor tyrosine kinase torso signaling: Lessons from Drosophila embryonic terminal development. **Developmental Dynamics**, 2005. 232(3): p. 656-672.

[166] Futran, A.S., A.J. Link, R. Seger, and S.Y. Shvartsman, ERK as a Model for Systems Biology of Enzyme Kinetics in Cells. **Current Biology**, 2013. 23(21): p. R972-R979.

[167] Cinnamon, E., A. Helman, R.B.H. Schyr, A. Orian, G. Jimenez, and Z. Paroush, Multiple RTK pathways downregulate groucho-mediated repression in Drosophila embryogenesis. **Development**, 2008. 135(5): p. 829-837.

[168] Choi, C.Y., Y.H. Kim, Y.O. Kim, S.J. Park, E.A. Kim, W. Riemenschneider, K. Gajewski, R.A. Schulz, and Y. Kim, Phosphorylation by the DHIPK2 protein kinase modulates the corepressor activity of groucho. **Journal of Biological Chemistry**, 2005. 280(22): p. 21427-21436.

[169] Jimenez, G., S.Y. Shvartsman, and Z. Paroush, The Capicua repressor - a general sensor of RTK signaling in development and disease. **Journal of Cell Science**, 2012. 125(6): p. 1383-1391.

[170] Grimm, O., V.S. Zini, Y. Kim, J. Casanova, S.Y. Shvartsman, and E. Wieschaus, Torso RTK controls Capicua degradation by changing its subcellular localization. **Development**, 2012. 139(21): p. 3962-3968.

[171] Jindal, G.A., Y. Goyal, R.D. Burdine, K.A. Rauen, and S.Y. Shvartsman, RASopathies: unraveling mechanisms with animal models. **Disease Models & Mechanisms**, 2015. 8(8): p. 769-U403.

[172] Schubbert, S., K. Shannon, and G. Bollag, Hyperactive Ras in developmental disorders and cancer. **Nature Reviews Cancer**, 2007. 7(4): p. 295-308.

[173] Rauen, K.A., The RASopathies. **Annual Review of Genomics and Human Genetics, Vol 14**, 2013. 14: p. 355-369.

[174] Zhao, C.L., A. Kniss, T. Levario, K. Shen, and H. Lu, Rapid and Simple Quantitative Phenotyping of Fluorescently-labeled Biological Systems with Relative Difference Filtering and Clustering. **Nature Communications (submitted)**, 2016.

[175] Levario, T.J., C. Zhao, S.Y. Shvartsman, and H. Lu, High-throughput arraying and imaging of laterally oriented live Drosophila embryos. **Lab on a Chip**, 2016.

[176] Coppey, M., A.N. Boettiger, A.M. Berezhkovskii, and S.Y. Shvartsman, Nuclear trapping shapes the terminal gradient in the Drosophila embryo. **Curr Biol**, 2008. 18(12): p. 915-9.

[177] Kuntz, S.G. and M.B. Eisen, Drosophila embryogenesis scales uniformly across temperature in developmentally diverse species. **PLoS Genet**, 2014. 10(4): p. e1004293.

[178] Stephens, G.J., B. Johnson-Kerner, W. Bialek, and W.S. Ryu, Dimensionality and dynamics in the behavior of C. elegans. **PLoS Comput Biol**, 2008. 4(4): p. e1000028.